University of Alberta

The Behavior of Loose Gassy Sand and its Susceptibility to Liquefaction

by

Jocelyn Louise Hayley Grozic ©

A thesis submitted to the Faculty of Graduate Studies and Research in partial
fulfillment of the requirements for the degree of
Doctor of Philosophy

in

Geotechnical Engineering

Department of Civil and Environmental Engineering

Edmonton, Alberta

Fall 1999

National Library
of Canada

Acquisitions and
Bibliographic Services

395 Wellington Street
Ottawa ON K1A 0N4
Canada

Bibliothèque nationale
du Canada

Acquisitions et
services bibliographiques

395, rue Wellington
Ottawa ON K1A 0N4
Canada

Your file Votre référence

Our file Notre référence

The author has granted a non-exclusive licence allowing the National Library of Canada to reproduce, loan, distribute or sell copies of this thesis in microform, paper or electronic formats.

L'auteur a accordé une licence non exclusive permettant à la Bibliothèque nationale du Canada de reproduire, prêter, distribuer ou vendre des copies de cette thèse sous la forme de microfiche/film, de reproduction sur papier ou sur format électronique.

The author retains ownership of the copyright in this thesis. Neither the thesis nor substantial extracts from it may be printed or otherwise reproduced without the author's permission.

L'auteur conserve la propriété du droit d'auteur qui protège cette thèse. Ni la thèse ni des extraits substantiels de celle-ci ne doivent être imprimés ou autrement reproduits sans son autorisation.

0-612-46843-7

Canada

University of Alberta

Library Release Form

Name of Author: Jocelyn Louise Hayley Grozic

Title of Thesis: The Behavior of Loose Gassy Sand and its Susceptibility to Liquefaction

Degree: Doctor of Philosophy

Year the Degree Granted: 1999

Permission is hereby granted to the University of Alberta Library to reproduce single copies of this thesis and to lend or sell copies for private, scholarly, or scientific research purposes only.

The author reserves all other publication and other rights in association with the copyright in the thesis, and except as hereinbefore provided, neither the thesis nor any substantial portion thereof may be printed or otherwise reproduced in any material from whatever without the author's prior written permission.

Jocelyn L. H. Grozic

7110 Brent Road
Site 16, Camp A1, RR #1
Peachland, British Columbia
V0H 1X0

Sept 22, 1999

Date Submitted to the Faculty of
Graduate Studies and Research

University of Alberta

Faculty of Graduate Studies and Research

The undersigned certify that they have read, and recommend to the Faculty of Graduate Studies and Research for acceptance, a thesis entitled **The Behavior of Loose Gassy Sand and its Susceptibility to Liquefaction** by **Jocelyn Louise Hayley Grozic** in partial fulfillment of the requirements for the degree of Doctor of Philosophy in Geotechnical Engineering.

Dr. P.K. Robertson (Supervisor)

Dr. N.R. Morgenstern (Supervisor)

Dr. R. Chalaturnyk

FEHicks

Dr. F.E. Hicks

Y. Feng.

Dr. Y. Feng

Gillian Sills

Dr. G.C. Sills (External Examiner)

Sept 20 1998

Date of Approval by Committee

ABSTRACT

Gas can be found in many soils, but none more common than seabed soils. Gas-charged sediments are widely distributed throughout the world's oceans. Occurrences have been reported in coastal and estuarine regions, across the continental shelves, and deep within ocean basins. Recently documented cases have observed several submarine slopes known to contain methane gas, to experience flow or cyclic liquefaction.

Although gassy soil behavior has been studied by various researchers, the emphasis has been on fine grained soils or in some instances dense sands. There appears to be no published research work that studies the effect of gas on the behavior of loose sand. The objective of this thesis was to determine how the presence of gas affects the potential for flow and cyclic liquefaction.

In setting up the experimental facilities, a new method to measure gas content using a time domain reflectometry mini-probe was developed. Laboratory testing consisted of static and cyclic triaxial tests performed on saturated and gassy samples. Static test results showed that loosely prepared specimens with an initial degree of saturation greater than approximately 80% strain softened and experienced flow liquefaction, while loose specimens with an initial degree of saturation less than 80% were not susceptible to flow liquefaction. Cyclic triaxial test results showed that the resistance to cyclic liquefaction was increased by the presence of even a small amount of gas.

A constitutive model, developed at the University of Alberta that simulates the behavior of saturated loose sand samples was modified to account for the effects of gas. The modifications involved incorporating the increased compressibility of the soil as well as the equilibrium behavior of gas. The modified model captured the behavior of loose gassy sands subjected to static loading.

This research has shown that loose gassy sand can experience flow and cyclic liquefaction. The laboratory results indicate that the resistance to liquefaction increases with decreasing degree of saturation. Guidelines for determining the potential for flow and cyclic liquefaction are suggested. By integrating the laboratory and numerical work, an initial understanding of the effect of gas on the liquefaction potential of loose sands was developed.

ACKNOWLEDGEMENTS

I thank my supervisors, Dr. Peter K. Robertson and Dr. Norbert R. Morgenstern, for their guidance and enthusiasm, and their continual encouragement through this endeavor. Their support throughout the research and writing of this thesis is gratefully appreciated. Dr. Robertson, thank-you for your attention to detail and advice through out this thesis. Dr. Morgenstern, thank-you for your global vision and with helping me keep the "big picture" in mind.

I thank the other staff members in the Geotechnical Group for their continuing encouragement. Thanks to Dr. Dave C. Sego for the opportunity to perform some consulting work and thereby broaden my laboratory skills, to Dr. Dave Chan, for introducing me to web publishing and teaching me that I can learn anything I set my mind to, and to Sally Petaske, for always being helpful. I would also like to thank the rest of the staff of the Department of Civil and Environmental Engineering.

I thank Steve Gamble for all his help in the laboratory, for the never-ending encouragement, and for putting up with my "bad" experimental days. I also wish to thank Gerry Cyre, for his help, humor, and ingenuity in the laboratory, and Christine Hereygers, for her laboratory help and sense of humor.

I would like to thank Harold Christian of the Geological Survey of Canada for his guidance early on in my research, as well as the opportunity to partake in an offshore drilling program. The exposure to laboratory and field work that my research provided me has been an immense benefit to my development.

I gratefully acknowledge the financial support provided by NSERC and the University of Alberta. I am grateful to the University of Alberta and the Department of Civil and Environmental Engineering for providing me with the opportunity to act as a teaching and research assistant and a sessional lecturer during my time in graduate studies. I

would also like to thank my students and the staff for the acknowledgement of my teaching efforts with the 1998 and 1999 Leonard E. Gads Teaching Assistant Awards from the Faculty of Engineering and the 1998 and 1999 Graduate Student Teaching Awards from University Teaching Services.

On a more personal note, I thank my parents, Don and Dianne, and my brothers, Sandy and Kevin, for their love, support, and encouragement through the last four years. I would like to thank both my parents for their eternal optimism. My Dad for his true love of engineering which is a constant source of inspiration, and my Mom for her connection to nature which has given me a sense of spiritualism. I am grateful for the encouragement from my grandmother, Isabel, and my in-laws, Maria and Graciano, Mark and Carmela, and Robert.

I would also like to thank my many friends and colleges who helped me through graduate school. A special thanks to my good friend and lab buddy, Michel Lefebvre, for his enormous help with the TDR; not only in developing the mini-probe but also for writing a special "crash-proof" version of his software for me. A special thanks also to my dear friend Kristi McKay for her constant support and encouragement. Thanks to my former office mate, Catherine Wride, for her grammar lessons and continuing friendship. I would also like to thank Reza Imam for not only providing me with an electronic copy of his constitutive model but for also the many tutorials. I am also grateful to Brian Wilson for showing me the "ins and outs" of consulting and for Dr. Elmer Brooker for teaching me that no task (or person) is too great to take on.

Finally, I would like to express my deepest gratitude and love for my husband, Edie Grozic. Not only did he proof read my entire thesis, but he also willingly and cheerfully read ever paper, poster, presentation over the last four years. His love and encouragement throughout my thesis provided me with the support I needed to undertake such an endeavor. His gentle manner and warm humor inspire me to be a better person. May we all be so lucky to have such a soul mate.

TABLE OF CONTENTS

Page

LIST OF TABLES

LIST OF FIGURES

LIST OF SYMBOLS

CHAPTER 1: INTRODUCTION

1.1 THE OCCURRENCE OF GAS CHARGED SEDIMENTS 1
1.2 THE IMPLICATIONS OF GAS CHARGED SEABED SOILS 2
  1.2.1 Detection of Gas 3
  1.2.2 Foundation Design 3
  1.2.3 Gas Accumulations 3
  1.2.4 Environmental Effects 4
  1.2.5 Submarine Flow Slides 4
1.3 LIQUEFACTION FLOW SLIDES IN SUBMARINE AND COASTAL SEDIMENTS 4
  1.3.1 Framework for Liquefaction 5
    a) Liquefaction Phenomenon 5
    b) Liquefaction Terminology 5
      (i) Flow liquefaction 5
      (ii) Cyclic liquefaction 6

1.3.2 History of Submarine Liquefaction Flow Slides 7
- a) Statically-Induced Liquefaction Flow Slides 7
  - *(i) The Netherlands* 7
  - *(ii) Norway* 7
  - *(iii) United States* 8
  - *(iv) Canada* 8
  - *(v) Observations from the historical flow slides* 9
- b) Earthquake-Induced Liquefaction Flow Slides 9
  - *(i) United States* 9
  - *(ii) Chile* 10
  - *(iii) Japan* 10
  - *(iv) Greece* 11
  - *(v) Observations from the historical earthquake-induced flow slides* 11

1.4 CASE HISTORIES 11

1.4.1 The Fraser River Delta 12
- a) Physical Setting 12
- b) Seabed Instability of the Fraser River Delta 13
- c) Instability of Gaseous Fraser River Delta Sediments 14
- d) Conclusions 14

1.4.2 The Klamath River Delta, California 15
- a) Physical Setting 15
- b) Liquefaction Flow Slide 16
- c) Seafloor Gas Seeps Triggered by the Earthquake 16
- d) Relation of Gas Seeps to Liquefaction 17
- e) Conclusions 17

1.4.3 Observations 17

1.5 THESIS OBJECTIVES 18

CHAPTER 2: OVERVIEW OF GASSY SOILS

2.1 INTRODUCTION 30

2.2 TERMINOLOGY 31

- **2.2.1 Unsaturated Soils** 31
- **2.2.2 Gassy Soils** 31

2.3 ORIGIN OF GAS 32

- **2.3.1 Organic Origins** 32
- **2.3.2 Inorganic Origins** 32
- **2.3.3 Gas Hydrates** 33

2.4 EVIDENCE OF GAS 33

- **2.4.1 Marine Sediments** 33
  - a) Seismic Evidence 33
  - b) Geochemical Evidence 35
  - c) Indirect Evidence 35
- **2.4.2 Athabasca Oilsands** 37
- **2.4.3 Alto Lazio Nuclear Power Plant, Italy** 37

2.5 PREVIOUS RESEARCH 38

- **2.5.1 University of Alberta** 38
- **2.5.2 United States** 39
- **2.5.3 Great Britain** 39
- **2.5.4 Norway** 41
- **2.5.5 Eckernförde Bay Study** 41
- **2.5.6 Other Research** 42

2.6 SUMMARY AND CONCLUSIONS 42

CHAPTER 3: LABORATORY PROGRAM

3.1 INTRODUCTION 47
3.2 GENERAL CONSIDERATIONS 48
  3.2.1 Material 48
  3.2.2 Gas Type 49
  3.2.3 Target Pressures 50
3.3 EQUIPMENT DESIGN FOR MONOTONIC TESTING 51
  3.3.1 Measuring Strains 51
  3.3.2 Measuring Pressures 51
  3.3.3 Measuring Deviatoric Stress 51
  3.3.4 Measuring Volume Change 52
  3.3.5 Cell Construction 52
  3.3.6 Loading Frame 52
  3.3.7 Data Acquisition 53
3.4 EQUIPMENT DESIGN FOR CYCLIC TESTING 53
  3.4.1 Measuring Strains 53
  3.4.2 Measuring Pressures and Volume Change 54
  3.4.3 Measuring Deviatoric Stress 54
  3.4.4. Cell Construction 54
  3.4.5 Loading Frame 54
  3.4.6 Data Acquisition and Computer Control 54
3.5 BUBBLE CHAMBER DESIGN 55
3.6 MEASUREMENT OF GAS CONTENT 56
  3.6.1 General Considerations 56
  3.6.2 Cell Volume Change 56
  3.6.3 Double Walled Triaxial 57
  3.6.4 Radial Strain Gauge 57
  3.6.5 P-Wave and Bender Elements 57
  3.6.6 Dielectric Constant 58

3.7 TIME DOMAIN REFLECTOMETRY TO MEASURE GAS CONTENT 58
  3.7.1 Dielectric Constant 58
  3.7.2 Theory of Time Domain Reflectometry 59
  3.7.3 Equipment and Waveform Analysis 61
    a) TDR Unit 61
    b) Probe Development 62
    c) Waveform Analysis 62
  3.7.4 Soil Moisture Content Determination 63
  3.7.5 Calibration for Volumetric Water Content and Degree of Saturation 64
  3.7.6 Using the TDR to Determine Gas Content 65
  3.7.7 Accuracy of the TDR Method 65
3.8 SUMMARY AND CONCLUSIONS 66

CHAPTER 4: LABORATORY TESTING PROCEDURE

4.1 INTRODUCTION 84
4.2 SPECIMEN PREPARATION 84
  4.2.1 A Summary of Sample Preparation Methods for Sand 85
  4.2.2 The Moist Tamping Technique 86
  4.2.3 Specimen Preparation using Moist Tamping 87
  4.2.4 Sample Assembly 88
  4.2.5 Specimen Uniformity 88
  4.2.6 Effect of Sample Preparation Technique on Static Undrained Shear Strength 89
  4.2.7 Effect of Sample Preparation Technique on Cyclic Resistance Ratio 90

4.3 TEST PROCEDURES 91
    4.3.1 Saturating with Water 91
    4.3.2 Ensuring Full Saturation 92
    4.3.3 Saturating with Water and Dissolved Carbon Dioxide Gas 92
    4.3.4 Consolidation 93
4.4 CALCULATION OF VOID RATIO 94
    4.4.1 Void Ratio based on Initial Specimen Dimensions 94
    4.4.2 Void Ratio based on Final Specimen Moisture Content 95
    4.4.3 Calculation of Void Ratio 95
4.5 MONOTONIC TRIAXIAL TESTING 96
    4.5.1 Stress Path 96
    4.5.2 Saturated Specimens 96
    4.5.3 Gassy Specimens 97
    4.5.4 Time Domain Reflectometry 97
4.6 CYCLIC TRIAXIAL TESTING 97
    4.6.1 Stress Path 97
    4.6.2 Saturated Specimens 98
    4.6.3 Gassy Specimens 98
    4.6.4 Time Domain Reflectometry 99
4.7 SUMMARY AND CONCLUSIONS 99

CHAPTER 5: MONOTONIC TRIAXIAL LABORATORY RESULTS

5.1 INTRODUCTION 104
5.2 STATE BOUNDARY SURFACE FOR VERY LOOSE SAND 105
5.3 RANGE OF RESPONSE 108

5.4 SPECIMEN RESULTS 109
5.4.1 Saturated Test Results 110
5.4.2 Gassy Test Results 111
5.5 STATE BOUNDARY SURFACE FOR OTTAWA SAND 113
5.6 FLOW LIQUEFACTION POTENTIAL OF LOOSE GASSY SAND 114
5.6.1 Effects of Density and Initial Consolidation Stress 115
5.6.2 Effect of Soil Structure 116
5.6.3 Effect of Grain Characteristics 116
5.6.4 Effect of Shearing Mode and Rate 117
a) Mode of Shearing 117
b) Rate of Shearing 118
5.6.5 Effect of Gas 119
a) Initial Degree of Saturation 119
b) Gas Characteristics 121
5.7 COMPARISON WITH PUBLISHED DATA 122
5.8 SUMMARY AND CONCLUSIONS 123

CHAPTER 6: CYCLIC TRIAXIAL RESULTS

6.1 INTRODUCTION 150
6.2 PREVIOUS RESEARCH 151
6.3 CYCLIC RESISTANCE BASED ON LABORATORY TESTING 152
6.4 LABORATORY RESULTS 154
6.4.1 Saturated Specimen Results 154
6.4.2 Gassy Specimen Results 155

6.5 CYCLIC LIQUEFACTION OF GASSY OTTAWA SAND 157
    6.5.1 Effect of Initial Confining Stress 157
    6.5.2 Effect of Density 158
    6.5.3 Effect of Soil Structure 159
    6.5.4 Effect of Grain Characteristics 159
    6.5.5 Effect of Loading Intensity, Duration, and Frequency 160
    6.5.6 Effect of Gas 160
6.6 COMPARISON WITH CANLEX DATA 163
6.7 SUMMARY AND CONCLUSIONS 164

CHAPTER 7: CONSTITUTIVE MODELING OF GASSY SOIL BEHAVIOR

7.1 INTRODUCTION 185
7.2 EQUILIBRIUM AND TRANSIENT BEHAVIOR OF GASSY SOILS 186
    7.2.1 Boyle's and Henry's Laws 187
        a) Boyle's Law 187
        b) Henry's Law 188
    7.2.2 Compressibility of the Pore Fluids 189
        a) Compressibility of a Gas 190
        b) Compressibility of a Liquid 192
        c) Compressibility of a Liquid/Gas Mixture 192
    7.2.3 Theoretical Pore Pressure Response 195
    7.2.4 Transient Response of Gas 197

7.3 **A CONSTITUTIVE MODEL FOR LOOSE SAND** 199
  7.3.1 **Model Characteristics** 201
  7.3.2 **Model Elements** 202
    a) The Yield Surface 202
    b) The Plastic Potential 204
    c) Sand Compressibility 206
    d) The Hardening Rule 206
      (i) Size hardening 206
      (ii) Shape of the yield surface 207
    e) Elasticity 207
  7.3.3 **Model Calibration** 208
  7.3.4 **Model Performance** 210
  7.3.5 **Summary** 211
7.4 **MODELING THE CONSTITUTIVE BEHAVIOR OF LOOSE GASSY SAND** 212
  7.4.1 **The Model** 212
  7.4.2 **Model Performance** 212
    a) Modeling the Effect of Gas 212
    b) Modeling the Collapse Behavior of Loose Saturated Ottawa Sand 214
    c) Modeling the Collapse Behavior of Loose Gassy Ottawa Sand 214
    d) Modeling the Effect of Gas Characteristics 216
  7.4.3 **Model Performance and Limitations** 217
7.5 **SUMMARY AND CONCLUSIONS** 218

CHAPTER 8: DISCUSSION AND CONCLUSIONS

8.1 OVERVIEW 242
8.2 GASSY SOILS 243
8.3 LABORATORY PROGRAM 244
8.4 FLOW LIQUEFACTION POTENTIAL OF LOOSE GASSY SAND 245
8.5 CYCLIC LIQUEFACTION RESISTANCE OF LOOSE GASSY SAND 248
8.6 MODELING THE CONSTITUTIVE BEHAVIOR OF LOOSE GASSY SAND 250
8.7 GUIDELINES FOR EVALUATING LIQUEFACTION POTENTIAL OF LOOSE GASSY SAND 251
    8.7.1 Potential for Flow Liquefaction 251
    8.7.2 Potential for Cyclic Liquefaction 252
    8.7.3 Cautionary Notes 252
8.8 CONTRIBUTIONS 253
8.9 RECOMMENDATIONS FOR FUTURE WORK 254
    8.9.1 Liquefaction of Gassy Soils 254
    8.9.2 Geotechnical Properties of Gassy Sands 255
8.10 FINAL REMARKS 256

REFERENCES

LIST OF REFERENCES 257

APPENDIX A: MONOTONIC TRIAXIAL TEST RESULTS

APPENDIX A 275

APPENDIX B: CYCLIC TRIAXIAL TEST RESULTS

APPENDIX B 299

APPENDIX C: CYCLIC TRIAXIAL TESTS THAT DID NOT FAIL

APPENDIX C 316

LIST OF TABLES

Page

CHAPTER 1

Table 1.1 Earthquake-induced flow slides in submarine deposits (after Chillarige et al. 1997a) 21

Table 1.2 Statically-induced liquefaction flow slides in submarine deposits (after Chillarige et al. 1997a) 22

CHAPTER 2

Table 2.1 Sources of natural gas (modified from Floodgate and Judd 1992) 44

CHAPTER 5

Table 5.1 Summary of specimen results 127

CHAPTER 6

Table 6.1 Correction factors for influence of earthquake magnitude on cyclic resistance ratio (after Seed et al. 1985) 167

Table 6.2 Specimen summary for cyclic triaxial results 168

CHAPTER 7

Table 7.1 Model parameters used in predictions for Ottawa sand. All unit dependent parameters are given assuming that (p) is substituted in the equations in terms of kPa, except were stated otherwise 221

APPENDIX A

Table A.1 Summary of monotonic triaxial results 279

APPENDIX B

Table B.1 Summary of cyclic triaxial results 300

APPENDIX C

Table C.1 Summary of cyclic triaxial results for specimens that did not fail 317

LIST OF FIGURES

Page

CHAPTER 1

Figure 1.1 Worldwide distribution of shallow water sediments that contain free gas. Most sites are based on seismo-acoustic survey techniques. The actual distribution of gassy sediments is probably much greater, especially in the poorly surveyed southern hemisphere. The numbers corresponds to references available from M.D. Richardson. (modified from Richardson and Davis 1992) 23

Figure 1.2 Schematic of undrained monotonic behavior of sand in triaxial compression (modified from Robertson 1994). LSS, limited strain-softening response; q_{ST}, static gravitational shear stress; S_u, ultimate undrained shear strength; SH, strain-hardening response; SS, strain-softening response; US, ultimate state 24

Figure 1.3 Schematic illustration of cyclic liquefaction (modified from Robertson 1994) 25

Figure 1.4 Schematic illustration of cyclic mobility (modified from Robertson 1994) 26

Figure 1.5 Fraser River delta front (after McKenna et al. 1992) 27

Figure 1.6 Surficial deposits in the Fraser River delta (after Luternauer and Finn 1983) 28

Figure 1.7 California – Oregon continental margin showing location and tectonic setting of study area and epicenter of November 8, 1980, earthquake (modified from Field et al. 1982) 29

CHAPTER 2

Figure 2.1 Undrained equilibrium behaviour of an element of soil on unloading: effect of amount of gas dissolved in pore fluid (modified from Sobkowicz and Morgenstern 1984) 45

Figure 2.2 Echo sounding, seismic reflection profiling, and side scan sonar surveying (modified from Judd and Hovland 1992) 46

CHAPTER 3

Figure 3.1 Particle size distribution of Ottawa Sand 68

Figure 3.2 Monotonic triaxial equipment (a) Triaxial apparatus setup and (b) Triaxial cell 69

Figure 3.3 Schematic of monotonic triaxial setup 70

Figure 3.4 Cyclic triaxial equipment (a) Triaxial setup ans associated computer controls and (b) Triaxial cell and loading frame 71

Figure 3.5 Schematic of cyclic triaxial setup 72

Figure 3.6 Bubble chamber (a) Bubble chamber system and (b) Upper bubble chamber 73

Figure 3.7 Schematic of bubble chamber design 74

Figure 3.8 Compression wave attenuation versus gas content (modified from Sills et al. 1991) 75

Figure 3.9 Multi-wire TDR probe geometry (modified from Zegelin et al. 1989) 76

Figure 3.10 Electrical fields surrounding multi-wire TDR probes (modified from Zegelin et al. 1989) 77

Figure 3.11 TDR equipment (a) TDR setup for cyclic triaxial tests and (b) TDR probe in monotonic triaxial base 78

Figure 3.12 Apparent dielectric constant versus volumetric water content 79

Figure 3.13 Apparent dielectric constant versus degree of saturation 80

Figure 3.14 Typical TDR waveforms (a) Saturated waveform and (b) Gassy waveform 81

Figure 3.15 TDR accuracy, Sample 19 82

Figure 3.16 TDR accuracy, Sample 23 83

CHAPTER 4

Figure 4.1 Variation in undrained stress-strain relationship due to the effect of difference in sample preparation (modified from Miura and Toki 1982) 101

Figure 4.2 Effects of specimen preparation method on cyclic stress ratio (modified from Tatsuoka et al. 1986) 102

Figure 4.3 Comparison of stress ratio versus number of cycles to initial liquefaction for MSP, dry tapped, and wet rodded specimens (modified from Miura and Toki 1982) 103

CHAPTER 5

Figure 5.1 State boundary surface for remolded clay (modified from Sasitharan 1994) 128

Figure 5.2 A shematic of state boundary surface for very loose sand (modifed from Sasitharan 1994) 129

Figure 5.3 Projection of the state boundary surface in deviator stress - effective mean normal stress space (modified from Sasitharan 1994) 130

Figure 5.4 Projection of the steady state curve in void ratio - effective mean normal stress space (modified from Sasitharan 1994) 131

Figure 5.5 Idealized stress-strain curves showing the possible range of sample responses (after Robertson et al. 1998) 132

Figure 5.6 Saturated stress - strain curves 133

Figure 5.7 Saturated effective stress paths 134

Figure 5.8 Saturated void ratio versus effective mean normal stress 135

Figure 5.9 Typical stress - strain curves for five gassy specimens 136

Figure 5.10 Typical effective stress path for five gassy specimens 137

Figure 5.11 Typical void ratio versus effective mean normal stress for five gassy specimens 138

Figure 5.12 Typical degree of saturation versus effective mean normal stress for five gassy specimens 139

Figure 5.13 Steady state curve for loose Ottawa sand in deviator stress - effective mean normal stress space 140

Figure 5.14 Effective stress paths for two saturated undrained tests with void ratios of 0.90........ 141

Figure 5.15 Steady state curve for loose Ottawa sand in void ratio - effective mean normal stress space 142

Figure 5.16 Steady state lines for other sands (based on results tabulated by Sasitharan et al. 1994)........ 143

Figure 5.17 Flow potential lines (modified from Yoshimine and Ishihara 1998) (a) Flow potential lines for triaxial compression and (b) Flow potential lines for triaxial compression and extension........ 144

Figure 5.18 Undrained behavior of Toyoura sand in triaxial compression, triaxial extension, and simple shear (modified from Yoshimine et al. 1999)........ 145

Figure 5.19 Brittleness index plotted against relative density (modified from Yoshimine et al. 1999) 146

Figure 5.20 Steady state curve in e - $\ln p'_{SS}$ space showing initial and final state and final degree of saturation........ 147

Figure 5.21 Steady state curve in e - $\ln p'_{SS}$ space showing initial and final state and initial degree of saturation........ 148

Figure 5.22 Initial void ratio versus initial degree of saturation with flow potential........ 149

CHAPTER 6

Figure 6.1 Relationship between earthquake magnitude and equivalent number of cycles of loading (modified from Wride and Robertson 1997a) (a) For number of cycles less than 28 (N < 28) and (b) For number of cycles greater than 28 (N > 28)........ 169

Figure 6.2 Typical saturated test result........ 170

Figure 6.3 Typical gassy test result 171

Figure 6.4 Cyclic failure of gassy and saturated specimens (a) Sample #30 (a), Gassy; σ_{dp}'=70 kPa, p'=299 kPa, $e_{initial}$=0.81, $S_{r\ initial}$=74%, (b) Sample #25, Saturated; σ_{dp}'=60 kPa, p'=296 kPa, $e_{initial}$=0.71, and (c) Sample #30 (c), Gassy; σ_{dp}'=140 kPa, p'=280 kPa, $e_{initial}$=0.77, $S_{r\ initial}$=76% 172

Figure 6.5 Liquefaction resistance curves of Fraser River sand at N=10 cycles (modified from Thomas 1992) 173

Figure 6.6 Effect of relative density on cyclic strength by cyclic torsional simple shear tests for isotropically consolidated Toyoura sand (modified from Tatsuoka et al. 1982) (a) Stress ratio versus number of loading cycles to 15% double amplitude strain and (b) Stress ratio versus relative density in ten loading cycles 174

Figure 6.7 Cyclic stress ratio versus number of cycles to 5% or 10% double amplitude axial strain for loose Toyoura sand (modified from Toki et al. 1986) (a) Number of cycles to 5% double amplitude strain and (b) Number of cycles to 10% double amplitude strain 175

Figure 6.8 Cyclic stress ratio versus number of cycles to 5% or 10% double amplitude axial strain for dense Toyoura sand (modified from Toki et al. 1986) (a) Number of cycles to 5% double amplitude strain and (b) Number of cycles to 10% double amplitude strain 176

Figure 6.9 Cyclic loading liquefaction resistance curves (modified from Thomas 1992) 177

Figure 6.10 Triaxial cyclic resistance ratio versus number of cycles to failure 178

Figure 6.11 Cyclic stress ratio versus initial degree of saturation 179

Figure 6.12 Cyclic stress ratio versus relative density 180

Figure 6.13 Change in relative density versus initial degree of saturation 181

Figure 6.14 Seed et al. (1985) limiting line 182

Figure 6.15 Increase in cyclic stress ratio versus initial degree of saturation for loose Ottawa sand 183

Figure 6.16 Cyclic stress ratio versus relative density showing CANLEX predictions 184

CHAPTER 7

Figure 7.1 Volumetric composition of the pore fluid in an unsaturated (gassy) soil (modified from Fredlund and Rahardjo 1993) 222

Figure 7.2 Initial and final pressure and volume conditions considered in Hilf's analysis (modified from Fredlund and Rahardjo 1993) 223

Figure 7.3 Yield surface with reduced friction angle at peak in extension, compared with experimental yield stresses (modified from Imam 1999) 224

Figure 7.4 Variation of stress ratio at peak (Mp) with void ratio obtained from drained constant deviator stress tests and undrained triaxial compression tests (modified from Imam 1999) 225

Figure 7.5 Comparison of the undrained effective stress path (UESP) with the shape of the yield surface for a sample of Ottawa sand with a void ratio of 0.805 consolidated to 550 kPa (modified from Imam 1999) 226

Figure 7.6 Correlation of the friction angle at phase transformation (PT) with void ratio and state parameter (modified from Imam 1999) 227

Figure 7.7 Definition of model parameters used to determine friction angles of sand: (a) at the peak of the yield surface and (b) at phase transformation (modified from Imam 1999) 228

Figure 7.8 Determination of the compressibility parameter β (Pestana and Whittle 1995) using compression data on Ottawa and Toyoura sands. Samples were prepared using moist tamping (MT), water pluviation (WP) and dry deposition (DD) methods (modified from Imam 1999) 229

Figure 7.9 Model predictions of saturated and gassy undrained triaxial compression tests with void ratios of 0.80 and consolidation pressures of 300 kPa (a) Stress strain curves and (b) Effective stress paths 230

Figure 7.10 Model predictions of saturated and gassy undrained triaxial compression tests with void ratios of 0.80 and consolidation pressures of 300 kPa (a) Void ratio versus effective mean normal stress and (b) Degree of saturation versus effective mean normal stress 231

Figure 7.11 Predicted and observed response for Sample #11, saturated, consolidated undrained with a void ratio of 0.89 and a consolidation pressure of 266 kPa (a) Stress strain curves and (b) Effective stress paths 232

Figure 7.12 Predicted and observed response for Sample #12, saturated, consolidated undrained with a void ratio of 0.91 and a consolidation pressure of 302 kPa (a) Stress strain curves and (b) Effective stress paths 233

Figure 7.13 Predicted and observed response for Sample #25, gassy, consolidated undrained with a void ratio of 0.85, a consolidation pressure of 272 kPa, and an initial degree of saturation of 91% (a) Stress strain curves and (b) Effective stress paths 234

Figure 7.14 Predicted and observed response for Sample #25, gassy, consolidated undrained with a void ratio of 0.85, a consolidation pressure of 272 kPa, and an initial degree of saturation of 91% (a) Void ratio versus effective mean normal stress and (b) Degree of saturation versus effective mean normal stress 235

Figure 7.15 Predicted and observed response for Sample #8, gassy, consolidated undrained with a void ratio of 0.92, a consolidation pressure of 286 kPa, and an initial degree of saturation of 80% (a) Stress strain curves and (b) Effective stress paths 236

Figure 7.16 Predicted and observed response for Sample #8, gassy, consolidated undrained with a void ratio of 0.92, a consolidation pressure of 286 kPa, and an initial degree of saturation of 80% (a) Void ratio versus effective mean normal stress and (b) Degree of saturation versus effective mean normal stress 237

Figure 7.17 Predicted and observed response for Sample #21, gassy, consolidated undrained with a void ratio of 0.90, a consolidation pressure of 296 kPa, and an initial degree of saturation of 80% (a) Stress strain curves and (b) Effective stress paths 238

Figure 7.18 Predicted and observed response for Sample #21, gassy, consolidated undrained with a void ratio of 0.90, a consolidation pressure of 296 kPa, and an initial degree of saturation of 80% (a) Void ratio versus effective mean normal stress and (b) Degree of saturation versus effective mean normal stress 239

Figure 7.19 Model predictions of gassy undrained triaxial compression tests with consolidation pressures of 300 kPa, initial void ratios of 0.80, and initial degree of saturations of 90% (a) Stress strain curves and (b) Effective stress paths 240

Figure 7.20 Model predictions of gassy undrained triaxial compression tests with consolidation pressures of 300 kPa, initial void ratios of 0.80, and initial degree of saturations of 90% (a) Void ratio versus effective mean normal stress and (b) Degree of saturation versus effective mean normal stress 241

CHAPTER 8

Figure 8.1 Potential for flow liquefaction of Ottawa sand 257

Figure 8.2 Cyclic stress ratio versus relative density, based on Seed et al. (1985) limiting line 258

Figure 8.3 Increase in cyclic stress ratio versus initial degree of saturation for loose Ottawa sand 259

APPENDIX A

Figure A.1 Sample #6, Saturated, CD 280

Figure A.2 Sample #8, Gassy, CU 281

Figure A.3 Sample #9, Gassy, CU 282

Figure A.4 Sample #10, Gassy, CU 283

Figure A.5 Sample #11, Saturated, CU 284

Figure A.6 Sample #12, Saturated, CU 285

Figure A.7 Sample #13, Gassy, CU 286

Figure A.8 Sample #14, Gassy, CU 287

Figure A.9 Sample #15, Gassy, CU 288

Figure A.10 Sample #16, Gassy, CU 289

Figure A.11 Sample #17, Gassy, CU 290

Figure A.12 Sample #18, Gassy, CU 291
Figure A.13 Sample #19, Saturated, CD 292
Figure A.14 Sample #20, Gassy, CU 293
Figure A.15 Sample #21, Gassy, CU 294
Figure A.16 Sample #22, Saturated, CU 295
Figure A.17 Sample #23, Saturated, CD 296
Figure A.18 Sample #24, Gassy, CU 297
Figure A.19 Sample #25, Gassy, CU 298

APPENDIX B

Figure B.1 Sample #16, Saturated 301
Figure B.2 Sample #18, Saturated 302
Figure B.3 Sample #19, Saturated 303
Figure B.4 Sample #20, Saturated 304
Figure B.5 Sample #25, Saturated 305
Figure B.6 Sample #28, Gassy 306
Figure B.7 Sample #32, Gassy 307
Figure B.8 Sample #33, Gassy 308
Figure B.9 Sample #36, Gassy 309
Figure B.10 Sample #37, Gassy 310
Figure B.11 Sample #38, Gassy 311
Figure B.12 Sample #39, Gassy 312
Figure B.13 Sample #40, Gassy 313
Figure B.14 Sample #41, Gassy 314

Figure B.15 Sample #42, Gassy 315

APPENDIX C

Figure C.1 Sample #30 (a), Gassy 318
Figure C.2 Sample #30 (b), Gassy 319
Figure C.3 Sample #30 (c), Gassy 320
Figure C.4 Sample #38 (a), Gassy 321
Figure C.5 Sample #38 (b), Gassy 322
Figure C.6 Sample #38 (c), Gassy 323
Figure C.7 Sample #38 (d), Gassy 324
Figure C.8 Sample #38 (e), Gassy 325
Figure C.9 Sample #38 (f), Gassy 326
Figure C.10 Sample #38 (g), Gassy 327
Figure C.11 Sample #39 (a), Gassy 328
Figure C.12 Sample #39 (b), Gassy 329
Figure C.13 Sample #39 (c), Gassy 330
Figure C.14 Sample #39 (d), Gassy 331
Figure C.15 Sample #39 (e), Gassy 332
Figure C.16 Sample #39 (f), Gassy 333
Figure C.17 Sample #39 (g), Gassy 334
Figure C.18 Sample #40 (a), Gassy 335
Figure C.19 Sample #40 (b), Gassy 336
Figure C.20 Sample #40 (c), Gassy 337
Figure C.21 Sample #41 (a), Gassy 338

Figure C.22 Sample #41 (b), Gassy 339

Figure C.23 Sample #41 (c), Gassy 340

Figure C.24 Sample #41 (d), Gassy 341

Figure C.25 Sample #42 (a), Gassy 342

Figure C.26 Sample #42 (b), Gassy 343

Figure C.27 Sample #42 (c), Gassy 344

LIST OF SYMBOLS, NOMENCLATURE, AND ABBREVIATIONS

$\bar{u}_g$	absolute gas pressure
$\bar{u}_g$	absolute pressure of dissolved gas
$\bar{u}_{atm}$	atmospheric pressure
$\bar{u}_{gf}$	final absolute gas pressure
$\bar{u}_{go}$	initial absolute gas pressure
$(CRR)_{SS}$	cyclic resistance ratio determined from simple shear tests
$(CRR)_{tx}$	cyclic resistance ratio determined from triaxial tests
$(CSR)_{SS}$	cyclic stress ratio determined from simple shear tests
$(CSR)_{tx}$	cyclic stress ratio determined from triaxial tests
A-D	alternating to direct
AP	air pluviation
a_p	difference between $sin\varphi_\mu$ from triaxial compression and $sin\varphi_\mu$ from triaxial extension, a shape hardening parameter
a_{PT}	difference between $sin\varphi_{cv}$ from triaxial compression and $sin\varphi_{cv}$ from triaxial extension, a stress dilatancy parameter
ASTM	American Society for Testing and Materials
atm	atmospheric
B	pore pressure coefficient as defined by Skempton
c	velocity propagation of light in free space
CANLEX	CAnadian Liquefaction EXperiment
CD	consolidated drained
C_g	compressibility of gas
C_{gl}	compressibility of gas - liquid mixture
CH_4	methane
Δ	change
C_l	liquid compressibility
cm	centimeter

$\mathrm{CO_2}$	carbon dioxide
CRR	cyclic resistance ratio
$CRR_{7.5}$	cyclic resistance ratio representing an equivalent earthquake magnitude 7.5
CSR	cyclic stress ratio
$CSR_{7.5}$	cyclic stress ratio representing an equivalent earthquake magnitude 7.5
CU	consolidated undrained
d	rate of dilatancy
D_{50}	mean grain size
D-A	direct to alternating
DA	double amplitude
DD	dry deposition
D_r	relative density
e	void ratio
e_{final}	void ratio at the end of shear
$e_{initial}$	void ratio at the beginning of shear
e_o	initial void ratio
EQ	earthquake
e_{SS}	void ratio at steady state
e_μ	value of the normalized void ratio corresponding to $sin\varphi_\mu$ in a $sin\varphi_p$ versus e_μ plot, a shape hardening parameter
f	frequency
G	elastic shear modulus
G_r	elastic shear modulus, an elastic parameter
H	coefficient of solubility, Henry's constant
h	volumetric coefficient of solubility, Henry's constant
Hz	Hertz
I_B	brittleness index
k	constant
K	dielectric constant
K	elastic bulk modulus
K'	real part of the dielectric constant

K''	imaginary part of the dielectric constant
K_a	apparent dielectric constant
K_{AIR}	dielectric constant of air
k_f	variation of the maximum friction angle (or stress ratio) that can be attained at failure, with the current state parameter, a failure parameter
kg	kilogram
km	kilometer
km^2	square kilometer
k_p	slope of the best fit straight line in a $sin\varphi_p$ versus e_μ plot, a shape hardening parameter
kPa	kilopascal
k_{PT}	slope of the best fit straight line in a $sin\varphi_{PT}$ versus ψ plot, a stress dilatancy parameter, a material constant
K_r	elastic bulk modulus, an elastic parameter
K_S	dielectric constant of soil solids
K_w	dielectric constant of water
L	liter
L	transmission length
lb	pound
lbs	pounds
LSS	limited strain softening
LVDT	linear voltage displacement transducer
M	magnitude (earthquake)
M	slope of the steady state line in deviator stress (q) – effective mean normal stress (p') space
M_c	slope of the straight line representing stresses at state (p'_{SS}, q_{SS}) for triaxial compression
$M_{c.c}$	stress ratio q/p at the critical state in triaxial compression
M_d	mass of dissolved gas
M_f	stress ratio at failure
min	minute

ml	millimeter
mm	millimeter
M_p	stress ratio, the ratio q/p at the point where the peak value of q occurs
$M_{p.c}$	stress ratio for triaxial compression
$M_{p.e}$	stress ratio for triaxial extension
MSF	magnitude scaling factor
MSP	multiple sieve pluviation
MT	moist tamping
n	an elastic parameter
N	number of cycles
n	porosity
n_o	initial porosity
^{o}	degrees
^{o}C	degrees Celsius
Ω	ohm
p	mean normal stress
P	pressure
p'	effective mean normal stress
$p'_{initial}$	effective mean normal stress at the beginning of shear
p'_{PT}	effective mean normal stress at phase transformation
p'_{SS}	effective mean normal stress at steady state
p_c	mean normal stress at consolidation
p_c'	mean isotropic effective confining stress
p_f	size of the yield surface at failure
psi	pounds per square inch
$\mathrm{p_{ss}}$	mean normal stress at steady state
PT	phase transformation
P-wave	compression wave
q	deviator stress (shear stress)
q_{cy}	cyclic shear stress
q_{SS}	deviator stress at steady state

QSS	quasi steady state
q_{ST}	static gravitational shear stress
R^2	regression coefficient
r_m	magnitude scaling factor
s	approximate slope of the state boundary surface in deviatoric stress (q) – effective mean normal stress (p') space
S	degree of saturation
SH	strain hardening
S_o	initial degree of saturation
$S_{r\,final}$	degree of saturation at the end of shear
$S_{r\,initial}$	degree of saturation at the beginning of shear
S_r	degree of saturation
SS	simple shear
SS	strain softening
S_u	undrained shear strength
T	temperature
t	time
TC	triaxial compression
TDR	time domain reflectometry
TE	triaxial extension
u	pore pressure
UESP	undrained effective stress path
u_f	flow potential
u_g	gas pressure
u_{go}	initial gauge gas pressure
u_l	liquid pressure
$u_{l/g}$	liquid/gas saturation pressure
US	ultimate (steady) state
USL	ultimate state line
V	volume
V_d	volume of dissolved gas

V_g	volume of free gas
V_{gf}	final volume of gas
V_{go}	initial volume of free and dissolved gas
V_l	volume of liquid
V_o	initial volume of soil
V_s	volume of soil solids
V_T	total volume
V_v	volume of voids
WAV	water vibration
WP	water pluviation
Γ	intercept of the best fit straight line between void ratio (e) and logarithmic effective mean normal stress (lnp') at $p'_{SS} = 1$ unit
Π	pie
α	attenuation
β	geometric factor for the dielectric mixing law
β	sand compressibility parameter
ε_1	major principal strain
ε_3	minor principal strain
ε_a	axial strain
ε_o	permitivity of free space
ε_p	mean normal strain
ε_q	deviatoric strain
ϕ	soil porosity
ϕ'_{SS}	steady state friction angle
γ	shear strain
η	stress ratio of the deviatoric stress (q) to the mean normal stress (p)
φ_{cv}	constant volume friction angle
φ_f	friction angle
φ_{PT}	friction angle at phase transformation
φ_μ	interparticle friction angle

λ	slope of the best fit straight line between void ratio (e) and logarithmic effective mean normal stress at steady state (lnp'_{SS})
ν	Poisson's ratio
v	propagation velocity
θ_v	volumetric water content
ρ_g	density of gas
ρ_l	density of liquid
σ	total stress
σ'	effective stress
σ'_{vo}	initial vertical effective stress
σ_1	total major principal stress
σ_1'	effective major principal stress
σ_2	total intermediate principal stress
σ_3	total minor principal stress
σ_3'	effective minor principal stress
σ_d	deviatoric stress
σ_d'	applied effective deviator stress
σ_d'	effective deviatoric stress
σ_{dc}	dc (direct current) electrical conductivity
σ_{dp}'	applied effective deviator stress
σ_v	vertical stress
τ_{cyc}	cyclic shear stress
ω	angular frequency
ψ	state parameter

CHAPTER 1

INTRODUCTION

1.1 THE OCCURRENCE OF GAS CHARGED SEDIMENTS

Gas can be found in many soils, but none more common than in seabed soils. Gas-charged sediments are known to be widely distributed throughout the world's oceans. Occurrences have been reported in coastal and estuarine regions, across the continental shelves, and within deep ocean basins.

Methane gas has been observed in many seabed soils. Figure 1.1 shows the location of shallow marine sediments known to contain free gas (as of 1992). Some of these locations include the North Sea (Long 1992; Hovland and Judd 1988), the Skagerrak between Norway and Denmark (Hovland 1992), the Baltic Sea (Whiticar 1982), the Gulf of Mexico (MacDonald et al. 1990; Prior et al. 1989; Langseth and Moore 1990), the Irish Sea (Yuan et al. 1992), the marine sediments of Hong Kong (Premchitt et al. 1992), the near-shore zones of North Carolina, USA, and western India (Evans 1988). In the United States, gas has been observed in Chesapeake Bay, Maryland (Schubel 1974), in San Francisco Bay, California (Vogel et al. 1982), and in the Mississippi River delta front (Whelan et al. 1977). Methane gas has also been observed in seabed soils on Canada's coastlines (Christian et al. 1997a; Christian 1998).

Gas has been reported on land in soils such as in Italy (D'Appolonia 1981), and in Alberta, gas has been found in the Athabasca oil sands (Ells 1926; Hardy and Hemstock 1963) and in their mine tailings (Lord 1998). Fewer gas charged sediments have been encountered on land, hence, the significance of gas will be discussed with respect to marine environments.

The objective of this chapter is to examine the significance of undissolved or free-gas on the engineering properties of soils. Special emphasis is placed on submarine flow slides.

1.2 THE IMPLICATIONS OF GAS CHARGED SEABED SOILS

Engineering in marine environments will be a significant industry and research focus area for the next several decades. The increasing consumption of non-renewable resources and the decreasing availability of land is applying pressure on marine environments, creating a potentially vast market for geotechnical ocean engineering. For example, as the world's resources decline and resource extraction technologies improve, offshore resource deposits previously considered uneconomical will become viable. Moreover, as land availability decreases and land costs increase, land reclamation from oceans will be more common place. The increasing activity in marine environments is creating a need to better understand the behavior of marine sediments, including the behavior of gas charged marine sediments.

Gas can occur in the seabed in three ways: in solution in the pore water, undissolved in the form of gas-filled voids, or as clathrates (gas hydrates). In the first case, the gas will have little affect on the physical properties of the seabed unless the ambient pressures are reduced. In the second case, the gas will affect the engineering properties of the seabed due to the high compressibility of the gas. In the third case, the gas only becomes hazardous if the clathrate melts (Sills and Wheeler 1992).

Soils found in marine environments will be affected by the presence of free gas, where even a small amount of gas could have significant geotechnical implications. The presence of gas may alter the shear strength, settlement characteristics, and liquefaction potential of a soil.

1.2.1 Detection of Gas

The detection of gas is most often performed by seismic methods. Richardson and Davis (1998) note that "the defense and petroleum industries will undoubtedly benefit from an improved understanding and predictability of gassy sediment environments. Interest lies both in the performance of higher frequency naval detection and classification sonar and lower frequency seismo-acoustic systems used to prospect for oil and gas." In addition, the identification of gas pockets can help avoid blowouts when drilling. Blowouts occur when pockets of high pressure gas, trapped beneath less permeable layers, are encountered during drilling.

1.2.2 Foundation Design

Offshore structures are designed for acceptable levels of settlement as well as for bearing capacity. Both long-term and short-term analysis of the soil compressibility and strength characteristics are required for settlement and bearing capacity designs. Gas affects the consolidation behavior of soils by causing an increase in the initial settlement. Wheeler et al. (1991) showed that a 1 to 2 percent volume fraction of gas (gas volume to total volume) causes the settlement to double, when compared with typical saturated soils. Bearing capacity is also a short-term problem because of the reduction of undrained strength exhibited by some gassy soils. Typically, the larger the volume fraction of gas, the lower the undrained shear strength. In addition, dynamic loading during storms can create short-term problems with the bearing capacity of offshore structures founded on gassy soils.

1.2.3 Gas Accumulations

As gas moves through the seabed it will partly diffuse and partly flow through fissures or alongside conductors installed for oil production. Sills and Wheeler (1992) note that there is a potential for gas accumulation beneath a production platform. Over a period of time, the accumulation of gas could build up volume and pressure. In the design of some platforms, gas vents have been provided above the skirts of the platform, so that any gas moving up from the seabed and collecting there may be released into the water.

1.2.4 Environmental Effects

Methane is an important greenhouse gas. The global warming potential of methane is 3.7 times that of carbon dioxide and up to 12 percent of greenhouse effects are the result of atmospheric methane (Lashof and Ahuja 1990). "It is therefore important to have an accurate inventory of sources and sinks of methane and to understand the dynamics of shallow-water methane generation, consumption, transport, and subsequent emission to the atmosphere" (Richardson and Davis 1998). Another environmental effect of methane gas is the enhanced biomass of macrofauna observed at some gas seep sites (Dando and Hovland 1992).

1.2.5 Submarine Flow Slides

Gas in marine sediments also affects the stability of submarine slopes. Coastal structures, offshore structures, and pipelines are all impacted by the concern of slope instability. A major source of instability in cohesionless sediments is the result of liquefaction flow slides. Section 1.3 discusses liquefaction slides in more detail.

1.3 LIQUEFACTION FLOW SLIDES IN SUBMARINE AND COASTAL SEDIMENTS

Soil liquefaction is a phenomenon that gives rise to a loss of shearing resistance or to the development of excess strains. Liquefaction can be a major cause of slope instability with many liquefaction events occurring in submarine slopes. Some of these slides can be attributed to cyclic liquefaction; however, the majority are induced by flow liquefaction. Chillarige et al. (1997a) summarized several published cases of earthquake-induced and statically-induced submarine flow slides. The earthquake-induced liquefaction slides are presented in Table 1.1 and the statically-induced liquefaction slides are presented in Table 1.2.

1.3.1 Framework for Liquefaction

a) Liquefaction Phenomenon

Liquefaction is a phenomenon that gives rise to a loss of shearing resistance or to the development of excess strains as a result of transient or repeated disturbance. Flow liquefaction is due to a transient disturbance, while cyclic liquefaction is due to a repeated disturbance.

Castro (1969) defined liquefaction as the strain softening and collapse of loose sand to an ultimate state of constant effective stress and deformation. During liquefaction, the de-structured mass of soil behaves as a thick viscous fluid. If the in-situ gravitational shear stresses are larger than the ultimate steady state strength, a catastrophic collapse and flow failure can occur if the soil is triggered to strain soften (Robertson 1994).

b) Liquefaction Terminology

Robertson (1994) suggested liquefaction terminology based on the differing mechanisms of liquefaction. These liquefaction definitions, summarized below, were used in this thesis.

(i) Flow liquefaction

Figure 1.2 shows a schematic summary of the undrained monotonic behavior of granular soil loaded in triaxial compression. A soil with an initial void ratio (e) higher than the ultimate state line (USL) will strain soften (SS) at large strains, eventually reaching an ultimate condition referred to as ultimate (or steady) state (US). A soil with an initial void ratio lower than the ultimate state line will strain harden (SH), at large strains, towards ultimate state. If a soil has an initial void ratio very close to the ultimate state line the soil can show limited strain softening (LSS), to a quasi steady state (QSS), but eventually at large strains, the soil hardens to the ultimate state.

In order to induce flow liquefaction the soil must have a strain softening response to undrained loading and the in-situ shear stress must be greater than the undrained residual (or steady state) strength. Flow liquefaction can be triggered by either monotonic or cyclic loading and can occur in very loose granular deposits, very sensitive clays, and loose loess deposits.

(ii) Cyclic liquefaction

Cyclic liquefaction requires undrained cyclic loading (e.g. earthquake loading) where shear stress develops. If the loading is sufficient to cause shear stress reversal, and to cause the effective confining pressure to essentially reach zero, cyclic liquefaction occurs (See Figure 1.3). Large deformations can develop during cyclic liquefaction, but they generally stabilize when the cyclic loading stops (Robertson 1994). If the applied cyclic loading results in shear stresses consistently greater than zero, then the effective stress will not reach zero, and this phenomenon is termed cyclic mobility (See Figure 1.4). Deformations during cyclic mobility will also stabilize when the loading ceases.

1.3.2 History of Submarine Liquefaction Flow Slides

a) Statically-Induced Liquefaction Flow Slides

Many static liquefaction flow slides have occurred in coastal and fluvial deposits, both in natural soil slopes and in man-made slopes and earth structures. Several of these historical slides are discussed below.

(i) The Netherlands

Flow slides in the coastal areas of the province of Zeeland have occurred regularly for many years (Koppejan et al. 1948). The exact locations of about 700 flow slides are known (Silvis and de Groot 1995). Most of the flow slides took place in loosely packed fine sands during periods of excessive tidal fluctuation.

(ii) Norway

Many flow slides have occurred in Norway. Although is appears that Norway has had a disproportionate number of slides, perhaps due to the emphasis on geotechnical engineering in Norway the flow slides were simply better documented.

A large flow slide occurred in the silty fine sand on the banks of Trondheim Harbor in 1888 damaging the railway station and killing one person (Andresen and Bjerrum 1968). A series of three related flow slides occurred in natural loose fine sand, silts, and silty clay during exceptionally low tide in the Orkalsfjord of Norway in 1930 destroying shoreline construction and breaking submarine cables (Terzaghi 1956; Andresen and Bjerrum 1968). Recently placed fill and a coastline of approximately 450 meters comprised a large slide in loose fine sand along the banks of Hommelvik Bay in Norway in 1942 (Bjerrum 1971). This slide occurred after spring low tide. Another flow slide took place in loose fine sand and silt deposits of the Follafjord in Norway in 1952 (Terzaghi 1956; Bjerrum 1971). A dredger working in the fjord was towed by the slide for a distance of about 300 meters. Finally, a railway embankment constructed on loose fine sand and coarse silt was involved in a flow slide in the Finnvika fjord in Norway in 1940 resulting in 100 meters of the embankment disappearing beneath the water surface as a result of a slide occurring during low tide (Bjerrum 1971).

(iii) United States

A flow slide occurred in Puget Sound in fine sand during low tide while dredging operations were being carried out (Kraft et al. 1992). In 1994, a flow slide occurred in silty sand near Skagway, Alaska destroying harbor dock facilities (Morgenstern 1995). Gas release was observed from the debris of the slide.

(iv) Canada

In 1955, a flow slide occurred on the north shore of Howe Sound in British Columbia destroying a warehouse and a wharf (Terzaghi 1956). The slide occurred in clean sand and gravel during conditions of low tide. Five major liquefaction flow slides occurred in 1983 during the construction of the Nerlek berm, a hydraulically placed subsea sand berm in the Beaufort sea (Sladen et al. 1985). The failures occurred in oversteppened sand placed at the side slopes. In 1975, a large flow slide occurred in sandy silts at the foreslope of the Kitimat River Delta in British Columbia during extreme low tides (Morrison 1984). The slide destroyed anchors and piles supporting a dock. In the Fraser River Delta in British Columbia, liquefaction flow slides in the silty sands are recurrent (McKenna et al.

1992). The Fraser River delta will be discussed in more detail in Section 1.4.1.

(v) Observations from the historical flow slides

The liquefaction flow slides in coastal sediments summarized in Table 1.2 share important characteristics. Kramer (1988) noted that the submarine liquefaction flow slides have most commonly been observed in loose, fine sands of uniform gradation. These soils are similar to those which have historically been observed to be susceptible to liquefaction. In addition, Kramer (1988) and Chillarige (1997a) noted that each of the flow slides occurred at some time shortly after the water level adjacent to the shoreline had dropped by at least a moderate amount for a sustained period.

b) Earthquake-Induced Liquefaction Flow Slides

Offshore earthquake-induced liquefaction flow slides have occurred in many coastal and fluvial sediments. A number of flow slides have been documented and many of the documented slides are summarized in Table 1.1. A few of the earthquake triggered liquefaction slides are mentioned briefly in this section.

(i) United States

One of the earliest well documented, earthquake-induced flow slides occurred in the loose sandy material along the banks of the Mississippi River as a result of the New Madrid earthquake which occurred in 1811 (Seed 1968).

In 1980, an earthquake with an estimated magnitude of 6.5 to 7.2 occurred off the coast of California (Field et al. 1982). A large area of the Klamath

River delta, consisting of muddy sands, failed by liquefaction and lateral spreading. Field and Jennings (1987) reported the presence of gas in these sediments, the increase in gas abundance immediately after the earthquake, and the gradual decline to pre-earthquake gas levels within about five years. In 1989 the Loma Prieta earthquake in California, magnitude 7.1, caused submarine flow slides in the offshore deposits of gravel, sand, silt, and clay (Greene et al. 1991).

Flow slides occurred at Port Valdez and Seward caused by the magnitude 8.3 Alaskan earthquake in 1964 (Holish and Hendron 1975; Morgenstern 1967; Seed 1968). The three flow slides (two occurred at Valdez) developed in loose silty sand and gravel deposits and destroyed harbor facilities and near-shore installations. Similar slides resulting from earthquakes have occurred in Valdez, Alaska in 1899, 1911, 1912, and in Yakutat, Alaska in 1899 (Seed 1968).

(ii) Chile

The Chilean earthquake of 1922, magnitude 8.3, resulted in submarine flow slides in sand and silts (Morgenstern 1967). In 1960, an earthquake of magnitude 8.4 in Puerito Montt, Chile, triggered the liquefaction and flow sliding of the loose sand and silt backfill of coastal quay walls (Seed 1968).

(iii) Japan

The Kwanto earthquake in 1923 had a magnitude 8.2 and caused flow slides in sand submarine deposits in Kwanto and coastal deposits in Sagami Wan, Japan (Morgenstern 1967; Seed 1968; Menard 1964).

(iv) Greece

In 1982 the Alkyonidhes mass flowed as a result of a magnitude 6.7 earthquake in the Corinth Gulf in Greece (Perissoratis et al. 1984). The Aegion earthquake in 1995 had a magnitude 6.1 and caused the liquefaction of sediments in the western Gulf of Corinth, Greece (Papatheodorou and Ferentinos 1997). The sediments consisted of cobble and pebble sized material interlayered by sand and silty sand that was known to contain gas.

(v) Observations from the historical earthquake-induced flow slides

By observing the historical records of earthquake-induced submarine flow slides, a few similarities can be noted. Most of the slides occurred in sand or silty sand deposits. These soils are commonly deemed most susceptible to liquefaction on land. Many of the soil deposits were deltaic in nature and a few of the deposits were known to contain gas. In addition, it can also be noted that most of the slides occurred in very gentle slopes (low slope angles), based on the information available.

1.4 CASE HISTORIES

In order to illustrate the significance of submarine flow slides two detailed case histories are presented in this section. The first case history, the Fraser River delta, has been subjected to reoccurring statically-induced liquefaction flow slides, while the second case history, the Klamath River delta, examines an earthquake-induced flow failure. These two particular case histories were chosen because of the presence of gas in the liquefied soils.

1.4.1 The Fraser River Delta

Interest in the submarine sediments of the Fraser River delta was first aroused by Johnston (1921) and later by Mathews and Shepard (1962) and Terzaghi (1962). This early research on the delta focused on sedimentation. Later studies recognized the instability of the delta sediments (e.g. Kostaschuk et al. 1991; Luternauer 1980; Kenyon and Turcotte 1985). McKenna et al. (1992) recognized five liquefaction flow slides that occurred near Sand Heads in the Fraser River delta between 1970 and 1985. Dykes, jetties, a lighthouse, submarine power cables, and structures such as the Tsawwassen ferry terminal and the Roberts Bank coal port are still at risk of damage due to potential instabilities of the submarine sediments.

a) Physical Setting

The Fraser River, the largest river in British Columbia, forms an actively prograding delta that extends 23 km west into the Strait of Georgia and south into Boundary Bay from a narrow gap in the Pleistocene uplands at New Westminster as illustrated in Figure 1.5 (Chillarige 1995). It is bounded to the north by Burrard Peninsula, to the east by the Surrey uplands, and to the south west by Point Roberts Peninsula (Luternauer 1980). The Fraser River delta is in a seismically active area.

The geology of the Fraser River delta has been described by Chillarige (1995). Burrard Peninsula consists of two pre-Pleistocene bedrock ridges trending east-west, overlain mainly by glacial and raised littoral deposits. Point Roberts Peninsula consists of similar Pleistocene material. Surrey uplands are evolved from glacio-marine gravelly clay deposits. Since the recession of the glaciers from the Fraser Canyon, the delta has built up deposits 90 to 200 meters thick over Pleistocene sediments.

The surficial environment of the delta, extending from east to west (Figure 1.6), is described by Monahan et al. (1993).

- An upper delta plain that extends 23 km west from the gap in the Pleistocene uplands at New Westminster, is mantled by flood plain silt and peat, and is now protected by dykes.
- A lower delta plain consisting of dominantly sandy tidal flats.
- A subaqueous delta plain, that is mantled by sand and is up to 2 km wide, and extends to the first major break in slope at a depth of up to 9 km below lowest low tide.
- A delta front and slope that descend at an average slope of 1.5 degrees to depths of up to 300 meters in the Strait of Georgia and are dominantly silty to the north and sandy to the south of the Main Channel.

Unlike almost all the other rivers of the glaciated coastline of western North America, the Fraser River is building its delta into relatively open water rather than into the sheltered head of some fjord (Mathews and Shepard 1962). The average sediment yield for the river is 20 million tonnes annually (Luternauer 1980) of which 88 percent discharges into the Strait of Georgia. Over 50 percent of the sediment load are sand-sized particles (Luternauer and Finn 1983).

For additional information on the physical setting of the Fraser River delta and the different dynamic processes influencing the deposition and dispersion of the river sediments, the reader is referred to Chillarige (1995), Mathews and Shepard (1962), McKenna et al. (1992), and Christian et al. (1997a; 1997b).

b) Seabed Instability of the Fraser River Delta

Liquefaction flow slides are a recurring phenomenon in the silty sands in the Fraser River delta, with five known liquefaction flow slides occurring between 1970 and 1985 (McKenna et al. 1992). Chillarige (1995) investigated a submarine liquefaction flow slide that occurred in 1985 on the Fraser River delta slopes. The study evaluated the contributions of different environmental processes in triggering the flow slide. Several possible triggers, such as sedimentation, surface waves, and tidal drawdown on saturated sediments, could not either alone, or combined account for the deep-seated flow failures that were observed.

c) Instability of Gaseous Fraser River Delta Sediments

Christian et al. (1997b) noted that high concentrations of methane gas was present in the pore fluid of the Fraser River delta. This observation prompted Chillarige (1995) to examine the effect of tidal drawdown on gassy sediments. It was observed that the residual pore pressures in the sediments during low tide conditions could lead to triggering of flow liquefaction failures. Christian et al. (1997b) concluded that the reduction in effective stress leading to flow liquefaction in the Fraser River delta is largely caused by the presence of small amounts of gas and resulting residual pore pressures. Once liquefaction occurs, progressive failure of the sediments can develop retrogressive flow slides (Chillarige et al. 1997b). Other flow liquefaction failures that have occurred at low tides, as listed in Table 1.2, could also have been affected by the presence of gas.

d) Conclusions

The Fraser River delta is an actively prograding delta on the west coast of Canada with documented submarine liquefaction flow failures. The recorded flow failures have been statically-induced; however, the delta is in an actively seismic area, and therefore the risk of earthquake-induced liquefaction flow failures also exists. A research program aimed at studying the triggering mechanisms for the observed failures concluded that the presence of gas results in residual pore-pressures, which during low tides can trigger submarine flow failures (Chillarige 1995).

1.4.2 The Klamath River Delta, California

On November 8, 1980, a major earthquake (magnitude 6.5 to 7.2) occurred 60 km off the coast of northern California (Field et al. 1982). Onshore the effects of the earthquake were minor when compared with other large earthquakes in California. A bridge collapsed, several rockfalls occurred, and sand boils were reported from bay-mouth spits (Lajoie and Keefer 1981). Offshore commercial fishermen reported the presence of ridges and scarps on the usually flat seabed off the Klamath River (Field et al. 1982). Within the month, a marine survey was conducted and compared to previous pre-earthquake surveys. Analysis of the data demonstrated that a large area of the Klamath delta (at least 20 km^2) had failed as a direct result of the earthquake (Field et al. 1982; Field 1984).

a) Physical Setting

The Klamath River delta is located on the northern coast of California, U.S., in an actively tectonic and sedimentologic area (Figure 1.7). The long-term seismicity records show that since 1920 there has been an average of about one earthquake per year of magnitude 5.0 or greater and one earthquake per decade of magnitude 6.0 or greater. Two earthquakes with a magnitude greater than 7.0 have been reported between 1920 and 1980 (Real et al. 1978).

The Klamath River mouth lies on the eastern margin of the Eel River Basin, a thick section of Neogene and Quaternary sediment (Hoskins and Griffiths 1971). The delta sediment overlies a late Quaternary erosional surface (Field et al. 1982). The delta lies on the continental shelf and is marked by a zone of major northwest-striking faults. Surficial sediments of the Klamath River delta consist of clayey silt seaward of the 60-m isobath and fine, poorly sorted, silty sand inshore of it (Welday and Williams 1975; Field et al. 1980).

The Klamath River delivers approximately 3.6 million tonnes of sediment to the continental shelf per year (Janda and Nolan 1979). A significant portion of this sediment is deposited in a submarine delta offshore of the Klamath River. Field et al. (1980) mapped a lobe of sediment 20 to 50 meters thick in water depths of 30 to 70 meters. During high flow periods, the deposited sediments contain high concentrations of plant debris.

Further details of the geography, geology, and seismology of the Klamath River delta can be found in Field et al. (1982; 1980).

b) Liquefaction Flow Slide

As a result of the 1980 earthquake, the fine to medium sand sediments of the Klamath River delta experienced earthquake-induced liquefaction and subsequent flow failure. The more cohesive clayey silts exhibited no signs of disruption (Field et al. 1982). The flow failure was inferred from high-resolution seismic-reflection data taken both before and after the earthquake. The major features associated with the failure were a terrace, a toe scarp, compressional ridges, sand boils, and collapse craters.

c) Seafloor Gas Seeps Triggered by the Earthquake

Marine geophysical surveys of the northern California shelf show evidence of the presence of gas, both before and after the earthquake (Field and Jennings 1987). Field and Jennings (1987) speculate that the gas originates in pre-Quaternary sediment and therefore may be derived from a thermogenic source as well as from biogenic origins. The results of the geophysical data show that the gas was present in significant quantities immediately after the earthquake. Field and Jennings (1987) write "our thesis is that the earthquake triggered the release of large quantities of gas through numerous vents, most of which are now inactive".

Five years after the earthquake, the seafloor appeared acoustically similar to pre-earthquake surveys.

d) Relation of Gas Seeps to Liquefaction

Field and Jennings (1987) examined the relationship between the gas seeps and the position of the liquefied sediments. Their study found that the gas seeps occurred in the same area as the sediment failure, suggesting a relationship between the gas seeps and the liquefaction failure. Their results concluded that following the earthquake, gas venting probably contributed to the loss of strength and failure of offshore deltaic deposits. Sediments in the failure zone were noncohesive fine muddy sands, which are typically susceptible to liquefaction (Field and Jennings 1987).

e) Conclusions

As the result of an earthquake in 1980, a submarine liquefaction flow failure of the fine sandy sediments in the Klamath River delta of northern California occurred. High-resolution seismic surveys conducted before and after the earthquake identified the presence of gas. Evidence suggests that enhanced gas seepage was triggered by the earthquake. Within five years following the earthquake, gas venting had returned to pre-earthquake levels. It is probable that the release of gas was an important factor contributing to flow liquefaction failure.

1.4.3 Observations

In examining the liquefaction slides which occurred in the Fraser River delta and the Klamath River delta several important observations can be noted. First, flow liquefaction failures whether statically-induced or earthquake-induced are a reasonably common phenomenon in submarine soils, yet the full impact of submarine slides is only experienced when they damage or adversely affect man-made structures or activities.

Second, the presence of gas in submarine sediments will affect the engineering properties, specifically the resistance to liquefaction. Third, the presence of gas may even trigger, or contribute to, flow liquefaction failure.

1.5 THESIS OBJECTIVES

The examples of the significance of gas in offshore operations presented in this chapter show the importance of determining the effects of gas on soil behavior. The Fraser River delta and Klamath River delta case histories indicate that gas has possibly contributed to the liquefaction of submarine sediments. Because gas can be found in many submarine soils, it is possible that gas contributed to some of the other submarine flow failures summarized in Tables 1.1 and 1.2.

Little is known about the effect of gas on the resistance of soils to liquefaction, both static and cyclic liquefaction. The overall goal of this research is to determine if loose gassy sand can strain soften and experience flow liquefaction and/or cyclic soften and experience cyclic liquefaction. If static or cyclic liquefaction of gassy sands is possible, then some guidelines could be established to determine how the amount of gas affects the liquefaction resistance.

By reviewing previous work on gassy sediments, the level of existing knowledge is established. An overview of gassy sediments is presented in ***Chapter 2***. First, the terminology used in this thesis, specifically the difference between gassy and unsaturated soils is presented. Next, the origin of gas and the evidence of gas in sediments are reviewed. Finally, previous research work on gassy sediments is examined.

A laboratory program was used to study the effect of gas on the response of loose sand. The equipment designs of the monotonic and cyclic testing setups are described in ***Chapter 3***. In addition, the potential methods of measuring gas content are reviewed and the selected method, an innovative way to measure the gas content, using time domain reflectometry, described.

Chapter 4 describes the laboratory testing procedure for both the monotonic and cyclic tests. The specimen preparation method and its affect on the measured strength are discussed. In addition, the procedure used to test the specimens and the method of calculating void ratio is described.

The results of static triaxial tests performed on saturated and gassy sands are presented in ***Chapter 5***. The objective of this chapter is to determine if loose gassy sand can strain soften and experience flow liquefaction. In this chapter, the sample results are analyzed within the framework of critical state soil mechanics. The flow liquefaction potential is evaluated by analyzing the effects of various factors. The elimination of influencing factors on the results allows for a critical assessment of the liquefaction potential as a function of density and gas content. Guidelines for determining the liquefaction potential of loose gassy sands are presented.

In ***Chapter 6***, the results of cyclic triaxial tests performed on saturated and gassy sand are presented. The goal of this chapter is to determine the influence of gas on the resistance of loose sand to cyclic loading. A few interesting studies relevant to the current research are discussed at the beginning of this chapter. Then the cyclic resistance based on laboratory testing is reviewed. Laboratory results are presented next. The next section of this chapter examines the cyclic liquefaction potential of loose gassy sand and the factors potentially effecting the results. Finally, guidelines for determining the cyclic resistance of gassy sand are presented and evaluated using previously published data.

Constitutive modeling of loose gassy sand behavior was performed with the objective of adding some theoretical confirmation to the laboratory results. ***Chapter 7*** begins by reviewing the equilibrium and transient behavior of gassy soils. Next, an existing constitutive model is presented and the model characteristics, elements, calibration, and performance are reviewed. Finally, the modifications made to the model to account for the presence of gas are discussed and the modified model performance evaluated.

Chapter 8 provides a general discussion and conclusions regarding the effect of gas on the liquefaction resistance of loose sand. The chapter recommends guidelines for evaluating liquefaction potential. Cautionary notes and limitations of the guidelines are also given. Finally, recommendations for future studies are given.

Table 1.1 –Earthquake-induced flow slides in submarine deposits (after Chillarige et al. 1997a).

Slide	Magnitude	Deposit	Nature of soil	Slope angle (°)	References
New Madrid earthquake, Mississippi River banks, 1811	-	River bank	Sands	-	Seed 1968
Yakutat, Alaska, 1899	-	Submarine deposit	Deltaic marine sediments (silty sand and gravel)	-	Seed 1968
Valdez, Alaska, 1899	-	Submarine deposit	Deltaic marine sediments (silty sand and gravel)	-	Seed 1968
Messina cone, 1908	7.5	Submarine deposit	Sand - silt	4	Schwarz 1982
Valdez, Alaska, 1911	6.9	Submarine deposit	Deltaic marine sediments (silty sand and gravel)	-	Seed 1968
Valdez, Alaska, 1912	7.25	Submarine deposit	Deltaic marine sediments (silty sand and gravel)	-	Seed 1968
Chile, 1922	8.3	Submarine deposit	Sand with silt	6	Morgenstern 1967
Sagami Wan, 1923	-	Submarine deposit	Sand	-	Menard 1964; Morgenstern 1967
Kwanto, Tokyo, 1923	8.2	Coastal hillsides	-	-	Seed 1968
Grand Banks, 1929	7.2	Submarine deposit	Fine sand and silt	3.5	Heezen and Ewing 1952
Suva, Fizi, 1953	6.75	Submarine deposit	Sand	3	Houtz and Wellman 1962
Orleansville, 1954	6.7	Submarine deposit	Sand	4 - 20	Heezen and Ewing 1965
San Fransico, 1957	5.3	Lake banks	Aeolin beach sands	-	Seed 1968
Puerito Montt, Chile, 1960	8.4	Coastal deposits	Loose sands and silts	-	Seed 1968
Valdez, Alaska, 1964	8	Submarine deposit	Silty sand and gravel	15 - 20	Holish and Hendron 1975
Seward, Alaska, 1964	8.3	Submarine deposit	Loose to medium sand, gravel	15 - 20	Holish and Hendron 1975; Seed 1968
Valdez, Alaska, 1964	8.3	Submarine deposit	Silty sands and gravel	4 - 10	Morgenstern 1967; Seed 1968
Seattle, 1965	6.7	Coastal bluff	-	-	Seed 1968
Klamath River delta, California, 1980	6.5	Submarine deposit	Fine sand	0.25	Field et al. 1982

Table 1.2 –Statically-induced liquefaction flow slides in submarine deposits (after Chillarige et al. 1997a).

Flow Slide	Nature of Soil	Failure conditions	Slope angle (°)	References
The Netherlands	Loose fine sand	Low tides	15	Koppejan et al. 1948
Magdalena River delta, 1935	Sand and silt	Rapid sedimentation	2 - 3	Menard 1964; Morgenstern 1967
Helsinki Harbour, 1935	Sand and silt	Rapid filling	4 - 5	Andresen and Bjerrum 1967
Follafjord slides, 1952	Loose fine sand, silt	Dumping of dredged soils	5 - 7	Terzaghi 1956; Bjerrum 1971
Orkdalsfjord, 1930	Loose fine sand, silt	Low tides	5 - 10	Terzaghi 1956; Andresen and Bjerrum 1967
Finnivaka slide, 1940	Loose fine sand, silt	Low tides	-	Bjerrum 1971
Hommelvika, 1942	Loose fine sand	Low tides	-	Bjerrum 1971
Trondheim, 1888	Loose fine sand, silt	Low tides	8 - 15	Terzaghi 1956; Bjerrum 1971
Scripps Canyon, 1959, 1960	Sand	Free gas and storm waves	25 - 35	Dill 1964; Morgenstern 1967
Puget Sound, 1985	Loose sand	Low tides	16	Kraft et al. 1992
Skagway, Alaska, 1994	Loose silty sand, silt	Low tides of 4 m	35	N.R. Morgenstern, personal communication, 1995
Howe Sound, 1955	Fine sand and gravel	Low tides	27 - 28	Terzaghi 1956
Kitimat Fjord, 1975	Loose silty sand	Low tides of 6 m	19	Morrison 1984
Nerlerk sand berms, 1983	Loose sand	Fill placement	10 - 12	Sladen et al. 1985
Fraser River delta, 1985	Loose fine sand, silt	Low tides of 5 m	23	McKenna and Luternauer 1987

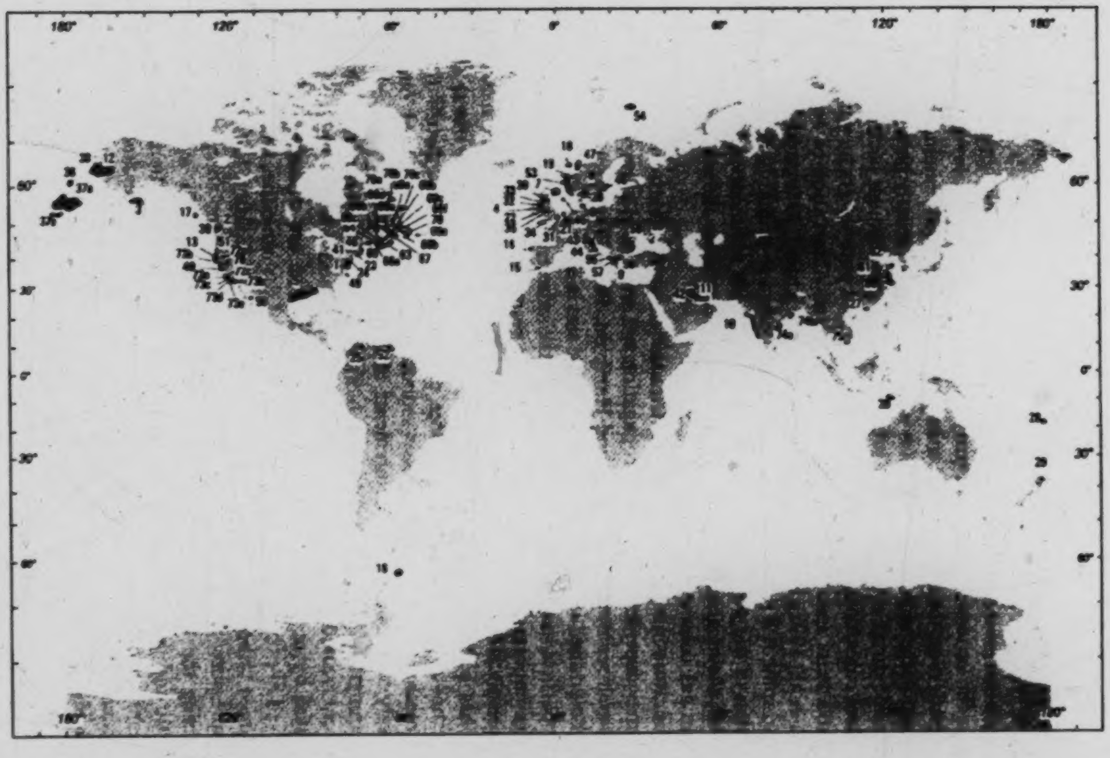

Figure 1.1 – Worldwide distribution of shallow water sediments that contain free gas. Most sites are based on seismo-acoustic survey techniques. The actual distribution of gassy sediments is probably much greater, especially in the poorly surveyed southern hemisphere. The numbers corresponds to references available from M.D. Richardson. (modified from Richardson and Davis 1992).

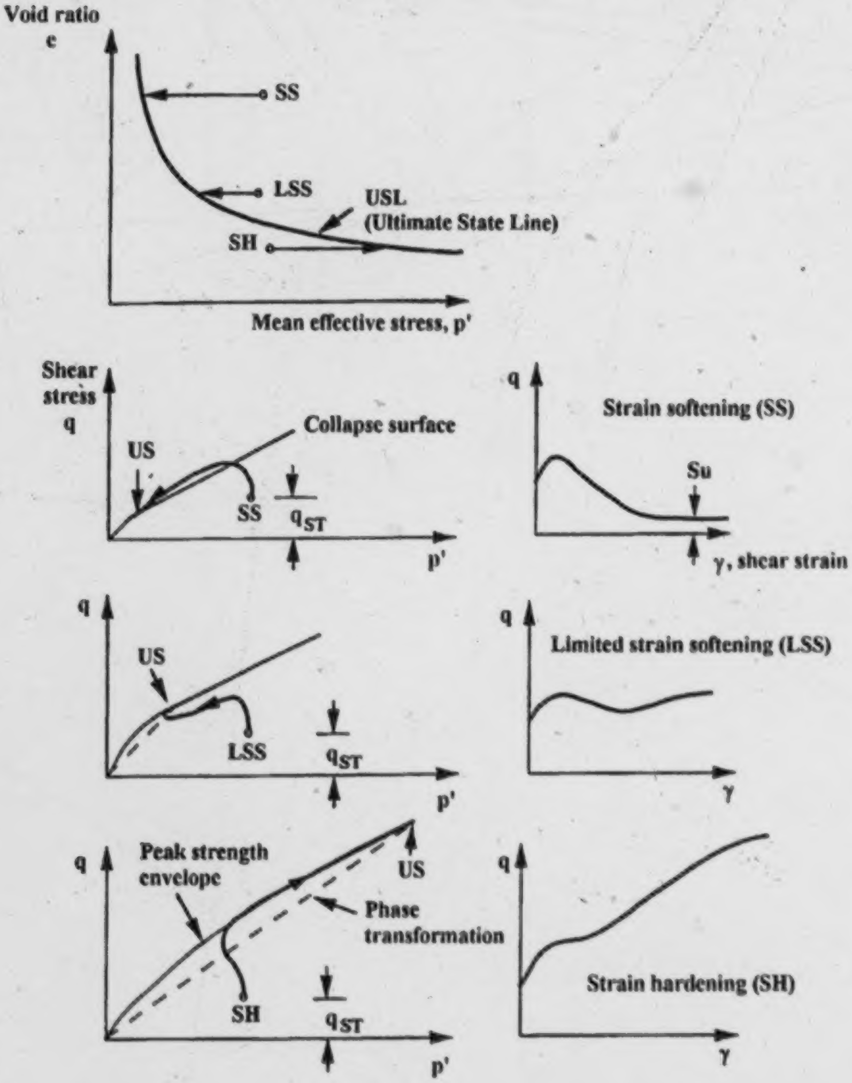
Void ratio
e
SS
LSS
USL
(Ultimate State Line)
SH
Mean effective stress, p'
Shear stress
q
Collapse surface
US
SS
q_{ST}
p'
q
Strain softening (SS)
Su
γ, shear strain
q
US
LSS
q_{ST}
p'
q
Limited strain softening (LSS)
γ
q
Peak strength envelope
US
Phase transformation
SH
q_{ST}
p'
q
Strain hardening (SH)
γ

Figure 1.2 - Schematic of undrained monotonic behavior of sand in triaxial compression (modified from Robertson 1994). LSS, limited strain-softening response; q_{ST}, static gravitational shear stress; S_u, ultimate undrained shear strength; SH, strain-hardening response; SS, strain-softening response; US, ultimate state.

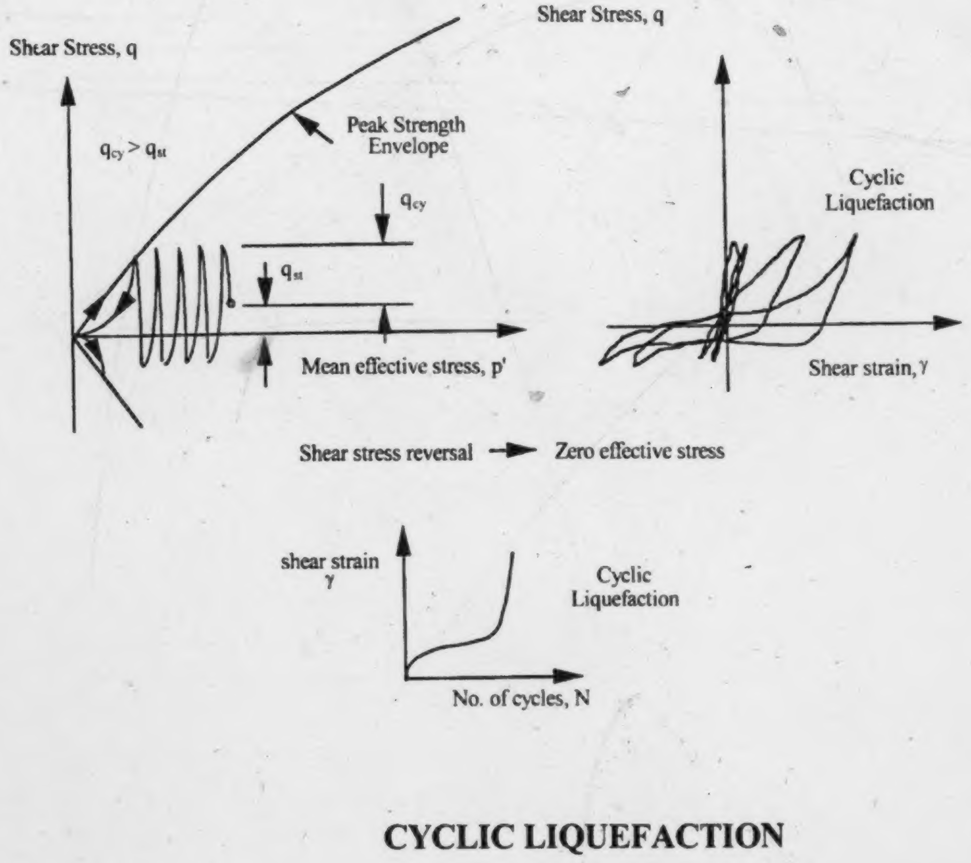
Shear Stress, q
$q_{cy} > q_{st}$
Peak Strength Envelope
q_{cy}
q_{st}
Mean effective stress, p'
Shear Stress, q
Cyclic Liquefaction
Shear strain, γ
Shear stress reversal → Zero effective stress
shear strain γ
Cyclic Liquefaction
No. of cycles, N
CYCLIC LIQUEFACTION

Figure 1.3 – Schematic illustration of cyclic liquefaction (modified from Robertson 1994).

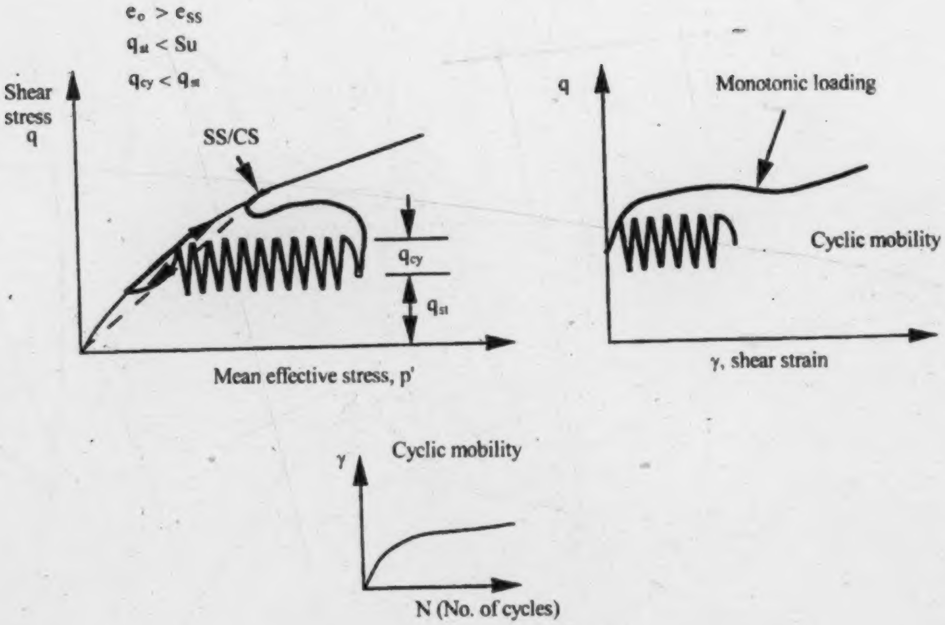
eₒ > e_SS
q_st < Su
q_cy < q_st
Shear stress q
SS/CS
q_cy
q_st
Mean effective stress, p'
q
Monotonic loading
Cyclic mobility
γ, shear strain
γ
Cyclic mobility
N (No. of cycles)

CYCLIC MOBILITY

Figure 1.4 –Schematic illustration of cyclic mobility (modified from Robertson 1994).

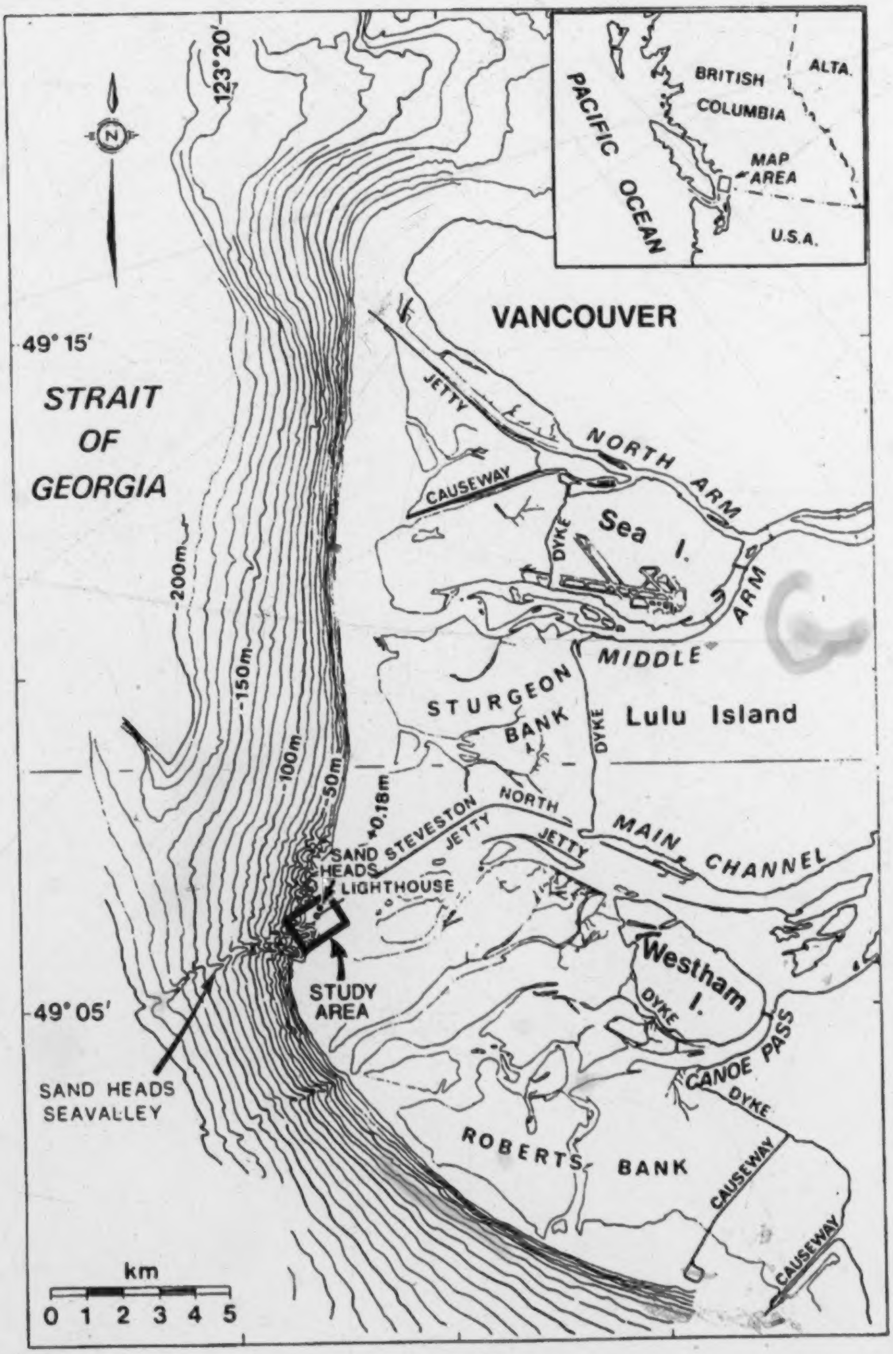
123°20'
BRITISH
COLUMBIA
ALTA.
PACIFIC OCEAN
MAP AREA
U.S.A.
VANCOUVER
49° 15'
STRAIT OF GEORGIA
JETTY
NORTH ARM
CAUSEWAY
DYKE
Sea I.
ARM
MIDDLE
200m
150m
100m
50m
STURGEON BANK
DYKE
Lulu Island
+0.18m
STEVESTON NORTH JETTY
MAIN CHANNEL
SAND HEADS
LIGHTHOUSE
STUDY AREA
Westham I.
DYKE
49° 05'
SAND HEADS SEAVALLEY
CANOE PASS
DYKE
ROBERTS BANK
CAUSEWAY
CAUSEWAY
km
0 1 2 3 4 5

Figure 1.5 – Fraser River delta front (after McKenna et al. 1992).

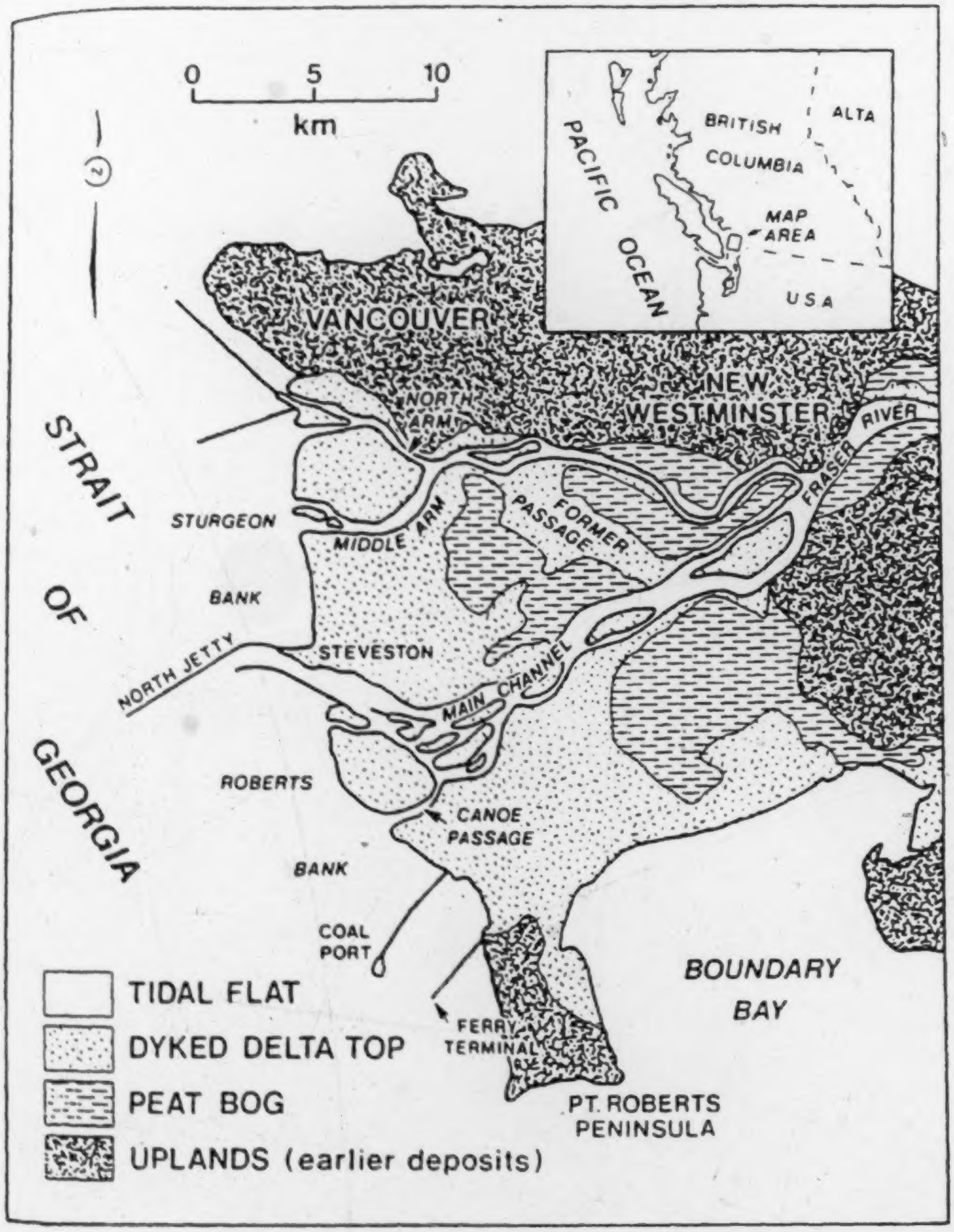
0
5
10
km
BRITISH
COLUMBIA
ALTA
PACIFIC OCEAN
MAP AREA
USA
VANCOUVER
NEW WESTMINSTER
NORTH ARM
FRASER RIVER
STRAIT OF GEORGIA
STURGEON
BANK
MIDDLE ARM
FORMER PASSAGE
NORTH JETTY
STEVESTON
MAIN CHANNEL
ROBERTS
BANK
CANOE PASSAGE
COAL PORT
FERRY TERMINAL
BOUNDARY BAY
PT. ROBERTS PENINSULA
TIDAL FLAT
DYKED DELTA TOP
PEAT BOG
UPLANDS (earlier deposits)

Figure 1.6 – Surficial deposits in the Fraser River delta (after Luternauer and Finn 1983).

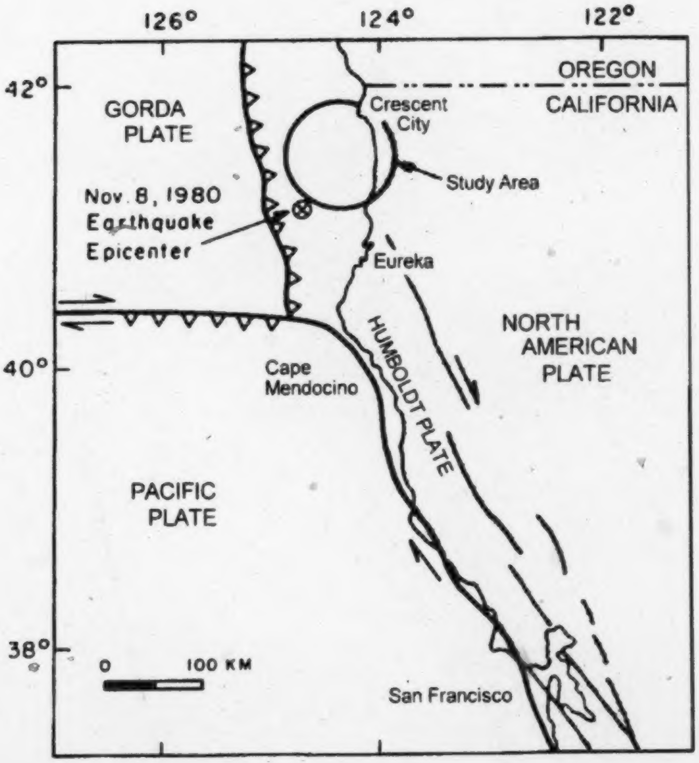
126°
124°
122°
42°
40°
38°
OREGON
CALIFORNIA
GORDA PLATE
Crescent City
Study Area
Nov. 8, 1980 Earthquake Epicenter
Eureka
NORTH AMERICAN PLATE
HUMBOLDT PLATE
Cape Mendocino
PACIFIC PLATE
0 100 KM
San Francisco

Figure 1.7 – California – Oregon continental margin showing location and tectonic setting of study area and epicenter of November 8, 1980, earthquake (modified from Field et al. 1982).

CHAPTER 2

OVERVIEW OF GASSY SOILS

2.1 INTRODUCTION

The presence of gas in soil affects the engineering properties and behavior of the soil. Little is known about the effect of gas on the response of loose sand subjected to static and cyclic loading. In subsequent chapters, the behavior of gassy soils is investigated. However, a review of gassy soils is necessary to establish a basis for discussion. This chapter presents an overview of gassy soils.

In this chapter, several important items related to gassy soils are reviewed. The first item is terminology. Gassy soils are often mistaken for unsaturated soils, although the two types of soil have different behavior. The second item is the origin of gas in sediments. Gas is found in both marine soils and on-land. The origin of the gas can be from organic sources, inorganic sources, or gas hydrates. The third item important for a review of gassy soils is the evidence that exists of the presence of gas. Gassy soils are typically located by seismic, geochemical, or indirect methods.

To complete the overview of gassy soils, previous research on the geotechnical engineering characteristics of gassy soils is reviewed. Research programs undertaken at the University of Alberta, in the United States, in Great Britain, in Norway, and in Germany are discussed. A review of the published research shows that no literature exists that examines the effect of gas on the geotechnical behavior of loose sand.

2.2 TERMINOLOGY

2.2.1 Unsaturated Soils

The effective stress theory was developed for saturated soils, the most common soil type. "Soils that are unsaturated form the largest category of materials which do not adhere in behavior to classical, saturated soil mechanics" (Fredlund and Rahardjo 1993). Unsaturated soils contain a small amount of gas, usually air, but occasionally methane. These soils can be unsaturated in situ because of moisture deficient conditions or can become unsaturated by unloading (Fredlund 1979). For unsaturated soils, any undrained decrease in total stress results in a decrease in pore pressure and a resultant decrease in effective stress (Figure 2.1). The effective stress always remains positive.

2.2.2 Gassy Soils

In the 1980's, an additional class of soil behavior was recognized, gassy soils. Gassy soils are characterized by the presence of a large amount of gas dissolved in the pore fluid. Figure 2.1 illustrates the differences in behavior between unsaturated and gassy soils. A gassy soil subjected to an undrained decrease in total stress has an equal decrease in pore pressure until the liquid gas saturation pressure is reached. At this point, gas exsolution begins and the pore pressures remain at or very near the liquid gas saturation pressure for a continual decrease in total stress. Therefore, the effective stress significantly decreases with changes in total stress. As the effective stress becomes very small, the soil compressibility increases and the pore pressures begin to decrease.

There is no single analytical expression based on classifiable attributes of the soil, which defines the boundary between unsaturated and gassy soils. Such a determination is based solely on the observed behavior (Sobkowicz 1982).

2.3 ORIGIN OF GAS

Gasses found in sediments include carbon dioxide, hydrogen sulfide, ethane, and methane; however, only methane is found in considerable quantities. All gases have either organic or inorganic origins. Natural sources of gas are summarized in Table 2.1.

2.3.1 Organic Origins

Gasses from organic origins may be classified as either biogenic or petrogenic (thermogenic). Biogenic gas is derived from bacterial activity mainly within the top few meters of sediment. However, Parkes et al. (1990) found bacterial activity hundreds of meters down in the sediment, off the coast of Peru. In areas of rapid sedimentation, shallow biogenic gas accumulations can be buried to depths well below those at which they were generated. Petrogenic gas is produced from organic precursors at high temperatures and pressures, and consequently normally exists at depths greater than 1000 m. This gas is derived from organic material by thermal alteration and is hence sometime referred to as thermogenic gas (Floodgate and Judd, 1992). It is possible for the deep petrogenic gas to migrate upward and become trapped as shallow gas accumulations.

2.3.2 Inorganic Origins

Gasses derived from inorganic origins are referred to as abiogenic. These gasses may come from volcanic or hydrothermal sources or may be primordial ("deep-earth") gas. Abiogenic carbon dioxide gas accumulations have been found in certain conditions which combine meteoric water, limestone rock, and geothermal heating. One such accumulation was found during excavations for the ENEL VI & VIII Nuclear Power Plants in Alto Lazio, Italy (D'Appolonia 1981; Morgenstern 1998).

2.3.3 Gas Hydrates

Another source of gas is from the destabilization of gas hydrates (clathrates). These are crystalline, ice-like compounds composed of water and natural gas, which occur under specific high pressure and low temperature conditions. Gas hydrates have been reported from both shallow arctic and deep oceanic sediments (Floodgate and Judd 1992).

2.4 EVIDENCE OF GAS

Gas-charged sediments are known to be widely distributed in seabed soils throughout the world's oceans. Occurrences have been reported in coastal and estuarine regions, across the continental shelves, and within deep ocean basins. Methane gas has been observed in seabed soils on Canada's coastlines.

Although not as common, gas has been found on land. In Alberta, gas has been found in the Athabasca oil sands and in their mine tailings. Gas charged soils were also encountered during an excavation in Italy.

2.4.1 Marine Sediments

Evidence of gas in marine sediments can be categorized into the broad areas of seismic evidence, geochemical evidence, and indirect features. Indirect features may be on or above the seabed. This section discusses the evidence of gas in marine deposits.

a) Seismic Evidence

The occurrence and distribution of gas in shallow seabed sediments can be mapped using geophysical methods. Both surface and subsurface seismo-acoustic records can be used to determine the presence of gas. These methods produce profiles of the sub-seabed by "reflecting an acoustic (pressure) pulse from the seabed and from sub-seabed rock or sediment layers" (Judd and Hovland 1992). Figure 2.2 shows a schematic of the common seismic methods: echo sounding, seismic reflection, and side scan sonar surveying. The presence of gas is detected by visually inspecting the seismic reflection profiles.

Evidence of gas might appear in any of the following forms:

- *Acoustic turbidity* - looks like a dark smear on the profile and may be caused by as little as one percent of gas (Fannin 1990).
- *Enhanced reflections* - are bright spots on the profile thought to characterize gas accumulations within porous (silt and sand-rich) sediments.
- *Columnar disturbances or gas chimney* – are vertical features in which the normal sequence of reflections has been destroyed by upward migration of pore fluids, probably gas (Hovland and Judd 1988).
- *Acoustic blanking* – are patches on the record where the reflections are faint or absent. These features are usually seen in association with other evidence of gas.
- *Digital seismic evidence* – Digital systems are often used to detect pockets of gas accumulations which may represent a hazard to drilling. The digital evidence includes the above but relies mainly upon the presence of a "bright spot" in the seismic profile. Because gas is not the only cause of these bright spots, is has become common practice to look for various seismic wave attributes characteristic of a gassified sediment including amplitude, phase reversal, acoustic velocity reduction etc. (Williams and Sarginson 1990).

It is important to note that although seismic methods can detect the presence of gas, a low concentration of gas will produce a similar response to complete gas saturation (Conn and Arthur 1990). There is currently no way to quantify the concentration or pressure of gas using seismic methods.

b) Geochemical Evidence

The presence of gas can be detected and quantified by analyzing samples in a gas chromatograph. The samples can come from the drilling mud, from seabed samples, or from seawater samples. Drilling mud is analyzed as the mud leaves the borehole. The mud is pumped into a tank where it is stirred; the evolved gases are pumped to a gas chromatograph for continual analysis of concentrations of methane, ethane, propane, and butane, and of total combustible gases. Seabed samples are obtained from the drilling cores; the pore fluids are then extracted and analyzed in the chromatograph. Seawater samples are first subjected to a vacuum to extract dissolved gasses, which are then analyzed in the chromatograph.

In all of the sampling methods discussed above, gas exsolution can occur as the sample is brought from seabed pressures up to shipboard (atmospheric pressures). In order to reduce the loss of gas by the change in pressure, special pressurized samplers have been developed. The soil sediment samples can be taken in pressurized core barrels where they are subsequently transferred to hyperbaric chambers and then tested at in situ pressures (Denk et al. 1981). In addition, the development of specialized BAT samplers to obtain pore fluid samples under pressure has resulted in new methods to analyze gas concentrations and back-calculate in-situ concentrations (Rad & Lunne 1994; Christian and Cranston 1997).

c) Indirect Evidence

Indirect evidence of gas in the seabed can be classified as seabed features, drilling experiences, or biological evidence.

Seabed features can be identified either by geophysical techniques or by visual observations (by remotely operated vehicles, manned submarines, or divers). Some seabed features that suggest the presence of gas are:

- *pockmarks* - seabed depressions cause by the removal of seabed sediments by escaping fluids;
- *seabed domes* - domes formed when gas displaces water in the pore spaces of upper sediments, causing a volume increase;
- *mud diapirs* - gas charged clay or mud that penetrate through the seabed due to their increased buoyancy;
- *giant gas mounds* - very large diapirs, up to a kilometer in diameter and over 100 m in height above the seabed;
- *seepages* - visible gas escaping from the seabed;
- *methane-derived carbonates* - carbonate precipitates which cement the normal seabed sediments to form a hard rock-like material; and
- *polynyas* - holes in sea-surface ice, possibly caused by gas seepages.

In addition to seabed features, many times the presence of gas is determined by anecdotal evidence during drilling. Samples recovered using standard techniques have been reported to "grow" out of the sampling tubes when exposed to atmospheric pressures on shipboard. This is the result of gas exsolution due to the reduction of pressure from in situ to atmospheric. Bubbles have been seen emerging from samples, and often the samples take on a frothy texture (Denk et al. 1981; Esrig and Kirby 1977).

In recent years, a number of biological studies have been completed in areas of known "gas-activity". These studies have found that the presence of methane at or near the seabed may enrich biological activity (Hovland and Judd 1988; Hovland and Thomsen 1989), or may inhibit development of benthic (bottom dwelling) communities (Dando et al. 1991).

2.4.2 Athabasca Oilsands

In the Athabasca region of northern Alberta, the oilsands have been under study for many years. Gas was reported escaping from the oilsands during drilling and exploration by Ells (1926). Hardy and Hemstock (1963) noted disturbance of core samples due to gas exsolution. Further evidence of gas in the oilsands was observed in excavations for foundations, when the base materials showed excessive swelling and softening, followed by settlement upon reloading. In addition, slopes cut into the oilsands exhibited swelling, softening, and surficial slabbing.

Oilsand is a dense, uncemented sand which contains bitumen and upon reduction of pressures dissolved gas “tends to come out of solution in large quantities” (Sobkowicz 1982). Both methane and carbon dioxide are present in substantial quantities in the pore water and bitumen of the oilsands.

Recently, Syncrude mine (in the Athabasca oilsands) found evidence of gas in some of their old and newly deposited tailings and containment dykes (Lord 1998). It is believed that the gas is either methane, produced by bacterial action, or carbon dioxide or sulphur, produced by carbonation or sulphurization due to the addition of gypsum.

2.4.3 Alto Lazio Nuclear Power Plant, Italy

During excavation for the ENEL VI and VIII Nuclear power plant in Alto Lazio, Italy, substantial heave was noted (D’Appolonia 1981). The silty clay and silty sand underlying the site were found to contain carbon dioxide gas believed to be formed from the combination of meteoric water, limestone rock, and geothermal heating (Morgenstern 1998).

2.5 PREVIOUS RESEARCH

The geotechnical implications of gas in sediments have been studied by a number of researchers.

2.5.1 University of Alberta

The University of Alberta began one of the first studies on gassy soils in the early 1960s. Early research work involved examining the effect of gas on dense sand. Hardy and Hemstock (1963) recognized the significant geotechnical implications of gas in dense sands, specifically in the Athabasca oil sands. They noted a loss of strength and change in deformation properties associated with gas exsolution. Dusseault (1977, 1979, 1980), Dusseault and Morgenstern (1978a, 1978b), and Dusseault and von Domselaar (1982) researched sample disturbance and the difference between in situ and disturbed strengths. They concluded that the oilsands, an extremely dense, uncemented, bitumen containing fine sand, exhibited low compressibilities and high in situ strengths. However, upon reduction of confining pressure, gas exsolution occurred, which resulted in large volume changes causing a loss of strength and an increase in compressibility.

Sobkowicz (1982) and Sobkowicz and Morgenstern (1984, 1987) studied the effect of gas with respect to the Athabasca oil sands. They examined gassy soil behavior by studying equilibrium behavior (independent of time) and non-equilibrium behavior (includes both transient processes and is time-dependent). A laboratory program inspected the gas exsolution process for both undrained and drained boundary conditions and proposed theories and solutions for these cases. The final result combined the consolidation and gas processes into one general theory of transient behavior that incorporated a linear elastic constitutive relationship for the soil. The research was applied to the problem of pore fluid changes around a shaft or borehole and characterized the soil behavioral response with a ground reaction curve for the soil.

2.5.2 United States

In the 1970s, American engineers (Coleman et al. 1974; Whelan et al. 1975, 1977, 1978; Esrig and Kirby 1977) studied the effect of gas on submarine landslides and the stability of marine structures. Their focus was on the soft marine clays of the Mississippi River delta, and they concluded that the presence of gas is one of the main causes of shear strength reduction and subsequent failure of submarine slopes.

Denk et al. (1981) continued the American study of gas by describing a new way of collecting gas charged marine samples using a pressurized core barrel. They proposed that by maintaining in situ pressures within the core, gas exsolution and the resulting sample disturbance due to the reduction of pressures would not occur. They obtained pressurized samples that were subsequently transferred to a hyperbaric chamber manned by geotechnically trained "divers". The samples were then tested at downhole pressures.

2.5.3 Great Britain

Perhaps the most comprehensive research conducted on gassy sediments was carried out in Great Britain. Wheeler (1986, 1988a, 1988b, 1991) and Wheeler and Gardner (1989) studied the effect of large gas bubbles on fine-grained soils. A conceptual model was developed to describe soils containing large gas bubbles and analyzed to yield upper and lower bound predictions for the undrained shear strength. An experimental program confirmed the model predictions and indicated that the undrained strength can be either increased or reduced by the presence of large gas bubbles, depending upon the values of consolidation pressure and the initial pore water pressure. Duffy et al. (1994) continued the work on large bubbles and found that the shear modulus could be reduced by up to fifty percent by the presence of a relatively small volume of large gas bubbles.

Nagaswaran (1983) and Sills and Nagaswaran (1984) developed a method of impregnating fine grained laboratory specimens with methane gas. The method involved exposing an inert chemical, zeolite, to methane. Zeolite has a strong affinity for polar molecules such as water, but in the absence of water, accepts other molecules of a suitable size into its crystal lattice (Breck 1974). The methane-saturated zeolite was mixed with wet soil, and the methane in the zeolite was replaced with water. Methane was released over a period of a few hours to form bubbles within the specimen. Gardner and Goringe (1988) went on to measure the gas bubble size distribution in laboratory specimens prepared with the above-mentioned method.

Thomas (1987), Wheeler et al. (1989), and Sills et al. (1991) studied the behaviour of gas in fine-grained offshore soils. They suggested upper and lower limits for the gas pressure, and identified factors likely to cause changes in the gas pressure. The behavior of gassy soils was studied by performing laboratory consolidation and triaxial tests. The results showed that the consolidation of gassy soils occurred in two stages; the first being initial settlement due to the compressibility of the gas, and the second being the classic time-dependent settlement due to migration of pore water pressures. The undrained shear strength was found to be either increased or reduced by the presence of gas. This research also showed that the speed and attenuation of compression waves are greatly affected gas bubbles within the soil.

In addition to soil behavior, Sills and Wheeler (1992) identified the significance of gas in different offshore operations. They noted that gas can occur in the seabed in three ways: in solution in the pore water, undissolved in the form of gas-filled voids, or as clathrates (gas hydrates). In the first case, the gas will have little affect on the physical properties of the seabed unless the ambient pressures are reduced. In the second case, the gas will affect the engineering properties of the seabed due to the high compressibility of the gas. In the third case, the gas only becomes hazardous if the clathrates melt.

All the above research performed in Great Britain studied the effect of gas on fine-grained soils. One laboratory program conducted by Sills (1988) investigated the undrained shear strength of dense gassy sand and found that the presence of gas reduces the undrained shear strength.

Recently, Sills (1997) has been conducting research on marine muds by performing triaxial tests on clay samples with naturally occurring gas. Additionally, research is underway at Oxford to study the cyclic resistance of fine-grained gassy soils.

2.5.4 Norway

The Norwegians (Rad et al. 1989; Rad & Lunne 1994; Rad et al. 1994) also became involved in gassy soil research. The outcome of their research was the development of an in situ test device capable of detecting, sampling, and quantifying in situ gases, and the determination of the effects of gas on soil behavior. An offshore BAT probe was modified and a new methodology to calculate in situ gas contents was developed. Premchitt et al. (1992) describe the successful employment of the BAT probe and methodology in Hong Kong waters. Static and cyclic triaxial tests performed on dense sand concluded that the higher the gas content, the weaker the specimen in undrained shearing. Tests on medium loose sand showed that the looser samples were not as affected by the presence of gas.

2.5.5 Eckernförde Bay Study

From 1993 to 1995, the fine-grained muddy methane-rich sediments of the Eckernförde Bay in the southwestern Baltic Sea were studied in a joint Unites States and German lead project. The objective of the project was to "physically characterize and model the effects of benthic boundary layer processes on seafloor structure, properties, and behavior in the gassy sediments of Eckernförde Bay" (Richardson and Davis 1998). A strong emphasis was placed on acoustic bubble interactions and the possible use of acoustics to characterize these gassy sediments.

The project looked into the oceanographic processes (Nittrouer et al. 1998), the concentration, distribution, and long and short-term changes of methane gas (Wever et al. 1998), the biochemical processes controlling methane (Martens et al. 1998; Albert et al. 1998), the groundwater seepage effect on methane (Bussmann and Suess 1998), the bubble population and acoustic interaction (Anderson et al. 1998), establishing a baseline geoacoustic model (Stoll and Bautista 1998), the influence of gas bubbles on the sediment acoustic properties (Wilkens and Richardson 1998), sonar evidence for methane ebullition (Jackson et al. 1998), and porosity, density, and electrical resistivity variabilities (Briggs et al. 1998).

The geotechnical properties of the Eckernförde Bay sediments were studied by Silva et al. (1996), Brandes et al. (1996), Ag (1994), Brogan (1995), Lavoie et al. (1996), Slowey et al. (1996) and Silva and Brandes (1998). Their objective was to assess the sediment properties and behavior including compressibility and permeability characteristics, stress history and state, stress strain and strength behavior, and gas content and distribution. The research found that there were significant seasonal variations in gas content in the upper 50 cm of sediment, that compressibility was high, permeability was low, undrained shear strength was low but increases linearly with depth, and friction angle was low.

2.5.6 Other Research

Rau and Chaney (1988) recommended procedures for triaxial testing of marine sediments with high gas contents and introduced a method to estimate the amount of gas that theoretically comes out of solution.

2.6 SUMMARY AND CONCLUSIONS

Gas-charged sediments are abundant in seabed soils, but also exist on land. Gassy sediments have a large amount of dissolved gas in their pore fluid. Gassy soils can be differentiated from unsaturated soils by their behavior. That is, when subjected to a decrease in total stress, near or below the liquid gas saturation pressure, gassy soils exhibit very little decrease in pore pressure.

Gasses found in sediments include carbon dioxide, hydrogen sulfide, ethane, and methane; however only methane is found in considerable quantities. These gasses may originate from biogenic (bacterial activity) or petrogenic (organic precursors) processes. Destabilization of gas hydrates is another source of gas. Gas may also come from volcanic or hydrothermal sources or may be primordial ("deep-earth") gas.

Previously published research has examined gas in dense sand, such as the Athabasca oil sands, or soft fine-grained marine soils. Previous research work focused on sample disturbance, equilibrium effects, shear strength, and the effect of large bubbles on consolidation, shear strength, and acoustics. Samplers and probes were modified to detect and sample gassy pore fluids and sediments, and new methodologies developed for calculating in situ gas contents. Laboratory strength testing of fine-grained muds with natural gas producing bacteria is currently being performed.

There appears to be no published research work that studies the effect of gas on the geotechnical behavior of loose sand.

Table 2.1 - Sources of natural gas (modified from Floodgate and Judd 1992).

Sources of natural gas		
Organic origins	Microbial degradation of organic matter in sediments	Biogenic
	Thermal degradation of organic matter in sediments	Thermogenic
	Destabilizating gas hydrates	
Inorganic origins	Volcanic and hydrothermal	Abiogenic
	"Deep-earth"/primordial gas	

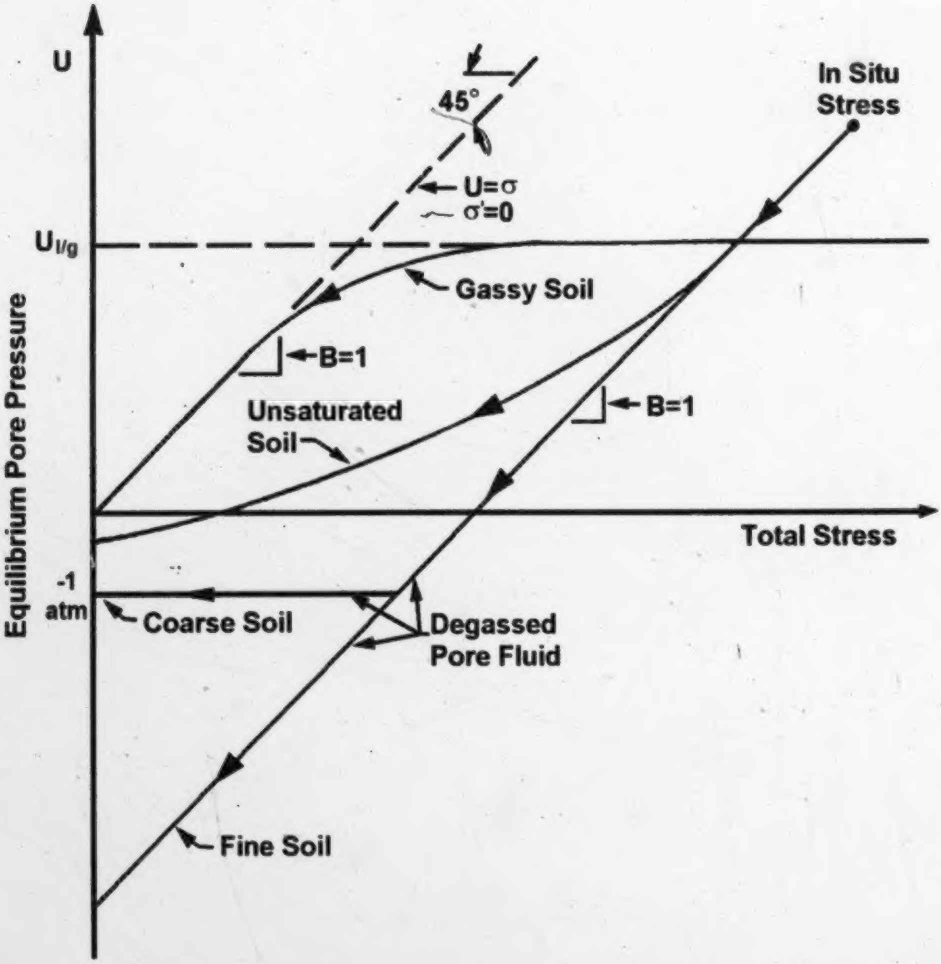
U
45°
U=σ
σ'=0
In Situ Stress
$U_{l/g}$
Gassy Soil
B=1
Unsaturated Soil
B=1
Equilibrium Pore Pressure
Total Stress
-1 atm
Coarse Soil
Degassed Pore Fluid
Fine Soil

Figure 2.1 - Undrained equilibrium behaviour of an element of soil on unloading: effect of amount of gas dissolved in pore fluid (modified from Sobkowicz and Morgenstern 1984).

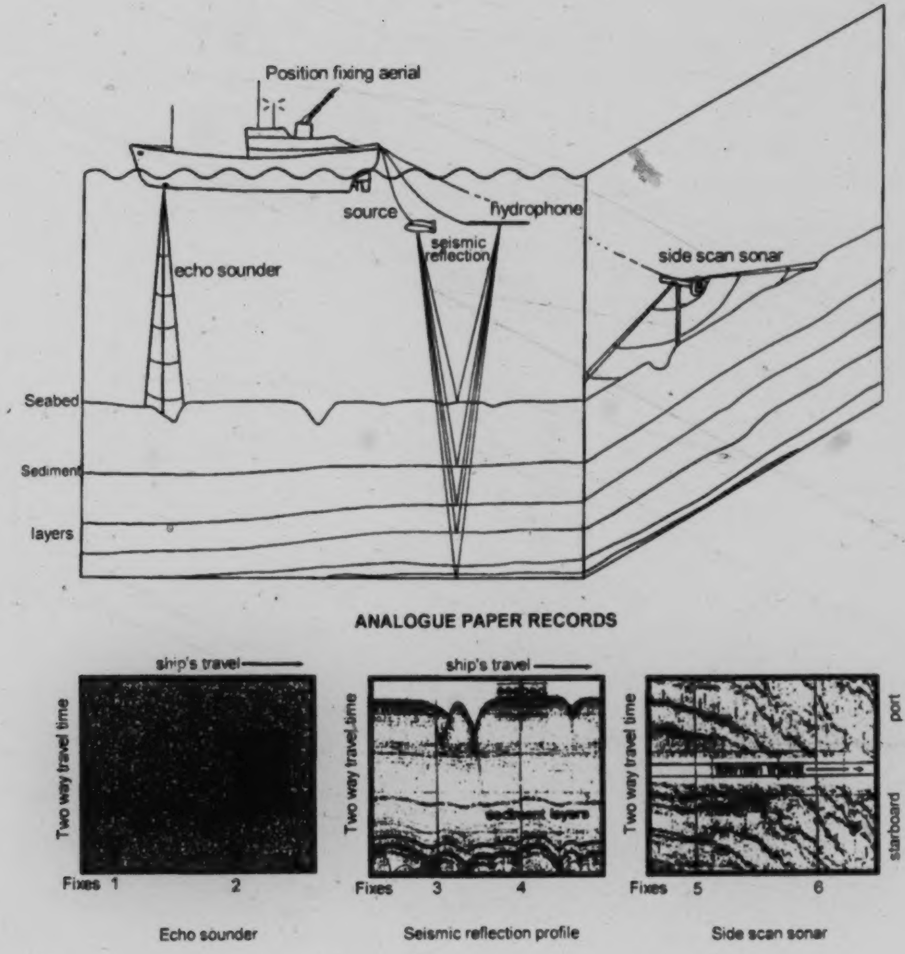
Position fixing aerial
source
hydrophone
seismic reflection
echo sounder
side scan sonar
Seabed
Sediment
layers
ANALOGUE PAPER RECORDS
ship's travel
ship's travel
Two way travel time
Two way travel time
Two way travel time
sediment layers
port
starboard
Fixes 1
2
Fixes 3
4
Fixes 5
6
Echo sounder
Seismic reflection profile
Side scan sonar

Figure 2.2 - Echo sounding, seismic reflection profiling, and side scan sonar surveying (modified from Judd and Hovland 1992).

CHAPTER 3

LABORATORY PROGRAM [1]

3.1 INTRODUCTION

A laboratory program was carried out to study the behavior of loose gassy sand. The objectives of the program were:

- To examine the response of loose gassy sand specimens subjected to monotonic and cyclic loading,
- to determine if loose gassy sand specimens could strain soften and experience flow liquefaction,
- to determine if loose gassy sand specimens could cyclic soften and experience cyclic liquefaction, and
- to examine how the quantity of free gas affects the resistance to flow and cyclic liquefaction.

Several different testing methods could have been undertaken to examine the behavior of loose gassy sands. Direct simple shear, shear ring, hollow cylinder, and triaxial compression and extension are common laboratory methods used to evaluate liquefaction potential. Shear ring and hollow cylinder are considered to be more complicated tests. The desired accuracy of the results could not justify the complexity of the tests. Triaxial testing was determined to be the testing method of choice.

---

[1] *A version of part of this chapter has been submitted for publication. Grozic, J.L., Lefebvre, M.E., Robertson, P.K., and Morgenstern, N.R. 1999. A new method to measure gas content in triaxial specimens using time domain reflectometry. Submitted to the Canadian Geotechnical Journal, September 17, 1999, 28 pages.*

Triaxial testing has a few advantages over the other testing methods. Triaxial testing is a common testing method and there are a number of recommended procedures published in addition to many published test results. Using a computer controlled triaxial apparatus enables cyclic testing to be performed. In addition, the triaxial apparatus is simple to operate and modify.

Specialized triaxial testing was undertaken. Two different triaxial systems were used for the monotonic and cyclic testing. The monotonic tests consisted of consolidated drained and undrained tests on saturated specimens and consolidated undrained tests on gassy specimens. The cyclic tests consisted of consolidated undrained tests on saturated and gassy specimens.

A suitable method for determining the gas content of the specimens had to be established. Several methods were reviewed, but shortcomings were found in all the methods. An innovative new way to measure gas content in a triaxial apparatus, using time domain reflectometry, was developed.

The laboratory program, including a description of the equipment and gas content measurement method, is discussed in this chapter.

3.2 GENERAL CONSIDERATIONS

To begin the laboratory program, some general items were considered; these items included the material being tested, the type of gas, and the target pressures.

3.2.1 Material

The objective of the laboratory program was to study the liquefaction of gassy specimens, therefore choosing an appropriate material for the specimen preparation was important.

Most existing methods for determining the potential for liquefaction are based on data obtained from the testing of clean sandy soils. Typically, corrections for the amount and type of fines must be made when silty sand or sandy soils containing fines are evaluated for liquefaction potential. Therefore, using clean sand to prepare the laboratory specimens eliminated some of the potential complexities in determining the liquefaction potential.

First, using Fraser River sand was considered. Many submarine slides have occurred in the Fraser River sediments. However, after further thought about the objectives of the research, to simply show the differences between the liquefaction potential of saturated and gassy specimens, it was decided that any clean sand would be sufficient. Fraser River sand is fine-grained and therefore somewhat difficult to work with. Choosing a sub-rounded slightly coarser sand, such as Ottawa sand, would make the specimen preparation simpler. Many triaxial tests have been performed on Ottawa sand. By choosing Ottawa sand, the results of the laboratory program could be compared to previously published data.

Ottawa sand (CT-109A), graded to meet ASTM C-778 standards, is a medium sand, comprised of round to sub-rounded quartz grains. Ottawa sand is uniform with a mean grain size (D_{50}) of 0.34 mm. A particle size distribution curve is shown in Figure 3.1. The specific gravity is 2.65. The maximum and minimum void ratios, determined using ASTM D2049, are 0.82 and 0.50, respectively.

3.2.2 Gas Type

As previously stated, the predominant gas in the seabed is methane. However, working with methane in the laboratory would require special procedures and equipment due to the explosive nature of the gas. In addition, methane is not easily dissolved in water (solubility coefficient of approximately 0.034L/L in fresh water (Yamamoto et al. 1976)) and very high pressures would be required to work with methane gas. Therefore, carbon dioxide (CO_2) was selected instead of methane. CO_2 is readily available, non-corrosive, and non-flammable. CO_2 is moderately to highly soluble in water, (solubility coefficient of approximately 0.86 L/L (Rad et al. 1994)) thus, test pressures could be kept at reasonable levels.

After the selecting the type of gas to be used, the differences in dissolved gas concentrations between the sample pore fluid and the cell fluid were addressed. The difference in gas concentration between the sample and cell fluid results in diffusion through the sample membrane into the cell. Sobkowicz (1982) performed a series of tests to determine the loss of CO_2 from a sample under various cell fluid and membrane combinations. He showed that using glycerol as a cell fluid and latex as a membrane could minimize diffusion. This combination worked well because carbon dioxide gas will not readily dissolve into glycerol. However, using glycerol as a cell fluid requires additional laboratory equipment. Trial tests performed using glycerol took roughly twice the time to complete as did similar tests using water as a cell fluid. When water was used as a cell fluid, experiment test times were relatively short (approximately 3 to 4 hours for monotonic tests and under 10 minutes for cyclic tests). Because of the short test times, the total amount of carbon dioxide gas lost through the membrane was not significant. It was therefore determined that the use of water as a cell fluid would be suitable.

3.2.3 Target Pressures

Target pressures were selected before testing the laboratory specimens. The liquid gas saturation pressure for carbon dioxide and water (about 510 kPa) governed the choice of cell pressure. Confining pressures were chosen to be at least 250 kPa higher than the liquid gas saturation pressure; therefore, a target value of 800 kPa was selected. The initial mean normal effective stress was selected to be approximately 300 kPa for all the specimens. By selecting the same initial effective pressure, the samples could be easily compared.

3.3 EQUIPMENT DESIGN FOR MONOTONIC TESTING

Figure 3.2 shows photographs of the monotonic testing equipment and Figure 3.3 shows a schematic of the testing apparatus. The following sections describe the details of the monotonic testing apparatus.

3.3.1 Measuring Strains

Axial strain was determined by measuring the axial load ram displacement, and converting this into a vertical strain. Vertical strains were measured with an LVDT (Linear Voltage Displacement Transducer). The LVDT was calibrated before setup and was accurate to ± 0.05 mm.

3.3.2 Measuring Pressures

Cell and sample pressures were measured using 1380 kPa (200 psi) strain-gauged diaphragm transducers with an accuracy of ± 0.2 kPa. The transducer for measuring pore pressure was mounted on the bottom of the triaxial, close to the sample. The pore pressure transducer was connected to the sample by a drainage line located in the base of the sample, covered by a coarse metallic filter stone. The cell pressure transducer was also located on the triaxial base, close to the cell fluid. A third transducer measured the applied backpressure and was located near the pressure source. All pressure transducers were calibrated prior to the laboratory setup. Calibrations were checked several times during the laboratory program. At the beginning of each sample setup assembly, all pressure transducers were saturated with de-aired distilled water.

3.3.3 Measuring Deviatoric Stress

Deviatoric stresses were applied using a diaphragm-operated air cylinder (trade name Bellofram). Deviatoric stress was measured with an external load cell for each loading increment during consolidation and for any manual changes in pressure. During shear, deviatoric stresses were measured with an internal load cell. The external load cell had a capacity of 907 kg (2000 lbs) and an accuracy of ± 0.5 kg. The internal load cell had an amplified capacity of 455 kg (1000 lb) and an accuracy of ± 0.1 kg. Both load cells were calibrated during the laboratory setup.

3.3.4 Measuring Volume Changes

Volume change of the saturated specimens was measured using an electronic volume change device. The electronic device used a system of two diaphragms, when the lower diaphragm expanded the upper diaphragm contracted. A rod was connected to a piston on the diaphragm and to an LVDT. The system was calibrated to a known volume. The electronic system was accurate to ± 0.05 ml. Unfortunately, the electronic volume change device required conditions of full saturation, therefore, it could not be used with the gassy samples. Volume change during consolidation of the gassy samples was measured using a burette filled with water and Kerosene. This system allowed the passage of gas out of the burette, and therefore just the sample water was measured. The burette system was accurate to ± 0.1 ml.

3.3.5 Cell Construction

The cell was constructed of Plexiglas and reinforced with fiberglass strips around the perimeter. This cell design allowed for pressures up to 1000 kPa. The TDR mini-probe was built into the bottom sample pedestal, screwed into the aluminum cell base, and sealed with silicon. The TDR cables passed through a hole in the cell intended for bender element cables.

3.3.6 Loading Frame

A modified Wykeham Farrance strain controlled loading machine was used.

3.3.7 Data Acquisition

An automated data acquisition system called LabVIEW was used to collect the laboratory test data. All measurements from the pressure transducers, the LVDT, and the electronic volume change device were passed through a Fluke signal conditioner and collected by LabVIEW.

3.4 EQUIPMENT DESIGN FOR CYCLIC TESTING

All cyclic tests were performed using an automated triaxial testing system, Auto Triaxial, built by Soil Equipment Co. for performing cyclic loading and specialized stress path testing. Photographs of the setup are shown in Figure 3.4. A schematic of the equipment setup is shown in Figure 3.5. The triaxial testing system consisted of a loading frame, a triaxial cell and a loading piston, a volume measuring device, a dual pneumatic loading system, a signal conditioning unit, a process interface unit, a computer, and a dot-matrix printer. The system used a total of five sensors.

Further details of the Auto Triaxial system can be found in Chan and Mulilus (1976) and Chan (1981).

3.4.1 Measuring Strains

Axial strain was calculated from the vertical displacement, measured with an LVDT attached to the axial load ram. The LVDT had a maximum travel of 25 mm and was accurate to ± 0.01 mm.

3.4.2 Measuring Pressures and Volume Change

Three pressure transducers detected chamber pressure, the effective pressure, and the volume change. The chamber and effective pressure transducers had a 1379 kPa (200 psi) capacity with an accuracy of ± 0.2 kPa. The volume change transducer measured the differential pressure of a burette. The burette had a water and compressed air interface, therefore, when gassy exsolution occurred the gas was released into the compressed air. This system enabled measurement of sample water only. The volume change device was accurate to ± 0.05 ml.

3.4.3 Measuring Deviatoric Stress

A load cell was used to monitor the axial load. Load was applied using the 1360 kg (3000 lb) load cell. The load cell was accurate to ± 0.15 kg.

3.4.4 Cell Construction

The cell was constructed of Plexiglas with no reinforcing. Cell pressures did not exceed 1000 kPa in this system. The mini TDR probe was built into the sample pedestal, screwed into the cell base, and sealed with a rubber O-ring and silicon. A hole in the cell base, beneath the sample pedestal, had to be drilled to allow for passage of the TDR wires through the cell.

3.4.5 Loading Frame

The loading frame was standard, and came with the Auto triaxial equipment.

3.4.6 Data Acquisition and Computer Control

The conditioned output signals of all five sensors were received by the process interface unit. The process interface formed the communication link between the computer converter, 8 channels of 12-bit, high-speed D-A converters, and a 24-channel digital input/output port.

For the automated triaxial testing system, nine channels of the A-D converters were used: five channels were used to monitor the signals from the five sensors equipped with the system; one was used to monitor drainage conditions (drained or undrained); two were used to monitor the e/p valve drive signals; and another one used as a zero reference to minimize the zero shift of the grounded system. The D-A converters were configured to two high resolution controllers to control the axial load and lateral pressure, respectively. The digital input/output port was not used in this system.

The computer received and stored the real time data in its memory and issued control signals to regulate the testing process accordingly. The dot-matrix printer was used to record output from the system. The computer system was driven by software written for the particular equipment.

3.5 BUBBLE CHAMBER DESIGN

Gassy samples were prepared using water saturated with carbon dioxide gas. When the back pressure in the specimens was reduced below the liquid/gas saturation pressure of carbon dioxide water, then gas exsolution occurred and occluded bubbles formed. It was necessary to develop a procedure to saturate water with carbon dioxide. A bubble chamber was constructed following the work of Sobkowicz (1982). Figure 3.6 shows photographs of the bubble chamber and Figure 3.7 shows a schematic. The set up consisted of two high pressure chambers partially filled with de-aired distilled water. One chamber was located approximately 0.5 m above the triaxial cell. The other chamber was located about 0.5 m below the cell. Carbon dioxide was allowed to bubble slowly through the upper chamber for a period of 2 hours. The pressure was controlled at approximately 750 kPa. During replacement of pore fluids with the carbon dioxide saturated water, the upper chamber was attached to the sample top and the lower chamber was attached to the sample base. In this way the gas saturated water was slowly circulated through the sample, driven by a head difference of approximately 1 m.

3.6 MEASUREMENT OF GAS CONTENT

An important part of the laboratory procedure was to measure the gas content at any time during the test. It was also required to accurately track the changes in gas content and to eventually convert this information to changes in void ratio as a function of the mean normal effective stress.

3.6.1 General Considerations

In determining a suitable method for obtaining degree of saturation (gas content) it was necessary to consider the accuracy of the measurements, the sample disturbance caused by some methods, the electrical conductivity of some transducers, and the high pressures necessary in aspects of the setup.

Several methods of determining degree of saturation were considered.

3.6.2 Cell Volume Change

The first method considered was to measure the amount of volume change from the cell fluid. This method assumes that any change in the sample volume due to gas solution or exsolution will result in an equal change in volume of the cell fluid. Measuring the cell fluid volume is very inaccurate due to the large volume of cell fluid in relation to the very small volume changes. Small amounts of air trapped in the cell fluid and water absorption by the Plexiglas cell further decrease the accuracy.

3.6.3 Double Walled Triaxial Cell

The second method that was considered was the double walled triaxial cell, which was used extensively by Sills (1988). This procedure for measuring degree of saturation also tracks volume change of the sample by measuring cell fluid changes. A greater degree of accuracy is obtained, compared to directly measuring cell fluid, because the volume change area is much smaller. Double walled cells are commercially available, but are quite expensive. More recently, research at Oxford University has moved away from using the double walled cell due to the inability to calibrate for the water absorption of the Plexiglas (Sills 1997).

3.6.4 Radial Strain Gauge

The third method considered was a circumference measurement device. Sobkowicz (1987) used a lightweight radial strain gauge with a circular caliper type mechanism and an attached linear voltage displacement transducer (LVDT) to determine volume change of dense gassy sands. Although the actual radial measurements were quite accurate, assumptions about the radius changes through the entire specimen height during the test were necessary. The accuracy of this method is similar to a double walled cell. This method could not be applied to this research because the samples are very loose, therefore, attaching anything to the sample would cause disturbance and the water used as cell fluid is electrically conductive so an LVDT could not be used in the cell. In an effort to overcome these difficulties, a lightweight high pressure non-conductive radial strain gauge was proposed. The lack of accuracy of this method combined with the high costs for custom making a strain gauge discouraged the use of this method.

3.6.5 P-Wave and Bender Elements

The fourth method considered was compression waves and bender elements. Compressional wave velocity and attenuation have been correlated with gas content (Sills et al. 1991). The compression wave can be generated and measured using bender elements in the top and bottom sample caps. The P-wave (compression wave) velocity drops significantly when gas is encountered. Accuracy is low due to the sudden, almost vertical drop, of the P-wave velocity when compared with gas content as shown in Figure 3.8.

3.6.6 Dielectric Constant

The final method that was considered was the use of time domain reflectometry (TDR) to obtain the dielectric constant of the soil solid, water, gas mixture. This method is described in Section 3.7.

3.7 TIME DOMAIN REFLECTOMETRY TO MEASURE GAS CONTENT

3.7.1 Dielectric Constant

The dielectric property of a material describes the ability of the material to store electrical potential energy under the influence of an electric field relative to that of air. The concept of dielectrics is described by Smith and Mullins (1991):

> "The practical definition of the dielectric constant K of a material is the ratio of the value of a capacitor with the material between the plates, compared with the value with air between the plates. A dielectric material is an insulator, as distinct from a metal, which is a conductor. Under the influence of an electric field, the positive and negative charges in a dielectric material are displaced with respect to each other and tiny electric dipoles are produced. Some materials such as water also have permanent dipoles. The electric dipoles are aligned by the electric field and the electric medium as a whole becomes polarized. The dielectric constant as defined above turns out to be a measure of polarization; as a consequence, a material whose molecules have a permanent

dipole movement are free to align with the electric field has a very large dielectric constant."

Water molecules are more readily polarized than the molecules which comprise soil or air, hence water has a much larger dielectric constant than soil or air. The dielectric constant of a soil is typically between 3 and 6. The dielectric constant of air is 1, of carbon dioxide is 1.002, and the dielectric constant of distilled water in air at 20°C is approximately 80. The dielectric constant of water varies slightly with temperature, but varies significantly with phase change. For example, water in solid state (ice) has a dielectric constant of about 3; this is because the molecules in ice cannot readily align themselves as they can in liquid water.

Since the dielectric property of soil and water in their aqueous phases is significantly different, it is possible to measure the dielectric constant of a soil-air-water system to determine soil moisture content. Because of the similar dielectric constant of ice and soil, it is also possible to evaluate the unfrozen water content in frozen soils as was done by Grozic (1997).

3.7.2 Theory of Time Domain Reflectometry

Time domain reflectometry (TDR) is a remote sensing electrical measurement technique that has been used for many years to determine the spatial location and nature of various objects (O'Connor et al. 1994). The first use of TDR, actually an early form of radar, was to find faults in cables and transmission lines (Andrews 1994). TDR emits an electromagnetic step pulse that travels along the transmission line and remains unaltered if the characteristics of the line remain the same. Probes of various geometry are used at the "end" of the line that alter the pulse and return a waveform back to the TDR receiver. From this waveform, the propagation velocity and the attenuation (resistance) of the pulse through the soil can be calculated. The propagation velocity, v, is indicative of the dielectric constant, which in turn, can be related to the volumetric water content (Lefebvre 1997). The attenuation, α, is indicative of the electrical conductivity of the soil. The dielectric constant can be determined from the travel time or the velocity of the pulse and the electrical conductivity can be determined from the magnitude of the pulse.

The propagation velocity and magnitude of electromagnetic waves have the following form:

$$v = \frac{c}{\sqrt{\frac{K'}{2}\left[1+\left(1+\left[\frac{K''+\frac{\sigma_{dc}}{\omega\varepsilon_o}}{K'}\right]^2\right)^{\frac{1}{2}}\right]}} \qquad [3.1]$$

and

$$\alpha = \frac{60\Pi\left(\omega\varepsilon_o K''+\sigma_{dc}\right)}{\sqrt{\frac{K'}{2}\left[1+\left(1+\left[\frac{K''+\frac{\sigma_{dc}}{\omega\varepsilon_o}}{K'}\right]^2\right)^{\frac{1}{2}}\right]}} \qquad [3.2]$$

where ω is the angular frequency, ε_o is the permittivity of free space, K' and K'' are the real and imaginary parts of the dielectric constant, respectively, σ_{dc} is the dc electrical conductivity, and c is the velocity of propagation of light in free space. If the imaginary dielectric term $K''+\frac{\sigma_{dc}}{\omega\varepsilon_o}$ is much less than the real dielectric K' then equations [3.1] and [3.2] simplify to:

$$v = \frac{c}{\sqrt{K'}} \qquad [3.3]$$

and

$$\alpha = \frac{60\Pi\left(\omega\varepsilon_o K'' + \sigma_{dc}\right)}{\sqrt{K'}} \qquad [3.4]$$

For a transmission line with length L, the travel time is down and back is given by:

$$t = \frac{2L}{v} \qquad [3.5]$$

Combining Equations [3.3] and [3.5], we get:

$$K' = \left(\frac{ct}{2L}\right)^2 \qquad [3.6]$$

In the application of TDR theory to soil, we assume that the electric loss (the imaginary term of the dielectric in Equations [3.1] and [3.2]) is negligible. This assumption is based on laboratory test results by Davis and Annan (1977) where they concluded that the real part of the dielectric constant (K') was strongly dependent on soil moisture. We define the dielectric constant measured by the TDR as the apparent dielectric constant, K_a. With the assumption stated above we can conclude that $K_a \approx K'$ (Topp et al. 1980).

3.7.3 Equipment and Waveform Analysis

a) TDR Unit

A Tektronix 1502C TDR unit was used to conduct the experiments. The TDR unit was connected to an IBM computer via an RS-232 cable, which allowed the waveforms to be downloaded as they were observed. Three probes were manufactured for use in the experiments, one for calibration, one for monotonic testing, and one for cyclic testing. A coaxial cable (50Ω RG58) 0.8 to 1.0 meters long was connected to the probe. The cable was passed through the base of the triaxial cell.

b) Probe Development

A "homemade" TDR mini-probe, was developed and built into the base of the triaxial cell. A probe length of 40 mm was adopted so that it would fit into the "dead" zone of the specimen, and therefore strength results would not be affected. The diameter across the probe was limited by the soil specimen diameter and by the spatial sensitivity of the probe. A discussion of spatial sensitivity of TDR probes can be found in Lefebvre (1997) and Knight (1991).

For this study, four wire probes were used, as opposed to the more typical two wire TDR probes. The probe geometry is shown in Figure 3.9. Multi-wire probes emulate coaxial transmission lines by creating similar electrical fields. Figure 3.10 shows a schematic of two, three, and four wire electrical fields. The similarity in electric fields between four wire probes and coaxial lines minimizes the impedance mismatch that occurs at the coaxial cable – waveguide connection point. This eliminates the need for impedance balancing transformers or baluns (Lefebvre 1997). These multi-wire probes were reasonably simple to construct, inexpensive, and provided clearer signals than twin rod probes. For additional discussion of multi-wire probes refer to Zegelin et al. (1989).

Photographs of the mini-probe in the base of the triaxial setup used for cyclic testing are shown in Figure 3.11.

c) Waveform Analysis

Historically, TDR users often plotted the waveform and manually measured the signal trace. This methodology is discussed by Topp et al. (1982). More recently, the manual calculation has been replaced with computer algorithms. Several commercial software packages are currently available for TDR waveform interpretation. For the purpose of this study, a windows software package (M-TDR version 1.4 "the Joce version") developed at the University of Alberta by Michel Lefebvre (Lefebvre 1997) was used. For details on the software and its operation, refer to Lefebvre (1997).

3.7.4 Soil Moisture Content Determination

The first practical application of TDR to the geosciences was published by Topp et al. (1980) where he showed that the apparent dielectric constant is dependent on the volumetric moisture content over a wide range of soils. The result of his research is the commonly used Topp equation:

$$K_a = 3.03 + 9.30\theta_v + 146.0\theta_v^{\,2} + 76.7\theta_v^{\,3} \qquad [3.7]$$

where θ_v is the volumetric water content defined as the volume of water divided by the total volume. Topp et al. (1980) found this relationship virtually independent of soil type, density, temperature, and salinity. As TDR gained popularity, its widespread use resulted in applications beyond the original scope (and calibration) of Topp's equation. Therefore, as an alternative to the empirically derived Topp's equation, Dirksen and Dasberg (1993) and Roth et al. (1990) made use of the dielectric mixing formula. In the mixing formula, soil is considered a mixture of three phases: water, soil, and air. The mixing law can be stated as:

$$K = \left[\theta K_W{}^{\beta} + (1-\phi)K_S{}^{\beta} + (\phi-\theta)K_{AIR}{}^{\beta}\right]^{\frac{1}{\beta}} \qquad [3.8]$$

where K is the dielectric constant of the composite mixture, ϕ is the soil porosity, K_W, K_S, and K_{AIR} are the dielectric constants of water, soil solids, and air, respectively, β is a geometric factor that depends on the spatial arrangement of the mixture and its orientation in the electric field. β ranges from +1 to –1 but in most cases is about 0.5.

Dobson et al. (1985) and Bohl and Roth (1994) modified the mixing model for cohesive soils, by taking into account the differing dielectric constants of the bound and free water.

For the specific purpose of this laboratory program, a relationship for determining the volumetric water content was developed. The above methods are useful for determining moisture content for general soils. In this case, a relationship, specific to the material and laboratory conditions was required in order to maintain the highest level of accuracy possible. The calibration of the probe to determine the necessary parameters is discussed in Section 3.7.5.

3.7.5 Calibration for Volumetric Water Content and Degree of Saturation

Calibration of the probe involved determining the apparent dielectric constant correlation with volumetric water content and degree of saturation for Ottawa Sand. As shown in Figure 3.12 and Figure 3.13, the calibrations provided very consistent results. The calibrations resulted in two third order polynomials, relating dielectric constant to volumetric water content and degree of saturation, respectively.

Factors affecting the measurement of the apparent dielectric are temperature, salinity, and density. Temperature was not a factor since the temperature fluctuation in the laboratory was within a few degrees, and salinity was not a factor since distilled water was used. However, the effects of density needed to be taken into account. In the calibration curves, it was noted that volumetric water content depended very little on density, however, degree of saturation was affected by density. The decision was made to make all samples as loose as possible, with void ratios equal to or greater than 0.8. When the degree of saturation calibration was limited to densities within this range, the scatter of the data was greatly reduced. It was determined that degree of saturation and ultimately void ratio could be found from TDR measurements. The TDR measurements involved determining the apparent dielectric constant, and then from the calibrations obtaining the volumetric water content and degree of saturation.

3.7.6 Using the TDR to Determine Gas Content

The method described in Section 3.7 was employed during testing. Waveforms were obtained after full saturation of the sample was ensured (i.e. after a B-test was performed). A typical saturated sample waveform is shown in Figure 3.14(a). Waveforms were also obtained during each stage of consolidation, and then during shearing. During monotonic shearing, waveforms were obtained every 15 to 30 seconds for the first few minutes, and less frequently thereafter. For cyclic loading, it was extremely difficult to determine the loading conditions for the specific waveform, therefore, waveforms were generated only at the beginning and end of cyclic shear. A typical waveform taken during monotonic shear is shown in Figure 3.14(b). The waveforms were analyzed to determine the dielectric constant using the method described in Section 3.7.5. The dielectric constant was recorded manually. For each data point, five waveforms were usually taken (with each waveform being the average of 16 waves). The dielectric for each waveform was determined and the average of the dielectrics was inputted into a spreadsheet. The exception was for the monotonic testing where it was impossible to obtain five waves at the same stress condition. In this case, each data point consisted of only one waveform.

The calibrations discussed above were then used to relate the dielectric constant to the volumetric water content and the degree of saturation. The volume of solids and the volume of water in the specimen were determined by taking the final moisture content of the entire specimen. By combining the volumetric water content, degree of saturation, volume of solids, and volume of water, the volume of voids and void ratio could be determined for the given dielectric. Hence, at any point during monotonic testing, the degree of saturation and void ratio was readily calculated from the TDR data.

3.7.7 Accuracy of the TDR Method

The accuracy of the TDR method to determine the degree of saturation and void ratio during testing was examined by obtaining TDR waveforms for saturated drained tests.

The results of two tests are presented in Figures 3.15 and 3.16. These figures show the void ratio versus mean normal effective stress obtained from measuring the volume of water with an electronic volume change device. The figures also present the void ratio versus mean normal effective stress as interpreted from the TDR data. From the two figures, a couple of observations can be made. First, the TDR data does not match exactly the data obtained from an electronic volume change device. Second, the general trend of the void ratio obtained from the TDR data follows the trend of the void ratio obtained from the volume change device.

The results obtained from the TDR data were considered sufficiently accurate for this study, as the intent of the testing was to show the change in soil response. In addition, Sills (1997) confirmed that the TDR method of determining degree of saturation seemed to have a similar accuracy to the double walled cell method.

3.8 SUMMARY AND CONCLUSIONS

The laboratory program involved the design and setup of specialized triaxial equipment. Ottawa sand and carbon dioxide gas were selected. Two different triaxial setups were used for the monotonic and cyclic tests.

Perhaps the most challenging aspect of the equipment design was determining a way to measure the gas content. Several methods of determining degree of saturation were considered. These included measuring the sample volume change from the cell fluid, determining the sample volume change from radial strain gauge measurements, using bender elements to measure compression wave attenuation, and using time domain reflectometry to determine the apparent dielectric constant. Time domain reflectometry was the method selected to measure gas content. The triaxial apparatus was modified to include a mini TDR probe in its base, enabling the measurement of apparent dielectric constant. Through a series of calibration curves developed from laboratory tests the volumetric water content, degree of saturation, and void ratio, could be determined. Tests results confirmed that time domain reflectometry met the required level of accuracy intended for this research program.

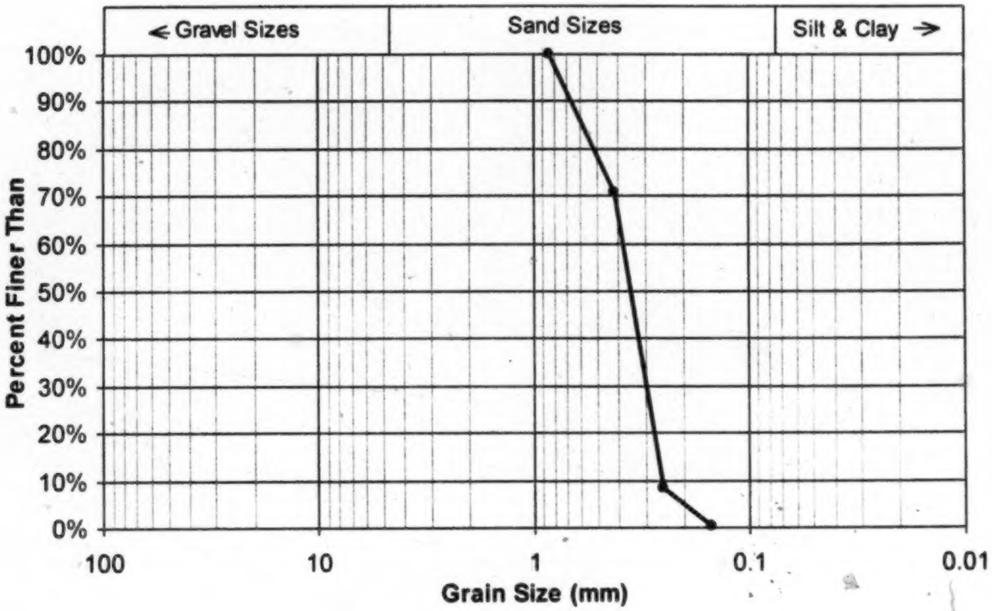

Figure 3.1 - Particle size distribution of Ottawa Sand.

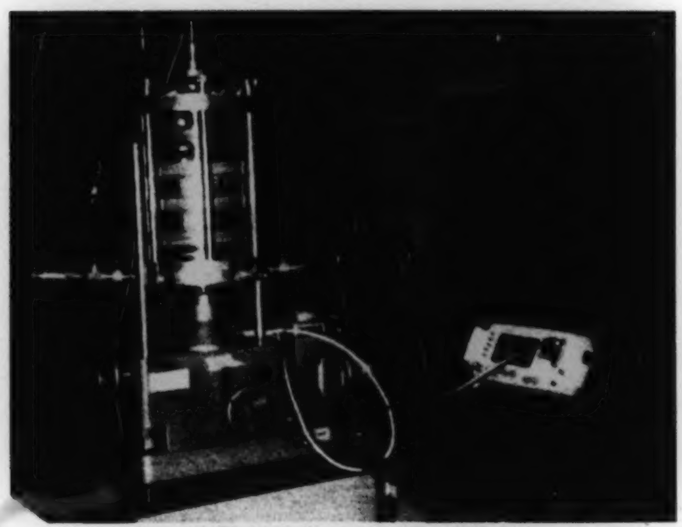

(a) Triaxial apparatus setup

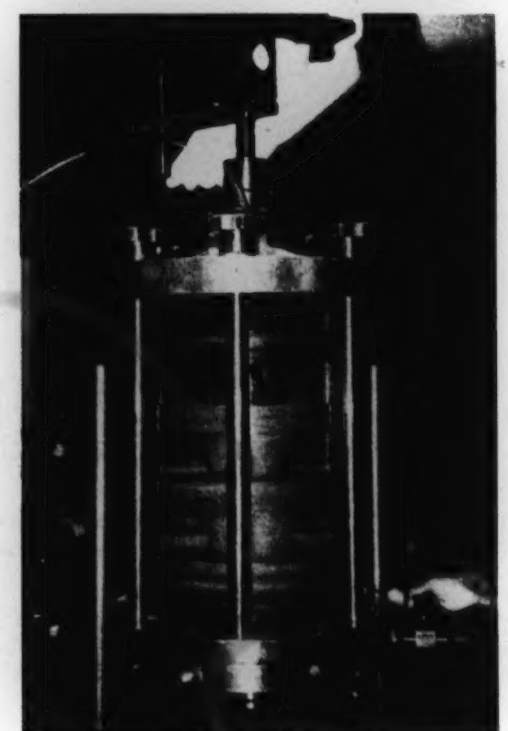

(b) Triaxial cell

Figure 3.2 - Monotonic triaxial equipment.

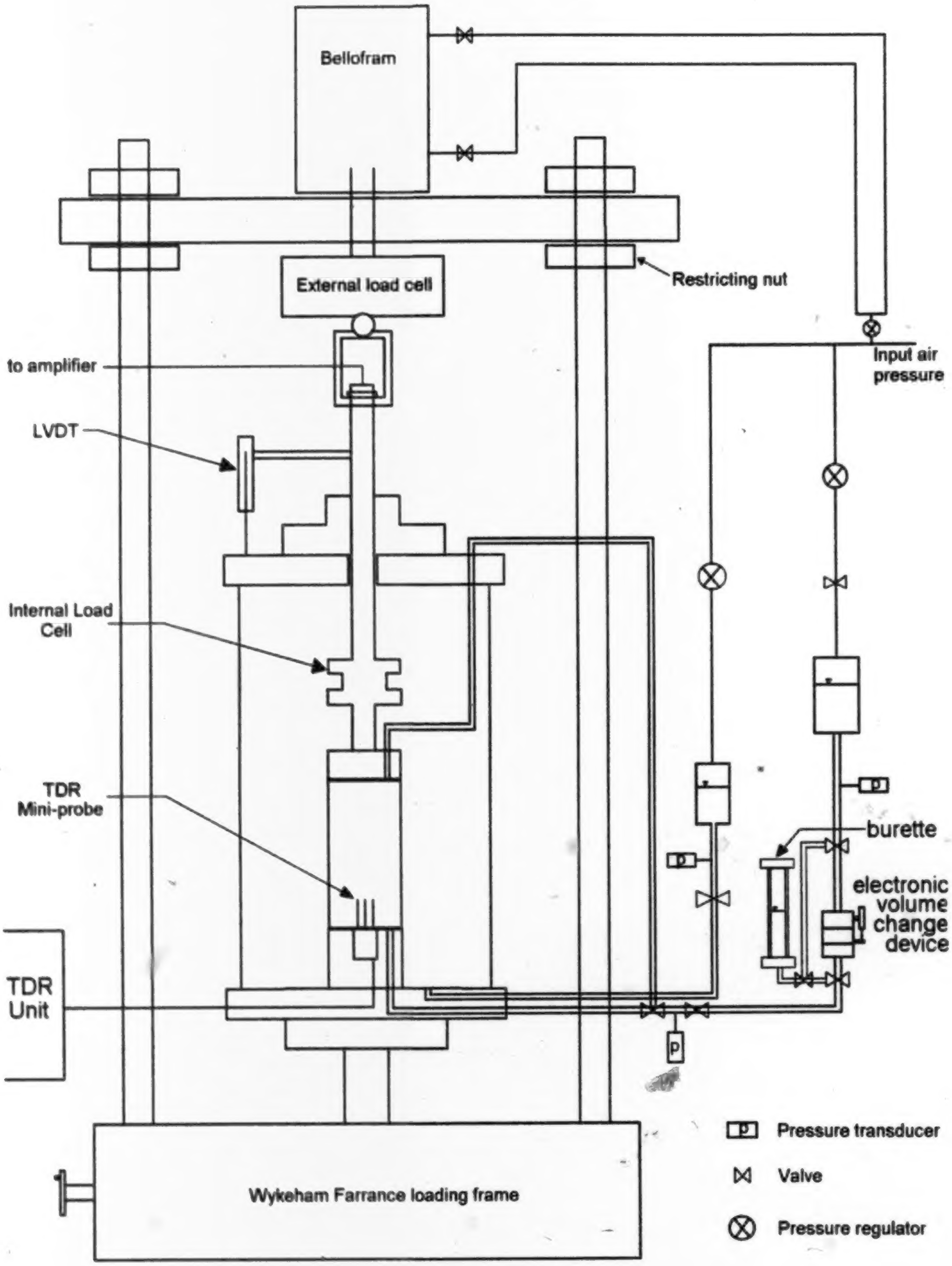
Bellofram
External load cell
Restricting nut
to amplifier
Input air pressure
LVDT
Internal Load Cell
TDR Mini-probe
burette
electronic volume change device
TDR Unit
P
Wykeham Farrance loading frame
Pressure transducer
Valve
Pressure regulator

Figure 3.3 - Schematic of monotonic triaxial setup.

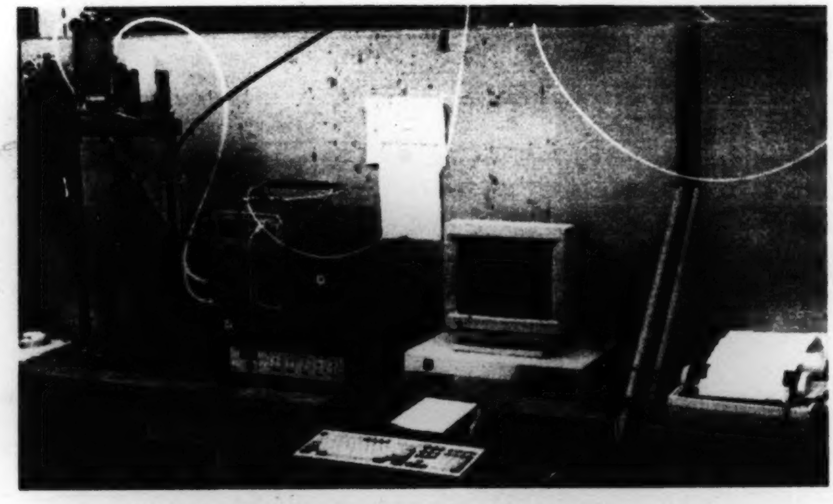

(a) Triaxial setup and associated computer controls

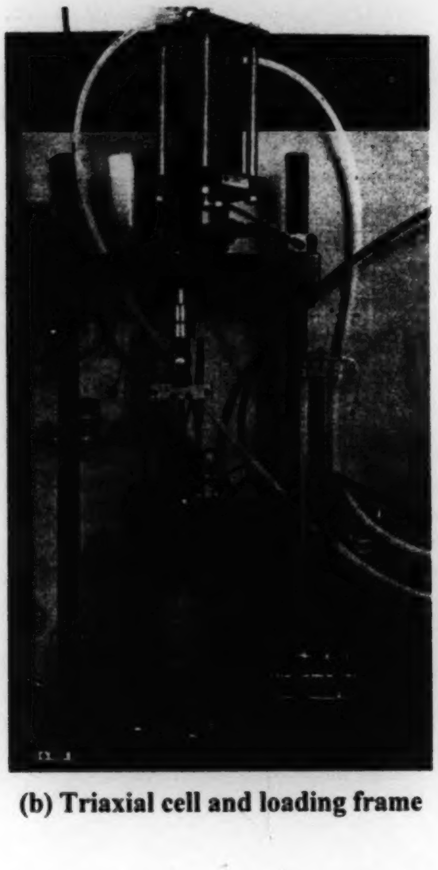

(b) Triaxial cell and loading frame

Figure 3.4 - Cyclic triaxial equipment.

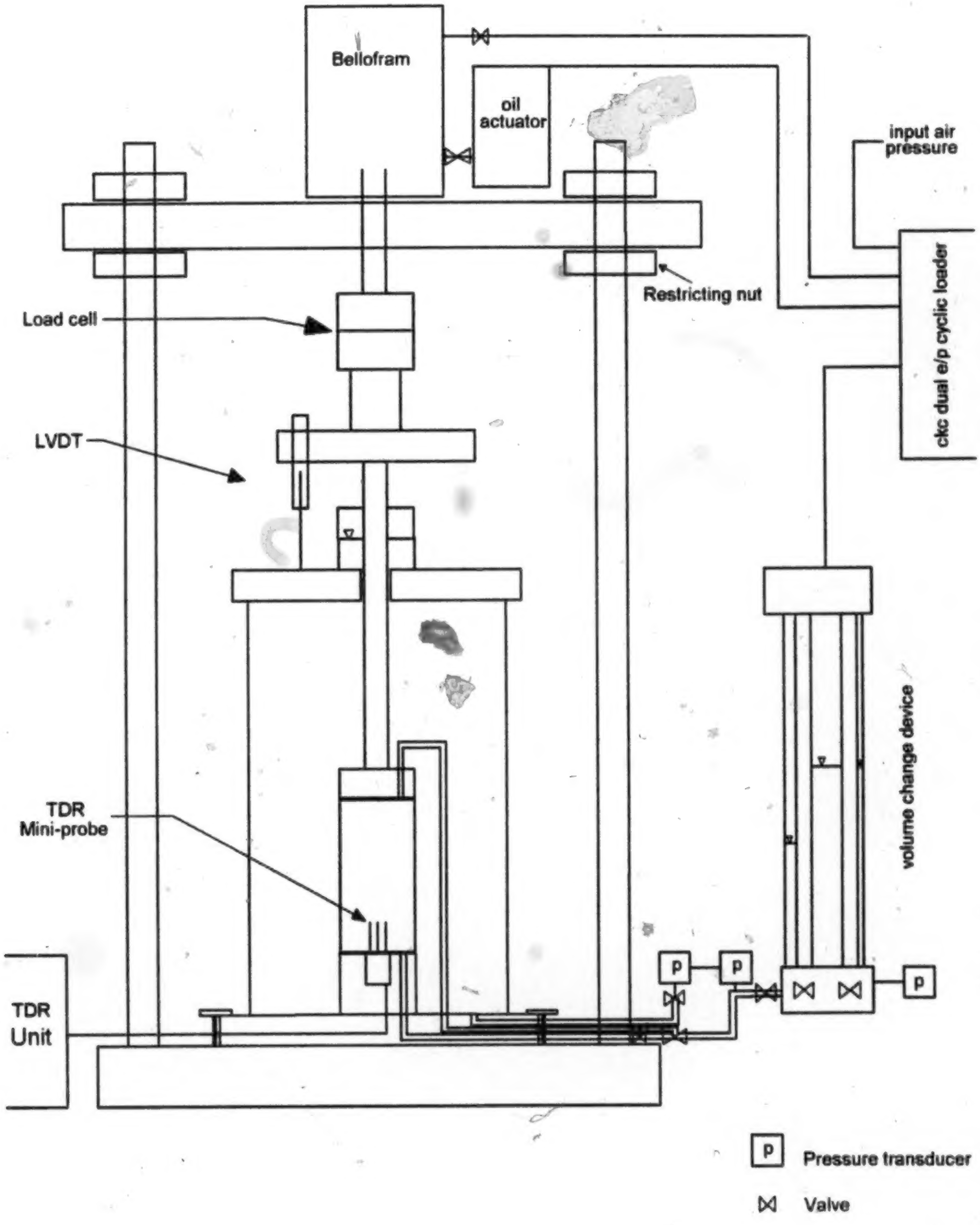
Bellofram
oil actuator
input air pressure
ckc dual e/p cyclic loader
Restricting nut
Load cell
LVDT
volume change device
TDR Mini-probe
TDR Unit
p
p
p
p
p
Pressure transducer
Valve

Figure 3.5 - Schematic of cyclic triaxial setup.

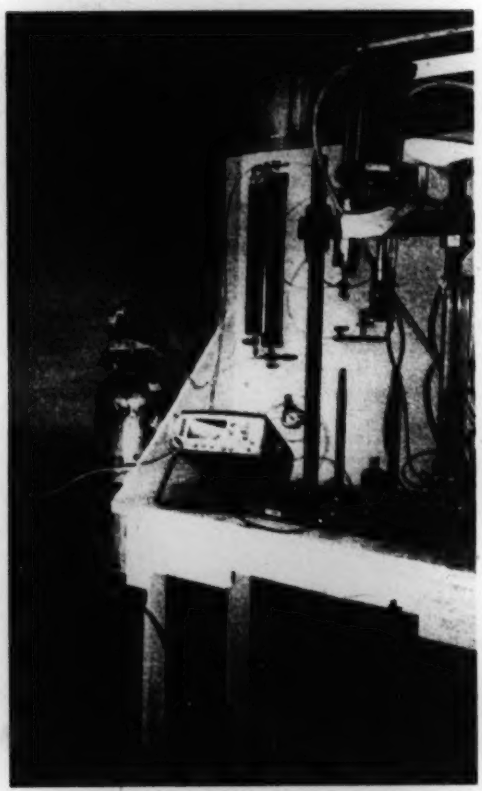

(a) Bubble chamber system

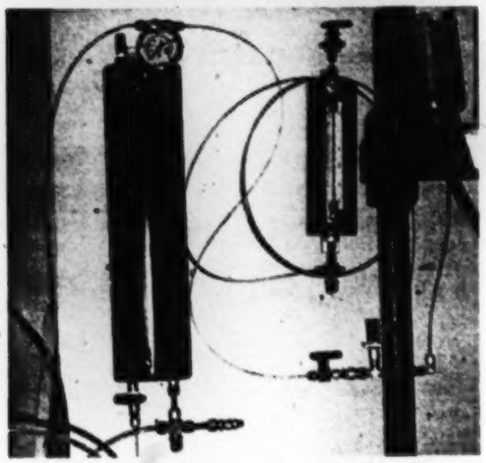

(b) Upper bubble chamber

Figure 3.6 - Bubble chamber.

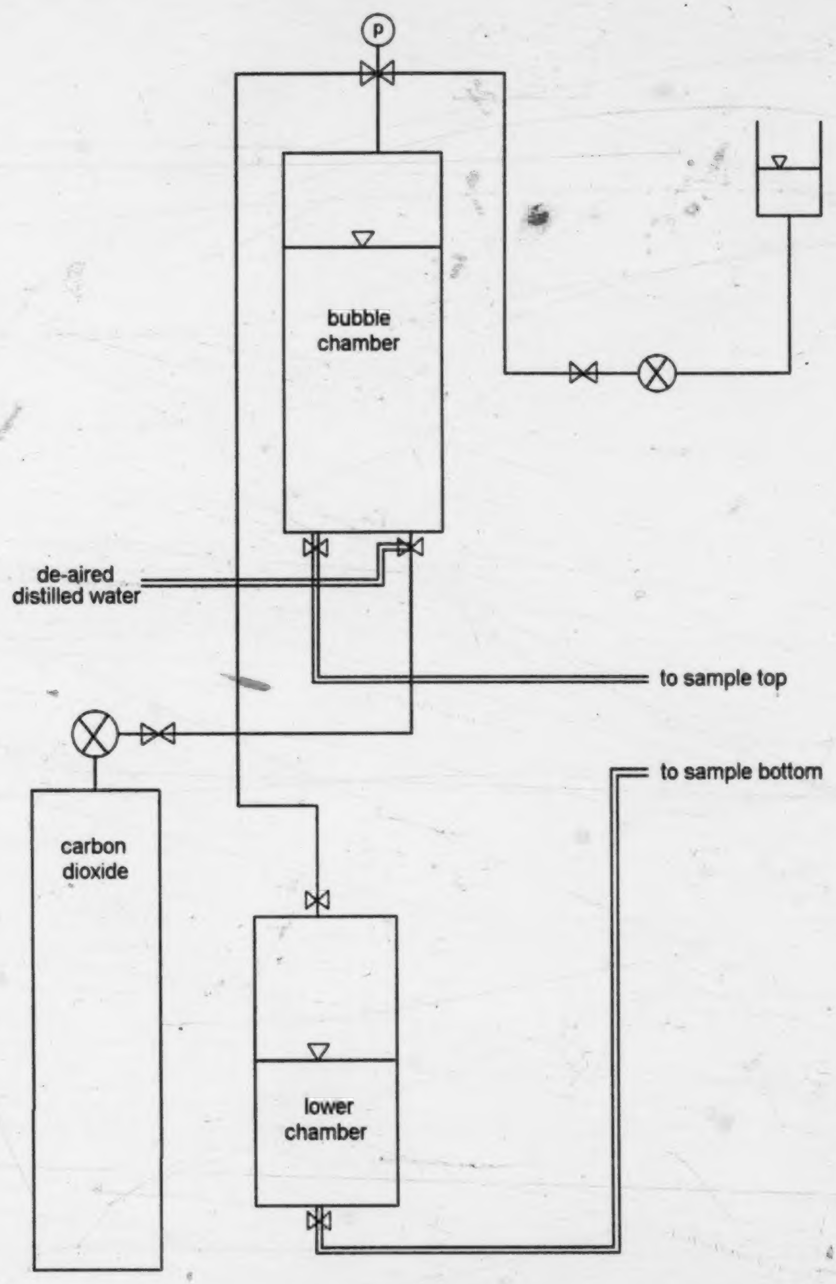
P
bubble chamber
de-aired distilled water
to sample top
to sample bottom
carbon dioxide
lower chamber

Figure 3.7 - Schematic of bubble chamber design.

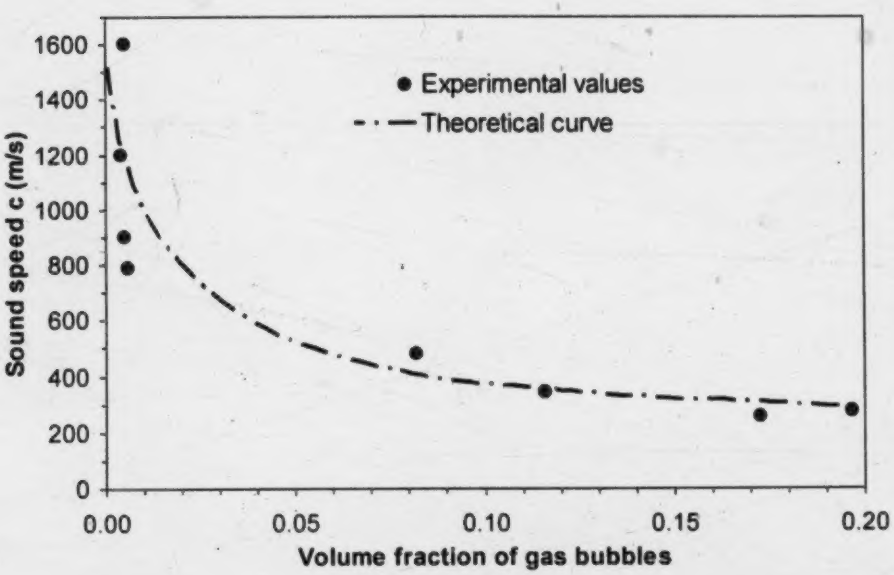

Figure 3.8 - Compression wave attenuation versus gas content (modified from Sills et al. 1991).

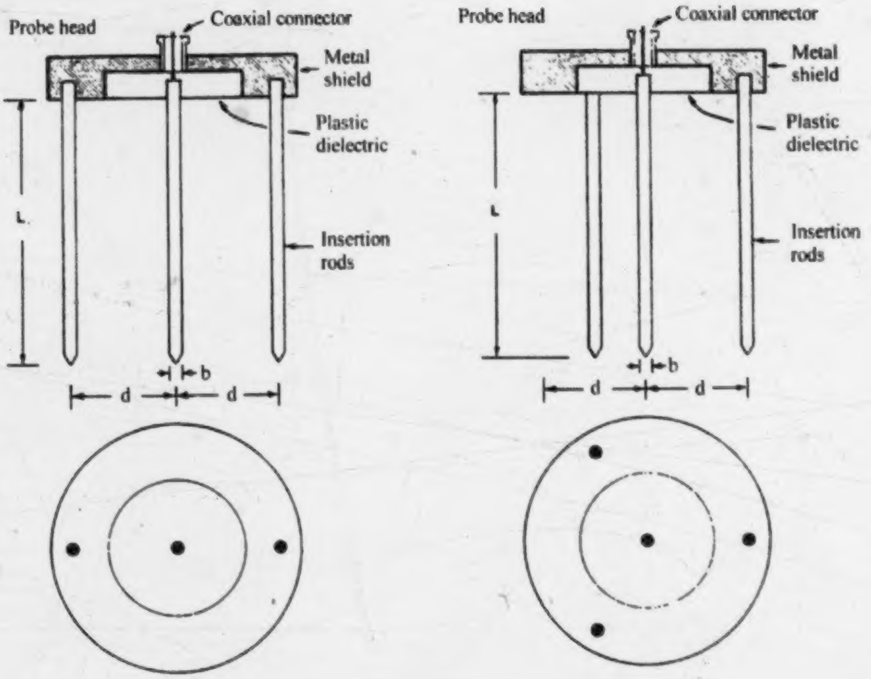
Probe head
Coaxial connector
Metal shield
Plastic dielectric
Insertion rods
L
b
d
d
Probe head
Coaxial connector
Metal shield
Plastic dielectric
Insertion rods
L
b
d
d

Figure 3.9 - Multi-wire TDR probe geometry (modified from Zegelin et al. 1989).

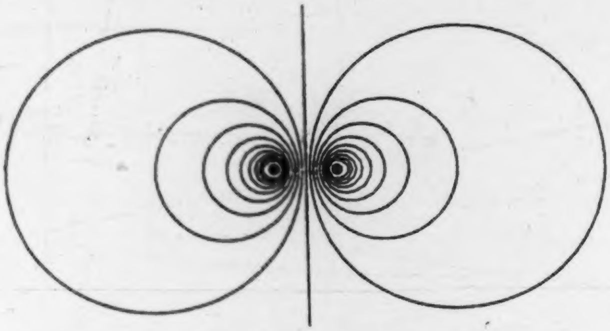

2 - wire waveguide

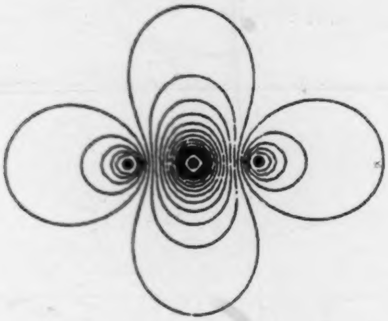

3 - wire waveguide

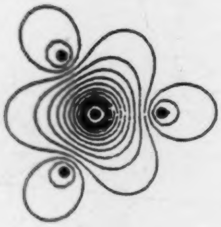

4 - wire waveguide

Figure 3.10 - Electrical fields surrounding multi-wire TDR probes (modified from Zegelin et al. 1989).

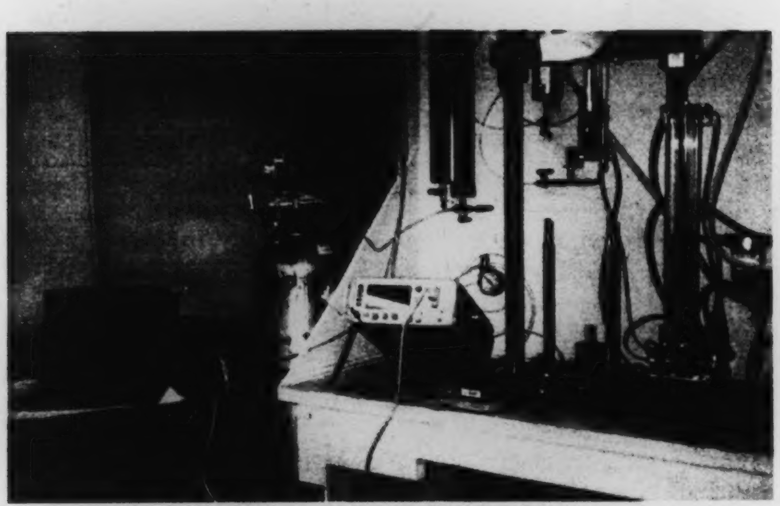
(a) TDR setup for cyclic triaxial tests

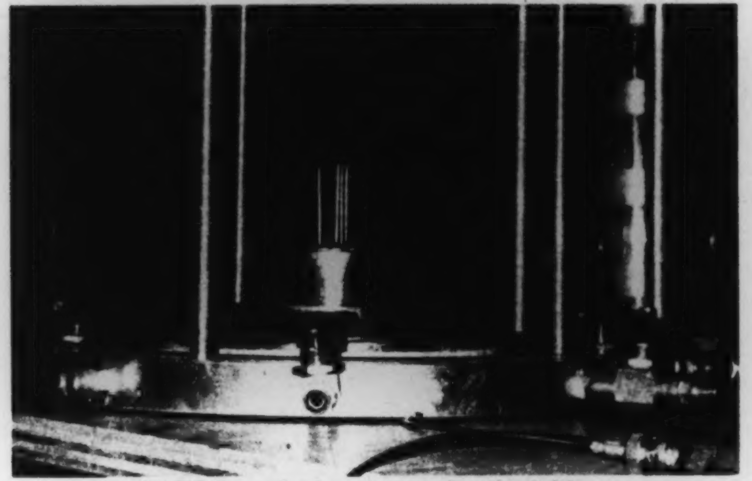
(b) TDR probe in monotonic triaxial base

Figure 3.11 – TDR equipment.

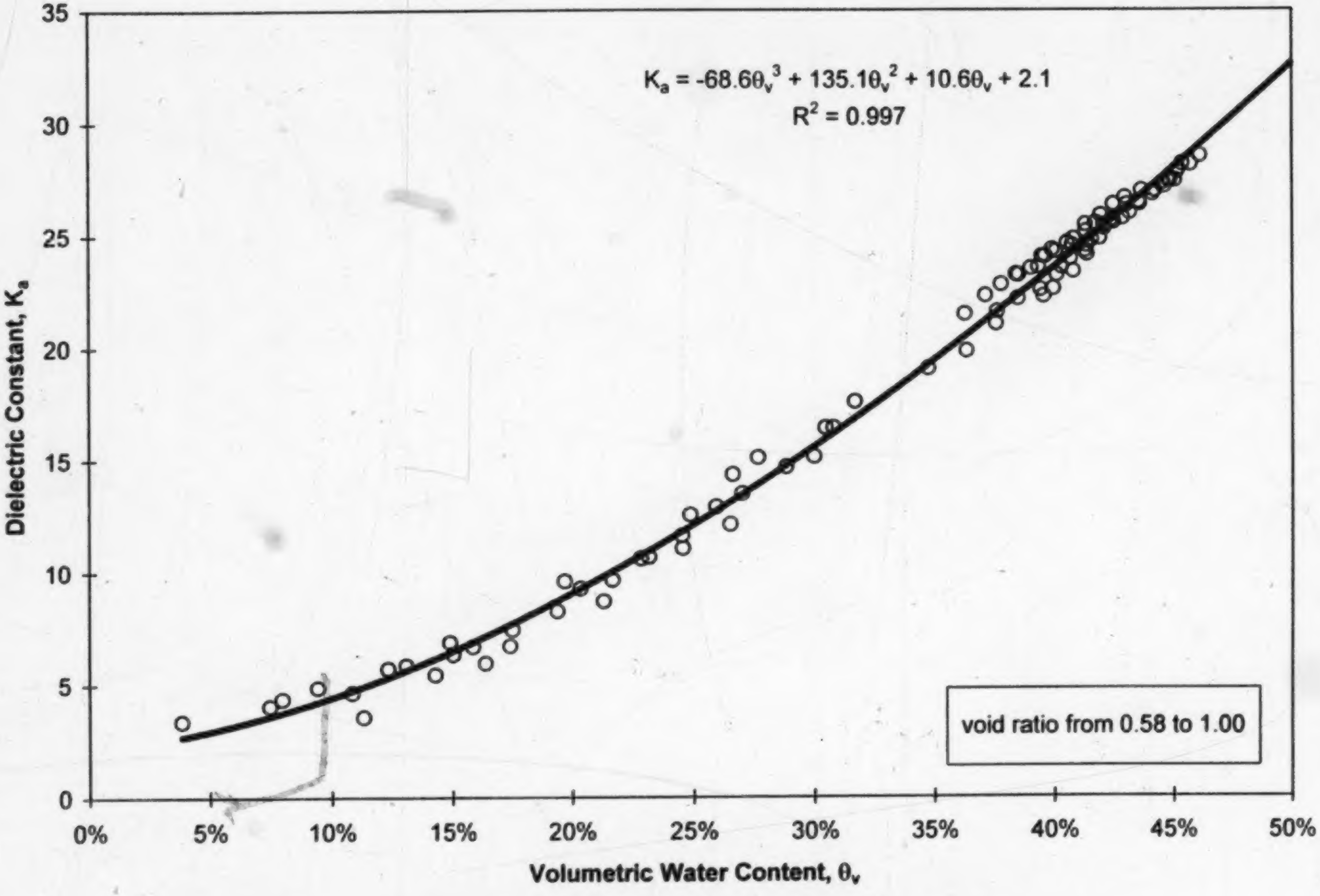

Figure 3.12 - Apparent dielectric constant versus volumetric water content.

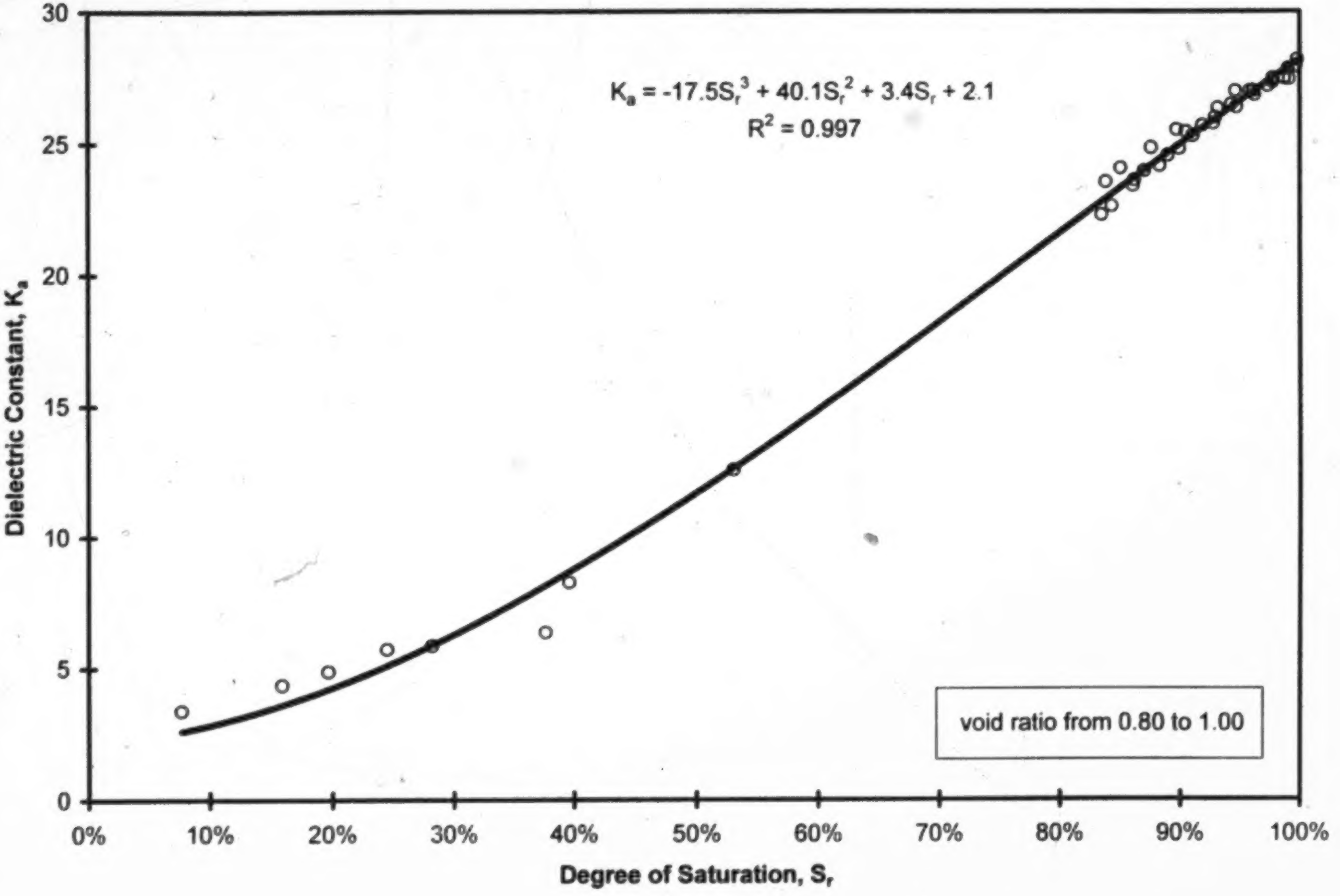

Figure 3.13 - Apparent dielectric constant versus degree of saturation.

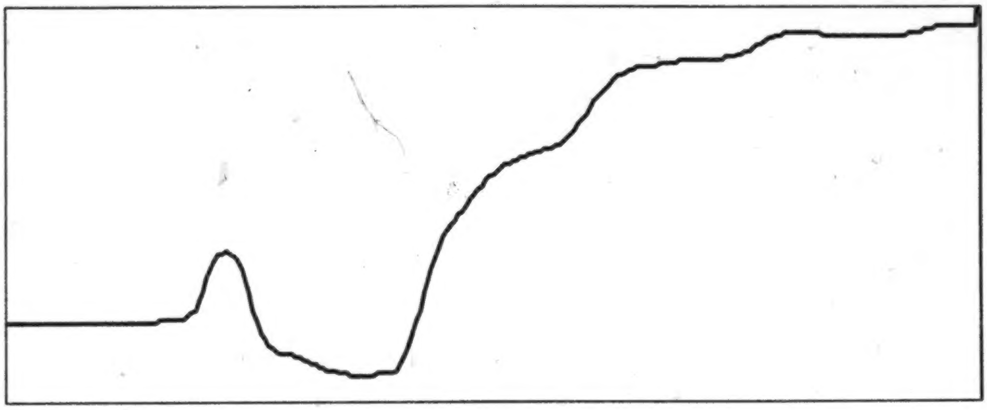

(a) Saturated waveform

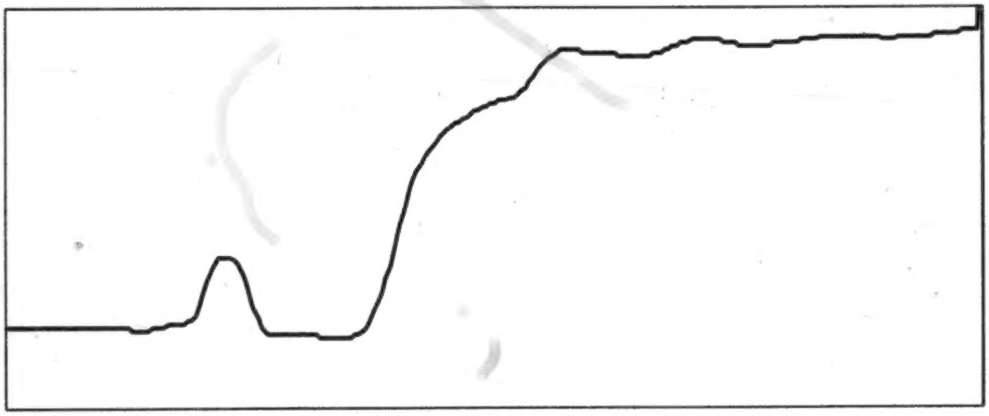

(b) Gassy waveform

Figure 3.14 – Typical TDR waveforms.

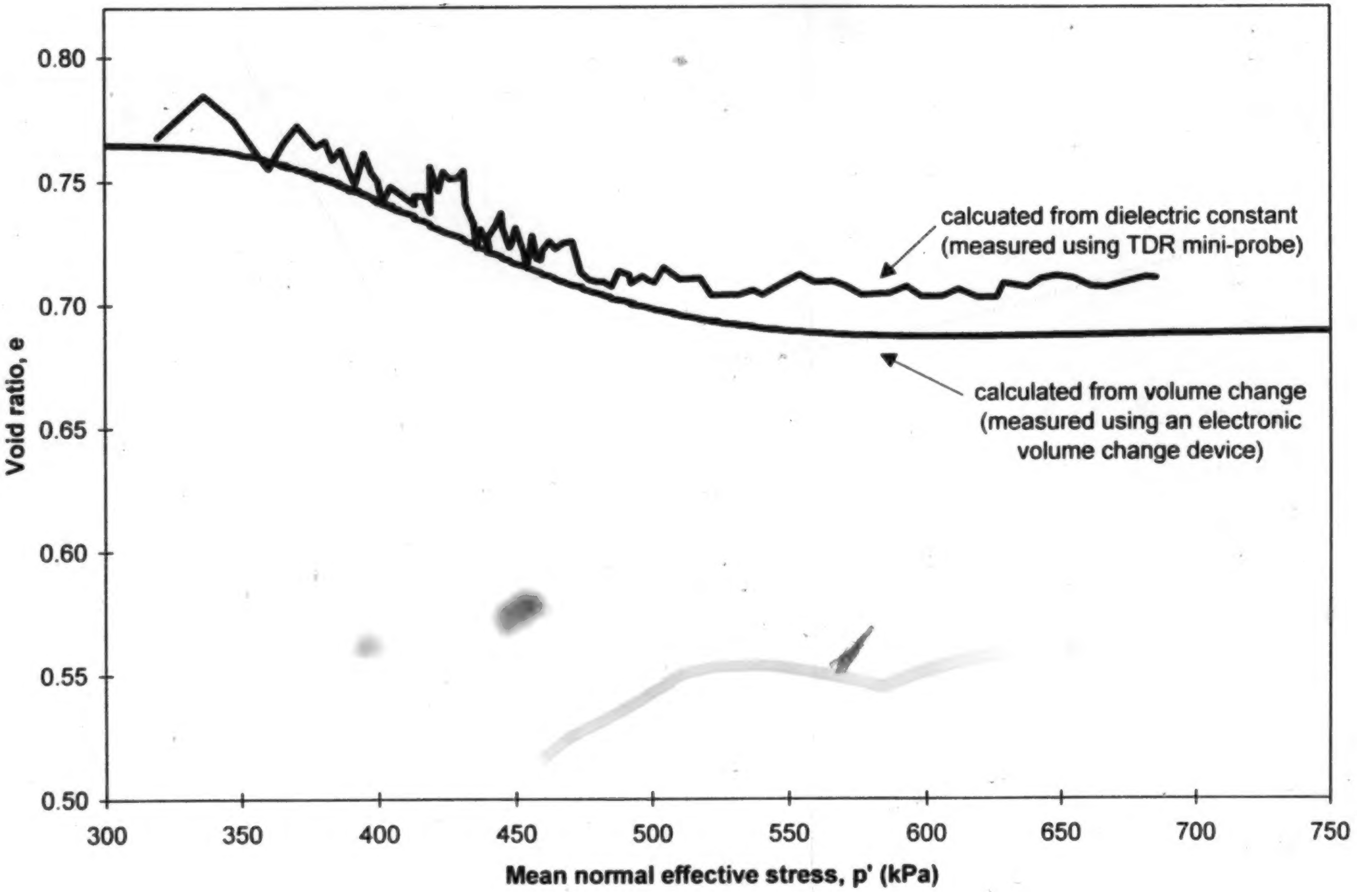

Figure 3.15 - TDR accuracy, Sample 19.

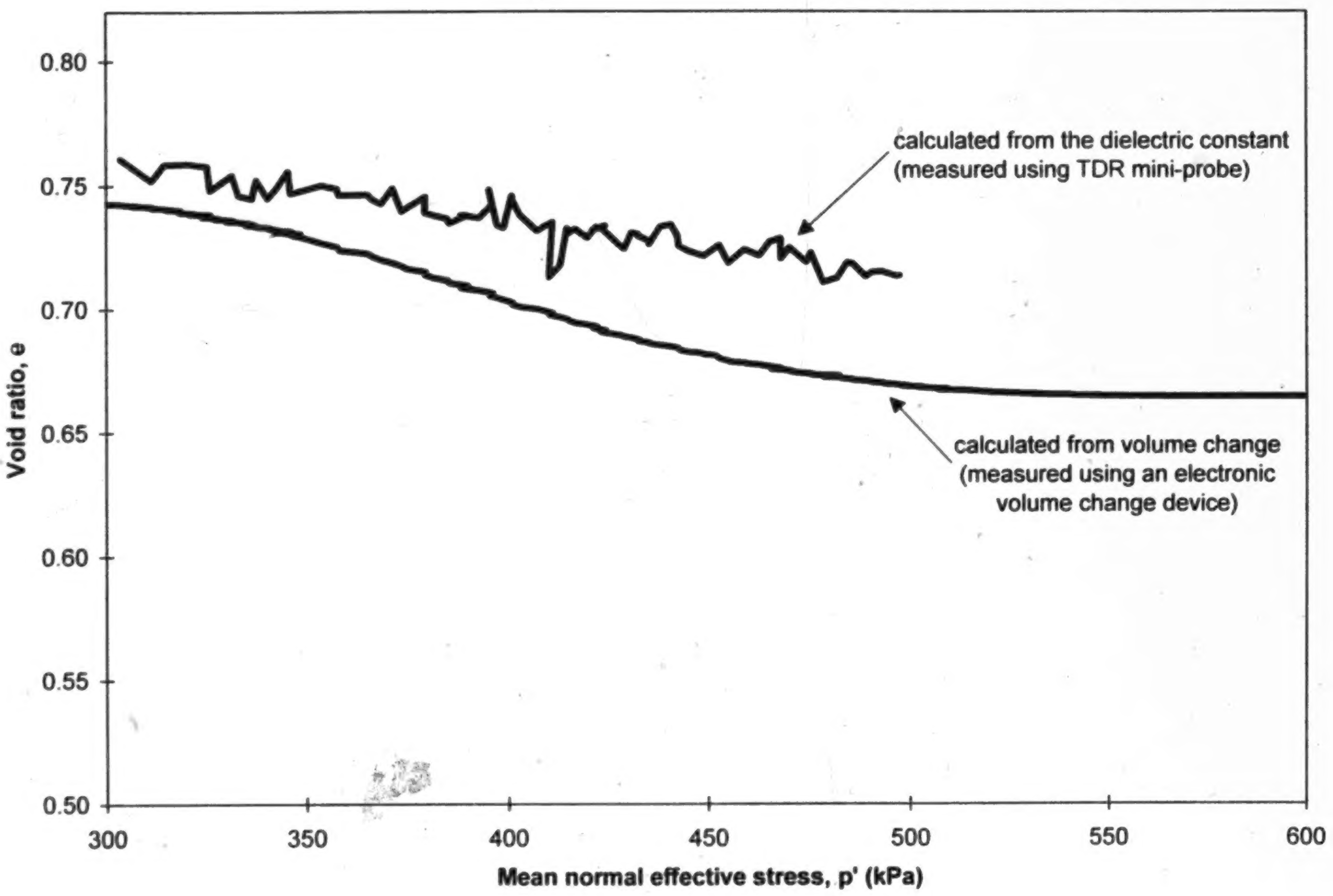

Figure 3.16 - TDR accuracy, Sample 23.

CHAPTER 4

LABORATORY TESTING PROCEDURE

4.1 INTRODUCTION

An important part of laboratory testing is the procedure used to prepare and test specimens. The method of specimen preparation must be consistent with the objectives of the laboratory program. The material type and gradation and the specimen uniformity are important considerations for sample preparation. The effects of the specimen preparation method on the results, the static and cyclic strength, must be understood as well.

In readying a specimen for testing, many stages such as saturation, testing for full saturation, and consolidation precede shearing. For gassy specimens, the pore fluid of the saturated specimen must be replaced with water containing dissolved carbon dioxide gas.

In this chapter, the general testing procedures, as well as the procedures specific to the monotonic triaxial tests and the cyclic triaxial tests are described.

4.2 SPECIMEN PREPARATION

All laboratory specimens were prepared using Ottawa sand from Ottawa, Illinois. Ottawa sand (CT-109A), graded to meet ASTM C-778 standards, is a uniform, medium grained sand comprised of sub-rounded to round quartz grains. Ottawa sand has a specific gravity of 2.65 and a mean grain size (D_{50}) of 0.34 mm. The maximum and minimum void ratios, determined using ASTM D2049, are 0.82 and 0.50, respectively.

4.2.1 A Summary of Sample Preparation Methods for Sand

Sand specimens can be prepared by several different methods. For liquefaction analysis, specimens must be loose enough to be susceptible to liquefaction. The following summarizes the existing common methods to prepare loose sand specimens:

Moist tamping: This technique consists of placing moist soil in layers into a mold and tamping each layer with a specified force and frequency of tamping. Capillary forces (water tension forces) between the moist grains result in a very loose specimen. Dense specimens can also be prepared using this method.

Air Pluviation: This method consists of dropping dry sand into a mold mimicking a loose wind blown aeolian deposit. The density of the specimen is a function of the height of particle drop and the rate of deposition. In well-graded sands, particle segregation is a problem, and this method may not be appropriate.

Water Pluviation: This technique is similar to air pluviation except that deposition occurs through water, rather than air, thereby ensuring sample saturation. Water pluviation simulates the deposition of sand in many natural environments, as well as in hydraulically placed fills. Particle segregation is a problem in well-graded sands, and therefore water pluviation may not be appropriate. The loosest possible structure that a specimen can be prepared at using this method is not as loose as if a specimen was prepared using the moist tamping technique.

Slurry Deposition: This method consists of mixing sand with water into a slurry, then depositing the slurry by pluviation through water. The slurry minimizes the height of particle drop through the water, and therefore controls particle size segregation. This method simulates soil deposited in a natural fluvial or hydraulic fill condition. Specimens prepared by this method are generally homogeneous and loose. This method produces looser specimens than the slurry deposition method, but not as loose as the moist tamping method.

Multiple Sieve Pluviation: This method consists of pluviating oven dried sand through a series of seven sieves. Specimen density is controlled by varying the pluviation nozzle diameter and the fall height. This method produces uniform samples varying from loose to very dense. Specimens can also be created at a very high density.

4.2.3 The Moist Tamping Technique

The laboratory specimens were reconstituted using the moist tamping method. This method has been shown to create the loosest possible structure (Sasitharan 1994). The moist tamping technique is perhaps the oldest method of sample preparation and is described by Lambe (1951).

The moist tamping method has been criticized for the development of large strains that occur during saturation. The very loose structure of a moist tamped sample is a result of water tension forces; forces that are removed by saturation. Researchers Marcuson et al. (1972), Chang et al. (1982), and Sladen et al. (1985) noted large strains in moist tamped silty sands during the saturation process.

Perhaps the greatest drawback of the moist tamping method is that the resulting soil structure "does not represent the actual soil structure in the field for most natural cases" (Konrad 1993). During the CANLEX (CAnadian Liquefaction EXperiment) project, soil freezing was undertaken to obtain undisturbed samples. It was noted that the void ratio of some of the frozen samples were higher (i.e. looser) than the maximum possible void ratio that could be produced by the wet pluviation or slurry deposition methods (Robertson 1998). This suggests that although the resulting structure might be different, natural soils can exist in a metastable state similar to that produced by the moist tamping method.

Casagrande (1976) noted that the moist tamping method produces samples which are particularly prone to liquefaction. Kerbis and Vaid (1988) also recognized the metastable structure of specimens prepared using moist tamping, and the increased susceptibility to liquefaction in monotonic loading.

The use of Ottawa sand, sub-rounded, uniform sand, minimizes any potential problems of uniformity or development of large strains during saturation. The increased liquefaction potential of specimens prepared using the moist tamping technique makes it an attractive method for this study.

It should be noted that many researchers have successfully used the moist tamping technique. It is perhaps, the most commonly used method for sample preparation.

4.2.3 Specimen Preparation using Moist Tamping

Using the moist tamping technique, a pre-determined amount of oven dried sand was mixed with distilled water. The mass of water added was between 6 and 8 percent of the mass of the dry sand. After thorough mixing, the moistened sand was placed in an airtight container.

At this point, a membrane was placed onto the bottom sample pedestal of the triaxial apparatus. Vacuum grease was applied to both the top and bottom pedestals. O-rings were placed over the membrane and a split mold was assembled around the bottom pedestal and membrane. The membrane was flipped over the top of the split mold and a vacuum was applied to hold the membrane taunt to the mold. Up until this point, the TDR mini probe was protected with a Plexiglas cylinder to ensure that the membrane was not punctured by the probe ends. After application of the vacuum the protective cylinder was removed.

A portion of the moistened soil was then carefully weighed and transferred to the split mold. The first layer, approximately 100 grams of moistened soil, was carefully tamped around the TDR probe using a small spatula. Subsequent layers were also carefully weighted and transferred to the split mold where they were tamped with a small drop hammer. The number of drops was increased with each layer in an effort to form a sample with a uniform density. Each sample was prepared in five layers.

The moist tamping procedure is also described by Sasitharan (1994) and Ladd (1978).

4.2.4 Sample Assembly

Upon completion of tamping, the top cap was placed over the sample and the top drainage line affixed. After the sample was leveled, the split mold vacuum was shut off while, simultaneously, a vacuum was applied to the bottom of the sample, through the bottom sample drainage port and did not exceed 25 kPa. The split mold was carefully disassembled and the sample was left to stand under the vacuum.

Sample dimensions were obtained using two methods. First, the sample diameter was determined using electronic calipers. A total of six measurements were taken, three measurements along the sample height at two orientations perpendicular to each other. The measurements were averaged and membrane thickness accounted for to obtain a good representation of sample diameter. Second, the sample height was determined by placing the triaxial apparatus under a dial gauge. The dial gauge measurement was recorded at three locations and compared to the gauge readings for a "dummy" sample, of known height, in order to obtain the sample height. All samples were approximately 63 mm in diameter and 125 mm in height.

4.2.5 Specimen Uniformity

When preparing very loose sand specimens, uniformity can be a problem. Sasitharan (1994) studied sample uniformity by freezing moist tamped specimens of Ottawa sand. Specimens were saturated and consolidated to 350 kPa. The specimens were then frozen without disturbance (i.e. at a rate such that "water could freely flow away from the advancing freezing front and the volume of water expelled equaled the volume expansion of the ice forming in pores" (Sasitharan 1994)). Sections were obtained from the top and bottom, and the void ratio and moisture content were calculated. Scanning electron microscope imagining was performed, in addition to a visual analysis. The results of this study indicated that the moist tamping sample preparation technique results in samples with uniform void ratios, even after saturation and consolidation.

Ladd (1978) also studied the moist tamping method, and determined that the method minimized particle segregation and lead to more consistent and repeatable tests when compared to other methods.

Contrary to the above conclusions, at least one researcher has found that moist tamping can result in non-uniform samples. Miura et al. (1984) showed that moist tamped samples resulted in non-uniform structure when miniature cone penetration tests were performed on samples prepared for triaxial testing.

The use of Ottawa sand minimizes non-uniformities resulting from sample preparation.

4.2.6 Effect of Sample Preparation Technique on Static Undrained Shear Strength

The method of sample preparation will affect monotonic triaxial compression testing results. Sample preparation in reconstituted specimens creates fabric, which affects the undrained shear strength.

Miura and Toki (1982) compared static triaxial test results for different specimen preparation methods. They showed that the method of sample preparation affected triaxial extension test results more than triaxial compression test results. Figure 4.1 shows the effective stress path of samples prepared using dry tapping, moist tamping (wet rodding), and their own method multiple sieve pluviation. Triaxial compression samples prepared by multiple sieve pluviation were stronger than samples prepared by dry tapping, which in turn were stronger than samples prepared by moist tamping. In triaxial extension, the moist tamped samples showed the strongest response.

4.2.7 Effect of Sample Preparation Technique on Cyclic Resistance Ratio

The sample preparation will also make a difference on the cyclic resistance ratio, or the resistance of the sample to cyclic loading. More research has been performed on the effects of sample preparation on the cyclic resistance than on the static shear strength. The literature seems to indicate that sample preparation has a greater affect on the cyclic resistance than on the static shear strength.

Tatsuoka et al. (1986) looked into some of the factors affecting cyclic undrained triaxial strength of sand, including the sample preparation method. The results of this study, comparing air pluviation (AP), multiple sieve pluviation, and water vibration (WAV), are shown in Figure 4.2. For loose specimens, the disparity between the different methods was minimized; however, weaker results were obtained for the multiple sieve pluviation while the air pluviation and water vibration gave stronger and similar results. The method of sample preparation is more evident for denser specimens. Air pluviation and multiple sieve pluviation produced similar results for denser specimens while water vibration resulted in considerably larger strengths.

Silver et al. (1980) compared the cyclic resistance of specimens prepared by air pluviation and wet tamping. The study indicated that the cyclic undrained strength of sand prepared by moist tamping was larger than the strength obtained from air pluviated specimens.

Miura and Toki (1982) found that the cyclic resistance was greater for specimens prepared by moist tamping than by dry rodding, and that the cyclic resistance of multiple sieve pluviated samples was less than either moist tamping or dry rodding (Figure 4.3). Tatsuoka et al. (1982) noted that, similar to static triaxial strength tests, the effects of sample preparation will be more evident for denser specimens.

In summary, under undrained cyclic triaxial loading, specimens prepared by the water pluviation method are generally weaker than those prepared by the air pluviation method; likewise specimens prepared by air pluviation are generally weaker than specimens prepared by the moist tamping method.

4.3 TEST PROCEDURES

The following test procedures are summarized for both monotonic and cyclic triaxial tests. After preparation of the specimen, the triaxial cell was assembled and a nominal confining pressure of approximately 25 kPa was applied.

4.3.1 Saturating with Water

Obtaining full saturation of samples can take a very long time, from several hours to several days. Part of the reason for the long saturation times is the low solubility of air in water. One method to shorten saturation times is to replace the air with a more soluble gas. This was accomplished by percolating carbon dioxide gas through the sample for a period of 20 to 30 minutes. The carbon dioxide gas entered the sample through the bottom drainage port and exited through the top drainage port. To ensure the carbon dioxide was flowing through the sample, the top drainage line was placed in a beaker of water. The bubbling of gas through the water ensured the flow of carbon dioxide. The pressure of gas was just enough to start and maintain the flow.

After the percolating carbon dioxide gas through the specimen, water was introduced. The de-aired distilled water, driven by the difference in head, was introduced slowly to allow the replacement and dissolution of the carbon dioxide. The water source was gravity driven. Water entered the sample through the bottom drainage port and exited through the top drainage port into a container open to atmosphere. The amount of water allowed to pass through the sample was roughly estimated to be 2 to 3 times the volume of voids. The saturation process took approximately one and a half to two hours.

After saturation, confining and back pressures were increased to at least 250 kPa higher than the liquid gas saturation pressure for carbon dioxide/water (about 510 kPa). Cell and back pressures were generally 800 kPa and 750 kPa, respectively. To ensure that the specimen remained isotropic, the axial load was adjusted in the monotonic setup. For the cyclic setup, the computer automatically adjusting the axial load maintained the condition of isotropy. The setup was then left overnight, or for several hours, to ensure that all remaining gasses within the specimen and the cell fluid were in solution.

4.3.2 Ensuring Full Saturation

B-tests were performed to ensure the specimens were fully saturated. For the B-test, all drainage lines were closed and the confining pressure was increase by a prescribed amount, in this case, between 25 and 40 kPa. The pore pressure within the specimen was monitored and when it had reached steady state, the value was recorded. The B-value is equal to the change in pore pressure divided by the change in confining pressure. Standard laboratory practice requires that B values are greater than 0.95 to ensure full saturation. Values of B greater than 0.98 were obtained for all specimens.

4.3.3 Saturation with Water and Dissolved Carbon Dioxide Gas

To produce gassy specimens, it was necessary to dissolve carbon dioxide gas into water. The bubble chamber setup discussed in Section 3.5 was used for this purpose. Carbon dioxide gas was allowed to percolate through de-aired distilled water under a pressure equal to the sample back pressure (usually 750 kPa) for a time period of a couple hours. After percolation of CO_2, the bubble chamber was closed to atmosphere. The top chamber was connected to the sample bottom and the lower chamber connected to the sample top. The carbon dioxide saturated water was allowed to flow from the upper chamber, through the sample, to the lower chamber. The movement was driven by a difference in height of about 1 meter between the upper and lower bubble chambers. A volume of approximately two to three times the volume of voids was passed through the sample. The displacement of the water with carbon dioxide saturated water was done in three stages with about 20 minutes between each stage, to allow the new, and any remaining old pore fluid to mix and equilibrate their dissolved CO_2 concentrations. At all times the pressure in the system was kept at or very near the targeted sample back pressure (250 kPa above the liquid gas saturation pressure for carbon dioxide and water).

4.3.4 Consolidation

After saturation of the specimen with CO_2 saturated water, isotropic consolidation was performed. Isotropic consolidation of triaxial specimens is usually accomplished by increasing the cell pressure while maintaining a constant back pressure, thereby increasing the effective stress. However, for this laboratory program consolidation was performed by reducing the back pressure while maintaining a constant cell pressure, which increased the effective stress. As the back pressure was reduced below the liquid gas saturation pressure, gas exsolution occurred. Specimens were consolidated to approximately 300 kPa effective pressure.

The consolidation occurred in five stages, with a back pressure reduction of 50 kPa for each stage. During consolidation, the pore fluid exiting the sample was monitored and recorded. For the monotonic tests, monitoring was performed using a burette, and for the cyclic tests, monitoring was performed using the differential pressure transducer, which measured the height of water in the burette. In both cases, as gas exsolution occurred the gas was allowed to escape and only the volume of pore fluid was recorded. For the saturated monotonic tests, volume change was recorded with an electronic volume change device.

In addition to monitoring of pore fluid, the degree of saturation was determined for each stage of consolidation. The degree of saturation and void ratio was determined by taking

TDR readings, recording the dielectric constant, and using the method described in Section 3.7. TDR readings were taken during both gassy and saturated tests.

At this point, the specimens were ready for shearing, either static or cyclic.

4.4 CALCULATION OF VOID RATIO

There are two primary methods to evaluate the void ratio of a specimen. These methods are discussed below.

4.4.1 Void Ratio based on Initial Specimen Dimensions

The first method of calculating void ratio involves measuring the initial height and diameter of the sample and calculating an initial volume. Then, during the percolation of carbon dioxide and de-aired water through the specimen, the change in height is tracked using a vertical LVDT (linear voltage displacement transducer). The axial strain is calculated from the change in height and the initial sample height. It is then necessary to make an assumption regarding the straining condition in order to calculate the volume change. Usually a condition of isotropic strain is assumed. Isotropic strain means that any change in sample height would result in a change in sample diameter such that the specimen changes uniformly throughout its volume. Applying this assumption, the axial strain is multiplied by three to obtain the volumetric strain. The volumetric strain is then multiplied by the initial sample volume, to obtain the change in volume. The change in volume is then used to calculate the new void ratio. During consolidation, the volume change of a saturated specimen can be determined from the amount of water displaced. Based on the volume change during setup and saturation, and subsequent changes in volume during consolidation, the void ratio at the beginning of shear can be determined.

4.4.2 Void Ratio based on Final Specimen Moisture Content

The second method of evaluating void ratio uses the water content of the specimen. In this method, the specimen is carefully disassembled after shearing and the entire specimen, along with all the water in the specimen, is placed in a pan for water content determination. All the sand must be carefully removed from the end platens and the membrane. The final void ratio of the specimen can be calculated from the final dry mass of the sample, the final water content, and the specific gravity of the soil. In a saturated undrained test, the void ratio does not change during shear; however, in a saturated drained test the void ratio at the beginning of shear must be calculated by taking into account the volume of water displaced from the specimen during shearing.

4.4.3 Calculation of Void Ratio

Verdugo and Ishihara (1996) investigated the reliability of these two methods of calculating void ratio. It was shown that for dense specimens the difference between the two methods was negligible. However, in loose specimens, the second method of evaluating void ratio was more reliable. The second method also consistently gave smaller numerical values of void ratio. Some of the discrepancy between the methods was attributed to additional volume changes during assembly of the triaxial apparatus that could not be accounted for by the first method. Based on these results, the second method to evaluate void ratio (final water content) was adopted in this research.

In the case of gassy specimens, the determination of void ratio was more complex. The final water content of the specimen was determined following the approach outlined in the second method of evaluating void ratio. Since all the gassy specimens were tested undrained, the volume of water retained in the specimen remained unchanged during shear. However, the void ratio of the specimen changed during testing due to changes in the degree of saturation. The void ratio at the beginning of shear was calculated from the final volume of water retained in the specimen, the final dry mass of the specimen, and the initial degree of saturation. The initial degree of saturation was estimated from the apparent dielectric constant as explained in Section 3.7.

4.5 MONOTONIC TRIAXIAL TESTING

4.5.1 Stress Path

Conventional triaxial compression testing follows an effective stress path controlled by increasing the effective major principal stress (σ_1') while maintaining the effective minor principal stress (σ_3') constant. In other words, the axial load is increased while the confining pressure is maintained. This conventional stress path was followed for all monotonic tests.

All specimens were tested under strain controlled conditions at a strain rate of 0.15 mm/min. Strain controlled tests apply loading at a constant rate of deformation.

4.5.2 Saturated Specimens

Several saturated samples were sheared in monotonic triaxial compression. The purpose of these saturated tests was to ensure the equipment was working properly and to serve as a reference for the gassy samples. It was anticipated that all the gassy sample responses would lie somewhere between the extremes of a saturated undrained test and a saturated drained test.

Samples were tested both drained and undrained. The drained tests allowed the pore fluid to escape from the specimen during the loading process. The drainage of pore fluid from the specimen was carefully monitored during testing. The undrained tests allowed no fluid to enter or leave the sample during shear. For these tests, pore pressure was carefully monitored.

4.5.3 Gassy Specimens

A number of gassy specimens were sheared in monotonic triaxial compression. The initial degree of saturation was varied for each specimens. The intent was to maintain the initial density the same for all specimens, however, the initial density did vary slightly. Gas contents were targeted by choosing a back pressure which encouraged more or less gas to come out of solution; however, in general the gas content that was obtained was by trial and error.

All gassy samples were tested undrained. No fluid was allowed to enter or leave the sample and the pore pressures were monitored. Although the samples were undrained, void ratio and degree of saturation changed during loading due to gas solution or exsolution.

4.5.4 Time Domain Reflectometry

As described in Section 3.7, a TDR mini probe was used to obtain the dielectric constant during shearing. The initial degree of saturation and initial void ratio of the specimen was determined from initial TDR readings. TDR readings were also taken during monotonic shear and used to determine the degree of saturation and void ratio during loading.

4.6 CYCLIC TRIAXIAL TESTING

4.6.1 Stress Path

Standard cyclic triaxial testing follows an effective stress path controlled by cycling the major principal effective stress (σ_1') from compression to extension while maintaining the minor principal effective stress (σ_3') constant. In other words, the axial load is cycled while the confining pressure is kept constant. In the laboratory program, this standard cyclic stress path was used with the deviatoric loading following a sinusoidal wave form.

All specimens were tested under stress controlled conditions. Successive cycles of loading were applied at a constant stress level. The loading pattern was symmetrical about zero. The magnitude of the compression and extension loading segments were equal. Symmetrical loading is occasionally referred to as "pure stress reversal".

The testing frequency, or the rate of loading, varied from 0.03 Hz to 0.08 Hz. The automated testing equipment limited the frequency range that could be used; the larger the deviatoric load applied the lower the allowable frequency. Although the frequencies that were used are slower than typical earthquake frequencies, the slower rate of loading allowed a higher resolution of the data.

4.6.2 Saturated Specimens

Several saturated specimens were subjected to cyclic loading. The saturated samples provided a check to ensure the equipment was working properly. The saturated specimens also provided a baseline, or a reference, to which the gassy specimens were compared.

All saturated specimens were tested undrained. No pore fluid was allowed to enter or exit the specimen during loading. Pore pressure was monitored.

4.6.3 Gassy Specimens

A number of gassy specimens were subjected to cyclic loading. Similar to the monotonic tests, a specified initial degree of saturation was aimed for; however, the actual degree of saturation obtained was usually a trial and error process.

All gassy specimens were tested undrained; no pore fluid was allowed to enter or exit the specimen. Pore pressures were monitored. Even during undrained shear, the degree of saturation and void ratio of the gassy specimens changed due to gas solution and exsolution.

4.6.4 Time Domain Reflectometry

As described in Section 3.7, a TDR mini probe was used to obtain the dielectric constant at the beginning and end of loading. TDR readings were not taken during loading. It took about 15 seconds to obtain one waveform and since the load reversal occurred quickly, it was impossible to determine the exact stress conditions for that waveform. However, the initial and final degree of saturation and void ratio of the specimen were determined from TDR readings taken before and after loading.

4.7 SUMMARY AND CONCLUSIONS

The common methods of sample preparation are moist tamping, air pluviation, water pluviation, slurry deposition, and multiple sieve pluviation. The sample preparation method chosen for this study was moist tamping. Moist tamping results in a uniform sample with a very loose structure. Although moist tamping has come under some criticism for not being a natural field placement method, the specimens prepared by this method are more susceptible to liquefaction and therefore in accordance with the objectives of this research. Moist tamping results in lower monotonic strengths in triaxial compression and higher strengths in triaxial extension, compared to other specimen preparation methods. Under cyclic loading, moist tamped samples display a higher resistance to cyclic loading. In both static and cyclic loading, the differences in sample preparation method are more apparent for denser specimens.

After preparation of the specimen, the triaxial cell was assembled and a nominal confining pressure was applied. Carbon dioxide, and then de-aired distilled water, was percolated through the specimen in order to obtain fully saturated specimens. Confining and back pressures were increased and full saturation was confirmed by performing a B-test. Meanwhile, de-aired distilled water was saturated with carbon dioxide gas in a bubble chamber. The CO_2 saturated water was then passed through the specimen, replacing the de-aired water. The replacement of de-aired water occurred in three stages. Each stage consisted of passing a volume of CO_2 saturated water, equal to approximately three times the volume of voids, through the sample and then leaving the specimen for a period of time to allow mixing of the pore fluids. Isotropic consolidation was performed by decreasing the back pressure while maintaining a constant cell pressure, thereby increasing the effective stress. The reduction of back pressure allowed the carbon dioxide gas to come out of solution. The specimen was then ready for shear.

The calculation of void ratio, and the use of different methods, is often a source of confusion for researchers. The two methods used to calculate void ratio are from the initial sample dimensions or from the final specimen water content. The method chosen was the determination of void ratio from the final specimen water content. For the gassy specimens, it was necessary to use the TDR data as well.

Monotonic triaxial compression testing was performed on saturated and gassy specimens. Saturated specimens were tested both drained and undrained while all gassy specimens were tested undrained. Testing was performed under strain controlled conditions. Cyclic triaxial testing was also performed on saturated and gassy specimens. All cyclic tests were performed undrained under stress controlled conditions.

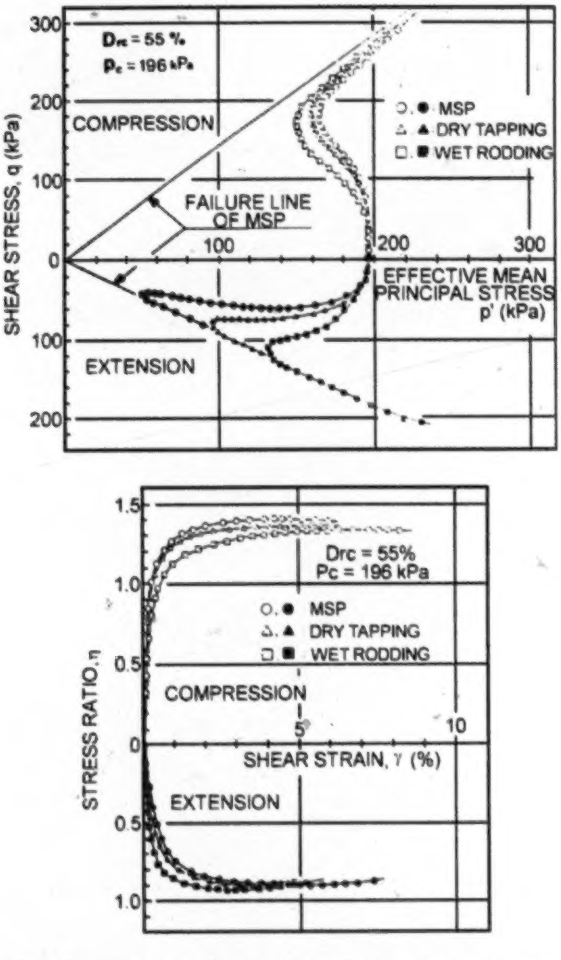

Figure 4.1 - Variation in undrained stress-strain relationship due to the effect of difference in sample preparation (modified from Miura and Toki 1982).

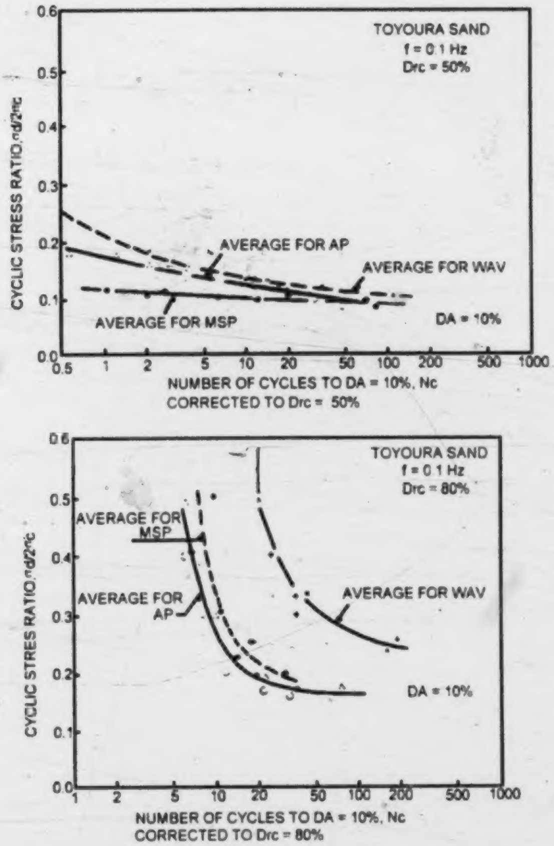

Figure 4.2 - Effects of specimen preparation method on cyclic stress ratio (modified from Tatsuoka et al. 1986).

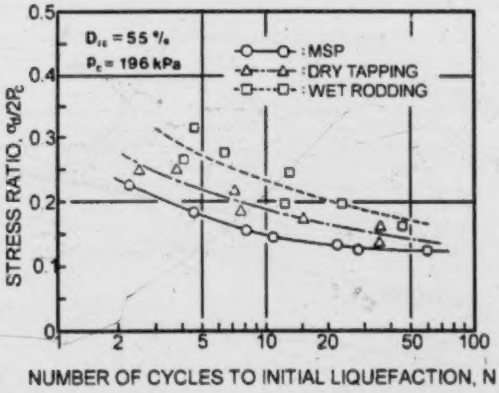

Figure 4.3 - Comparison of stress ratio versus number of cycles to initial liquefaction for MSP, dry tapped, and wet rodded specimens (modified from Miura and Toki 1982).

CHAPTER 5

MONOTONIC TRIAXIAL LABORATORY RESULTS [1,2]

5.1 INTRODUCTION

One method to determine the liquefaction potential of sand is to perform monotonic triaxial compression testing. Traditionally, it was thought that sand that contained gas would not be susceptible to liquefaction. However, flow liquefaction events in soils known to contain gas created questions about the liquefaction potential of gassy sands. In this laboratory program, undrained triaxial compression tests were performed on loose gassy sand specimens. The aim was to understand how the presence of gas affects liquefaction. Saturated specimens, tested both drained and undrained, were used as reference tests.

To better understand the liquefaction potential of loose sand, tests are analyzed within the framework of critical state soil mechanics. Specimen results for both the saturated and gassy tests are presented within this framework. The range of specimen responses to loading is also discussed.

The state boundary surface is determined from the laboratory results. In this chapter, the state boundary surface for Ottawa sand is determined using both the saturated and gassy test results. The state boundary surface is also compared to previously published state boundary surfaces for Ottawa sand.

---

[1] *A version of part of this chapter has been published. Grozic, J.L., Robertson, P.K., and Morgenstern, N.R. 1998. The behavior of loose gassy sand. Proceedings of the 51st Canadian Geotechnical Conference, October 4-7, 1998, Edmonton, Alberta, Canada, pp. 697-704.*

[2] *A version of part of this chapter has been accepted for publication. Grozic, J.L., Robertson, P.K., and Morgenstern, N.R. 1998. The static behavior of loose gassy sand. Accepted for publication in the Canadian Geotechnical Journal, November 12, 1998, 36 pages.*

The potential for flow liquefaction of loose gassy sand will depend on the soil state (density, initial consolidation stress, and soil structure) and grain characteristics. Mode and rate of shearing will also influence the liquefaction potential of a specimen. For the specialized case of gassy specimens, the liquefaction potential also depends on the degree of saturation and the gas and pore fluid characteristics. This chapter presents and discusses the factors that determine the liquefaction potential of a sand. Many variables were held constant for all the tests, therefore, eliminating them from a comparison of the test results. The use of the similar values allows a better comparison of the effect of the initial degree of saturation on liquefaction potential.

The objective of this chapter is to determine if loose gassy sand can strain soften under shear and experience flow liquefaction.

5.2 STATE BOUNDARY SURFACE FOR VERY LOOSE SAND

Critical state soil mechanics states that the deviator stress, q, the effective mean normal stress, p', and the void ratio, e, are uniquely related in the region between the normally consolidated state and a critical state (Roscoe et al. 1958). These parameters are defined as follows:

$$q = \sigma_1' - \sigma_3' \qquad [5.1]$$

$$p' = \frac{1}{3}\left(\sigma_1' + 2\sigma_3'\right) \qquad [5.2]$$

Figure 5.1 shows this critical surface, which separates the states that samples can achieve from the states that a sample can never achieve. In other words, the critical surface is a state boundary surface (Sasitharan 1994).

Following the development of critical state soil mechanics for clays, Castro (1969) showed that loose sands can collapse and strain soften during monotonic undrained loading. Castro established the concept of "steady state", a state of constant resistance during which the effective stress state does not change. Loose samples tested undrained will reach a peak and then strain soften to steady state. Been et al. (1991) then went on to show that this steady state is also a critical state, implying that steady state is independent of the stress path followed.

When studying very loose sands, Sladen et al. (1985) developed the collapse surface approach to liquefaction analysis. This approach showed that a surface exists in deviator stress – effective mean normal stress – void ratio space that can trigger collapse and strain soften leading to steady state under undrained loading. Several researchers, such as Ishihara et al. (1991), have shown that the collapse surface can be defined by the post peak portion of monotonic undrained stress paths. Sasitharan (1994) showed that loose saturated sand could collapse during drained loading when the stress path tries to cross the collapse surface. Skopek (1994) showed that even dry sand would collapse when the stress path tries to cross the collapse surface.

Sasitharan (1994) studied the shape of the state boundary surface by performing monotonic undrained triaxial compression loading and constant void ratio stress paths on loose sand specimens. The results of this study indicated that the state boundary could be defined by the post peak portion of the undrained stress paths for very loose sand. Figure 5.2 schematically shows the state boundary surface and Figure 5.3 shows the projection of this surface into *q-p'* space. The steady state line in *q-p'* space can be defined mathematically as:

$$q = sp' + (M - s)p'_{SS} \qquad [5.3]$$

where:

M = slope of the steady state line in deviator stress – effective mean normal stress space

s = approximate slope of the state boundary surface in deviator stress – effective mean normal stress space

q_{SS} = deviator stress at steady state
p'_{SS} = effective mean normal stress at steady state
q = deviator stress of a stress state on state boundary
p' = effective mean normal stress of a stress state on state boundary.

The projection of the state boundary surface in *e–lnp'* space is shown in Figure 5.4. The void ratio and effective mean normal stress at steady state can be approximated by a straight line if plotted with a logarithmic scale for the effective mean normal stress. The line relating void ratio and effective mean normal stress can be defined mathematically as:

$$e = \Gamma - \lambda \cdot \ln p'_{SS} \qquad [5.4]$$

where:

λ = slope of the line
Γ = the intercept of the line at $p'_{SS} = 1$.

By combining equations [5.3] and [5.3] the following result is obtained:

$$q = s \cdot p' + (M - s) \cdot \exp\left(\frac{\Gamma - e}{\lambda}\right) \qquad [5.5]$$

where M, s, Γ, and λ are constants and can be obtained by performing undrained tests for loose sand. Sasitharan (1994) outlined these constants:

" M – The slope of the straight line representing stresses at steady state (p'_{SS}, q_{SS})

s – The slope of the straight line approximation of the post peak portion of undrained stress paths with identical void ratio.

λ – The slope of the best fit straight line between void ratio (e) and logarithmic effective mean normal stress at steady state (lnp'_{SS}). Here, the value of l will depend on the unit chosen for the effective mean normal stress.

Γ – The intercept of the best fit straight line between void ratio (e) and logarithmic effective mean normal stress ($\ln p'_{SS}$) at $p'_{SS} = 1$ unit."

It should, however, be noted that equation [5.5] represents a linear approximation to the actual curved state boundary surface for very loose sand.

Along the steady state line, q and p' are related by M, which is a function of the friction angle and direction of loading. Wood (1990) proposed the following theoretical value of M for triaxial compression:

$$M_C = \left(\frac{q_{SS}}{p'_{SS}} \right)_C = \frac{6 \sin \phi'_{SS}}{3 - \sin \phi'_{SS}} \qquad [5.6]$$

where:

ϕ'_{SS} – the steady state friction angle

The results of the monotonic triaxial testing performed in this study will be analyzed using the concepts of state boundary surface outlined above. The steady state constants M, s, Γ, and λ, as well as ϕ'_{SS}, will be determined from this testing program.

5.3 RANGE OF RESPONSE

In the summary report of the CANLEX Project, Robertson et al. (1998) described the range of responses of sandy soils subjected to monotonic undrained loading. This work resulted in a plot of four idealized stress-strain curves representing samples subjected to anisotropic initial stress states. Figure 5.5, modified to represent isotropic initial stress states, presents the possible range of responses. Lines A to D represent completely strain-softening, quasi-steady state, plateau, and completely strain-hardening responses.

The weakest response is illustrated by line A and the strongest response is illustrated by line D. Lines B and C are intermediate responses.

Robertson et al. (1998) reported that, "in all cases, one would expect the stress-strain curve to eventually level off as ultimate state is approached. However, in general, the level of strain required to reach ultimate state often exceeds the capabilities of the laboratory equipment." The results of the laboratory testing for samples showing response Type B, C, or D are presented as the "end-of-test" points, which may or may not be coincident with ultimate state. All monotonic undrained test results from this research have been classified according to Figure 5.5.

In addition to undrained tests, monotonic consolidated drained tests were also performed on saturated specimens. All drained tests exhibit a completely strain-hardening response, therefore, the resulting stress-strain curve from a drained test would appear similar to line D in Figure 5.5. The results of the drained tests are also presented as the "end-of-test" point.

5.4 SPECIMEN RESULTS

Monotonic triaxial compression testing was performed on loose specimens of gassy sand tested in undrained loading. Saturated specimens were tested in undrained and drained conditions. Twenty-five specimens were tested; the results of twenty of these tests are summarized in Table 5.1. All specimens were consolidated to approximately the same mean normal effective pressure, (p'), of 300 kPa, for comparison.

5.4.1 Saturated Test Results

Six saturated specimens were tested in monotonic triaxial compression. The saturated test results are summarized in Table 5.1. Test results for each specimen are presented in Appendix A.

Half of the saturated specimens were tested under drained conditions, while the other half were tested undrained. In the drained tests, pore fluid was allowed to escape the specimen. The volume of pore fluid was carefully monitored. The test was performed at a slow enough rate to maintain a condition of no pore pressure. In the undrained tests, no pore fluid was allowed to enter or exit the specimen. Pore pressures developed and were closely monitored.

The initial void ratio of the saturated specimens ranged from 0.733 to 0.910, corresponding to relative densities ranging from 27% to –28%. These specimens can be classified as loose to very loose. The initial confining pressure of all specimens was very close to 300 kPa.

No final moisture content was taken on Samples 6, 11, and 12. For these specimens, the void ratio was calculated from the initial specimen dimensions, as discussed in Chapter 4. This method of calculating void ratio generally gives higher numbers.

The stress strain curves and the effective stress paths of the saturated specimens are shown in Figures 5.6 and 5.7, respectively. A plot of void ratio versus mean normal effective pressure is presented in Figure 5.8. These figures illustrate that all the drained specimens had a strain hardening response, while all the undrained specimens had a strain softening response. A strain hardening response to loading is idealized as curve D on Figure 5.5, while a strain softening response to loading is idealized as curve A.

5.4.2 Gassy Test Results

Thirteen gassy specimens were tested in monotonic triaxial compression. The test results are summarized in Table 5.1. Individual test results are presented in Appendix A.

All the gassy specimens were tested undrained. No pore fluid was allowed to enter or leave the specimen during loading and the pore pressures were monitored. Unlike the saturated undrained tests, the gassy undrained tests experienced volume changes during the test. The volume change was due to the compressibility of the free gas in the pores and due to the solution or exsolution of free gas.

The initial void ratio of the gassy specimens ranged from 0.77 to 1.07 corresponding to relative densities ranging from 16% to –78%. These specimens can be classified as loose to very loose. The initial confining pressure of all specimens was very close to 300 kPa.

No final moisture content was taken on Samples 8, 9, and 13. For these specimens, the void ratio was calculated from the initial specimen dimensions, as discussed in Chapter 4. This method of calculating void ratio generally gives higher numbers.

The initial degree of saturation ranged from 71.7% to 97.0 %. All specimens, with the exception of Sample #18, showed a net increase in degree of saturation. Sample #18, showed no increase in saturation. The final degree of saturation ranged from 75.2% to slightly greater than 100%. (The saturations slightly greater than 100% are due to the accuracy limitations of the TDR method).

The response of the gassy specimens varied from completely strain softening to completely strain hardening. Loose gassy specimens with an initial void ratio greater than 0.83 and an initial degree of saturation greater than about 90% had a completely strain softening response to loading. Sample #8 had an initial degree of saturation of only 80%, yet still had a strain softening response due to its very loose structure (initial void ratio of 0.92). Only Sample #14, which had an initial degree of saturation of 97% but a void ratio of only 0.77, responded in a quasi-steady state manner. With the exception of one *extremely* loose specimen, all specimens with an initial degree of saturation less than 90% responded in a strain hardening manner. All specimens with initial degrees of saturation less than about 80% responded in a strain hardening manner, regardless of density. A strain hardening response to compressive loading is idealized as curve D on Figure 5.5, while a quasi-steady state response is represented by curve B and a strain softening response is represented by curve A.

Figures 5.9 and 5.10 present the stress strain curves and the effective stress paths, respectively, for five representative gassy specimens tested undrained. The hollow symbols represent the start of the test and the shaded symbols represent the end of the test. The gassy specimens plotted somewhere between a saturated undrained specimen and a saturated drained specimen with similar void ratios, with their location depending on the initial degree of saturation. The higher the initial degree of saturation, the closer the specimen behavior was to a saturated undrained test. In Figure 5.11, void ratio is plotted versus mean normal effective stress. A gassy specimen having an initial degree of saturation less than roughly 90% showed an initial decrease in void ratio followed by a constant void ratio with increasing mean normal effective stress. Specimens with initial degrees of saturation greater than about 90% also had some initial decrease in void ratio and, eventually, the void ratio became constant with decreasing mean normal effective stress.

This phenomenon is illustrated in Figure 5.12, which plots degree of saturation (S_r) versus mean normal effective stress (p'). The specimens with initial S_r less than 90% showed an increase in degree of saturation while p' remained almost constant. Eventually, with increasing p', the specimens experienced a gradual decrease in degree of saturation. Specimens with an initial S_r greater than 90% quickly increased in S_r with very little increase in p', and at some point all the gas went into solution and the specimen became essentially saturated. Therefore, p' decreased as the specimen remained at approximately S_r equal to 100%. In other words, the pore pressures showed an initial dramatic increase and then quickly leveled off with increasing axial strain, while the mean normal total stress, *p*, continued to increase.

5.5 STATE BOUNDARY SURFACE FOR OTTAWA SAND

The state boundary surface for soils can be approximated by equation [5.5] in deviator stress (q) – effective mean normal stress (p') – void ratio space (e) as described previously. Figure 5.13 shows the relation between deviator stress and effective mean normal stress for Ottawa sand obtained from the laboratory tests on both saturated and gassy specimens. The relationship between q_{SS} and p'_{SS} can be approximated as a straight line with a slope (M) equal to 1.50. Using equation [5.6], this slope corresponds to a friction angle of 37°.

Figure 5.14 shows stress paths for two saturated undrained tests with very similar void ratios, but slightly different consolidation stresses. If assumed that the post-peak portion of the stress paths form a straight line, then the slope of this straight line (s) is equal to 0.80.

Figure 5.15 shows the variation of void ratio with effective mean normal stress at steady state. The effective mean normal stress is plotted on a logarithmic scale. The relationship between e and $\ln p'_{SS}$ can be approximated as a bi-linear curve.

Figure 5.16 illustrates the steady state lines for other sands (Sasitharan et al. 1994). For most sands, the steady state line curves downward at high stresses. Ishihara (1993) also indicated that the steady state line is curved in nature. The steady state line can be approximated by a bi-linear relationship. The relationship can be broken down into straight line portions over various stress ranges, with each portion having an associated Γ and λ (Wride and Robertson 1997a).

The bi-linear representation of the steady state line shown in Figure 5.15 changes slope at approximately an effective mean normal stress of 250 kPa. The location of the slope change appears to be consistent with the bi-linear steady state lines for other sands shown in Figure 5.16. The straight line corresponding to stress levels less than 250 kPa has a slope (λ) of 0.0159 and an intercept at $p'_{SS} = 1$ kPa (Γ) of 0.92. The straight line representing stress levels greater than 250 kPa is much steeper with a slope (λ) of 0.153 and an intercept (Γ) of 1.67.

The state boundary surface for loose Ottawa sand can be represented by using equation [5.5] with the following parameters:

$M = 1.50$
$s = 0.8$

for $p' < 250$ kPa	for $p' > 250$ kPa
$\lambda = 0.0159$	$\lambda = 0.153$
$\Gamma = 0.92$	$\Gamma = 1.68$

5.6 FLOW LIQUEFACTION POTENTIAL OF LOOSE GASSY SAND

The propensity of a sand specimen to liquefy is a function of the soil state (density, initial consolidation stress, and soil structure) and grain characteristics. Soil structure includes fabric, age, and cementation, while grain characteristics include features such as grain-size distribution, grain shape, and mineralogy. Mode and rate of shearing will also influence the liquefaction potential of a specimen. For the specialized case of gassy specimens, the liquefaction potential also depends on the degree of saturation and the gas and pore fluid characteristics.

5.6.1 Effects of Density and Initial Consolidation Stress

The effects of density and initial consolidation stress can be discussed together. Yoshimine and Ishihara (1998) introduced the concept of flow potential to capture the effects of initial conditions on liquefaction. The flow potential can be represented by the maximum excess pore water pressure ratio achieved during undrained monotonic loading, u_f. Flow potential is defined as:

$$u_f = \left(1 - \frac{p'_{PT}}{p'_C}\right) \times 100(\%) \qquad [5.7]$$

where:

p'_{PT} = mean normal effective principle stress at *phase transformation* including steady state (phase transformation is the point of minimum effective mean stress that appears where dilatancy behavior changes from contractive to dilative)

p'_C = mean isotropic effective confining stress

u_f = flow potential

Flow potential is "not an index of material property fixed by initial conditions alone, but is strongly affected by the stress conditions during deformation such as direction of principal stress and magnitude of the intermediate principle stress" (Yoshimine and Ishihara 1998). If the sample preparation method and mode of shearing are fixed, then flow potential becomes a function of the initial confining stress and density only. Based on an extensive laboratory program, the result of the flow potential research are summarized in Figure 5.17. Part (a) shows the flow potential lines for triaxial compression and part (b) shows the flow potential lines for both compression and extension.

Using Figure 5.17(a), the effects of density and initial confining stress can be analyzed. For the same relative density, the flow potential will be greater when the initial confining stress is large. When the densities are very small, i.e. very loose, the flow potential lines are almost horizontal indicating that initial confining pressure has little influence on the flow potential of very loose samples. For the same confining pressure, the flow potential will be higher for specimens with lower densities. The flow potential lines are very close together in the area of low confining pressure and low density. This indicates that at low initial confining pressures the soil behavior is very sensitive to density.

In this laboratory program, the same value of initial confining pressure was targeted for every test. This eliminated the effects of confining pressure. In addition, the specimen densities ranged from loose to very loose. By maintaining similar values, the effects of density were reduced.

5.6.2 Effect of Soil Structure

Soil structure includes fabric, age, and cementation. In reconstituted laboratory specimens only fabric is a factor. In nature, soil structure is dictated by fabric, age, and cementation and all these variables will affect the liquefaction potential of the soil mass under consideration.

Fabric is generated by the method in which a specimen is preparation. The effect of specimen preparation on test results was discussed in Section 4.2.6. In this laboratory program, specimens were prepared by moist tamping. Moist tamping generally results in the loosest structure and the lowest strengths, or the highest propensity to liquefy.

5.6.3 Effect of Grain Characteristics

Grain characteristics include features such as grain-size distribution, grain shape, and mineralogy. The most important grain characteristic affecting liquefaction is the presence of fines. Lade and Yamamuro (1997) and Sladen et al. (1985) performed laboratory studies of the liquefaction potential of sands and silty sands. They found that the liquefaction potential of clean sand is much lower than sand containing fines. Lade and Yamamuro (1997) hypothesis that the increased liquefaction potential of dirty sands is due to particle structure in which silt particles occupy locations near the sand grain contact points, thereby pushing the sand grains slightly apart. When this metastable structure is subjected to loading, the silt particles slide into the voids and collapse is initiated. The addition of fines also has the effect of reducing permeability and increasing compressibility, therefore making an undrained response to a given loading condition is more likely. Natural and man-made submarine slopes and hydraulic fills, may be susceptible to developing a metastable structure with a high liquefaction potential.

Preparing specimens with clean sand eliminated the effects of grain characteristics.

5.6.4 Effect of Shearing Mode and Rate

a) Mode of Shearing

The effect that the mode of shearing has on the undrained behavior of sands has been described by Yoshimine et al. (1999), Yoshimine et al. (1998), and Yoshimine and Ishihara (1998). Figure 5.18 shows the results of a study by Yoshimine et al. (1999) on Toyoura sand. The stress strain curves and the effective stress paths are presented for loose specimens of similar relative density. The figure shows that the triaxial compression tests resulted in the most dilative behavior, while the triaxial extension tests resulted in the most contractive behavior. Simple shear tests resulted in a behavior between the compression and extension tests.

The brittleness index is an indicator of the collapsibility of strain-softening sand when sheared undrained (Bishop 1971). A liquefied soil mass with a high brittleness index may experience very high accelerations (Yoshimine et al. 1999). Figure 5.19 shows the relationship between brittleness index and relative density for Toyoura and Kawagishi-cho sands sheared under different modes. The figure indicates that triaxial compression tests will have the lowest brittleness and triaxial extension tests will have the highest brittleness.

The effects of mode of shearing can also be analyzed using the concept of flow potential (Yoshimine and Ishihara 1998) introduced in Section 5.6.1. Figure 5.17(b) shows the differences between the flow potential of specimens tested in triaxial compression and triaxial extension. These flow potential lines show that triaxial compression tests have a higher resistance to liquefaction than triaxial extension tests. The large space between the extension lines indicates that triaxial compression tests are more sensitive to density changes than triaxial extension tests.

Yoshimine et al. (1999) also examined case histories and found that laboratory tests performed in simple shear best matched observed field performances.

Due to its simplicity, triaxial compression is the most commonly used laboratory shearing mode. For a given relative density, triaxial compression tests result in the highest undrained shear strength and lowest brittleness. Thus with regards to flow liquefaction problems, triaxial compression tests result in unconservative judgements.

b) Rate of Shearing

Been et al. (1991) investigated the effect of strain rate on undrained compression tests using Erksak sand. He varied the rate of strain from 4% per hour to 300 000% per hour. No significant difference was found in the steady state behavior of the specimens. However, the researchers postulated that strain rate may influence the behavior of fine silty sands.

In this study, the strain rate was maintained constant for all tests. Therefore, when comparing the test results, the effects of strain rate are eliminated.

5.6.5 Effect of Gas

a) Initial Degree of Saturation

Two previous research programs have studied the effect of gas on the undrained shear strength of medium to dense sands. The first program conducted by Sills (1996) consisted of a series of laboratory tests on very dense sand. Both saturated and gassy sand specimens were tested in triaxial compression. The results showed that the presence of gas reduced the undrained shear strength of dense sand. Sills also noted that the presence of gas prevented the pore water pressure from dropping as fast, or as low, as it would in saturated sand.

The second program, conducted by Rad et al. (1994), examined the effect of gas on medium and dense sand specimens. Triaxial compression tests were performed on dense saturated and gassy specimens. The results showed that dense sand specimens containing free gas exhibited lower peak strengths than saturated specimens; the residual strengths of the gassy and saturated specimens were similar.

The purpose of this laboratory program was to examine the effect of gas on flow (static) liquefaction. The effect of initial degree of saturation on the liquefaction potential of loose sands is presented in Figures 5.9 to 5.12. For loose specimens of similar initial density, the potential for liquefaction was reduced as the initial degree of saturation dropped below 100%. The liquefaction potential continued to decrease with decreasing degrees of saturation. When the degree of saturation dropped below about 70%, the specimens exhibited a strain hardening response.

Figures 5.9 to 5.12 also show that in general, if the initial degree of saturation was less than about 88%, the specimen was not susceptible to flow liquefaction. A specimen could be susceptible to liquefaction if it is extremely loose and the initial degree of saturation was less than 88% but greater than 80%.

The effect of the initial degree of saturation on the state boundary surface is presented in Figure 5.20. The shaded symbols represent the final state (either minimum or end of test) and the hollow symbols represent the state at the beginning of shear. The final degree of saturation is indicated adjacent to the final states of the gassy specimens. The gassy specimens plotted above the saturated state boundary surface. Generally, the lower the initial degree of saturation, the higher the data point was above the saturated surface. Figure 5.21 shows the same test results but with the initial degree of saturation indicated adjacent to the initial state. It is interesting to note that specimens with initial degrees of saturation greater than 88% moved towards the left, i.e. they strain softened, while specimens with initial degrees of saturation less than 88% moved down and towards the right, i.e. stain hardened. The effect of initial degree of saturation was to move the state boundary surface up. Similar results have been presented for unsaturated soils (Wheeler and Sivakumar 1993).

To further examine the effect of saturation on liquefaction potential, the results of the laboratory program were analyzed using the flow potential concept introduced in Section 5.6.1. Figure 5.22 is a plot of initial void ratio versus initial degree of saturation. The flow potential value is indicated beside each data point. A flow potential of zero means that the specimen behaved in a strain hardening manner, and was therefore not susceptible to flow liquefaction. A line separates the liquefiable zone from the non-liquefiable zone. A solid line separates the test results, while a dashed line shows the predicted extension of the solid line. In addition, a line limiting the void ratio has been sketched. All the lines shown on this plot were drawn based on engineering judgement. These lines show that if the initial degree of saturation is 100% then flow liquefaction can occur if the specimen is loose enough (in this case void ratios between approximately 0.75 to 0.95). It is generally not possible to prepare specimens of Ottawa sand with void ratios higher than about 0.95. As the initial degree of saturation decreases, flow liquefaction is only possible if the specimens are very loose (i.e. above the solid line). The maximum possible void ratio becomes slightly higher as the degree of saturation decreases. This is due to bulking of the specimens as gas exsolution occurs. When the initial degree of saturation drops below about 75%, liquefaction is not possible regardless of the initial void ratio. It should be noted that these lines apply to Ottawa sand under triaxial compression loading. They are approximations and should be used for guidance only. A similar zone of potential liquefaction could be identified for specimens tested in direct simple shear. The simple shear liquefiable zone would plot lower than the triaxial compression zone shown in Figure 5.22.

The presence of gas may also affect the measurement of pore pressures in the laboratory specimens by creating a small time lag between the measured and actual pore pressures. This lag would be more pronounced with greater gas contents and would have the effect of shifting the stress path slightly to the left.

b) Gas Characteristics

Rad et al. (1994) performed a series of triaxial tests on dense sand specimens saturated with carbon dioxide or methane gas. The initial degree of saturation of all the tests was 100%. The results of their study showed that specimens experienced volumetric straining due to gas exsolution and subsequent gas expansion. Rad et al. (1994) explained that "the more soluble the gas (i.e. CO_2 relative to CH_4), the stronger the gas exsolution and the subsequent volumetric expansion, the less intense the pore pressure reduction, and thus, the lower the undrained shear strength". Stated another way, as the pore pressure was reduced during loading, gas began to come out of solution. The gas retarded the increase of effective stress (as compared with saturated specimens). This resulted in a state of partial drainage, even in an undrained test. If a more soluble gas is used to prepare a specimen, gas exsolution will be more rapid, and the increase of the effective stress will be retarded earlier resulting in a lower undrained strength.

When subjected to undrained loading, loose specimens contract resulting in an increase in pore pressure, while dense specimens dilate resulting in a decrease in pore pressure. If a loose specimen prepared with a more soluble gas (say CO_2 as opposed to CH_4) is loaded undrained, the gas should go into solution more rapidly. This would result in a more rapid build up pore pressures, therefore, less effective stress and lower undrained shear strength.

In this study, only carbon dioxide gas was used. However, the most predominate gas in natural soils is methane. Based on the above studies, natural soils containing methane gas should have a lower liquefaction potential than soils tested in the laboratory with carbon dioxide gas. Hence, laboratory studies investigating the liquefaction potential of gassy specimens by using carbon dioxide gas will be conservative.

5.7 COMPARISON WITH PUBLISHED DATA

To date there have been no studies published that study the potential for flow liquefaction of loose gassy sand. However, several studies have looked into the state of Ottawa sand. Sasitharan (1994) determined the state boundary surface for Ottawa sand. The following parameters for representation of the state boundary surface where produced from his study:

$M = 1.197$
$s = 0.8$
$\lambda = 0.0168$
$\Gamma = 0.867$

Skopek (1994) looked into the behavior of dry Ottawa sand and obtained the following parameters for defining the state boundary surface:

$M = 1.154$

$s = 0.6$

$\lambda = 0.0337$

$\Gamma = 0.9303$

The parameters quoted by Sasitharan and Skopek are consistent with the parameters obtained in this study (see Section 5.5). The value of M obtained in this study was slightly higher than the values obtained by the other researchers. The values of s, λ, and Γ were all close to the values presented by Sasitharan and Skopek.

5.8 SUMMARY AND CONCLUSIONS

A laboratory program studying the behavior of loose gassy sand was carried out. Undrained monotonic triaxial compression tests were performed on saturated and gassy specimens. Drained monotonic triaxial compression tests were performed on saturated specimens. The range of possible responses to the monotonic loading varied from completely strain softening to completely strain hardening.

The results of the laboratory program showed that all loose saturated specimens tested undrained responded in a strain softening manner while all loose saturated specimens tested drained responded in a strain hardening manner. The gassy specimens with high initial void ratios and high initial degrees of saturation responded in a strain softening manner. As the initial degree of saturation decreased below about 88%, the loose specimens responded in a strain hardening manner. A few very loose specimens with initial degrees of saturation less than 88% responded in a strain softening manner. All specimens with degrees of saturation less than about 80% responded in a strain hardening manner.

The results of the monotonic laboratory program were evaluated using the framework of critical state soil mechanics. This framework introduces a state boundary surface, a unique surface which relates deviator stress (q), effective mean normal stress (p'), and void ratio (e). The shape of the state boundary surface can be approximated by a straight line in deviator stress – effective mean normal stress space and a straight line in void ratio – logarithm effective mean normal stress space. The parameters representing these lines for Ottawa sand were determined from the laboratory program and are summarized as:

$M = 1.50$
$s = 0.8$

for $p' < 250$ kPa	for $p' > 250$ kPa
$\lambda = 0.0159$	$\lambda = 0.153$
$\Gamma = 0.92$	$\Gamma = 1.68$

The potential for flow liquefaction of loose gassy sand will depend on the soil state (density, initial consolidation stress, and soil structure) and grain characteristics. Mode and rate of shearing will also influence the liquefaction potential of a specimen. For the specialized case of gassy specimens, the liquefaction potential also depends on the degree of saturation and the gas and pore fluid characteristics.

The effect of density and initial consolidation stress can be evaluated using the concept of flow potential. As the density increases, the potential for liquefaction decreases, and as the initial confining pressure increases (for constant void ratio), the potential for liquefaction increases. Initial confining pressure has less influence on loose samples. In this study, the initial confining pressure for all specimens was the same and the initial densities of all specimens were similar. By keeping these parameters essential fixed, the laboratory program could better analyze the effects of gas.

Soil structure includes fabric, age, and cementation. Soil structure is induced by specimen preparation. This laboratory program used specimens prepared by moist tamping, which generally results in the loosest structure and the lowest strength, or the highest propensity to liquefy.

Grain characteristics include features such as grain-size distribution, grain shape, and mineralogy. The most important grain characteristic affecting liquefaction is the presence of fines. The liquefaction potential of a clean sand is generally lower than a sand containing fines. In this study, clean Ottawa sand was used to prepare all specimens.

Mode and rate of shearing will affect liquefaction potential. Triaxial compression, the most commonly used laboratory shearing mode, gives the highest undrained shear strength and lowest brittleness for a given relative density. This results in the most unconservative judgement for flow liquefaction problems. Examination of case histories has shown that laboratory tests performed in simple shear best match observed field performances. Studies have shown that rate of shearing has little affect on the liquefaction potential. In this study, all specimens were sheared in triaxial compression under a constant strain rate.

Determining the effect of the presence of gas on the liquefaction potential of loose sand was one of the main objectives of this laboratory program. All previous studies of gassy specimens have been performed on very dense sands. The presence of gas decreased the initial degree of saturation, which had a couple effects. First, the state boundary surface in $e - \ln p'_{SS}$ shifted upwards. Either a higher void ratio, or a higher effective mean normal stress, would be necessary to trigger collapse. Second, the liquefaction potential, for a given density, was decreased. The results of the laboratory program on Ottawa sand showed that if the initial degree of saturation dropped below about 88% that liquefaction was only possible in extremely loose specimens and if the initial degree of saturation dropped below about 80% that flow liquefaction was essentially impossible.

The type of gas present will affect the liquefaction potential. For loose specimens, the higher the solubility of the gas in the pore fluid the greater the liquefaction potential. In this study, only carbon dioxide gas was used.

A comparison of the laboratory results with previously published data is desirable. No published data was found on the liquefaction of gassy sand; however, data was available on saturated Ottawa sand. The state boundary surface for Ottawa sand determined by other researchers was very similar to the state boundary surface determined in this study.

The main conclusion of the laboratory tests is that if specimens of Ottawa sand are sufficiently loose and if the initial degree of saturation is sufficiently high (in this case, greater than about 88%), then the specimens tested in triaxial compression can strain soften and experience flow liquefaction similar to fully saturation specimens.

Table 5.1 Summary of specimen results.

Sample	Test Type		Initial p'	Initial Sr *		Void Ratio †	Response	Peak		Minimum		End of Test	
					Final			p'	q'	p'	q'	p'	q'
6	Saturated	CD	301.0	100%	100%	0.825	D					596.4	893.6
8	Gassy	CU	286.2	80%	88%	0.917	A	278.4	304.1	110.2	184.2		
9	Gassy	CU	295.2	72%	77%	1.066	D					374.0	548.3
10	Gassy	CU	258.6	91%	95%	0.986	A	195.1	155.7	37.5	75.3		
11	Saturated	CU	266.3	100%	100%	0.896	A	197.9	121.9	10.5	32.9		
12	Saturated	CU	302.1	100%	100%	0.910	A	240.3	134.4	17.0	29.8		
13	Gassy	CU	303.6	83%	90%	0.883	D					411.4	584.8
14	Gassy	CU	301.5	97%	104%	0.771	B	283.2	318.8	187.2	254.4	189.77	273.36
15	Gassy	CU	312.5	80%	84%	0.874	D					486.1	824.9
16	Gassy	CU	317.1	82%	87%	0.876	D					472.9	713.6
17	Gassy	CU	298.5	77%	81%	0.890	D					458.3	703.5
18	Gassy	CU	296.1	76%	75%	0.883	D					535.1	866.7
19	Saturated	CD	295.0	100%	100%	0.765	D					768.3	1427.5
20	Gassy	CU	300.7	86%	92%	0.872	D					318.6	499.6
21	Gassy	CU	296.3	80%	82%	0.897	D					484.7	799.6
22	Saturated	CU	301.4	100%	100%	0.733	A	191.0	137.1	12.9	49.7		
23	Saturated	CD	287.4	100%	100%	0.743	D					618.8	1005.9
24	Gassy	CU	283.9	97%	106%	0.835	A	236.3	133.9	-4.8	-11.6		
25	Gassy	CU	271.7	91%	96%	0.852	A	226.1	117.3	9.6	0.0		

* Initial degree of saturation is calculated from TDR data at the beginning of shear.

† Void ratio is at the beginning of shear.

Note: p' is the mean normal effective stress defined as $^1/_3\,(\sigma_1 + 2\sigma_3)$

q' is the deviator stress defined as $(\sigma_1 - \sigma_3)$

CU - Consolidated Undrained triaxial test

CD - Consolidated Drained triaxial test

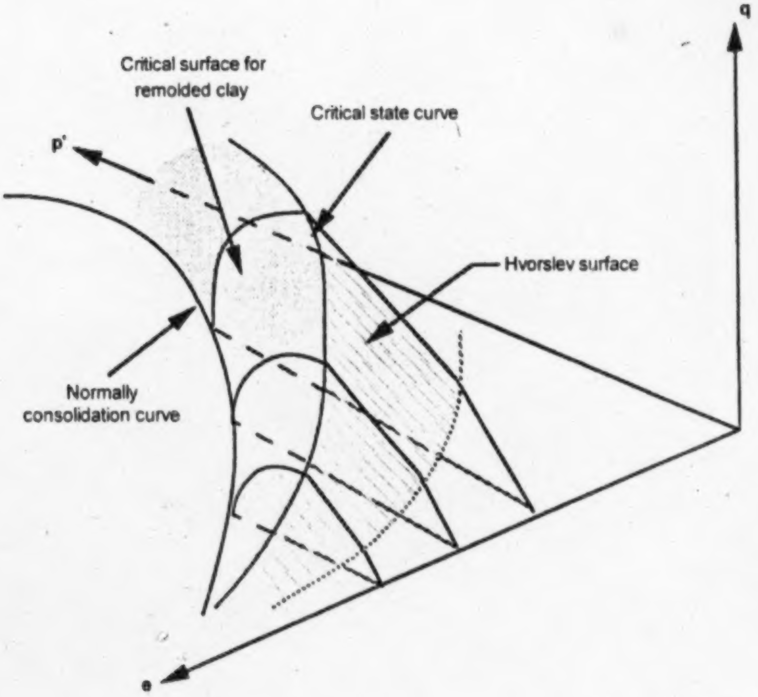
q
Critical surface for remolded clay
Critical state curve
p'
Hvorslev surface
Normally consolidation curve
e

Figure 5.1 - State boundary surface for remolded clay (modified from Sasitharan 1994).

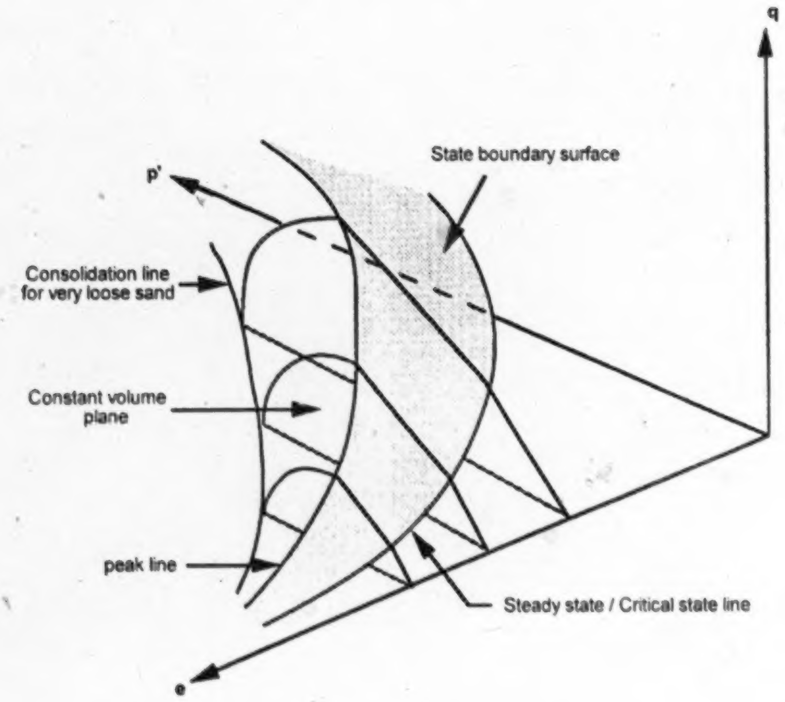
q
State boundary surface
p'
Consolidation line for very loose sand
Constant volume plane
peak line
Steady state / Critical state line
e

Figure 5.2 - A schematic of state boundary surface for very loose sand (modified from Sasitharan 1994).

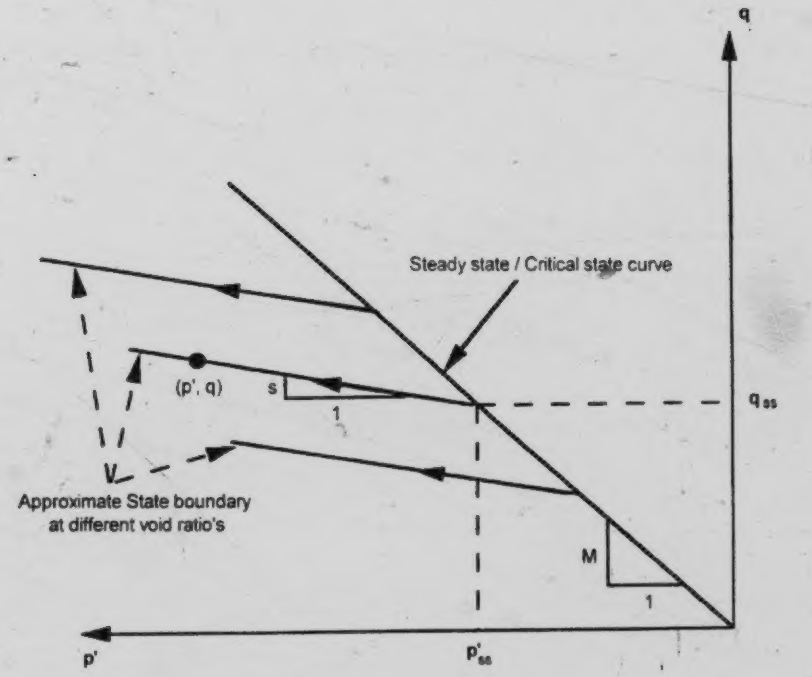
q
Steady state / Critical state curve
(p', q)
s
1
q_ss
Approximate State boundary
at different void ratio's
M
1
p'
p'_ss

Figure 5.3 - Projection of the state boundary surface in deviator stress - effective mean normal stress space (modified from Sasitharan 1994).

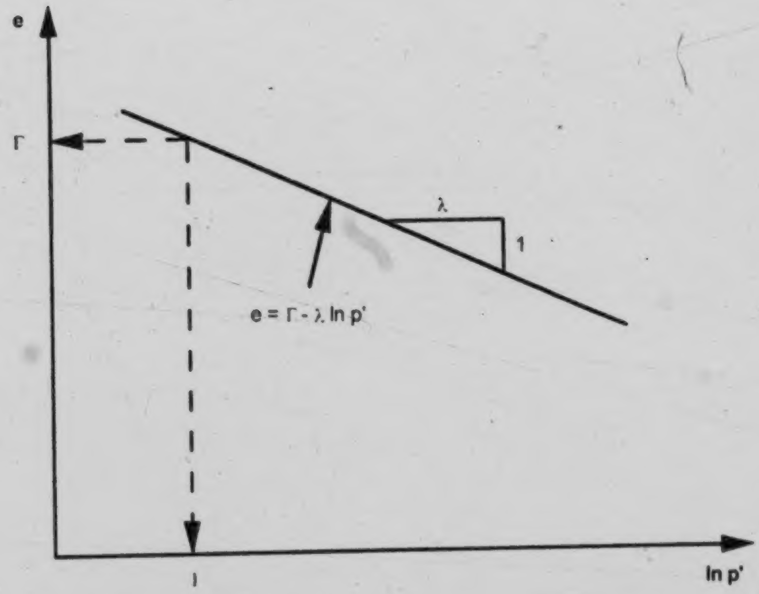
e
Γ
λ
1
e = Γ - λ ln p'
1
ln p'

Figure 5.4 - Projection of the steady state curve in void ratio - effective mean normal stress space (modified from Sasitharan 1994).

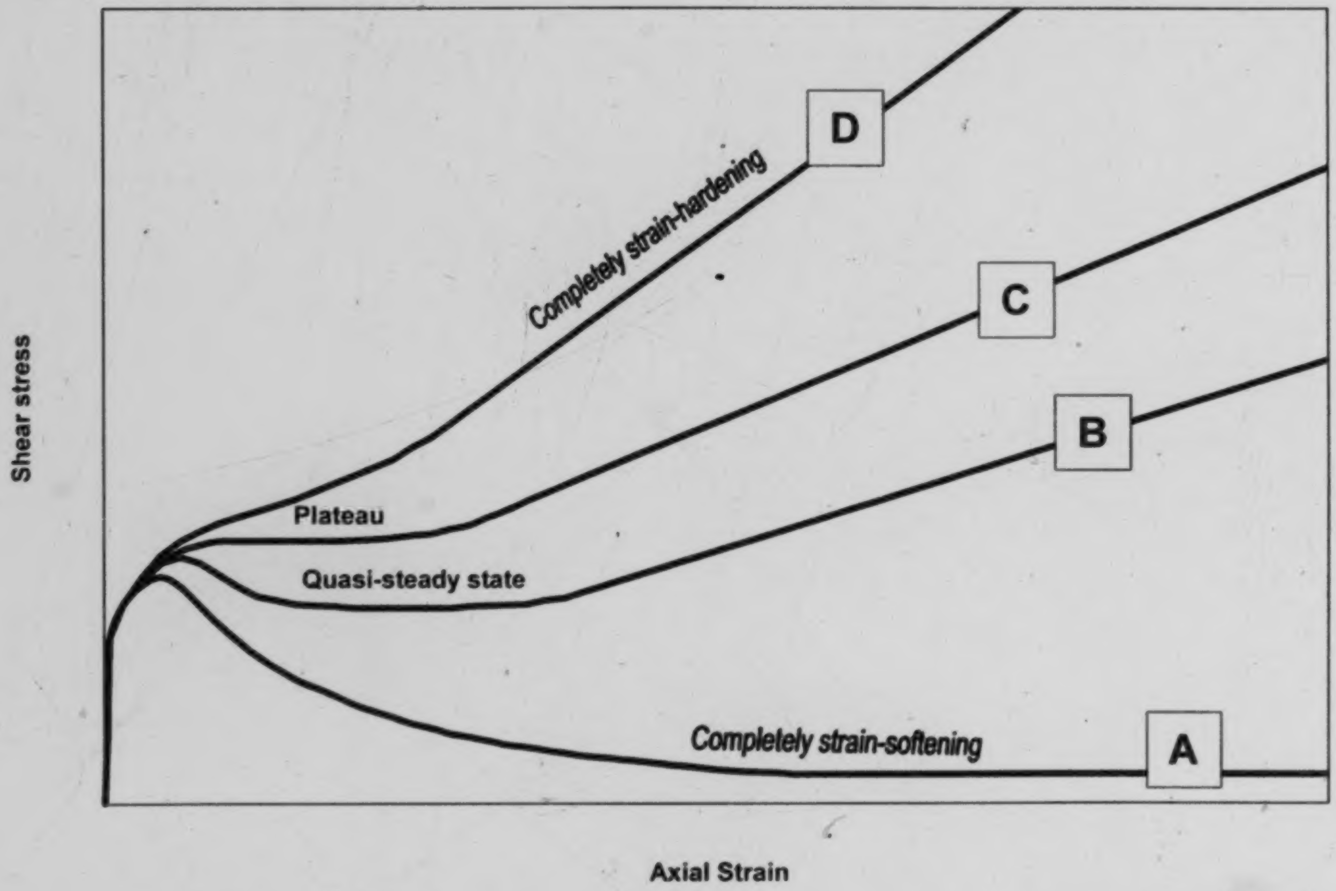

Figure 5.5 - Idealized stress-strain curves showing the possible range of sample responses (after Robertson et al. 1998).

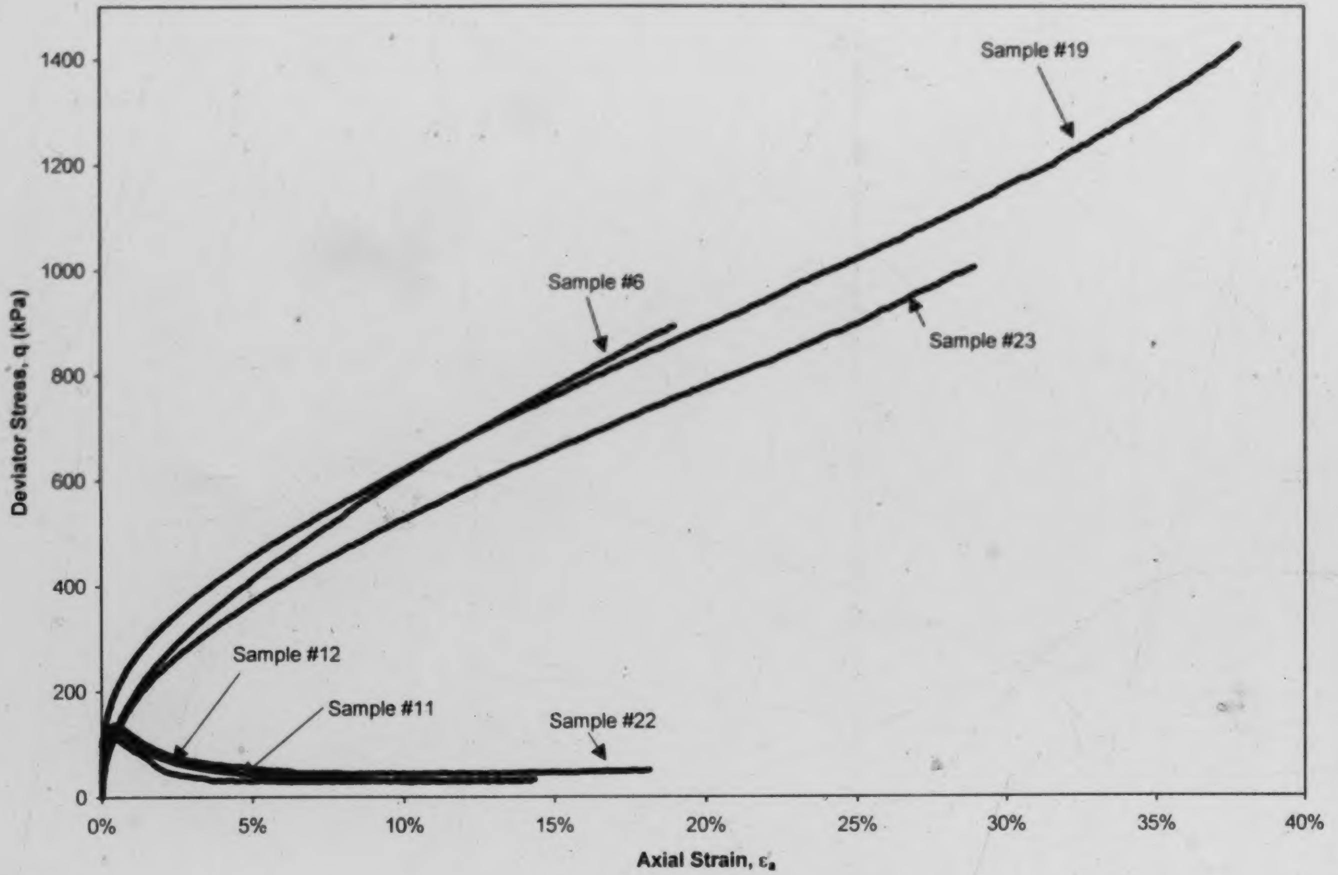

Figure 5.6 - Saturated stress - strain curves.

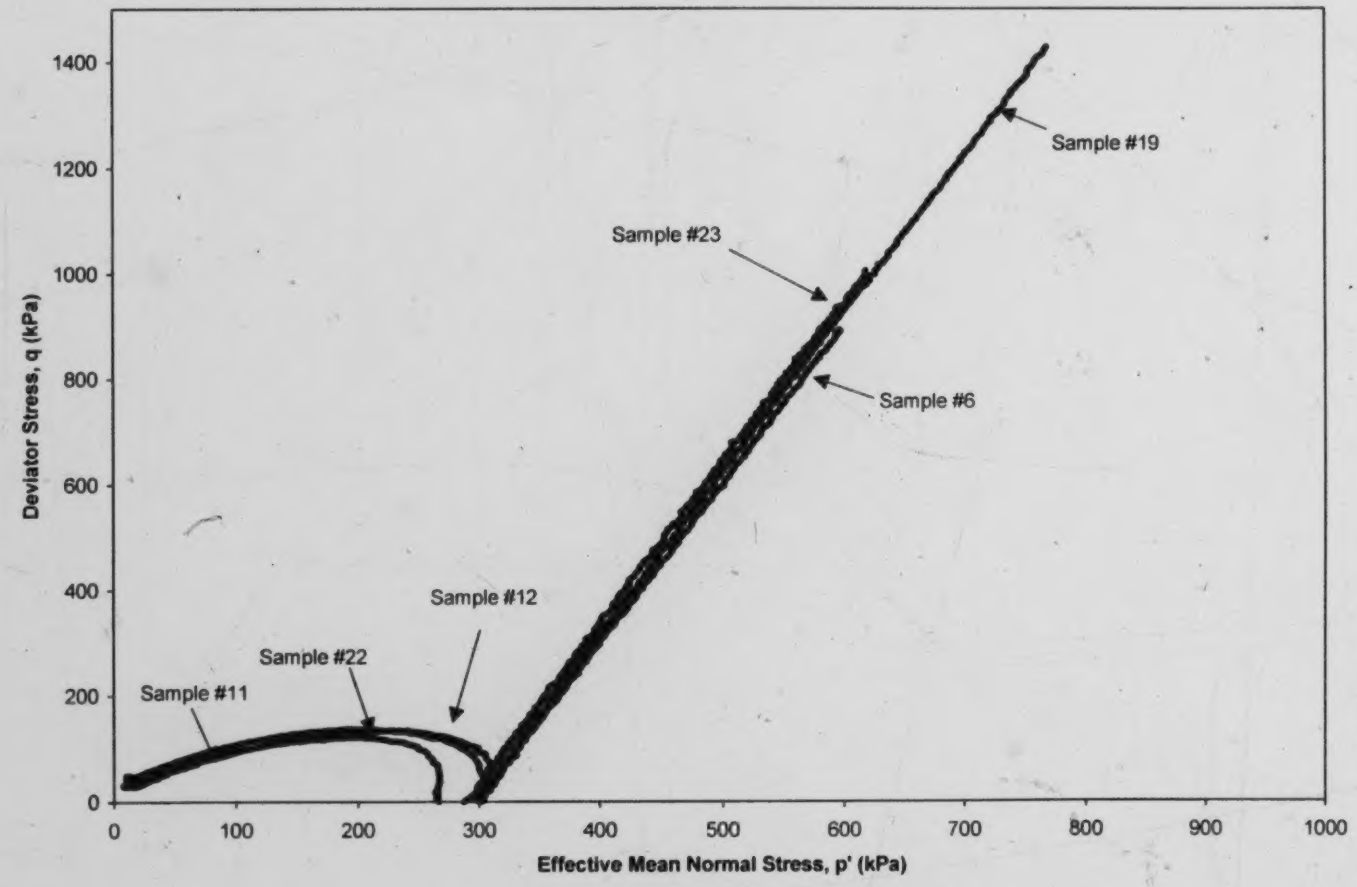

Figure 5.7 - Saturated effective stress paths.

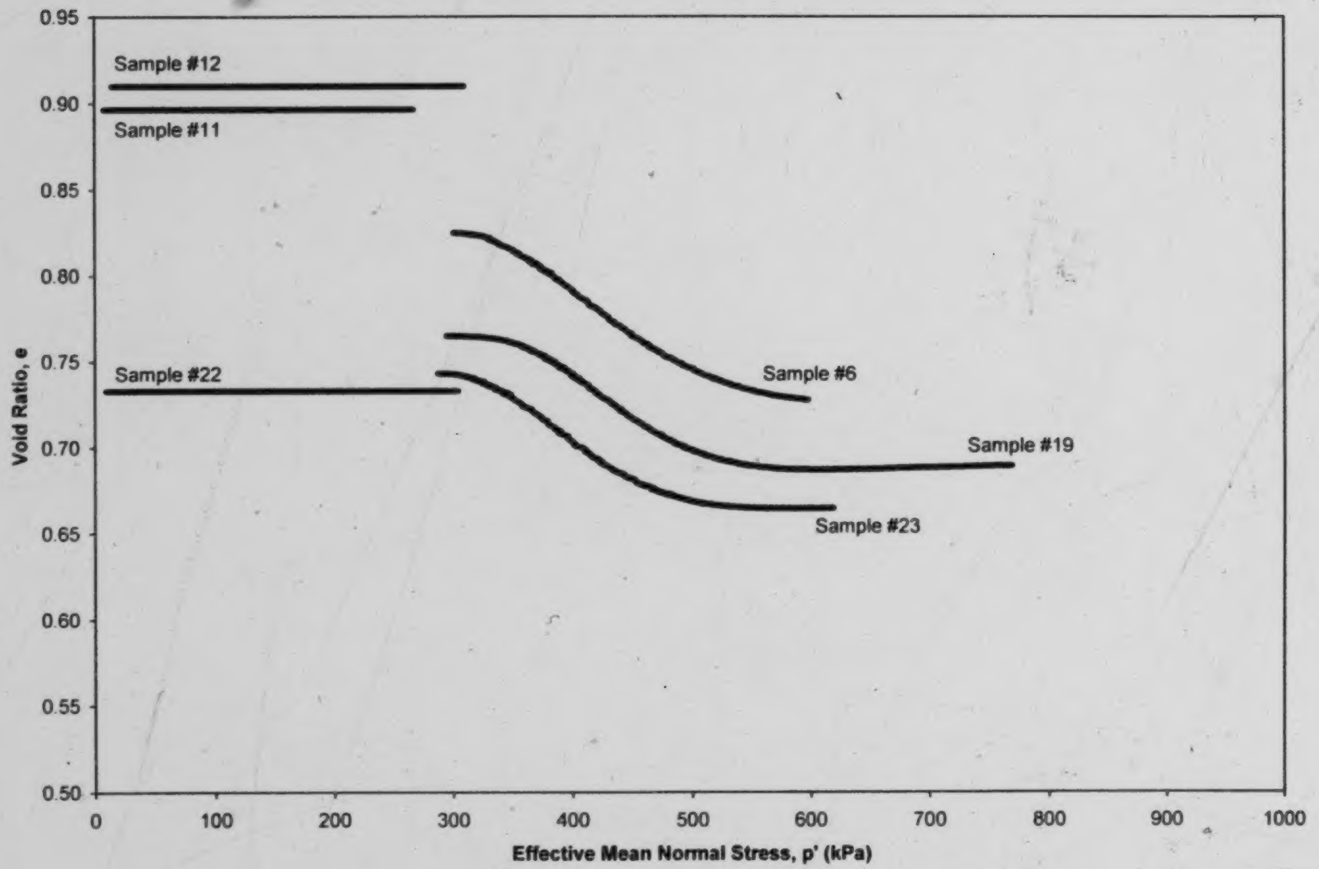

Figure 5.8 - Saturated void ratio versus effective mean normal stress.

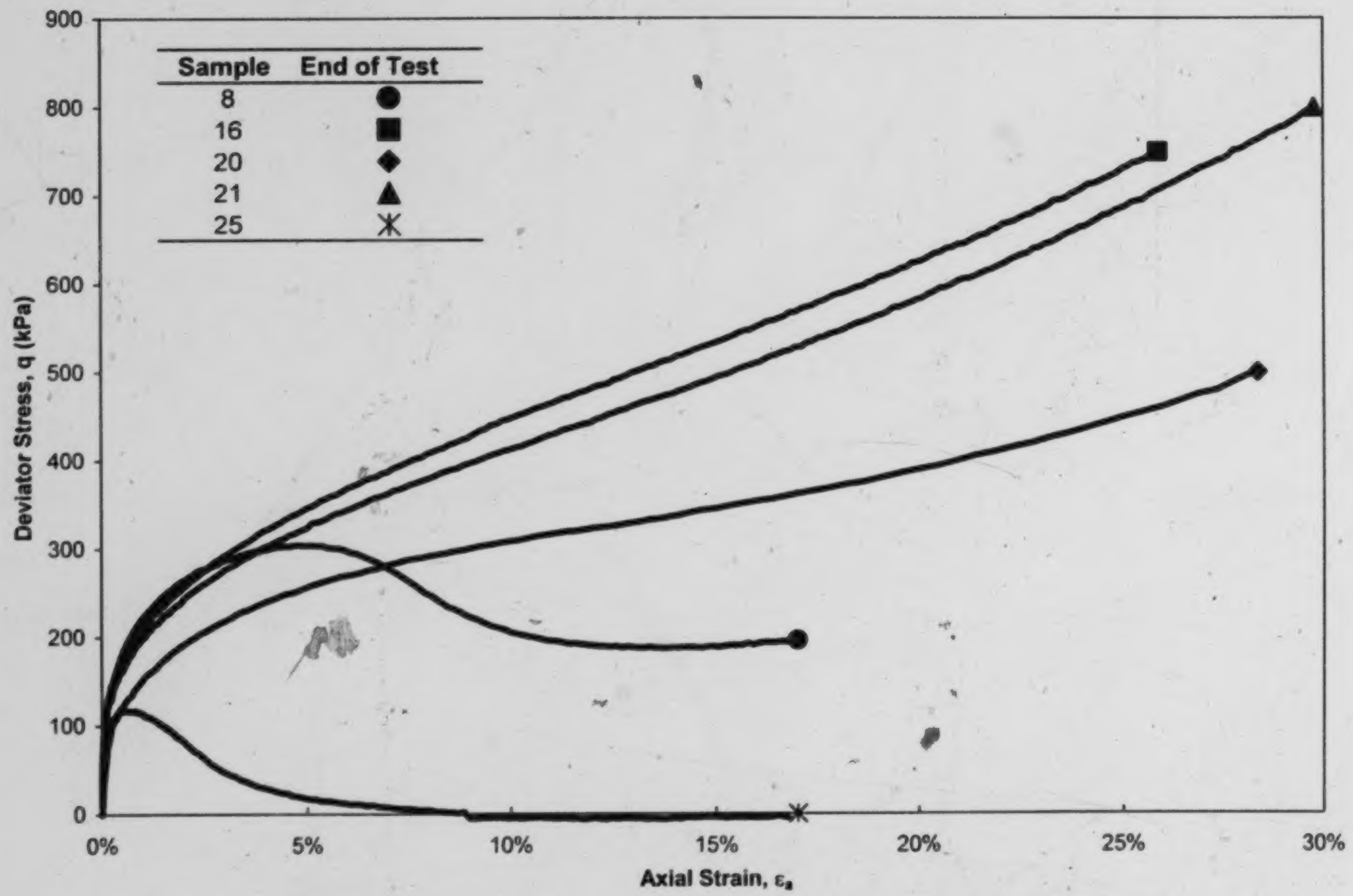

Figure 5.9 – Typical stress - strain curves for five gassy specimens.

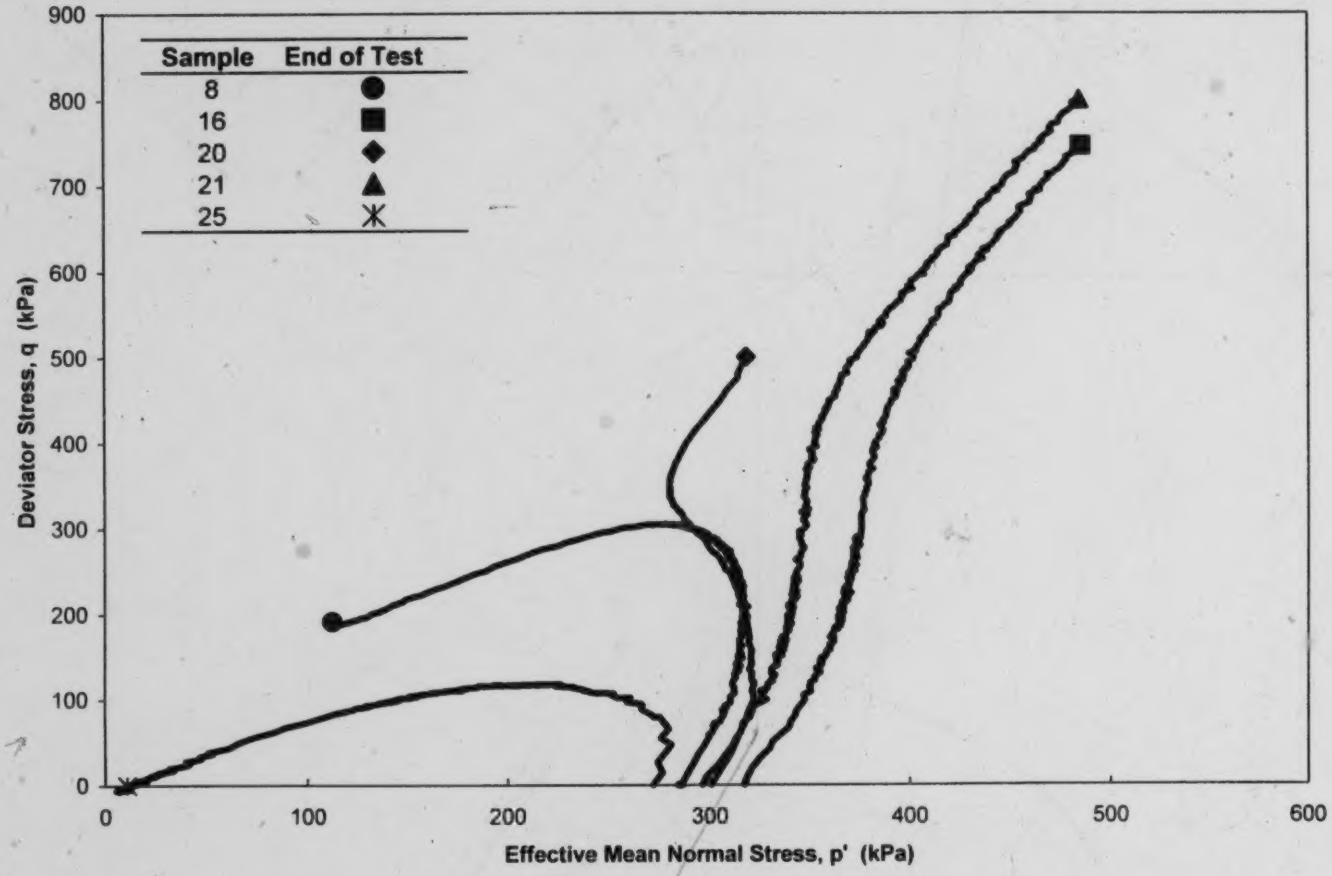

Figure 5.10 - Typical effective stress path for five gassy specimens.

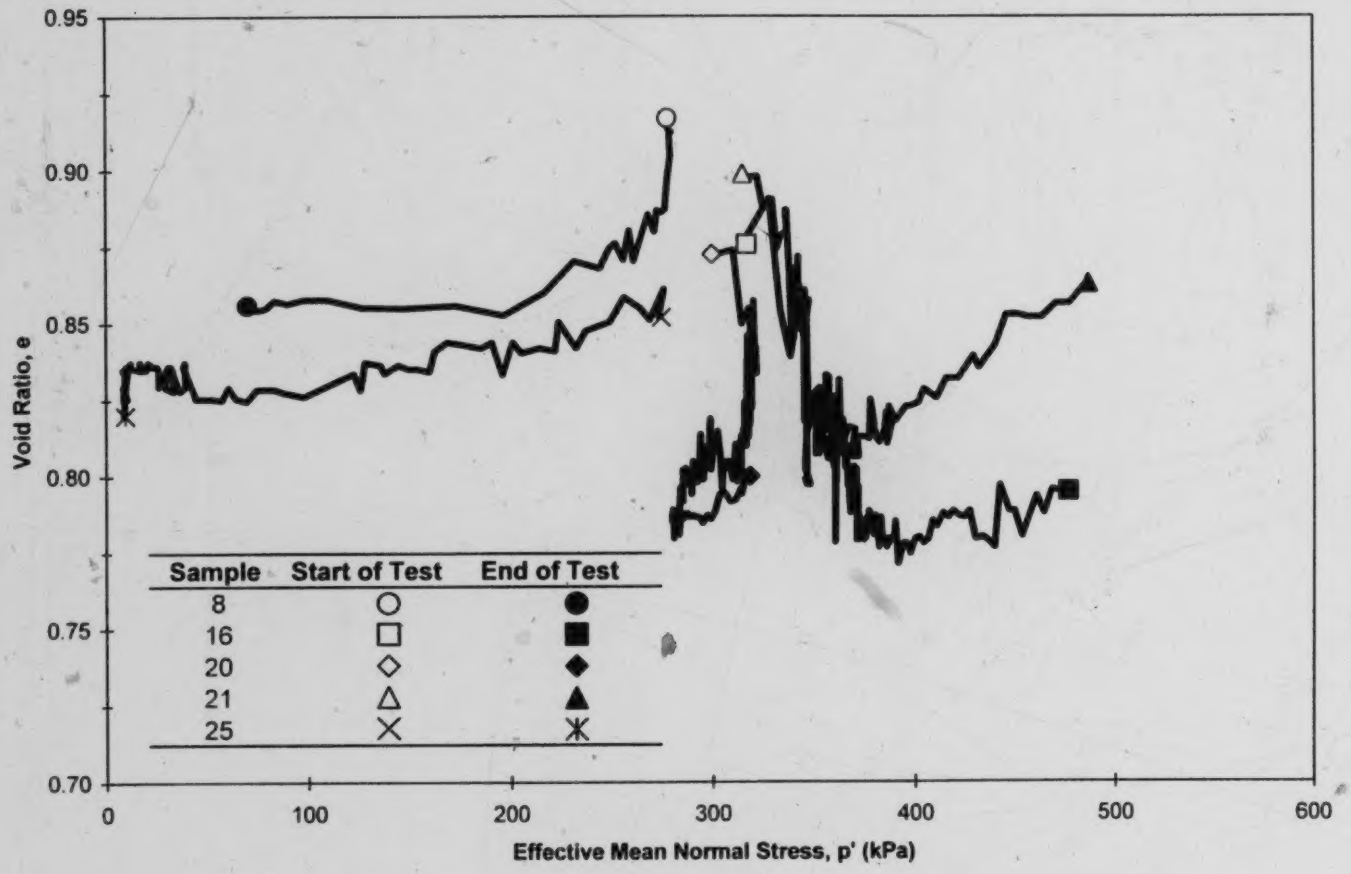

Figure 5.11 - Typical void ratio v[illegible] effective mean normal stress for five gassy specimens.

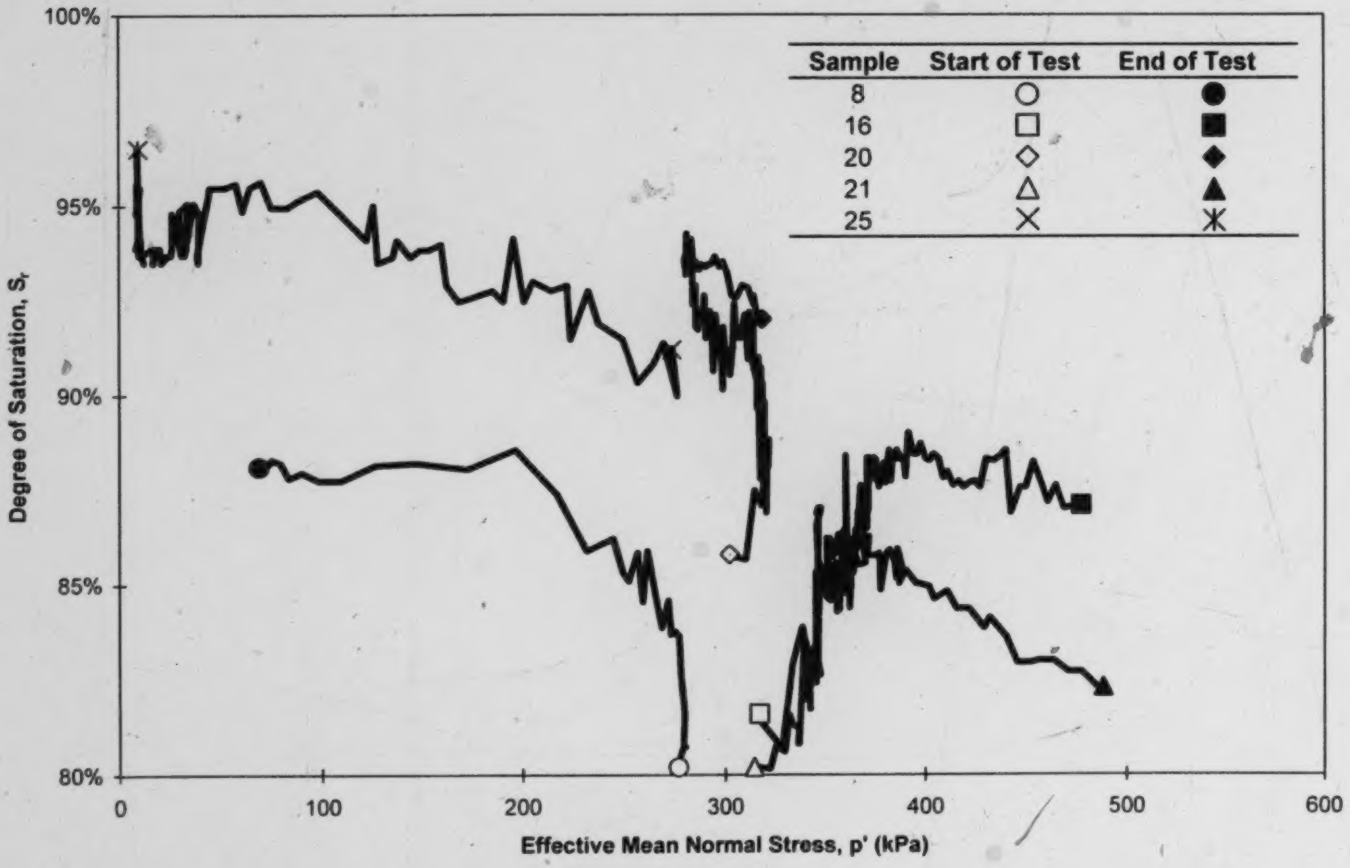

Figure 5.12 - Typical degree of saturation versus effective mean normal stress for five gassy specimens.

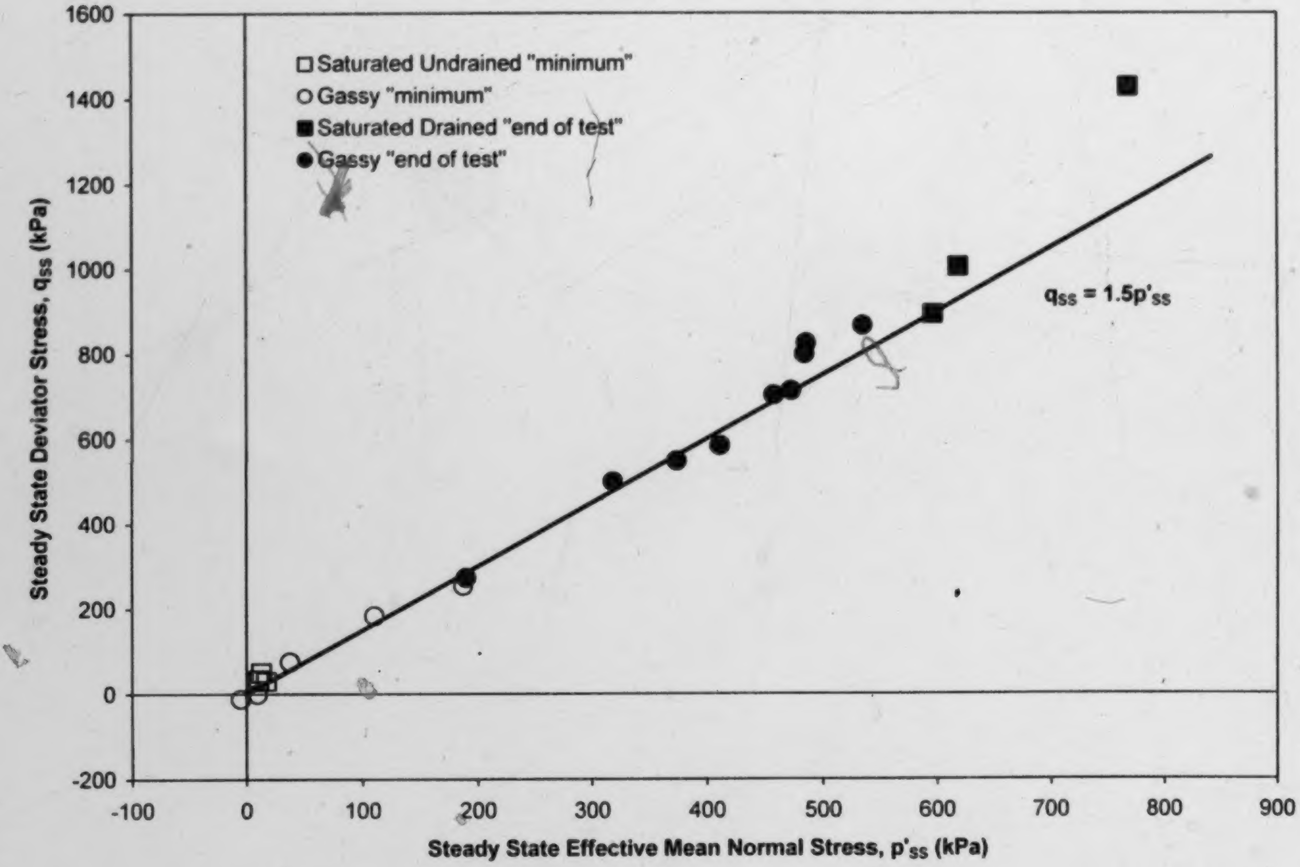

Figure 5.13 - Steady state curve for loose Ottawa sand in deviator stress - effective mean normal stress space.

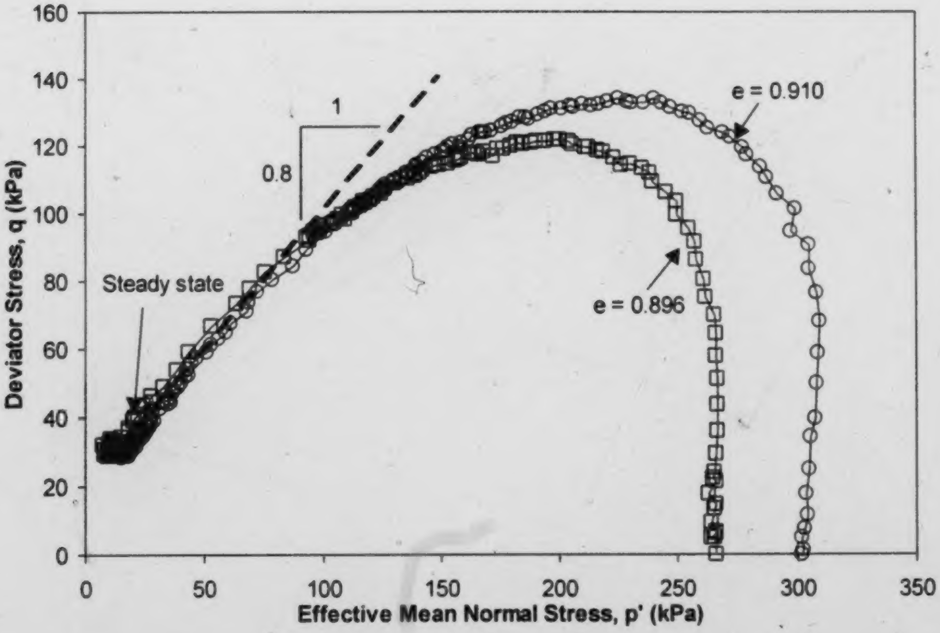

Figure 5.14 – Effective stress paths for two saturated undrained tests with void ratios of 0.90.

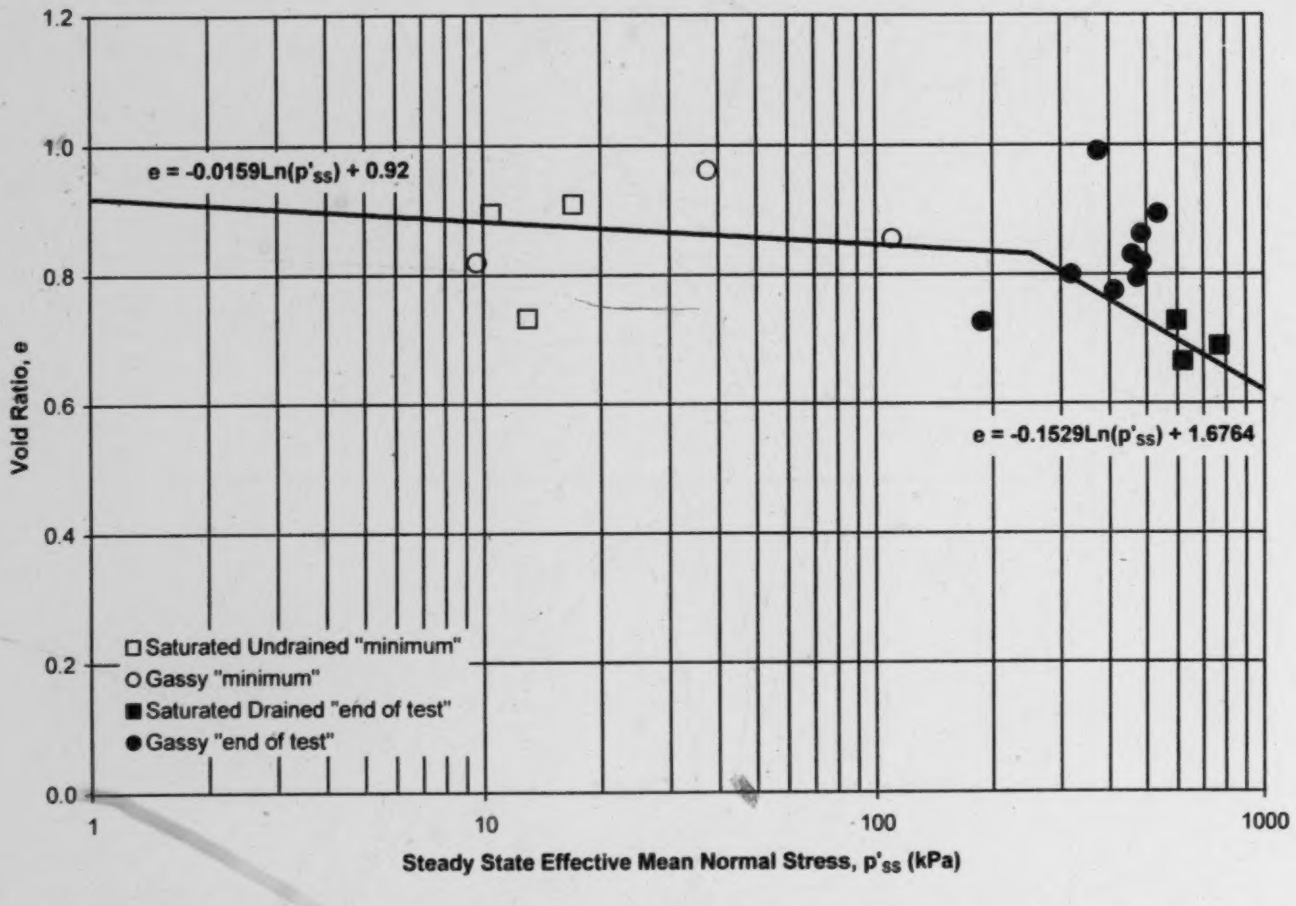

Figure 5.15 - Steady state curve for loose Ottawa sand in void ratio - effective mean normal stress space.

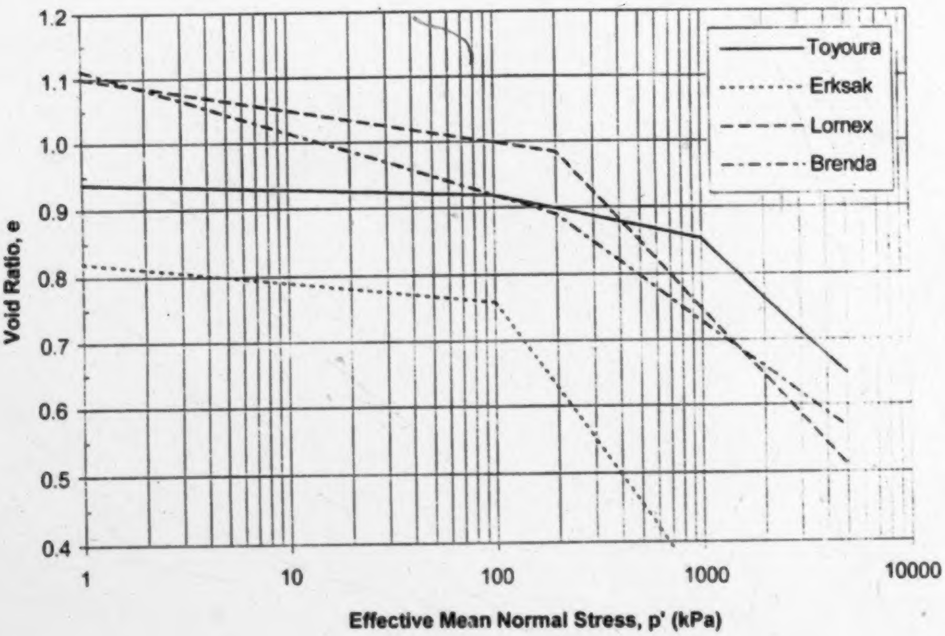

Figure 5.16 - Steady state lines for other sands (based on results tabulated by Sasitharan et al. 1994).

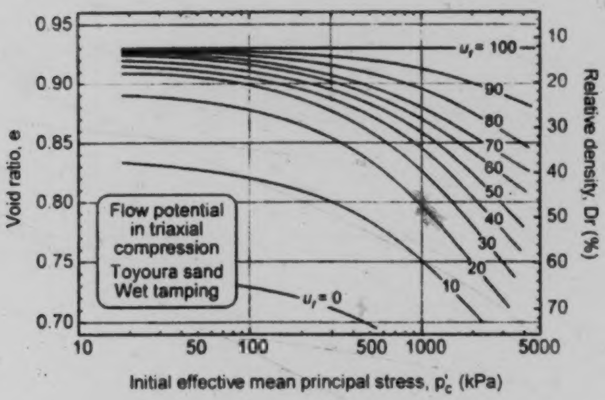

(a) flow potential lines for triaxial compression

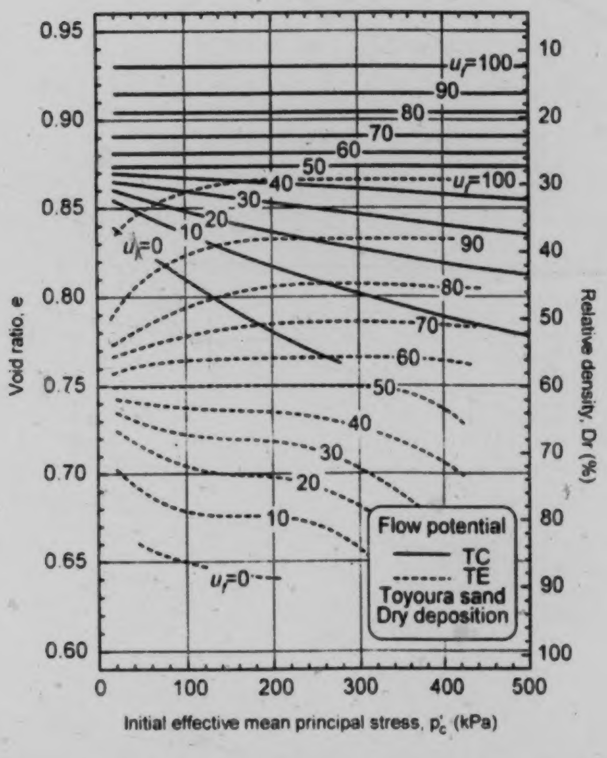

(b) flow potential lines for triaxial compression and extension

Figure 5.17 - Flow potential lines (modified from Yoshimine and Ishihara 1998).

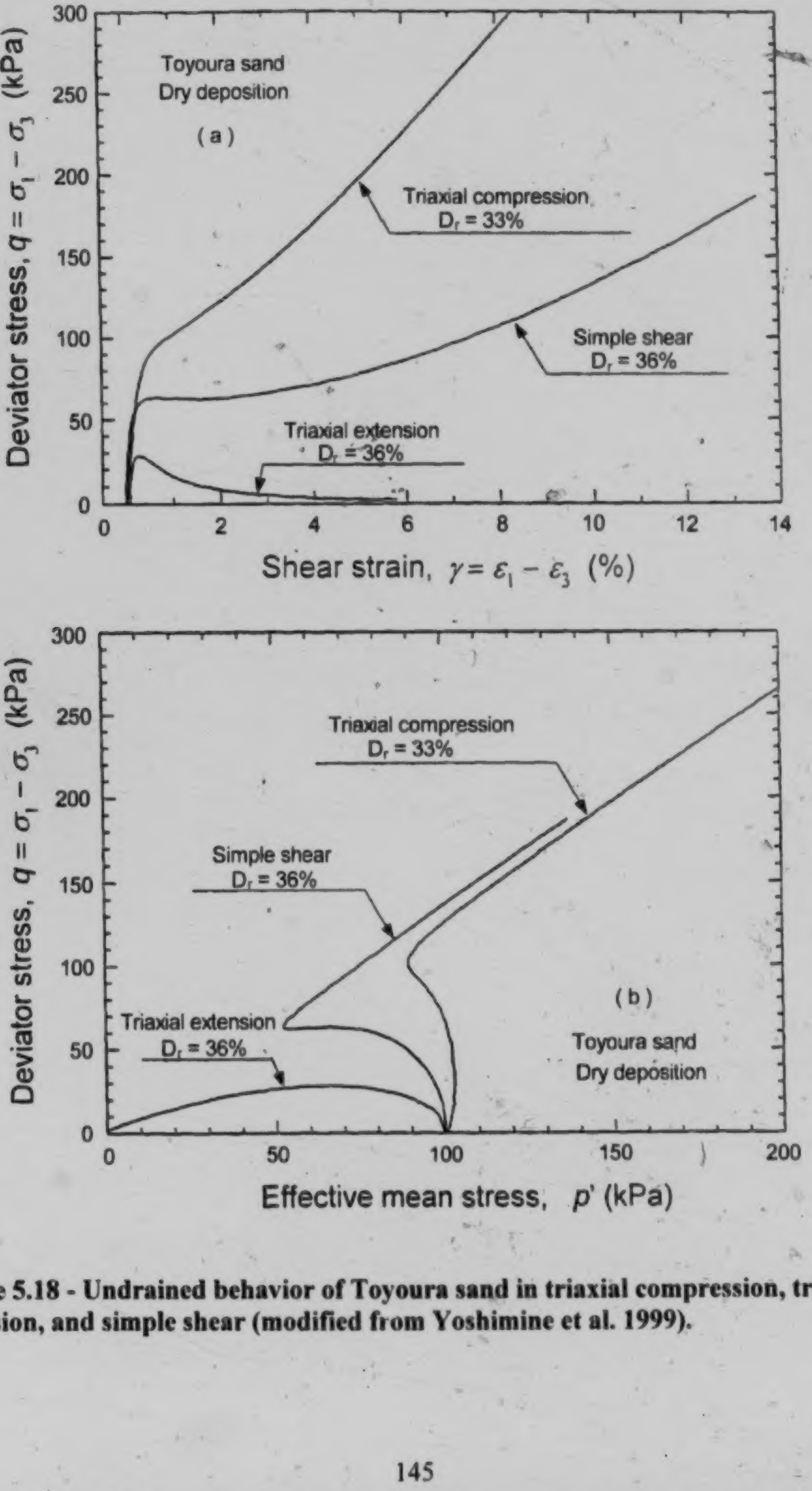

Figure 5.18 - Undrained behavior of Toyoura sand in triaxial compression, triaxial extension, and simple shear (modified from Yoshimine et al. 1999).

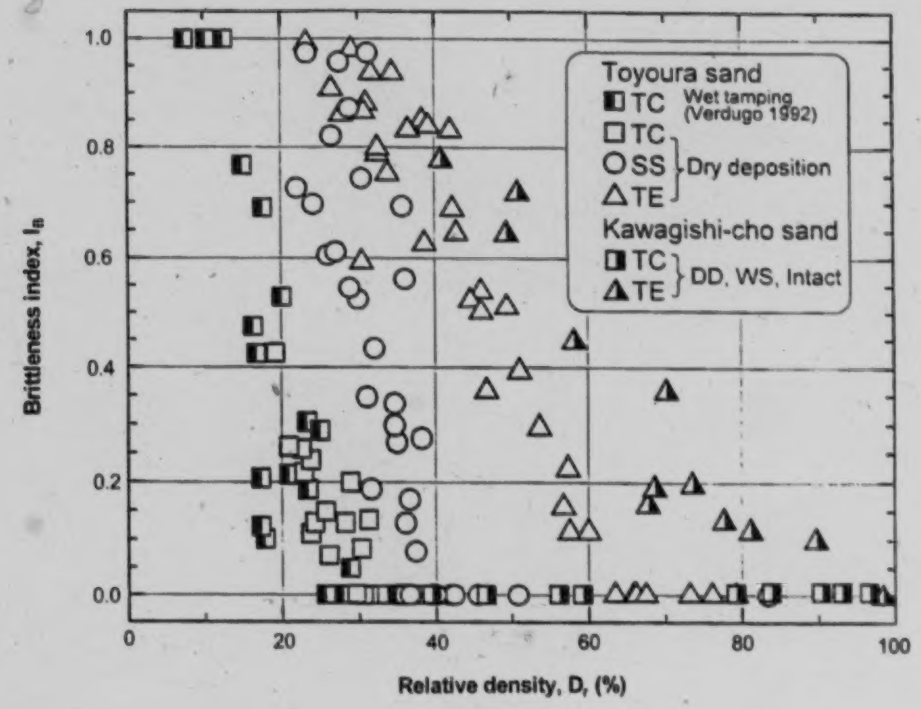

Figure 5.19 - Brittleness index plotted against relative density (modified from Yoshimine et al. 1999).

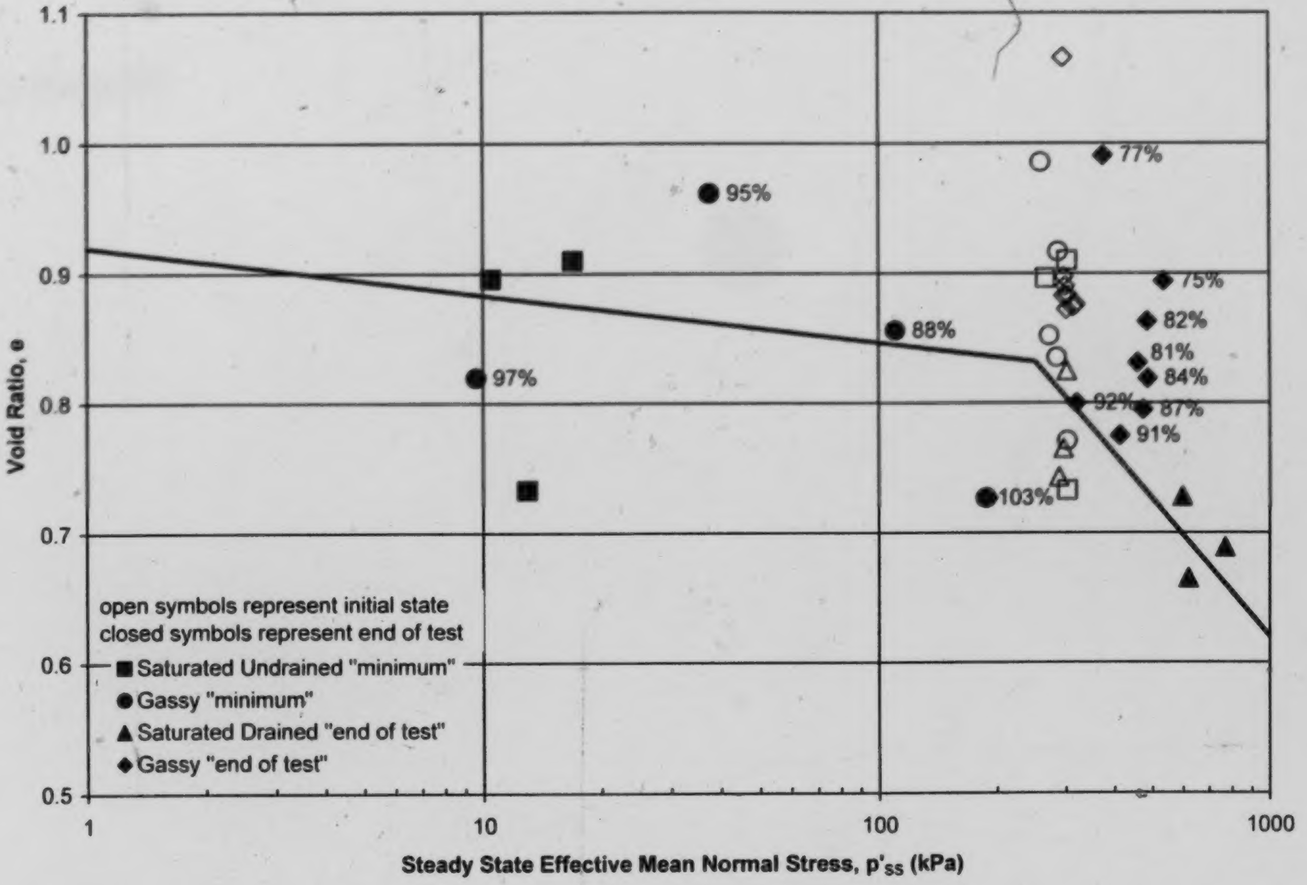

Figure 5.20 – Steady state curve in e - lnp'$_{SS}$ space showing initial and final state and final degree of saturation.

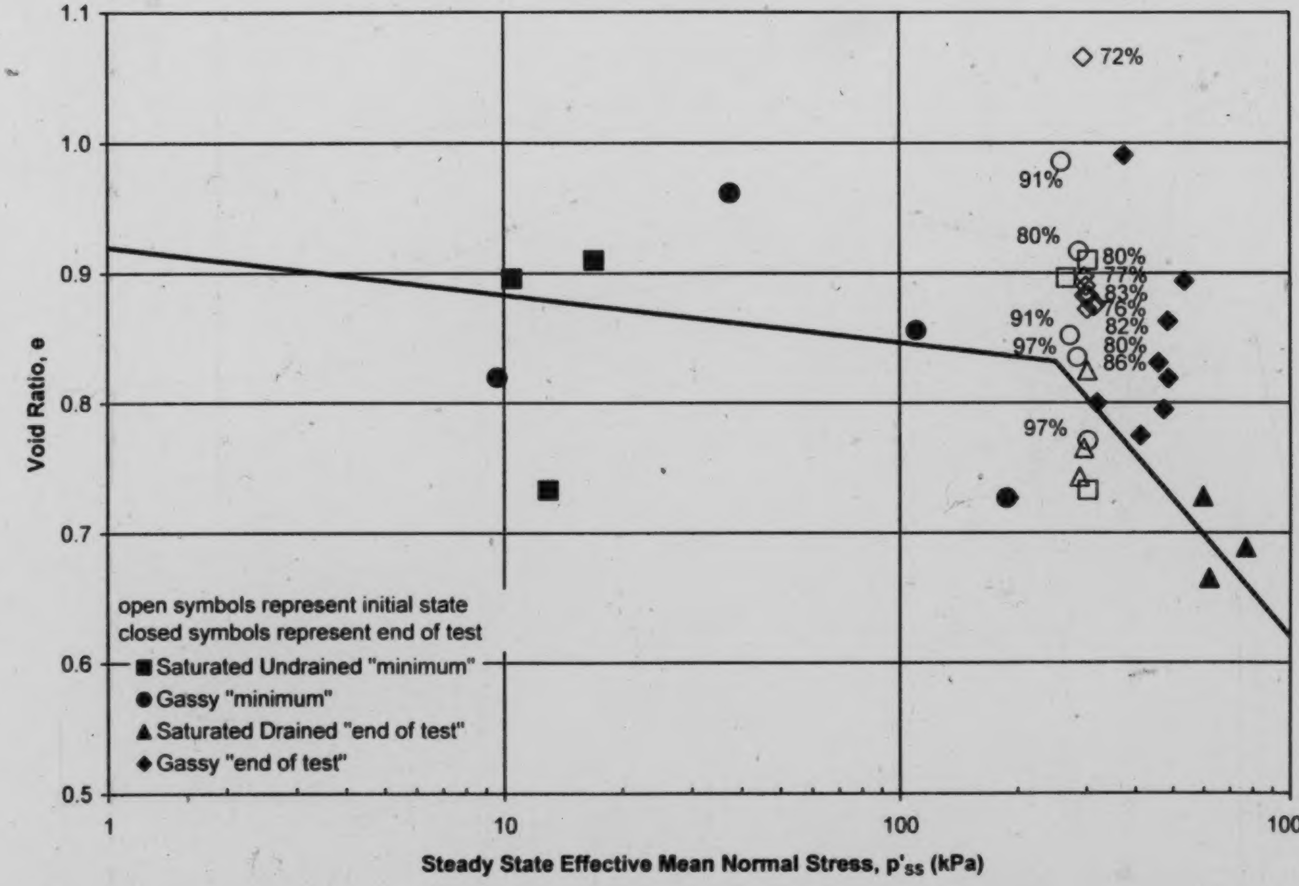

Figure 5.21 - Steady state curve in e - lnp'$_{SS}$ space showing initial and final state and initial degree of saturation.

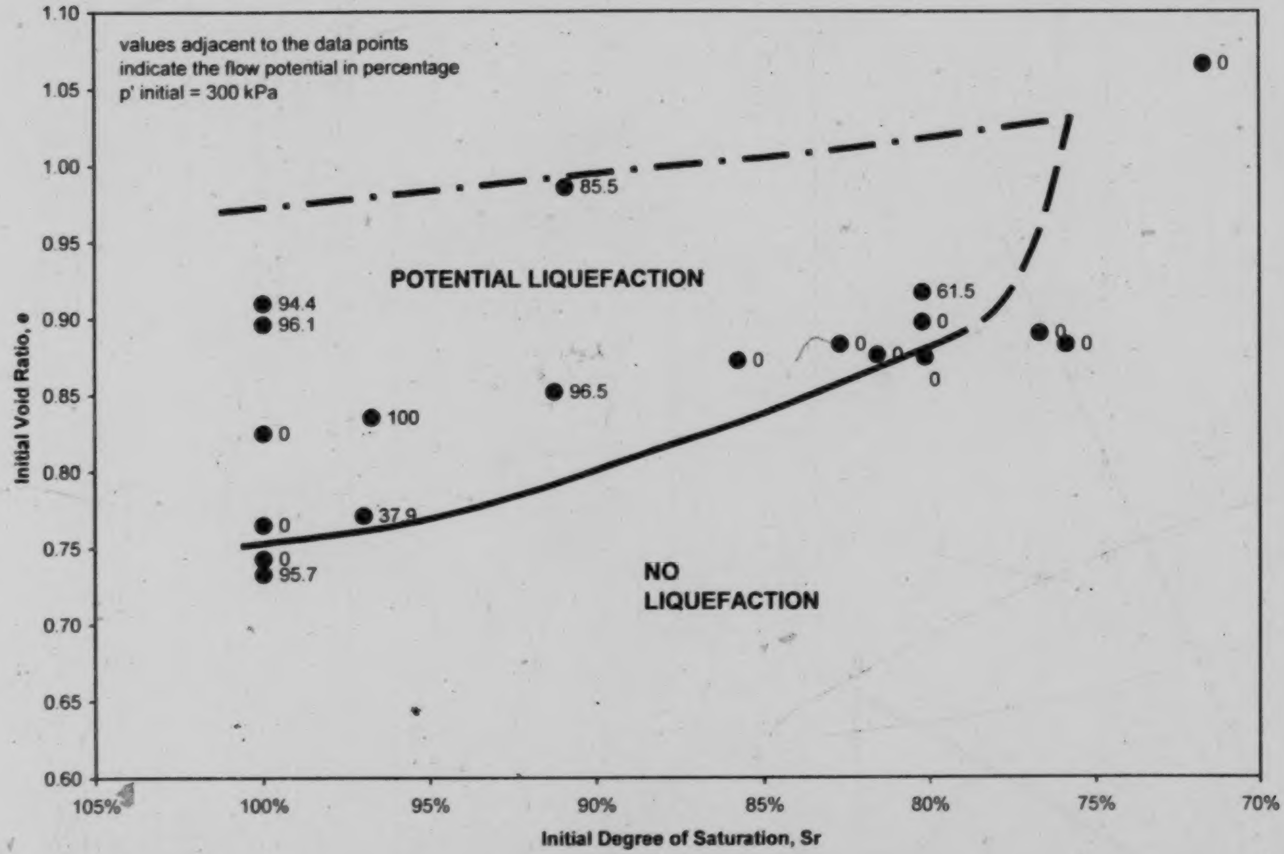

Figure 5.22 - Initial void ratio versus initial degree of saturation with flow potential. Liquefaction zones based on Ottawa sand, triaxial compression loading, moist tamped specimens, and engineering judgement.

CHAPTER 6

CYCLIC TRIAXIAL RESULTS [1,2]

6.1 INTRODUCTION

Cyclic liquefaction is a phenomenon that gives rise to a loss of shearing resistance or to the development of excessive strains due to a repeated disturbance such as an earthquake. Little is know about the behavior of gassy soils subjected to cyclic loading. Using undrained cyclic triaxial tests, the response of gas charged sands subjected to cyclic loading was investigated.

A soil's propensity to liquefy is represented by a cyclic resistance ratio, defined as the cyclic stress ratio to cause liquefaction, or to cause a specified amount of strain. To determine the cyclic resistance ratios, saturated and gassy specimens were tested in the laboratory.

The resistance of a soil to cyclic loading is influenced by the applied shear stress as well as the soil state (void ratio, effective confining pressure, and soil structure) and grain characteristics. In addition, the loading intensity, duration, and frequency will affect the soil's resistance to cyclic loading. In the case of gassy specimens, the resistance to liquefaction will also be influenced by the initial degree of saturation and the gas characteristics.

---

[1] *An abstract for a version of this chapter has been accepted for publication. Grozic, J.L., Robertson, P.K., and Morgenstern, N.R. 1999. The response of loose gassy sand subjected to cyclic loading. Proceedings of 9th International Conference on Soil Dynamics and Earthquake Engineering, August 9-12, 1999, Bergen, Norway.*

[2] *A version of this chapter has been submitted for publication. Grozic, J.L., Robertson, P.K., and Morgenstern, N.R. 1999. Cyclic liquefaction of loose gassy sand. Submitted to the Canadian Geotechnical Journal, May 19, 1999, 39 pages.*

This chapter presents the results from the laboratory program and briefly discusses the factors influencing the resistance to cyclic loading by examining previous research. By maintaining many of the above mentioned variables constant in all the tests, many of the variables were essentially eliminated from the test results. By eliminating some variables, the effects of gas on the resistance of loose sand to cyclic liquefaction could be studied.

The objective of this chapter is to determine the influence of gas on the response of loose Ottawa sand subjected to cyclic loading.

6.2 PREVIOUS RESEARCH

Although previous research on the general topic of gassy soils was detailed in Chapter 2, there are three additional studies, which are relevant to the cyclic response of gassy soils. These are discussed below.

The first study consisted of a series of cyclic laboratory tests on dense gassy sand performed by Rad et al. (1994). Five specimens of dense sand were prepared with methane gas. The initial degrees of saturation ranged from fully saturated (two specimens) to occluded bubbles (one specimen) to interconnected bubbles (two specimens). This corresponds to a range of initial degrees of saturation from 100% to 66%. The laboratory results showed that the greater the amount of gas, the higher the average axial strain, especially in extension. The increased strain in extension was the result of specimens with free gas having less negative pore pressure build up during extension than the saturated specimens. Therefore, the gassy specimens had lower effective stresses. Specimens with gas reached the failure envelope in extension and momentarily experienced high axial strains.

The second study of interest on the cyclic resistance of unsaturated soils was undertaken by Xia and Hu (1991). As noted in Section 2.2, the behavior of unsaturated and gassy soils is different. However, some insight can be gained on the effects of saturation on gassy soils by exploring unsaturated soils. Four sets of unsaturated fine sand specimens were subjected to cyclic triaxial loading. The initial degrees of saturation ranged from 97.8% to 100%. The results of this study showed that as the degree of saturation decreased, the resistance to cyclic liquefaction increased. Xia and Hu proposed that the cyclic resistance ratio increased linearly with decreasing degree of saturation, for range of saturations from 97.8% to 99.5%.

The third study is the CANLEX (CAnadian Liquefaction EXperiment) project. The CANLEX project was a collaborative research project with the objective of "studying the phenomenon of soil liquefaction" (Robertson et al. 1998). The project summary and conclusions are described by Robertson et al. (1998). The project included field and laboratory studies. The aim of one of the laboratory studies was to determine the cyclic resistance of undisturbed sand samples. Samples chosen for testing had in situ degrees of saturation less than 100%, possibly due to the presence of gas. The result of the cyclic testing on these gassy specimens is discussed in Section 6.6.

6.3 CYCLIC RESISTANCE BASED ON LABORATORY TESTING

A cyclic stress ratio is usually used to represent resistance to cyclic loading. The cyclic resistance ratio (*CRR*) is the cyclic stress ratio (*CSR*) that causes liquefaction, or a specified amount of strain. The *CRR* can be determined from laboratory tests, either triaxial tests or simple shear tests. In cyclic triaxial tests, the strain to cause liquefaction is usually specified as 5% double-amplitude axial strain and the *CRR* is defined as the cyclic shear stress divided by two times the effective confining pressure, i.e. $(CRR)_{tx} = \sigma_d/2\sigma'_3$. In simple shear tests the *CRR* is the cyclic shear stress divided by the initial vertical effective stress, i.e. $(CRR)_{SS} = \tau_{cyc}/\sigma'_{vo}$. Robertson and Wride (1998) noted that the triaxial and simple shear tests impose different loading conditions and the resulting *CRR* values are not equivalent. Generally, it is believed that simple shear loading better represents actual earthquake conditions; however, triaxial tests are simpler to perform. Hence, correction factors have been developed to estimate $(CRR)_{SS}$ from the $(CRR)_{tx}$ (Ishihara 1993).

The cyclic resistance ratio can be referenced to 15 cycles of uniform loading, representing an equivalent earthquake of magnitude 7.5, i.e. $CRR_{7.5}$. Based on the work of Seed et al. (1985), laboratory tests can be normalized to a magnitude 7.5 earthquake by multiplying the *CRR* by a correction factor (*1/MSF*). The magnitude scaling factor (*MSF*) is dependent upon the measured number of cycles to failure, *N* (or the equivalent earthquake magnitude, *M*). *M* can be approximated from *N*. Table 6.1 shows the correction factors proposed by Seed et al. (1985). Note that Seed used the term $1/r_m$ in lieu of the term *1/MSF*. Figures 6.1(a) and (b) show the best-fit curves for the *M* and *N* data in Table 6.1, as proposed by Wride and Robertson (1997a). The following equations are obtained from these curves:

$$M = -0.0038N^2 + 0.2442N + 4.7034 \quad \text{(for N<28)} \qquad [6.1]$$

and

$$M = 1.3831\ln(N) + 3.7876 \text{ (for N>28).} \qquad [6.2]$$

In the 1996 NCEER workshop (Youd and Idriss 1998) the most commonly used magnitude scaling factors were reviewed and guidelines for their use recommended. Tokimatsu and Yoshimi (1983) also suggested that the *MSF* could be approximated by the following equation:

$$MSF = \frac{0.65}{0.1(M-1)} \qquad [6.3]$$

For simplicity, this thesis has adopted the above procedure by Tokimatsu and Yoshimi for normalizing the *CRR*.

Using Equations [6.1], [6.2], and [6.3], the *CRR* applied in the laboratory was corrected to an equivalent *CRR* at N=15 cycles.

6.4 LABORATORY RESULTS

Undrained cyclic triaxial testing was performed on loose specimens of gassy Ottawa sand. Twenty saturated and gassy specimens were tested. All the specimens were consolidated to approximately the same mean normal effective pressure (p') of 300 kPa, for comparison.

6.4.1 Saturated Specimen Results

Five saturated specimens were subjected to cyclic loading. The results of the saturated tests are summarized in Table 6.2. In addition, the test results of each specimen are presented in Appendix B.

All the saturated specimens were tested undrained. During the undrained tests, no pore fluid was allowed to enter or leave the specimen. The pore pressures that developed were closely monitored.

The void ratios at the beginning of shear ranged from 0.736 to 0.706, which corresponds to relative densities of 26% to 36%. These specimens are classified as loose. The initial confining pressure of all the specimens was very close to 300 kPa. The applied deviatoric stress ranged from 55 to 60 kPa.

A typical saturated test result is shown in Figure 6.2. When subjected to cyclic loading, the saturated specimens developed pore pressure, which resulted in a decrease in the effective confining pressure. Very little axial strain developed before failure. All specimens reached approximately zero effective confining pressure and experienced stress reversal. Failure occurred suddenly, therefore, it is classified as cyclic liquefaction according to the definitions presented in Section 1.3.1. The number of cycles to failure ranged from 1 to 38. The cyclic resistance ratios $(CRR)_{tx}$ varied from 0.085 to 0.101, which corresponds to normalized cyclic resistance ratios $(CRR_{7.5})_{SS}$ of 0.070 to 0.082.

6.4.2 Gassy Specimen Results

Cyclic triaxial testing was also performed on specimens of loose gassy sand. Ten gassy specimens were subjected to undrained cyclic loading. The results of these tests are summarized in Table 6.2. Individual specimen results are also presented in Appendix B.

All the gassy specimens were tested undrained. No pore fluid was allowed to enter or exit the specimen during loading and the pore pressures were monitored. During undrained testing, the saturated specimens experienced no change in volume, while the gassy specimens experienced volume change. The volume change experienced by the gassy specimens was caused by the compressibility and the solution and exsolution of the gas in the pores.

All specimens were consolidated to approximately 300 kPa. The void ratios at the beginning of shear ranged from 0.789 to 0.674, which corresponds to relative densities of 10% to 46%. The specimens were loose to very loose. Initial degrees of saturation varied from 76% to 100%. The applied deviator load ranged from 70 to 158 kPa.

A typical gassy test result is shown in Figure 6.3. In the gassy specimens, the pore pressures either built up very rapidly, and failure occurred within about four cycles, or the pore pressures remained approximately constant, and failure did not occur. A small amount of extensive axial straining usually occurred before failure in the gassy specimens. All gassy specimens reached approximately zero effective confining pressure and experienced stress reversal. This failure is classified as cyclic liquefaction.

The gassy specimens failed in 1 to 4 cycles with cyclic resistance ratios $(CRR)_{tx}$ varying from 0.118 to 0.299. The corresponding normalized cyclic resistance ratios $(CRR_{7.5})_{SS}$ varied from 0.055 to 0.135. Although all specimens were tested undrained, the presence of gas in the pore fluid resulted in the void ratio and degree of saturation changing throughout the test. The void ratio decreased during loading and the final void ratios varied from 0.725 to 0.608. The degree of saturations increased during loading and the final saturation varied from 81% to 100%.

A few of the gassy specimens were initial subjected to an applied deviatoric stress that did not cause failure. When it became apparent that liquefaction would not occur (i.e. the pore pressures were no longer increasing), then the test was stopped and a greater load was applied. Before testing the specimen under a larger deviatoric stress, the initial conditions were re-recorded. The deviatoric stress was incrementally increased until liquefaction occurred. When failure finally did occur, it happened within 1 to 3 cycles. The results of these tests are presented in detail in Appendix C.

Figure 6.4 illustrates the difference in response between a gassy and a saturated specimen. Figure 6.4(a) shows the stress path of a gassy specimen subjected to a deviatoric stress of 70 kPa. The gassy specimen was cycled 49 times without any significant build up of pore pressure. Figure 6.4(b) shows the stress path of a saturated specimen subjected to a slightly lower deviatoric stress of 60 kPa. In contrast to the gassy specimen, pore pressures began building immediately and the mean normal effective stress decreased until failure occurred at 27 cycles. The gassy specimen was subjected to greater deviatoric loads and finally failed under an applied load of 140 kPa (Figure 6.4(c)). The failure occurred within one cycle and could be classified as a monotonic failure.

6.5 CYCLIC LIQUEFACTION OF GASSY OTTAWA SAND

The resistance of a soil to cyclic loading is influenced by the applied shear stress as well as the soil state (void ratio, effective confining pressure, and soil structure) and grain characteristics. In addition to soil state and grain characteristics, the soil resistance to cyclic loading will be affected by the loading intensity, duration, and frequency. In the case of gassy specimens, the resistance to liquefaction will also be affected by the initial degree of saturation as well as the gas characteristics.

6.5.1 Effect of Initial Confining Stress

The effect of the initial confining stress on the cyclic resistance was investigated by Thomas (1992). The results of this study are summarized in Figure 6.5, a plot of cyclic resistance ratio versus the effective confining stress at a fixed number of cycles to liquefaction ($N = 10$). His work showed that the effective confining stress had very little influence on the response of loose specimens. However, for dense specimens, the cyclic stress ratio required for liquefaction, at a fixed number of cycles, decreased with increasing effective confining stress. The rate of decrease increased with increasing density. In other words, the confining stress had a greater affect on liquefaction resistance of dense specimens. The results obtained by Thomas (1992) are consistent with the results of an earlier study performed by Seed and Harder (1990). Seed and Harder found that increasing the confining stress decreased the resistance to cyclic liquefaction, for medium to dense specimens with the same relative density.

In this program, the effective confining stress was maintained at approximately 300 kPa for all specimens to allow for the investigation of the influence of degree of saturation on cyclic liquefaction.

6.5.2 Effect of Density

Relative density affects the resistance of soil to cyclic loading. Tatsuoka at al. (1982) summarized a number of cyclic test results to develop a relationship between the cyclic undrained strength and the relative density (Figure 6.6(a)). Figure 6.6(a) shows that as the relative density increases, the resistance to cyclic liquefaction also increases. Stated another way, if the tests are normalized to a specified number of cycles to liquefaction, say 10 cycles, then a larger stress ratio (or load) is required to cause the denser specimens to liquefy (Figure 6.6(b)).

The effects of density on the cyclic resistance of Toyoura sand was also studied by Toki et al. (1986) by using the results of a cooperative test program. The cooperative test program involved five laboratories that all prepared both loose and dense specimens of Toyoura sand by the same specimen preparation method (air-pluviation). The results of the study are presented in Figures 6.7 and 6.8. Toki et al. (1986) noted that for dense specimens, the relationship between the cyclic resistance ratio (*CRR*) and number of cycles (*N*) depended strongly on the strain value for which failure was defined. This was not the case for loose specimens. Also, the shape of the curve was different for loose and dense specimens, with the difference being more pronounced when the failure was defined for a larger strain value (note the differences between Figure 6.7(b) and Figure 6.8(b)). Toki explained the difference as different degrees of volume expansion, due to shear straining or dilatancy, between the loose and dense specimens.

The effect of density on the cyclic resistance of Fraser River sand was studied by Thomas (1992). The results of this study are presented in Figure 6.9, a plot of the cyclic stress ratio to cause liquefaction in 10 cycles versus relative density. This plot confirms the results of the previously mentioned studies; as relative density increases, the resistance to cyclic liquefaction also increases.

In this research, the range of initial relative densities was very small. All specimens were prepared loose. By only preparing loose specimens, the effects of degree of saturation were more pronounced.

6.5.3 Effect of Soil Structure

Soil structure includes fabric, age, and cementation. In laboratory testing of reconstituted specimens, soil fabric is manifested by the preparation method. The effect of the specimen preparation method on the cyclic resistance is discussed in Section 4.2.7. In undrained cyclic triaxial loading, specimens prepared by the water pluviation method are generally weaker than those prepared by the air pluviation method; likewise specimens prepared by air pluviation are generally weaker than specimens prepared by the moist tamping method (Silver et al. 1980, Miura and Toki 1982, Tatsuoka et al. 1986).

In field situations, the soil structure will include fabric, age, and cementation. All these variables will affect the liquefaction potential of the soil mass under consideration.

6.5.4 Effect of Grain Characteristics

Grain characteristics include features such as grain-size distribution, grain shape, and mineralogy. Ishibashi (1985) studied the effect of grain characteristics on the liquefaction potential of sand. He found that the cyclic resistance ratio could vary by as much as 200 percent because of changes in the grain characteristics. The study demonstrated that even slight variations in grain characteristics could account for large changes in cyclic resistance ratio.

When a sandy soil has fine grains or contains some fine particles, some cohesion can develop between the fine particles. In general, a greater resistance to cyclic liquefaction is exhibited by sandy soils that contain some fines (Robertson and Wride 1998). Ishihara (1993) noted that the increase in resistance is a function of the nature of the fines contained in the sand. Using a series of laboratory tests, Ishihara and Koseki (1989) demonstrated that one of the most important index properties influencing the cyclic resistance was the plasticity index of the fines. As the plasticity index increased, the resistance to cyclic liquefaction increased (Ishihara 1993).

In this study, Ottawa sand graded to CT-109A specifications, containing no fines, was used in the preparation of all specimens.

6.5.5 Effect of Loading Intensity, Duration, and Frequency

In addition to soil state and grain characteristics, the loading intensity, duration, and frequency will affect the soil's resistance to cyclic loading. Tatsuoka et al. (1986) summarized the results of a cooperative test program on the cyclic strength of Toyoura sand and found that the effect of loading frequency, between 0.05 Hz and 1.0 Hz, on the cyclic strength was minimal. The effect of frequency on the results of simple shear tests was found to be minimal by Peacock and Seed (1968). Yoshimi and Oh-oka (1975) also found that the results of ring shear tests were not affected by frequency. In this study, all cyclic tests were performed at similar frequencies.

The effects of loading intensity and duration are represented by the cyclic resistance ratio and number of cycles to failure, respectively.

6.5.6 Effect of Gas

The study performed by Xia and Hu (1991) on unsaturated soils showed that the resistance to liquefaction increased when the degree of saturation decreased. The purpose of the program described in this chapter was to determine the effect of gas on the cyclic resistance of loose gassy sands. This effect was investigated by analyzing the laboratory results.

The results of the cyclic tests are presented in Figure 6.10, a plot of the cyclic resistance ratio $(CRR)_{tx}$ versus the number of cycles to failure. The initial degree of saturation is indicated adjacent to each gassy test result. This figure reveals that the cyclic resistance was greatly increased by the addition of gas. The lower the initial degree of saturation (i.e. the higher the gas content), the higher the cyclic resistance. The increase in cyclic resistance was in the order of 200% to 300%.

The cyclic resistance ratio obtained from the triaxial results was normalized to an equivalent simple shear result for a magnitude 7.5 earthquake, as described in Section 6.3. The normalized cyclic resistance ratio $(CRR_{7.5})_{SS}$ is plotted against the initial degree of saturation in Figure 6.11. From this plot, it is apparent that as the degree of saturation decreased, the $(CRR_{7.5})_{SS}$ increased. The value of initial void ratio is indicated beside each data point. The initial densities of the specimens were consistently loose to medium dense, with little variation; hence, the results showed limited dependence on density. However, it would be expected that as the density increased the resistance to cyclic loading would also increase.

Figure 6.12 presents the cyclic resistance ratio $(CRR_{7.5})_{SS}$ versus relative density. For reference, the limiting line, or peak cyclic pore pressure ratio = 100%, for N=15 from Seed et al. (1985) is also shown on this figure. The initial observation from this diagram is that the saturated specimens plotted very close to the reference line. This suggests that the cyclic resistance ratio of saturated specimens of this sand could be reasonably approximated using the limiting line developed by Seed et al. (1985). However, it should be noted that the limiting line proposed by Seed was developed based on field observations and is not linked directly to laboratory data. The second observation is that the density of the gassy specimens increased during cyclic loading while the density of the saturated specimens remained constant. For the gassy specimens, the initial densities (shown as filled circles) were generally located to the left of the limiting line, while the final densities (shown as shaded circles) plotted close to the limiting line. The increase in density of a gassy specimen towards the limiting line indicates that it might be possible to predict the increase in cyclic resistance of a gassy specimen from its corresponding change in density.

In order to understand how the degree of saturation affects resistance to cyclic loading, the change in relative density versus initial degree of saturation is shown in Figure 6.13. This relationship can be approximated as a linear function with the following simplified expression:

$$\Delta D_r = -0.98S_r + 0.98. \qquad [6.4]$$

Although there is significant scatter in the data, the proposed equation fits the data within the boundaries of this problem. As the degree of saturation decreases, there is a greater change in the relative density during loading. The above approximation is for loose specimens only; for dense specimens, little change in density would be expected regardless of the initial degree of saturation. The most general representation would include a family of curves with decreasing slopes to represent increasing initial densities. However, the most problematic soils from a liquefaction perspective are loose sands.

The results of Figure 6.12 and Figure 6.13 indicate that the initial gassy state of the specimens resulted in an increase in relative density tending toward the limiting line proposed by Seed. The portion of the limiting line that represents loose to medium dense specimens, D_r from 0% to 75%, can be approximated as a linear function with the following equation: (Figure 6.14)

$$(CRR_{7.5})_{SS} = 0.2515D_r - 0.0002. \qquad [6.5]$$

Combining the above two equations and their associated figures results in Figure 6.15, a plot of the change (increase) in $(CRR_{7.5})_{SS}$ versus initial degree of saturation. The following equation is obtained from this relationship:

$$\Delta(CRR_{7.5})_{SS} = -0.247S_r + 0.247 \qquad [6.6]$$

For any initial degree of saturation, the increased resistance to cyclic loading can be estimated from this simple relationship. It is important to note that the above method is based on limited laboratory data for only one type of sand and for carbon dioxide gas; therefore, it should be used only as a guideline where no other information is available.

6.6 COMPARISON WITH CANLEX DATA

As part of the CANLEX (CAanadian Liquefaction EXperiment) project, cyclic triaxial and cyclic simple shear tests were performed. Of particular interest to this research was the Phase I undisturbed samples of Syncrude sand tested under cyclic triaxial loading. As reported by Wride and Robertson (1997b) several samples had varying degrees of in situ saturation. The samples were not saturated prior to testing, therefore, initial saturations ranged from 77% to 100%. Robertson et al. (1998) speculated that the undisturbed samples (taken from below the groundwater table) contained gas generated from residual bitumen.

The CANLEX data was added to the plot of $(CRR_{7.5})_{SS}$ versus relative density and to produce Figure 6.16. Although these samples are medium to dense, it is interesting to note that the gassy samples plot to the left of the limiting line, while the one sample with an initial saturation of 100% plots very close to the line. Unfortunately, neither the final degrees of saturation, nor the final densities, were determined for these tests. The CANLEX data confirms the general trend that gassy samples will have an increased resistance to cyclic loading.

The proposed method of estimating the increase in cyclic resistance due to the presence of gas was applied to the CANLEX data. Although the method is suggested for only loose to medium dense samples, some indication of its usefulness can be determined from these test results. The steps in this procedure were as follows. Firstly, the cyclic resistance was predicted from the initial relative density using Figure 6.14. Secondly, the initial degree of saturation was used with Figure 6.15 to predict the increase in cyclic resistance. Finally, the increase in resistance was added to the resistance obtained from the first step and the total resistance versus initial density is presented in Figure 6.16. The results of this exercise show that the proposed method predicts a cyclic resistance ratio close to the measured value.

6.7 SUMMARY AND CONCLUSIONS

A laboratory program studying the response of loose gassy Ottawa sand subjected to cyclic loading was carried out. Undrained cyclic triaxial tests were performed on saturated and gassy specimens. Previous studies have investigated the behavior of dense gassy sand or unsaturated sands under cyclic loading; no published work has looked into the cyclic response of loose gassy sand.

The results of the laboratory tests showed that all cyclic triaxial tests reached essentially zero effective confining pressure and experienced cyclic liquefaction. Gassy specimens either built up pore pressures rapidly and failure occurred within four cycles, or pore pressures did not build up and failure did not occur. This observation suggests that the applied cyclic load must be very close to the load required for monotonic failure. In other words, the gassy specimens were exhibiting a monotonic type failure under high cyclic loads.

The resistance of a soil to cyclic loading is influenced by the applied shear stress as well as the soil state (void ratio, effective confining pressure, and soil structure) and grain characteristics. In addition to soil state and grain characteristics, the soil's resistance to cyclic loading is affected by the loading intensity, duration, and frequency. In the case of gassy specimens, the resistance to liquefaction is also affected by the initial degree of saturation as well as the gas characteristics.

Initial effective confining stress has little affect on loose specimens, but for dense specimens, the cyclic resistance decreases with increasing confining pressure. Increasing the relative density has the effect of increasing the resistance to cyclic liquefaction. Both the confining pressure and density were kept essentially fixed so that the laboratory program could better analyze the effects of gas.

Soil structure, induced by the specimen preparation method, influenced the cyclic resistance. In general, specimens prepared by the moist tamping method have the highest resistance to cyclic loading when compared with specimens prepared to the same density by other specimen preparation methods.

Grain characteristics have an impact on the cyclic resistance, with even slight variations in grain characteristics accounting for large changes in the cyclic resistance. The presence of fines in sandy soils increases the resistance to cyclic liquefaction. In this study, clean Ottawa sand was used to prepare all specimens.

The effects of loading intensity and duration on the cyclic resistance are represented by the cyclic resistance ratio and number of cycles to failure, respectively. Previous research has shown that the effect of frequency on the resistance to cyclic liquefaction is minimal.

Determining the effect of the presence of gas on the cyclic liquefaction resistance of loose sand is one of the main objectives of this laboratory program. The presence of gas increased the resistance to cyclic loading by 200 to 300 percent. The gassy specimens increased in both density and degree of saturation during loading, while the saturated specimens remained at a constant density. By comparing the laboratory data to the limiting line proposed by Seed et al. (1985), it was noted that the cyclic resistance of the saturated tests were similar to the values that would be predicted by the limiting line. The cyclic resistance and final density of the gassy specimens also plotted close to the limiting line. This observation lead to a method to predict the increased resistance of the gassy specimens using the limiting line proposed by Seed et al. (1985), the initial density, and the initial degree of saturation.

The proposed method to calculate the resistance to cyclic liquefaction of gassy specimens was successfully applied to the CANLEX gassy sample data.

The main conclusion of this laboratory work is that the presence of gas increases the resistance of loose Ottawa sand specimens to cyclic liquefaction.

Table 6.1 - Correction factors for influence of earthquake magnitude on cyclic resistance ratio (after Seed et al. 1985).

Earthquake Magnitude, M	No. of represenative cycles at 0.65 tmax	$r_m = \frac{\text{CRR for M=M}}{\text{CRR for M=7.5}}$
8.5	26	0.89
7.5	15	1.0
6.75	10	1.13
6	5 to 6	1.32
5.25	2 to 3	1.5

Table 6.2 - Specimen summary for cyclic triaxial tests.

Sample	Type	σ_{dp}' (kPa)	p' initial (kPa)	Period (Sec)	e* initial	e* final	Sr* initial	Sr* final	CRR $\sigma_d'/(2\sigma_3')$	N	M	Correction $CRR_M/CRR_{M=7.5}$	CRR_{tx} (M=7.5)	CRR_{SS} (M=7.5)
16	Saturated	55	300.5	12	0.736	0.736	100%		0.092	25	8.433	0.8744	0.105	0.073
18	Saturated	55	297.7	12	0.716	0.716	100%		0.092	1	4.944	1.6482	0.056	0.039
19	Saturated	55	296.4	12	0.713	0.713	100%		0.093	38	8.819	0.8313	0.112	0.078
20	Saturated	50	294.3	12	0.708	0.708	100%		0.085	34	8.665	0.8480	0.100	0.070
25	Saturated	60	296.3	14	0.706	0.706	100%		0.101	27	8.518	0.8646	0.117	0.082
28	Gassy	70	296.7	15	0.711	0.699	100%	103%	0.118	3	5.328	1.5017	0.079	0.055
32	Gassy	70	294.1	15	0.724	0.707	99%	103%	0.119	4	5.604	1.4117	0.084	0.059
33	Gassy	140	271.6	30	0.754	0.701	87%	94%	0.258	2	5.101	1.5851	0.163	0.114
36	Gassy	130	291.8	26	0.775	0.690	78%	86%	0.223	1	4.934	1.6521	0.135	0.094
37	Gassy	115	291.0	24	0.795	0.711	76%	84%	0.198	1	5.003	1.6239	0.122	0.085
38	Gassy	148	270.1	30	0.731	0.700	83%	86%	0.277	3	5.380	1.4841	0.186	0.131
39	Gassy	155	213.1	31	0.789	0.694	74%	83%	0.299	2	5.199	1.5478	0.193	0.135
40	Gassy	125	283.9	24	0.753	0.698	84%	90%	0.243	3	5.384	1.4826	0.164	0.115
41	Gassy	158	270.9	31	0.674	0.608	75%	82%	0.297	2	5.124	1.5762	0.188	0.132
42	Gassy	140	212.0	27	0.713	0.658	79%	85%	0.276	2	5.177	1.5563	0.177	0.124

* Void ratio and degree of saturation are calculated from TDR data.

Note: σ_{dp}' is the applied effective cyclic stress.

p' is the mean normal effective stress defined as $^1/_3\,(\sigma_1' + 2\sigma_3')$.

N is the number of cycles to failure.

M is the equivalent earthquake magnitude.

All specimens were tested undrained.

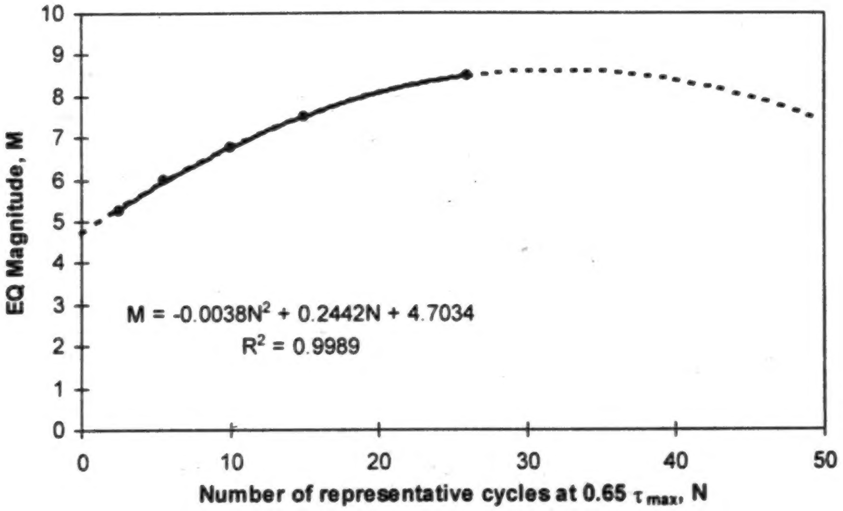

(a) for number of cycles less than 28 (N < 28)

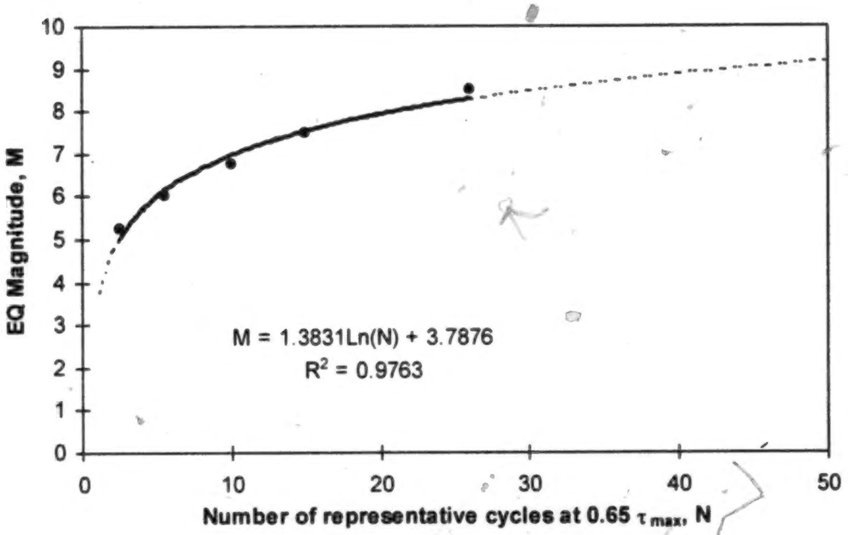

(b) for number of cycles greater than 28 (N > 28)

Figure 6.1 - Relationship between earthquake magnitude and equivalent number of cycles of loading (modified from Wride and Robertson 1997a).

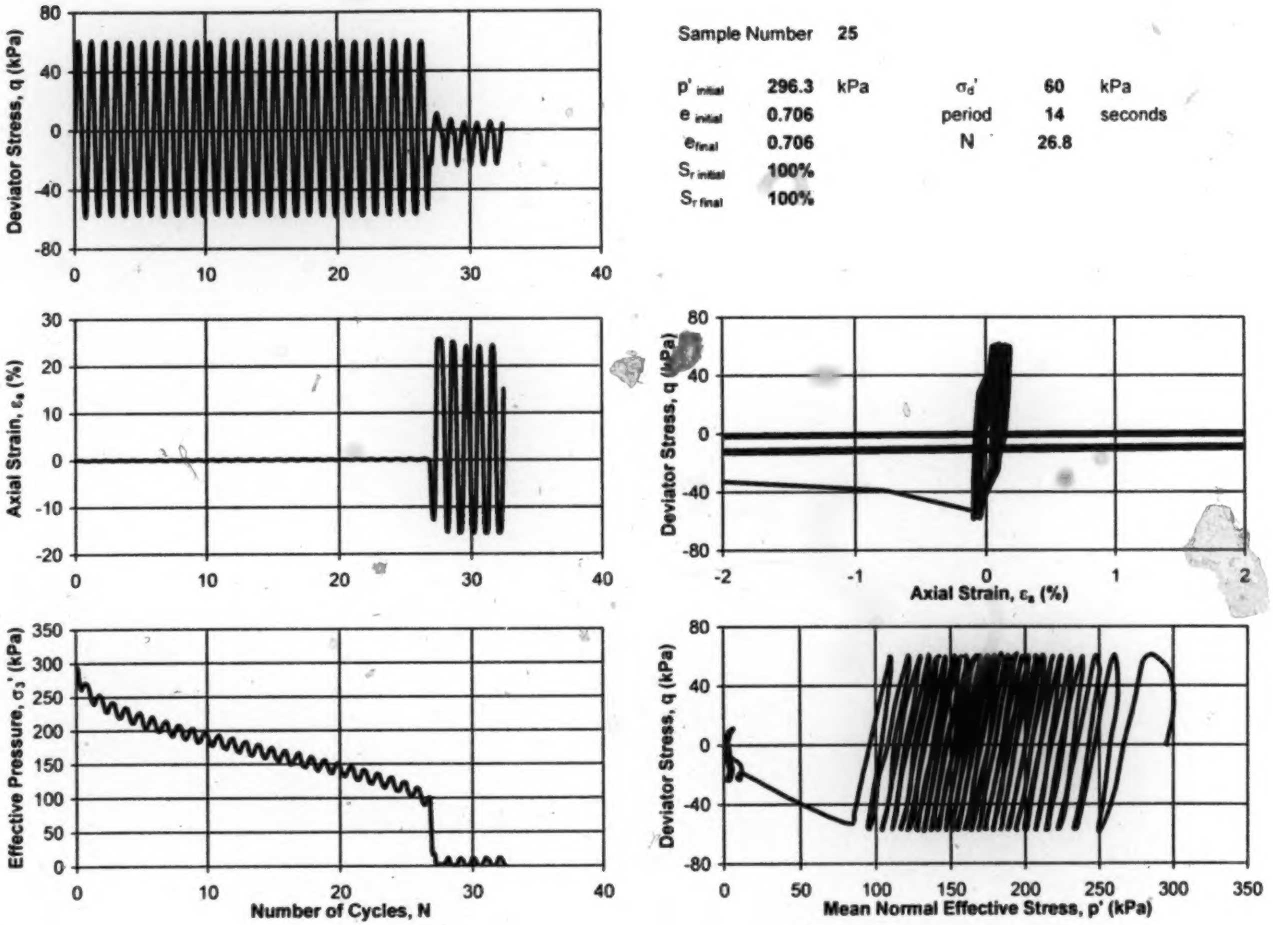

Sample Number	25				
$p'_{initial}$	296.3	kPa	σ_d'	60	kPa
$e_{initial}$	0.706		period	14	seconds
e_{final}	0.706		N	26.8	
$S_{r\ initial}$	100%				
$S_{r\ final}$	100%				

Figure 6.2 – Typical saturated test result.

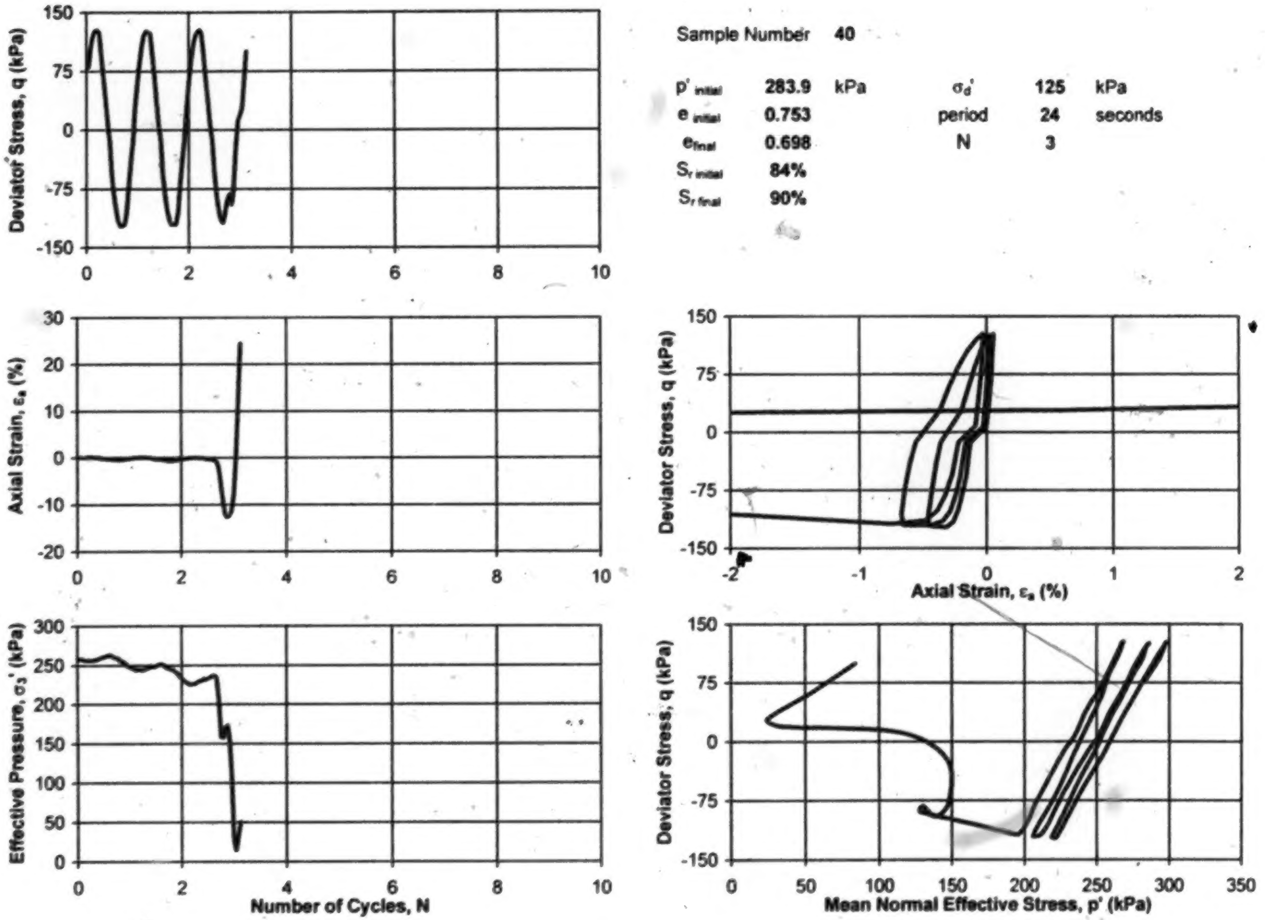

Figure 6.3 - Typical gassy test result.

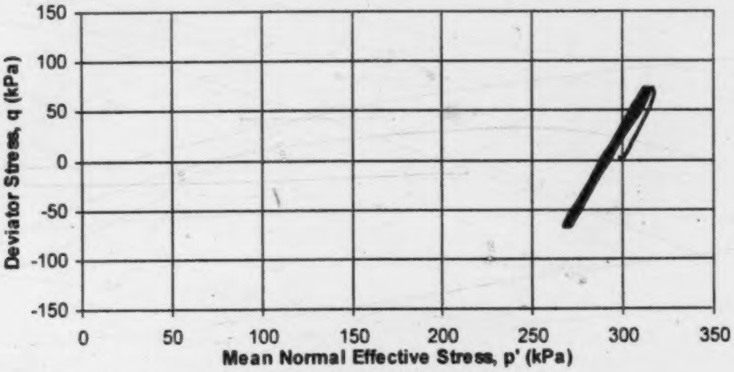

(a) Sample #30 (a), Gassy; $\sigma_{dp}'=70$ kPa, $p'=299$ kPa, $e_{initial}=0.81$, $S_{r\ initial}=74\%$.

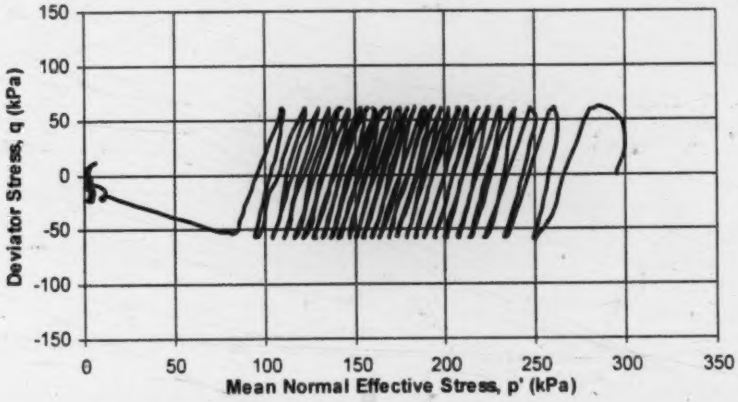

(b) Sample #25, Saturated; $\sigma_{dp}'=60$ kPa, $p'=296$ kPa, $e_{initial}=0.71$.

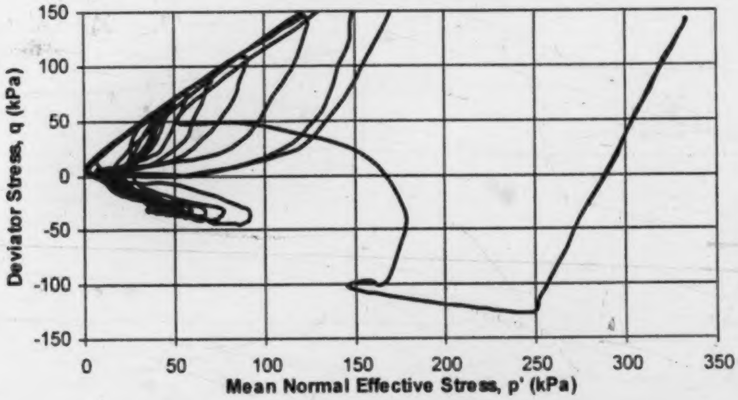

(c) Sample #30 (c), Gassy; $\sigma_{dp}'=140$ kPa, $p'=280$ kPa, $e_{initial}=0.77$, $S_{r\ initial}=76\%$.

Figure 6.4 - Cyclic failure of gassy and saturated specimens.

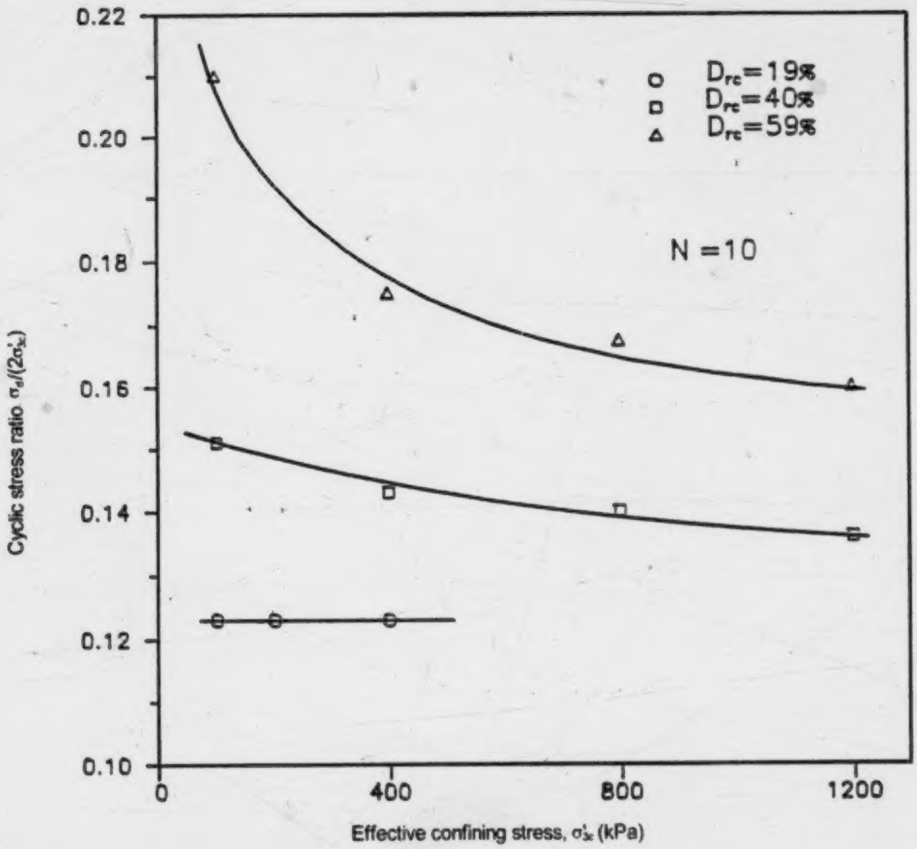

Figure 6.5 - Liquefaction resistance curves of Fraser River sand at N=10 cycles (modified from Thomas 1992).

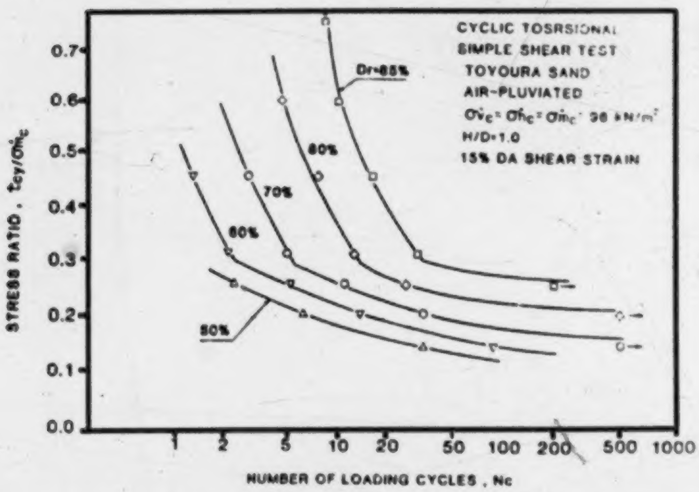

(a) Stress ratio versus number of loading cycles to 15% double amplitude strain

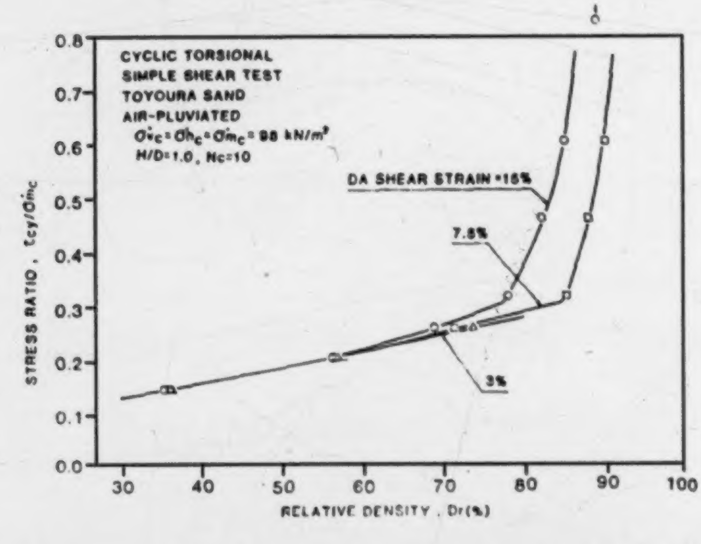

(b) Stress ratio versus relative density in ten loading cycles

Figure 6.6 - Effect of relative density on cyclic strength by cyclic torsional simple shear tests for isotropically consolidated Toyoura sand (modified from Tatsuoka et al. 1982).

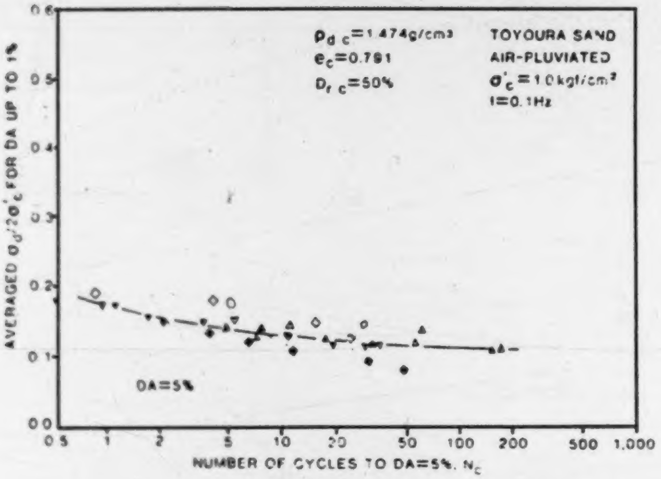

(a) Number of cycles to 5% double amplitude strain

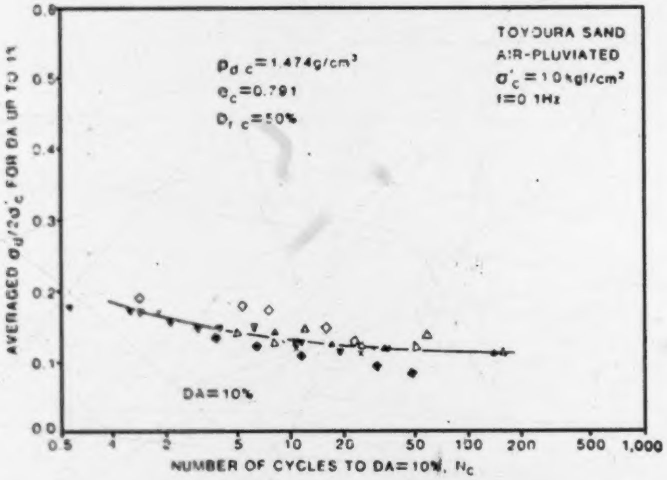

(b) Number of cycles to 10% double amplitude strain

Figure 6.7 – Cyclic stress ratio versus number of cycles to 5% or 10% double amplitude axial strain for loose Toyoura sand (modified from Toki et al. 1986).

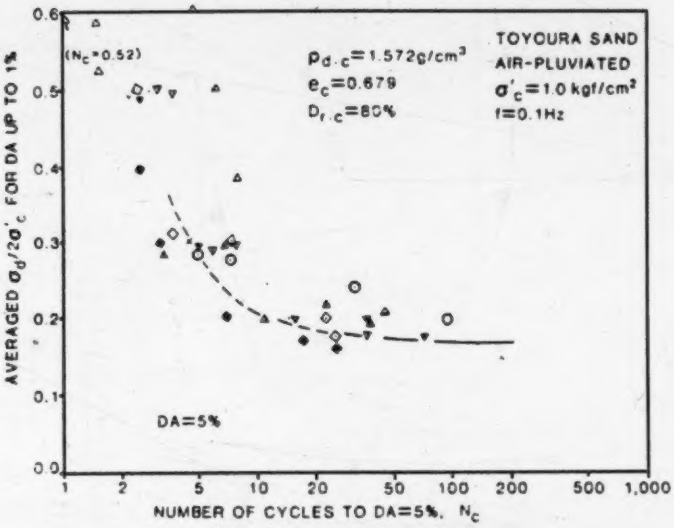

(a) Number of cycles to 5% double amplitude strain

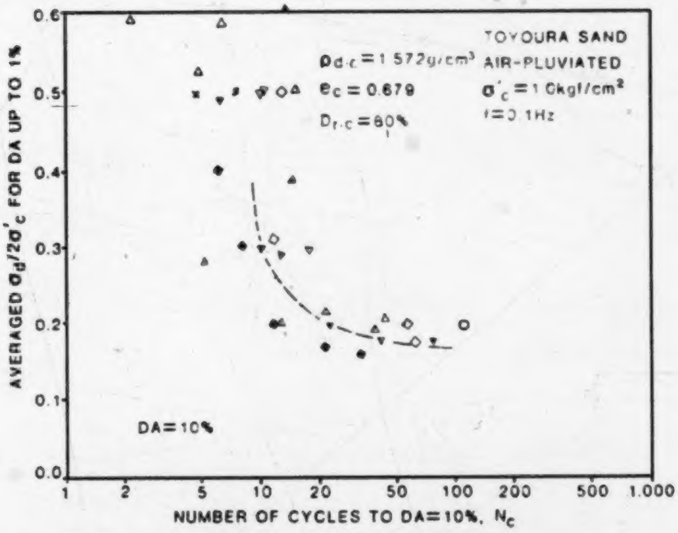

(b) Number of cycles to 10% double amplitude strain

Figure 6.8 - Cyclic stress ratio versus number of cycles to 5% or 10% double amplitude axial strain for dense Toyoura sand (modified from Toki et al. 1986).

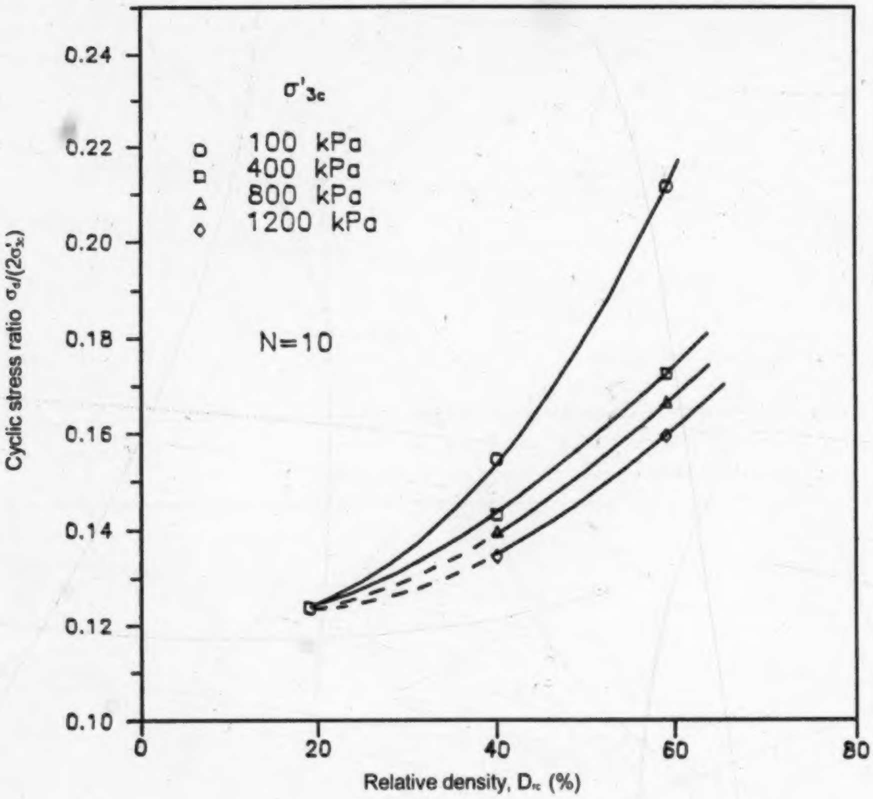

Figure 6.9 - Cyclic loading liquefaction resistance curves (modified from Thomas 1992).

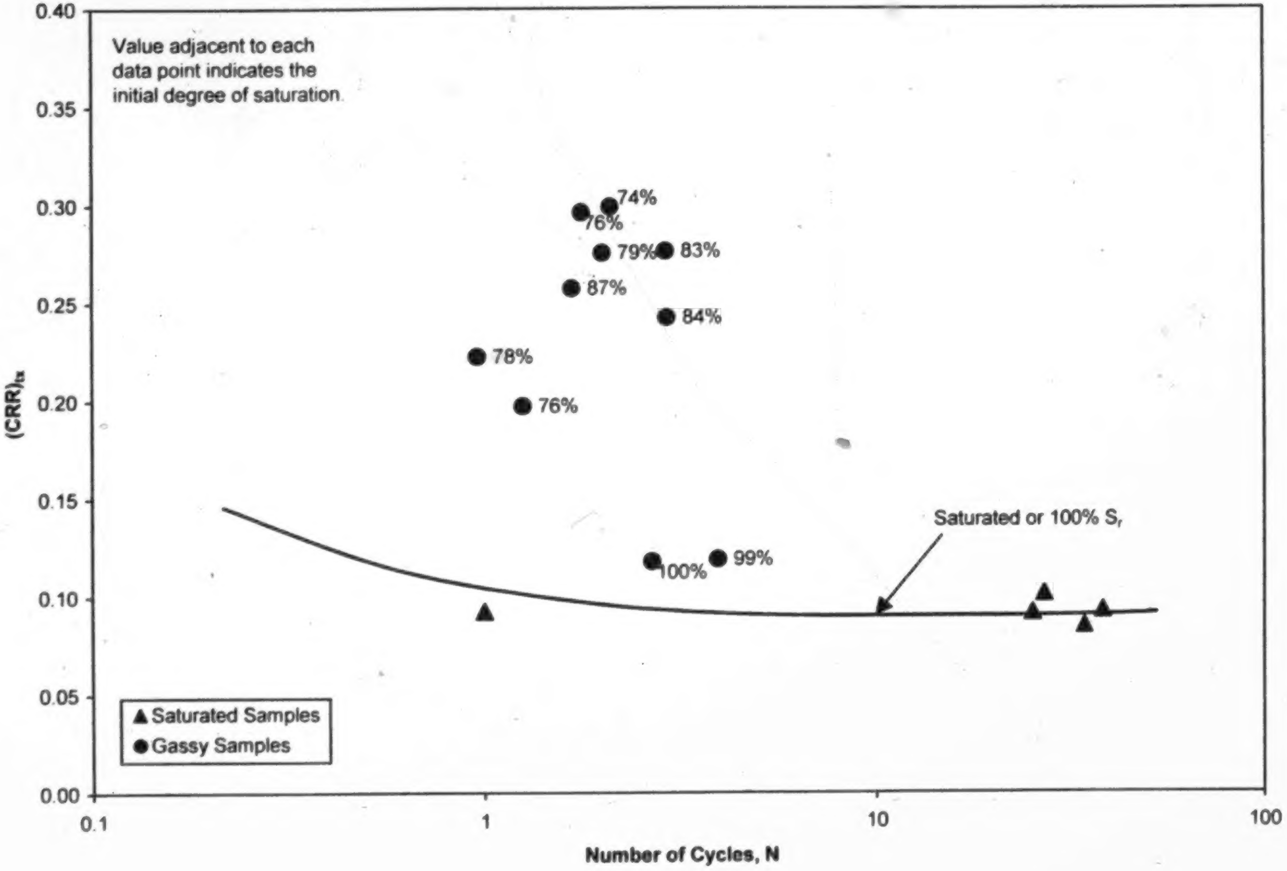

Figure 6.10 – Triaxial cyclic resistance ratio versus number of cycles to failure.

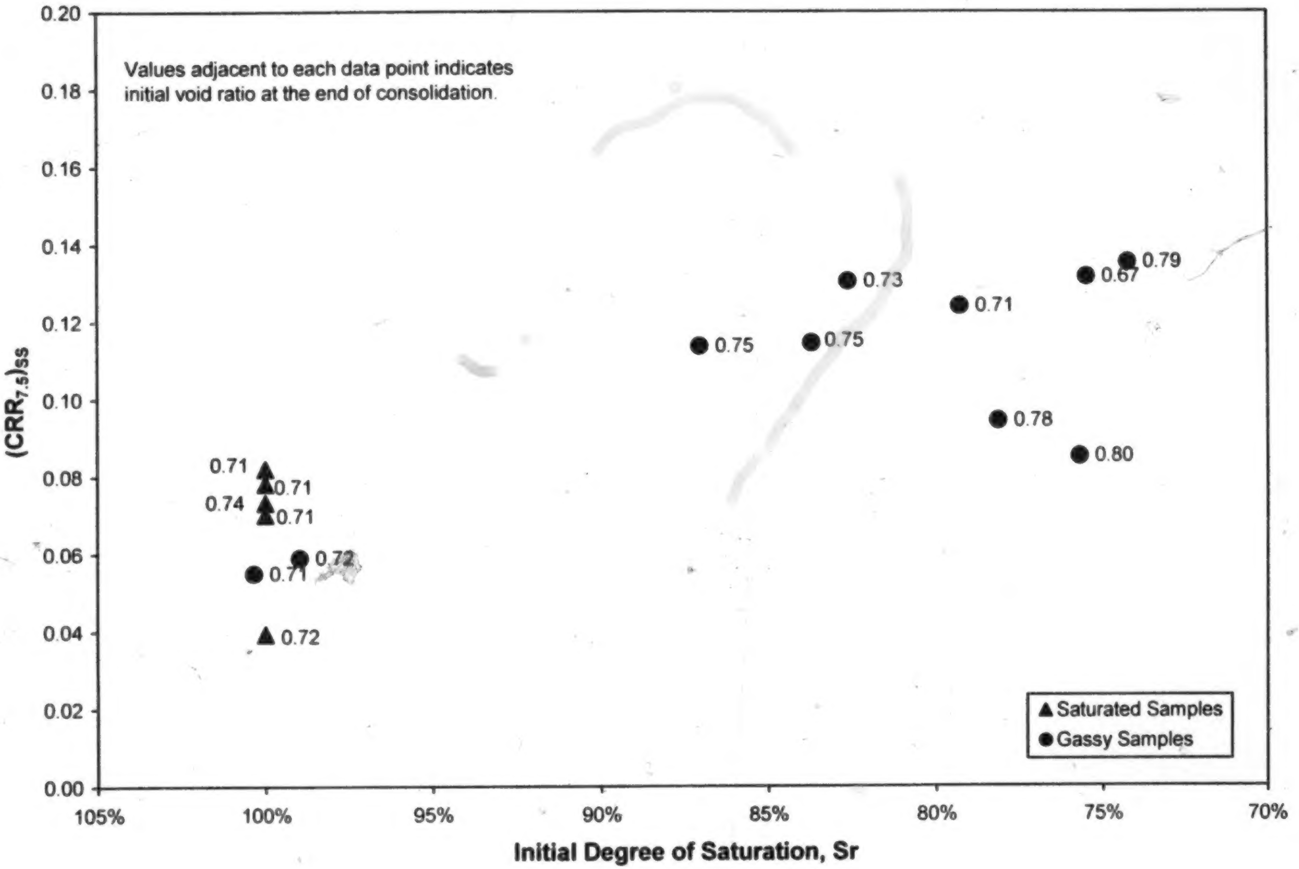

Figure 6.11 - Cyclic resistance ratio versus initial degree of saturation.

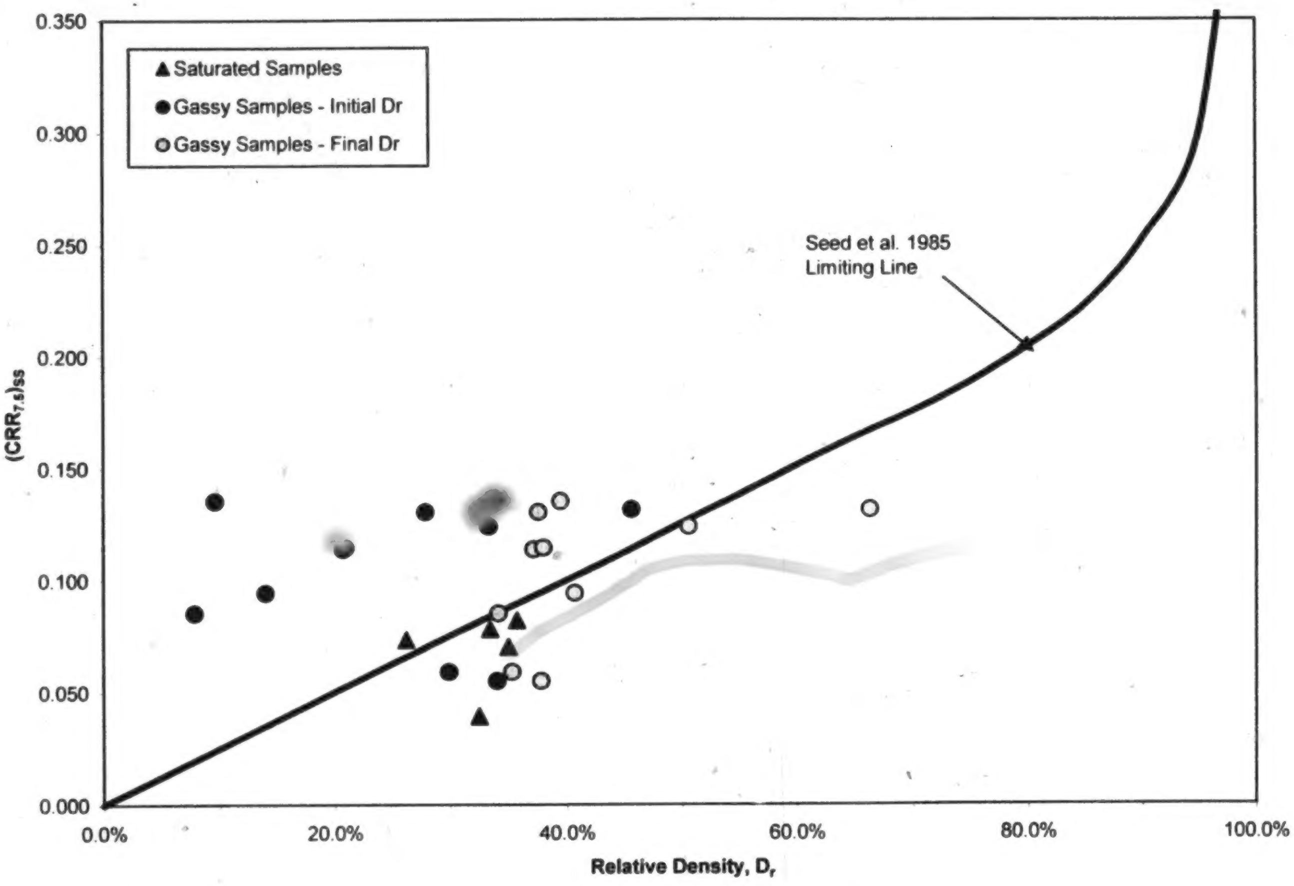

Figure 6.12 - Cyclic resistance ratio versus relative density.

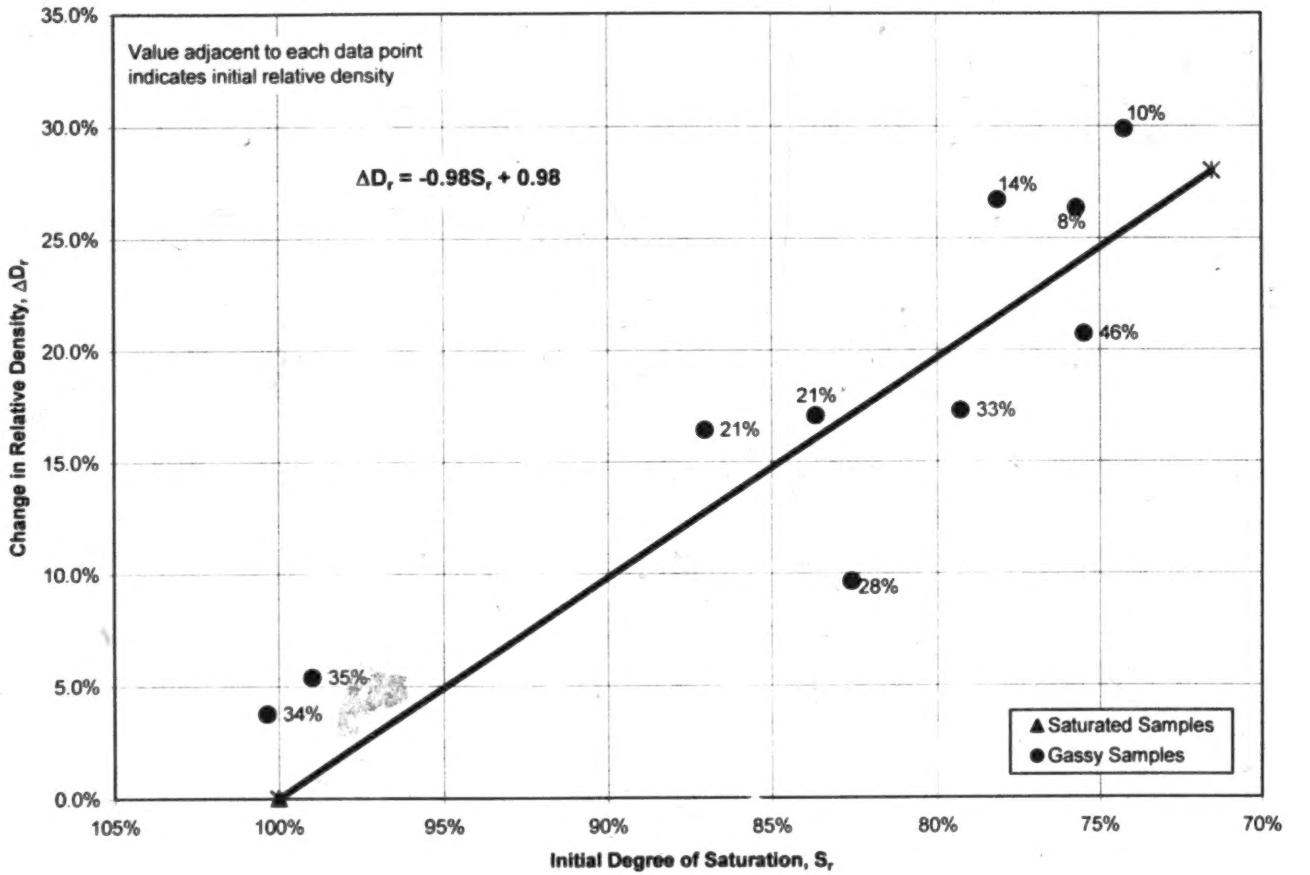

Figure 6.13 - Change in relative density versus initial degree of saturation.

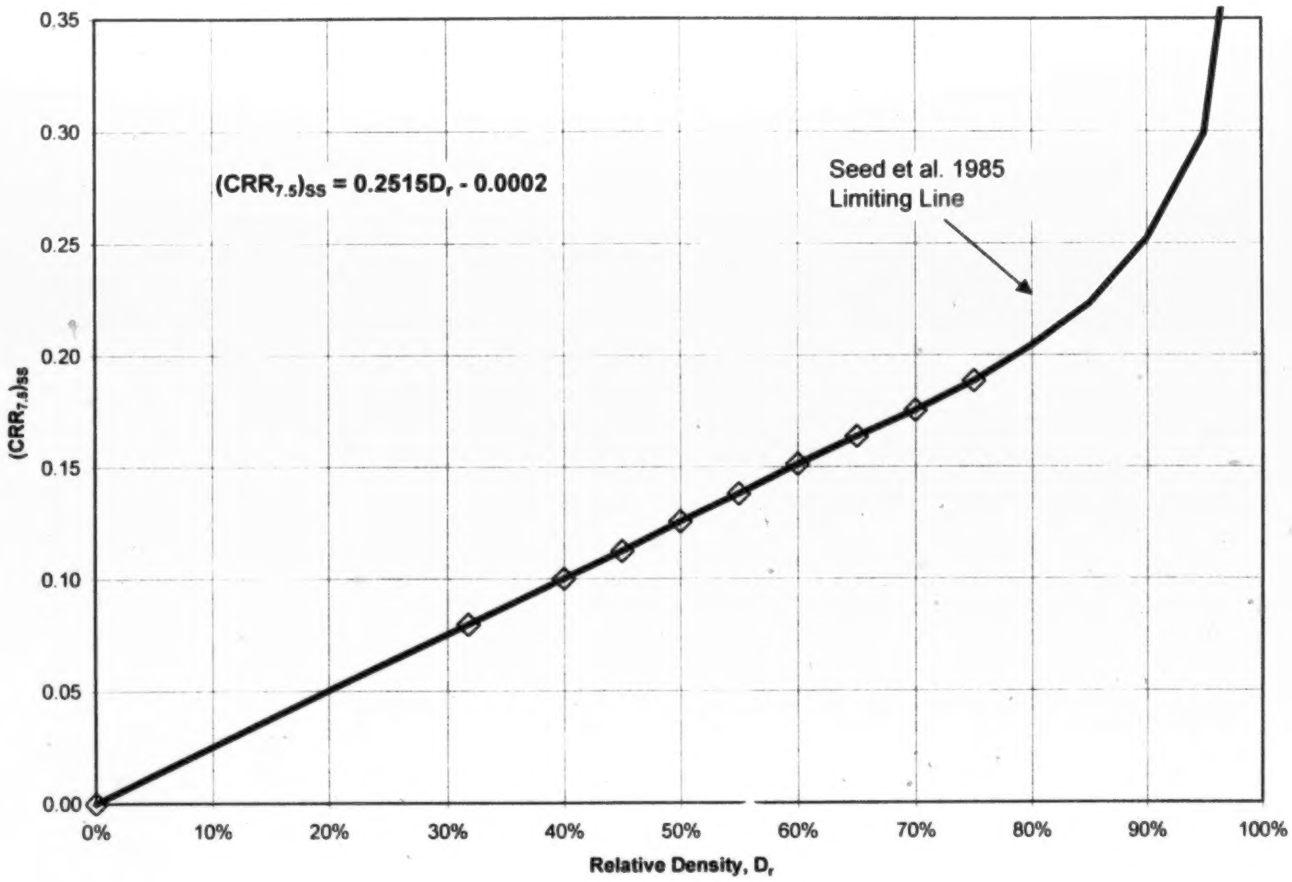

Figure 6.14 - Seed et al. (1985) limiting line. Seed developed this line from field observations.

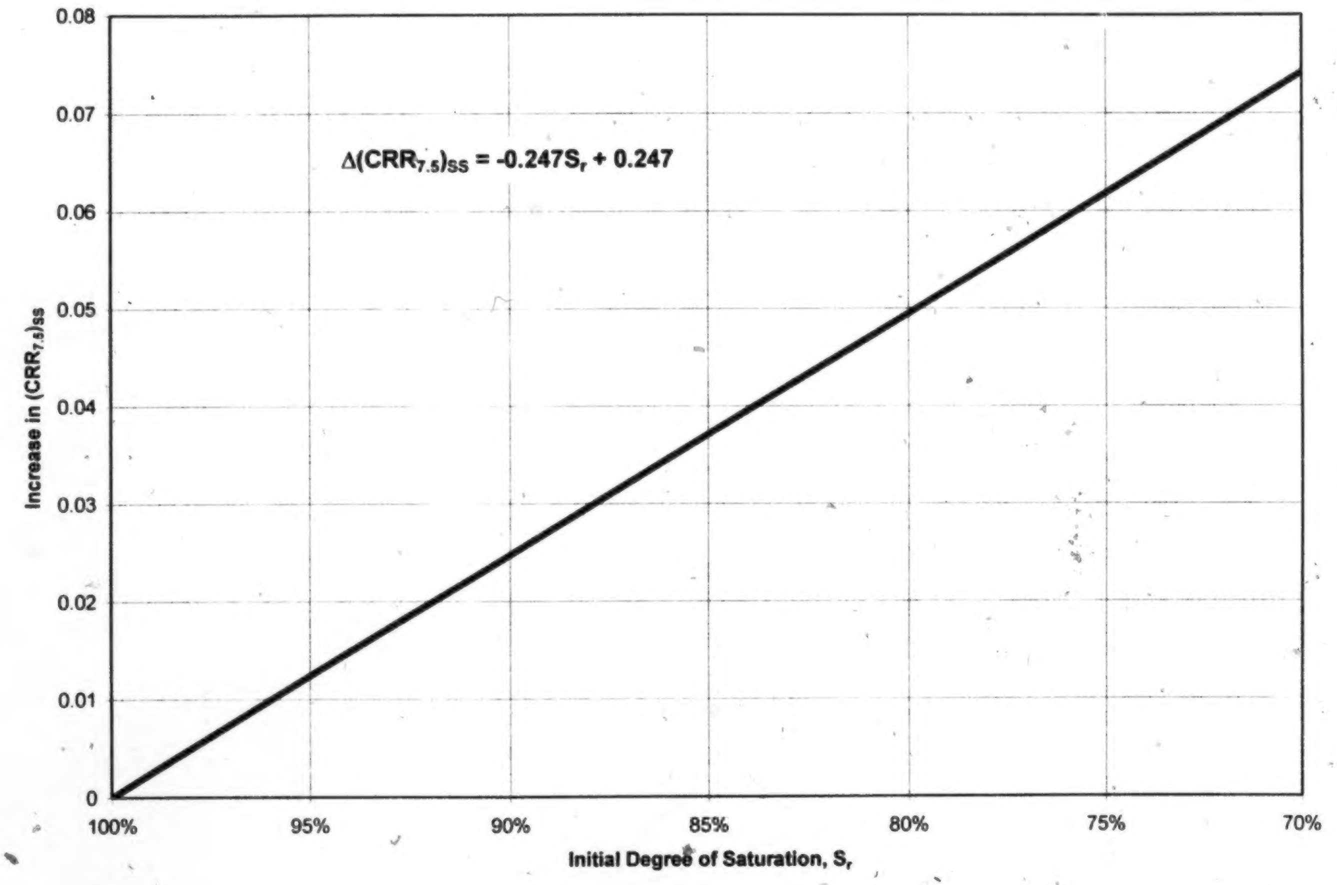

Figure 6.15 - Increase in cyclic resistance ratio versus initial degree of saturation for loose Ottawa sand.

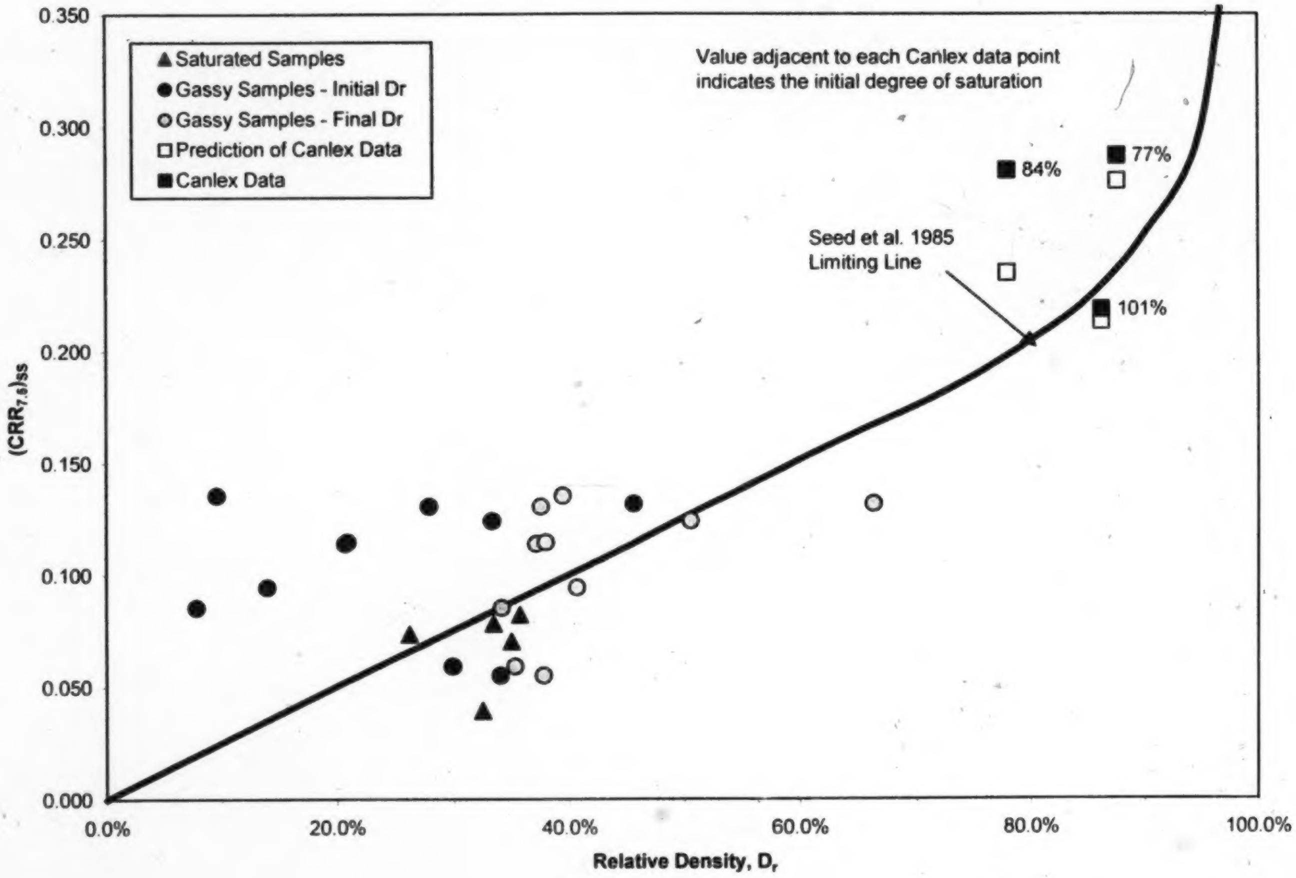

Figure 6.16 - Cyclic resistance ratio versus relative density showing CANLEX predictions.

CHAPTER 7

CONSTITUTIVE MODELING OF GASSY SOIL BEHAVIOR

7.1 INTRODUCTION

Numerical models are useful tools for the prediction of soil behavior and for providing theoretical confirmation of laboratory results. Models enable the analyses of large quantities and ranges of data, often in a more timely and cost effective manner than laboratory testing. Laboratory results can be restricted by equipment limitations while models have no such restrictions.

The development of new numerical techniques to solve complicated problems has enabled detailed analyses of the behavior of sand during liquefaction. Any numerical analysis requires a realistic account of the constitutive behavior. Previous constitutive models tended to focus on cyclic liquefaction predictions, although some recent models enable the prediction of flow liquefaction events. In order to model flow liquefaction of loose sands, there is a need for a suitable stress-strain formulation. Many current models have numerous shortcomings when they are applied to loose granular soils. Currently, no constitutive models exist that enable the prediction of the flow liquefaction of loose sands containing gas.

In this chapter, the theoretical behavior of gassy soils is reviewed. The equilibrium behavior is detailed and equations are derived that describe the compressibility of liquid/gas mixtures as well as the theoretical pore pressure response of a gassy soil element to an applied total stress. The transient behavior of gas is discussed only in a qualitative manner.

The next section describes a constitutive model for loose sand developed by Imam (1999). The shortcomings of other constitutive models, along with the current model characteristics, elements, calibration, and performance are summarized. The model developed by Imam was modified to take into account the effect of gas in the pore fluid. The modified model is evaluated and compared to the laboratory data. Performance and limitations of the modified model are discussed.

7.2 EQUILIBRIUM AND TRANSIENT BEHAVIOR OF GASSY SOILS

This section discusses the theoretical behavior of gassy soils. The behavior of a gassy soil will be affected by changes in the pore-gas and pore-liquid pressures. The application of an external load is one condition that will lead to the development of pore pressures.

The pore pressures that are generated immediately after loading are referred to as the undrained pore pressures. In the undrained condition, the applied total stress is carried by the soil structure, the pore-gas and pore-liquid depending upon their relative compressibilities (Fredlund and Rahardjo 1993). The induced pore pressures can be written as a function of the applied total stress. If drainage is allowed, the induced pore pressures will dissipate with time and the applied total stress will eventually be carried by the soil structure.

This section presents the relationship for the pore pressures generated from an application of total stress to the soil under undrained conditions. First, the physical laws governing free and dissolved gas behavior, and how these laws influence the compressibility of the pore fluids, is presented. Next, the equilibrium behavior of gassy soils, or the behavior that is governed by processes, which are or have become independent of time, is presented. Fredlund and Rahardjo (1993) and Sobkowicz (1982) have presented both these subjects in detail, and only a summary of the main points will be given here.

Finally, following the work of Sobkowicz (1982), a very brief discussion of the transient behavior of gassy soils is presented.

7.2.1 Boyle's and Henry's Laws

Consider the case of a soil element containing some pore fluid. The pore fluid may consist of a combination of gases and liquids that may be totally miscible, totally immiscible, or a combination of the two. An immiscible mixture is a combination of gases and fluids without any interaction, while a miscible mixture is a combination of gases and fluids that interact. In this thesis, the simple case of a single gas and a single liquid will be examined. It is assumed that the gas will be somewhat soluble in the liquid, depending on the gas to liquid ratio in the soil element. The ratio of gas to liquid, and the pore pressure, will determine if there is any free gas in the pores of the soil element.

The presence of gas will affect the compressibility of the soil element. If free gas is present then the pore fluid compressibility may be higher. If the gas and liquid are miscible to some extent then the compressibility will be a function of the pressure, the compressibility of the gas, and the solubility of the gas in the liquid. Boyle's and Henry's laws govern these physical processes.

a) Boyle's Law

Boyle's law states that the volume, V, of a gas varies inversely with its pressure, P, at constant temperature, T. That is at constant temperature:

$$V = \frac{1}{P} \qquad [7.1]$$

or

$$P \cdot V = k\,. \qquad [7.2]$$

Therefore, Boyle's law governs the compressibility of free gas.

b) Henry's Law

Henry's law states that the mass of gas dissolved in a fixed quantity of liquid, at constant temperature, is directly proportional to the absolute pressure of the gas above the solution. Stated another way, if the temperature remains constant, the ratio of the mass and the absolute pressure of the gas is constant:

$$\frac{M_{d1}}{\bar{u}_{g1}} = \frac{M_{d2}}{\bar{u}_{g2}} = \text{constant} \qquad [7.3]$$

where:

M_{d1}, $\bar{u}_{g1}$ = mass and absolute pressure of the dissolved gas, respectively, at condition 1

M_{d2}, $\bar{u}_{g2}$ = mass and absolute pressure of the dissolved gas, respectively, at condition 2.

The ratio between the mass of each gas that can be dissolved in a liquid, and the mass of the liquid, is called the coefficient of solubility, *H*. The ratio of the volume of dissolved gas, V_d, in a liquid to the volume of the liquid is called the volumetric coefficient of solubility, *h*:

$$\frac{V_d}{V_l} = \text{constant} = \text{h} \qquad [7.4]$$

or

$$V_d = h \cdot V_l \qquad [7.5]$$

where:

V_d = volume of dissolved gas

V_l = volume of liquid

h = volumetric coefficient of solubility (Henry's constant).

The volumetric coefficient of solubility varies slightly with temperature.

Both the coefficient of solubility, H, and the volumetric coefficient of solubility, h, are referred to as Henry's constant. The two constants are related by:

$$h = \left(\frac{\rho_l}{\rho_g} \right) H \qquad [7.6]$$

where:

ρ_l = density of the liquid

ρ_g = density of the gas.

When looking up values of Henry's constant in chemistry handbooks, it is important to know which equation the constant applies to (i.e. is Henry's constant the coefficient of solubility or the volumetric coefficient of solubility). In this thesis, only the volumetric coefficient of solubility will be discussed. That is, the term Henry's constant will be used to mean the volumetric coefficient of solubility, h.

Henry's constant will be different for different gas/liquid combinations. For an air/water mix, $h = 0.02$ and for carbon dioxide/water, $h = 0.85$.

7.2.2 Compressibility of the Pore Fluids

In undrained loading the pore liquid and pore gasses are not allowed to leave the sample. Therefore, any increase in applied pressure results in some increase in pore pressure. In the case of gassy (or unsaturated) soils, there is also an associated volume change. The volume change is a result of the compressibility of the pore fluids (if it is assumed that the compressibility of the soil solids is negligible). The compressibility of the pore fluid will consist of compression of the free gas and compression of the liquid.

a) Compressibility of a Gas

The compressibility of a gas can be expressed as:

$$C_g = \frac{-1}{V_g}\frac{dV_g}{du_g} \qquad [7.7]$$

where:

C_g = compressibility of gas

V_g = volume of gas

dV_g/du_g = gas volume change with respect to a gas pressure change

u_g = gas pressure.

The volume – pressure relationship during undrained loading can be expressed using Boyle's law:

$$V_g = \frac{\overline{u}_{go}V_{go}}{\overline{u}_g} \qquad [7.8]$$

where:

$\overline{u}_{go}$ = initial absolute gas pressure ($\overline{u}_g = u_{go} + \overline{u}_{atm}$)

u_{go} = initial gauge gas pressure

$\overline{u}_{atm}$ = atmospheric pressure (101.3 kPa)

V_{go} = initial volume of gas

$\overline{u}_g$ = absolute gas pressure ($\overline{u}_g = u_g + \overline{u}_{atm}$).

Differentiating the volume of gas, V_g, with respect to the absolute gas pressure, $\bar{u}_g$, gives:

$$\frac{dV_g}{d\bar{u}_g} = -\frac{1}{\bar{u}_g^2}\left(\bar{u}_{go}V_{go}\right). \qquad [7.9]$$

Substituting Boyle's law into Equation [7.9] gives:

$$\frac{dV_g}{d\bar{u}_g} = -\frac{V_g}{\bar{u}_g} \qquad [7.10]$$

The derivative of the volume with respect to the absolute pressure is equal to the derivative with respect to the gauge pressure. Atmospheric pressure is assumed to remain constant, therefore Equation [7.10] can be substituted into Equation [7.7] to give:

$$C_g = \frac{1}{\bar{u}_g}. \qquad [7.11]$$

Equation [7.11] shows that the compressibility of the gas is inversely proportional to the absolute gas pressure.

The finite difference formulation of the above relationships is:

$$\bar{u}_{g1}V_{g1} = \bar{u}_{g2}V_{g2}$$

$$V_{g2} = \bar{u}_{g1}\frac{V_{g1}}{\bar{u}_{g2}}$$

$$\Delta V_g = V_{g2} - V_{g1} = V_{g1}\cdot\left(\frac{\bar{u}_{g1}}{\bar{u}_{g2}} - 1\right)$$

$$\Delta V_g = V_{g1} \cdot \frac{-\Delta\bar{u}_g}{\bar{u}_g + \Delta\bar{u}_g} \tag{7.12}$$

$$C_g = -\frac{1}{V_g} \cdot \frac{\Delta V_g}{\Delta\bar{u}_g} = \frac{1}{\bar{u}_g + \Delta\bar{u}_g} \tag{7.13}$$

In the limit, as $\Delta\bar{u}_g$ approaches zero, C_g approaches $1/\bar{u}_g$.

b) Compressibility of a Liquid

The compressibility of a liquid can be expressed as:

$$C_l = -\frac{1}{V_l}\frac{dV_l}{du_l} \tag{7.14}$$

where:

C_l = liquid compressibility

V_l = volume of liquid

dV_l/du_l = liquid volume change with respect to liquid pressure change

u_l = liquid pressure.

Dorsey (1940) found that water saturated with dissolved air had virtually the same compressibility as de-aired water. In this thesis, it will be assumed that the compressibility of carbon dioxide saturated water is the same as de-aired water. The differences between the two compressibilities are negligible.

c) Compressibility of a Liquid/Gas Mixture

The compressibility of a partly miscible liquid/gas mixture can be developed. Consider the volumetric relations of the gas, liquid, and solids as shown in Figure 7.1. Assuming the soil has a degree of saturation, *S*, and a porosity, n, then the total volume will be the sum of the volume of solids, liquid, and gas (i.e. $V_T = V_s + V_l + V_g$). If an infinitesimal increase in total stress, $d\sigma$, is applied to the undrained soil element then the pore pressure (pore gas and pore liquid) pressure will increase, while the volume (gas volume and liquid volume) decrease. The compressibility of the gas-liquid mixture, for an increase in total stress, can be written as:

$$C_{gl} = -\frac{1}{V_l + V_g}\left[\frac{d(V_l - V_d)}{d\sigma} + \frac{d(V_g + V_d)}{d\sigma}\right] \qquad [7.15]$$

where:

C_{gl} = compressibility of gas – liquid mixture

$(V_l + V_g)$ = volume of the gas – liquid mixture

V_l = volume of liquid

V_g = volume of free gas

$d(V_l - V_d)/d\sigma$ = liquid volume change with respect to a total stress change

$d(V_g + V_d)/d\sigma$ = gas volume change with respect to a total stress change

V_d = volume of dissolved gas.

The term $(d(V_l - V_d)/d\sigma)$ in Equation [7.15] is equal to $(dV_l/d\sigma)$ because the dissolved gas is a fixed volume internal to the liquid. As such, its volume does not change. The total volume of liquid is therefore used in computing the compressibility of the liquid (i.e. $C_l = -(1/V_l)(dV_l/du_l)$).

The change in the volume of gas is a result of the compression of the free gas in accordance with Boyle's law and the dissolving of the free gas into the liquid in accordance with Henry's law.

Applying the chain rule of differentiation to Equation [7.15] gives:

$$C_{gl} = \frac{-1}{V_l + V_g}\left[\frac{dV_l}{du_l}\frac{du_l}{d\sigma} + \frac{d(V_g + V_d)}{du_g}\frac{du_g}{d\sigma}\right] \qquad [7.16]$$

where:

dV_l/du_l = liquid volume change with respect to a pore-fluid pressure change

$du_l/d\sigma$ = liquid pressure change with respect to a total stress change

$d(V_g+V_d)/du_g$ = gas volume change with respect to a pore gas pressure change

$du_g/d\sigma$ = gas pressure change with respect to a total stress change.

Rearranging Equation [7.16] gives:

$$C_{gl} = -\left[\frac{V_l}{V_l + V_g}\frac{1}{V_l}\frac{dV_l}{du_l}\right]\frac{du_l}{d\sigma} - \left[\frac{V_g + V_d}{V_l + V_g}\frac{1}{V_g + V_d}\frac{d(V_g + V_d)}{du_g}\right]\frac{du_g}{d\sigma}. \qquad [7.17]$$

Substituting in the volume relations from Figure 7.1 and Equations [7.7] and [7.14] into Equation [7.17] yields the compressibility of a gas-liquid mixture:

$$C_{gl} = SC_l\left(\frac{du_l}{d\sigma}\right) + (1 - S + hS)C_g\left(\frac{du_g}{d\sigma}\right). \qquad [7.18]$$

Since the isothermal compressibility of gas, C_g, is equal to the inverse of the absolute gas pressure:

$$C_{gl} = SC_l\left(\frac{du_l}{d\sigma}\right) + \frac{(1-S+hS)}{\bar{u}_g}\left(\frac{du_g}{d\sigma}\right). \qquad [7.19]$$

7.2.3 Theoretical Pore Pressure Response

Hilf (1948) outlined a procedure to calculate the change in pore pressure in compacted earth fills subjected to an applied total stress. The derivation, based on Henry's and Boyle's law, established a relationship between total stress and pore pressure. Although Hilf developed the analysis for the specialized case of air and water in the soil voids, the derivation can be generalized to a gas and liquid in the void. The initial and final conditions considered in Hilf's analysis are shown in Figure 7.2.

The total volume of gas associated with the initial condition, V_{go}, can be written as follows:

$$V_{go} = \{(1-S_o)n_o + hS_on_o\}V_o \qquad [7.20]$$

where:

V_{go} = initial volume of free and dissolved gas
S_o = initial degree of saturation
N_o = initial porosity
V_o = initial volume of the soil.

The first and second terms represent the free and dissolved gas volumes, respectively. The initial absolute gas pressure is denoted as $\bar{u}_{go}$ and can be assumed to be at atmospheric conditions (i.e. 101.3 kPa). If an increment of major principal stress, $\Delta\sigma$, is applied to the soil, the total volume of gas decreases and the gas pressure increases, in accordance with Boyle's law. The gas volume change is equal to the void volume change, ΔV_v, since the soil solids and liquid are assumed incompressible. Therefore, the gas volume change can be written as a change in porosity (i.e. $\Delta n = \Delta V_v / V_o$) times the initial volume of soil, V_o, as illustrated in Figure 7.2.

The total volume of gas under final conditions, V_{gf}, can be expressed as:

$$V_{gf} = \{(1 - S)n_o + hS_o n_o - \Delta n\}V_o \qquad [7.21]$$

where:

V_{gf} = final volume of free and dissolved gas
Δn = change (i.e. decrease) in porosity.

The final absolute gas pressure, $\bar{u}_{gf}$, can be written as the initial absolute pore gas pressure plus the change (i.e. increase) in pore pressure:

$$\bar{u}_{gf} = \bar{u}_{go} + \Delta\bar{u}_g \qquad [7.22]$$

where:

$\Delta\bar{u}_f$ = change (i.e. increase) in absolute pore gas pressure.

Boyle's law can be applied to the initial and final conditions of the free and dissolved gas:

$$\bar{u}_{go}V_{go} = \bar{u}_{gf}V_{gf} \qquad [7.23]$$

Substituting the initial conditions (Equation [7.20]) and final conditions (Equation [7.21] and [7.22]) into Equation [7.23] gives:

$$\bar{u}_{go}\{(1-S_o)n_o + hS_on_o\}V_o = (\bar{u}_{go} + \Delta\bar{u}_g)\{(1-S_o)n_o + hS_on_o - \Delta n\}V_o \qquad [7.24]$$

Rearranging Equation [7.24] yields an expression for the change in pore gas pressure, $\Delta\bar{u}_{go}$:

$$\Delta\bar{u}_g = \left[\frac{\Delta n}{\{(1-S_o)n_o + hS_on_o - \Delta n\}}\right]\cdot\bar{u}_{go}. \qquad [7.25]$$

Equation [7.25] is commonly referred to as Hilf's equation. It relates the change in pore gas pressure and the change in pore gas volume (i.e. Δn) during undrained loading. An alternate form for Hilf's equation (Equation [7.25]) can be obtained by replacing Δn with $(\Delta V_v/V_o)$:

$$\frac{\Delta V_v}{V_o} = \left(\frac{\Delta\bar{u}_g}{\bar{u}_{go} + \Delta\bar{u}_g}\right)(1 - S_o + hS_o)n_o \qquad [7.26]$$

where:

$\Delta V_v/V_o$ = Change in volume of voids, referenced to the initial volume of the soil (i.e. porosity change, Δn)

Equation [7.26] describes the volume change due to the compression of gas.

7.2.4 Transient Response of Gas

A soil element containing gas subjected to undrained loading will have a transient response caused by gas exsolution or solution. When a soil is loaded undrained, the pore pressure can either increase or decrease depending on the soil density and the soil compressibility. If the pore pressure decreases, gas exsolution will occur; if the pore pressure increases, gas solution will occur. The exsolution or solution, forces the compressibility of the gaseous component of the pore fluid to become time dependent. The compressibility of the pure liquid component of the pore fluid, and that of the soil skeleton, is not influenced by gas exsolution/solution.

Sobkowicz (1982) developed two theoretical models for the undrained response of an element of gassy soil. Both models incorporated the influence of:

- a non-equilibrium condition at the beginning of the time-interval over which the change in pore pressure was to be calculated; and
- a change in the volume of free gas that is a function of the change in time.

The first model, or method, adopted a simple approach that uncoupled gas compression and gas exsolution. The second model attempted to account for the influence of free gas compression on the nature of the dissolved gas disequilibrium, and therefore, on gas exsolution. A comparison of the models showed that the coupled solution was more efficient than the uncoupled model. However, as Sobkowicz (1982) mentioned "it must be understood that, unlike the theoretical equations for equilibrium behavior, both solutions are approximate and only become exact as Δt approaches 0. This is due to the assumptions made in combining the gas compression and exsolution effects."

The models that were proposed by Sobkowicz (1982) to account for the transient behavior of gas are approximate. In the following sections, the constitutive model developed by Imam (1999), as well as the modification made to the model to account for the effect of gas, are described. The modification involved introducing the response of gas to a change in pressure, but did not take into account the transient behavior of gas. The transient behavior of gas was not studied in the laboratory, therefore, it was felt that the complexities of transient behavior would not be introduced into the model. The intent of the model was to provide some "theoretical" results to complement the laboratory results.

7.3 A CONSTITUTIVE MODEL FOR LOOSE SAND

Although the constitutive modeling of the behavior of clay is reasonably well developed, the constitutive modeling of sand is more complex and less understood. The modeling of sand behavior has focused mainly on cyclic liquefaction prediction and evaluation. With the recent advances in computing and the development of new numerical techniques to solve complicated problems, detailed analyses of the behavior of sand during liquefaction is now possible. Any numerical analysis requires a realistic account of the constitutive behavior.

Flow liquefaction is the result of a rapid loss of strength of very loose sand, which exhibits a drop in shear strength under undrained loading conditions. In order to model flow liquefaction of loose sands, there is a need for a suitable stress-strain formulation. Imam (1999) summarized some of the main shortcomings of current constitutive models for sand:

- Many current models are either presented in, or validated by, results of triaxial tests. Some of these models are for triaxial compression only, while some have been theoretically extended to other loading conditions. In general, the performance of the models for other conditions of loading is poor.
- In more comprehensive models, calibration often involved determination of parameters which are either very difficult to obtain from conventional tests, or have no physical meaning.
- In many models, the shapes of the yield surfaces have been chosen approximately. In very loose sand, this can cause imprecise modeling.
- Many models deal with isotropic conditions only, not the natural conditions of anisotropy.
- Except for some recent models, most sand models do not recognize the existence of the ultimate (steady) state condition at large strain.

- In many models, parameters are determined only for a certain range of conditions (i.e. density or pressure) and re-calibration is often required for other soil states.
- The determination of the ultimate state line in triaxial compression is often difficult and even imprecise. Models that rely heavily on the ultimate state line can have significant difficulties in predicting the response of soil to different loading conditions.
- Constitutive models that attempt to predict the behavior of sand over a wide range of states and loading conditions are often very complicated and difficult to use.

In response to the limitations listed above, a research program was undertaken by Imam (1999) with the objectives of:

- Studying the variation of the stress state or friction angle at the peak of the undrained effective stress path for different soil states and loading conditions. The variations were formulated such that they helped in assessing the susceptibility of loose sand at various states, subjected to different loading conditions. The results of the formulations were related to the constitutive behavior of sand and used in the development of a constitutive model, which emphasized the behavior of loose sand.
- Developing a constitutive model that can predict the behavior of granular materials over a wide range of states and loading conditions using a unique set of parameters. The model overcomes some of the limitations of current models and addresses some aspects of sand behavior, which are especially important for loose, liquefiable sand.

The existing model developed by Imam (1999) was selected to study the theoretical behavior of loose sand. The model, which captures the important aspects of loose sand behavior, was modified to account for the presence of gas. Imam's model was selected because of its ability to predict the behavior of loose sand, specifically its ability to model flow liquefaction. In addition, the model was developed at the University of Alberta.

A brief summary of the model elements, calibration, and performance is presented in the following section. The reader is encouraged to read Imam (1999) for a full review of previous and current constitutive models, and the complete model formulation both for triaxial and general stress space.

7.3.1 Model Characteristics

The constitutive model proposed by Imam (1999) was developed for monotonic triaxial stress conditions as well as for general stress conditions. The main characteristics of the model proposed by Imam (1999) are:

1. A "cap" shape for the yield surface of sand was used, which is a function of void ratio, consolidation stresses, and direction of loading. Yield parameters were related to the response of sand observed in conventional triaxial tests. The use of a precise shape for the yield surface ensured accurate prediction of the behavior of sand at different densities, especially very loose sand.
2. The differences in the yielding of sand, resulting from loading in different directions, were captured through a stress ratio, M_p. The stress ratio can be measured directly from the undrained effective stress path of sand sheared while at a contractive state. The stress ratio is used to account for the effects of density, pressure, and direction of loading on the yielding of sand. The position and movement of the yield surface can be traced using this stress ratio.
3. A single set of model parameters was used to predict responses of sand at a wide range of densities and consolidation stresses, subjected to loading in different directions. A unique ultimate state line is used in the model, regardless of the direction of loading. Model parameters were related to the fundamental and well-established concepts of soil strength and deformability; they can be measured readily from routine tests and have clear physical meaning.

4. The friction angle at phase transformation is not always equal to that at the ultimate state. A simple linear dependency of the friction angle, $sin\varphi_f$ (or $sin\varphi_{PT}$), on the state parameter was adopted, and shown to approximate experimental results reasonably well. This allowed for the comparison of the behavior in triaxial compression and triaxial extension with a single stress variable, which is independent of the intermediate principle stress.
5. The maximum friction angle attainable at failure was assumed to depend on the current state parameter. In this formulation, the value of $\sin\phi$ at failure is linearly related to the state parameter, similar to other strength-related parameters.

7.3.2 Model Elements

Each element of the constitutive model is discussed separately in this section. Relationships presented in Imam (1999) can be used with the model elements to obtain the stress-strain relationship. The model elements presented here focus on isotropic consolidation and subsequent triaxial compression.

a) The Yield Surface

The yield surface defines the yielding stresses or the direction of loading in a constitutive model. This element distinguishes many constitutive models from one another. The yield surface was a focal point of the model developed by Imam (1999).

Based on the results of experimental studies, the following yield function was adopted to define the yield surface of sands (isotropically consolidated) in the p-q stress space:

$$\eta^2 - 5M_p^2\left(1-(p/p_c)^{1/2}\right)=0 \qquad [7.27]$$

where:

η = the current ratio of the deviatoric stress, q ($q = \sigma_1 - \sigma_3$), to the mean normal stress, p ($p = (\sigma_1+\sigma_2+\sigma_3)/3$))

M_p = the ratio q/p at the point where the peak value of q occurs

p_c = the consolidation pressure.

Figure 7.3 shows the shape of the yield surface compared with experimental yield points.

By determining the values of the yield parameters p_c and M_p for experimental results, Imam found that the peak stress ratio, M_p, was related linearly to the void ratio of the sand, as shown in Figure 7.4. If the value of M_p as a function of void ratio is substituted into Equation [7.27], then the yield surface becomes a function of the void ratio and consolidation pressure.

Using the above procedure, Imam plotted the equation defining the yield surface, with a specified void ratio and consolidation pressure (Figure 7.5). The effective stress path for a sample tested in undrained triaxial compression, with the same void ratio and consolidation pressure was also plotted. The two curves closely resemble each other. Therefore, Imam concluded that for loose states, the undrained effective stress path could be used to represent the yield surface for the same void ratio and consolidation pressure.

The above observation lead Imam to suggest that the stress ratio at the peak of the yield surface could be approximated by the stress ratio at the peak point of the undrained effective stress path. The agreement between the two methods to obtain M_p was very good.

b) The Plastic Potential

In constitutive modeling, a plastic potential function, or a flow rule, defines the direction of plastic flow. In clays, it is often assumed that an "associative flow rule", which assumes that the direction of loading coincides with the direction of plastic strains, will produce realistic modeling of soil behavior. However, sands are known for their non-associative plastic behavior. The non-associative behavior necessitates the establishment of yield surfaces and plastic potentials for sands separately.

In the model proposed by Imam (1999), the plastic potential was based on Rowe's stress dilatancy relationship (Rowe 1962) as formulated by Wood (1990). Wood's formulation for triaxial compression is as follows:

$$d = \frac{d\varepsilon_p}{d\varepsilon_q} = \frac{9(M_{c,c} - \eta)}{9 + 3M_{c,c} - 2M_{c,c}\eta} \qquad [7.28]$$

where:

d = rate of sand dilatancy

$d\varepsilon_p$ = $(d\varepsilon_1 + 2d\varepsilon_3)$ where $d\varepsilon_1$ and $d\varepsilon_3$ are the major and minor strain increments, respectively

$d\varepsilon_q$ = $(2(d\varepsilon_1 - d\varepsilon_3)/3)$ where $d\varepsilon_1$ and $d\varepsilon_3$ are the major and minor strain increments, respectively

$M_{c.c}$ = stress ratio q/p at the critical state in triaxial compression

η = current stress ratio.

Results reported by Rowe (1962, 1969) showed that a value of friction angle, φ_f, varying about 6 or 7 degrees, gave a realistic soil stress-dilatancy relationship. In constitutive modeling of sands, fixing the friction angle to a value equal to that of the steady state (constant volume) friction angle is more convenient, and may result in acceptable stress-dilatancy relationships for certain soil states. This is particularly true if calibration for other model parameters can compensate for possible changes in the friction angle. This, in addition to the difficulty of determining the variations of φ_f with soil state or density, seemed to be the reason for using a constant value for this angle in the majority of existing models. However, when the behavior of sand over a wide range of states is modeled using a unique set of parameters, it is not possible to adjust model parameters according to soil state or density. In such cases, neglecting variations of φ_f may result in significant deviations of the predicted behavior from the observed response.

In the model proposed by Imam, the variations in φ_f were taken into account by using a variable value of φ_f. The difficulty in determining its variation with soil state or density was resolved by relating it to the friction angle at phase transformation, φ_{PT}. Figure 7.6 shows the variation used. The variation of $sin\varphi_{PT}$ with soil state, ψ, is formulated as a linear dependency as follows:

$$\sin\varphi_{PT} = \sin\varphi_{cv} + k_{PT}\psi \qquad [7.29]$$

where:

k_{PT} = a material constant

φ_{cv} = constant volume friction angle measured from triaxial compression tests

ψ = state parameter

The stress-dilatancy relationship obtained using the above procedure is sufficient to determine the direction of plastic flow of the soil at any state in triaxial compression.

c) Sand Compressibility

Unlike clay, samples of normally consolidated sand can exist at different void ratios under the same consolidation pressure. The model proposed by Imam uses a simplified version of a comprehensive compression model for sands suggested by Pestana and Whittle (1995). The simplified model can be used for the range of pressures encountered in most practical applications. For the case in which only plastic volumetric strains are to be obtained, the simplified version requires only one parameter. This parameter can be determined from compressibility test results on sand at different initial densities. Since the Imam model employs the conventional power law to predict elastic volumetric strains, the simplified relationship that determines only plastic volumetric strains is sufficient.

d) The Hardening Rule

During hardening or softening, the size and/or shape of the yield surface may change. A hardening rule defines the evolution of the yield surface with strains. Size hardening occurs when the value of p_c in Equation [7.27] changes, and shape hardening may occur due to changes in M_p.

(i) Size hardening

During shearing, changes in the size of the yield surface occur such that p_c approaches a value of p_f that corresponds to the size of the yield surface at soil failure. The size of the yield surface at failure, p_f, is determined from the stress ratio of the soil at failure, M_f, which is a function of the current state parameter of the soil.

At any soil state, the increment of hardening caused by an increment of plastic shear strain is a function of the difference between the current size of the yield surface, p_c, and the size of the yield surface at failure, p_f. In the constitutive model being discussed, Imam uses a hardening rule similar in form to that used in the original Nor-sand model (Jefferies 1993). This relationship accounts for hardening that results from the application of shear stresses, which produce both shear and volumetric plastic strains because of the dilatancy characteristics of the material.

Hardening at zero shear stress results in only volumetric changes and is governed by the isotropic consolidation law. The nature of the volumetric strains induced by shearing and isotropic consolidation are different; therefore, different hardening laws govern the two processes.

(ii) Shape of the yield surface

The stress ratio M_p that appears in the equation of the yield surface determines the shape (i.e. the width) of the surface. The stress ratio M_p is a function of the void ratio, as shown in Figure 7.6(a). The initial value of M_p can be determined from the void ratio and pressure at consolidation. Small changes in M_p may occur subsequently during shearing but these changes are neglected to retain simplicity. Imam found that satisfactory model predictions where obtained despite this simplification.

e) Elasticity

Two parameters are needed to characterize the behavior of an isotropic linear elastic material, namely, the elastic bulk modulus K and the elastic shear modulus G. Alternatively, one of these two parameters can be used together with Poisson's ratio such that the other one can be calculated.

Elastic moduli, with power dependency on the mean normal stress, p, were used in Imam's model formulation. As in many other models, a constant value was assumed for Poisson's ratio, and elastic stiffness parameters were used that were functions of the mean normal stress and density.

7.3.3 Model Calibration

If model predictions are to be made for the response of sand to loading in both triaxial compression and triaxial extension, the following parameters need to be determined in the calibration of Imam's model:

a) Shape hardening parameters: a_p, k_p, e_μ
b) Stress-dilatancy parameters; φ_{cv}, a_{PT}, k_{PT}
c) Failure: k_f
d) Sand compressibility parameter: β
e) Elastic parameters: n, G_r, K_r (or ν)
f) Steady (ultimate) state line

If model predictions are to be made only for triaxial compression conditions, 9 parameters will be needed. The position of the ultimate state obtained from triaxial compression tests will also be needed.

Shape hardening parameters: Parameters a_p, k_p, and e_μ can be obtained from results of undrained triaxial compression and extension tests in which the undrained effective stress path exhibits undrained softening after reaching a peak. The void ratio e_μ is the value of the normalized void ratio corresponding to $sin\varphi_u$ in a $sin\varphi_p$ versus e_μ plot (Figure 7.7(a)). The actual value of the interparticle friction angle φ_μ is of less importance since it is an arbitrary reference point on the $sin\varphi_p$ versus e_μ line that helps determine the position of the line along with the slope k_p. A value of 7 degrees smaller than φ_{cv} is assumed for φ_μ. A minimum of two undrained tests are required, preferably with states as far apart as possible, to obtain the parameters required for prediction of triaxial compression.

Stress-dilatancy parameters: Parameters k_{PT} and a_{PT} can be obtained by plotting variations of $sin\varphi_{PT}$ versus ψ obtained from triaxial compression and extension tests (Figure 7.7(b)). A minimum of two triaxial compression tests and one triaxial extension test are required. The angle φ_{cv} is the steady state friction angle reached when the material is sheared to sufficiently large strains such that no volume changes occur upon further loading. This angle can be measured either directly from tests in which the ultimate state is reached, or from plots of $sin\varphi_{PT}$ versus ψ. The value of φ_{PT} corresponding to $\psi = 0$ is taken to be φ_{cv}.

Failure: Parameter k_f determines the variation of the maximum friction angle (or stress ratio) that can be attained at failure, with the current state parameter. This parameter can be determined from friction angles at failure, measured from drained tests at different soil states. In addition to maximum strength, changes in shear strength with strain are also controlled by this parameter. A larger value for k_f results in larger peak strength and more rapid reduction in shear strength after peak.

Compressibility parameter: The parameter β can be determined through the use of an equation (presented in Imam 1999) to fit results of isotropic compression tests on samples with different initial void ratios. Since the rather complicated compression behavior of sand is formulated by a single parameter, β, it is necessary to choose a value for this parameter that gives reasonable predictions for the range of pressures under consideration. Figure 7.8 shows the experimental isotropic compression data used in obtaining parameter β for Ottawa and Toyoura sands. Imam found that the use of a single value for β produced a satisfactory match to the majority of experimental results obtained from tests conducted over a range of pressures encountered in most practical applications.

Elastic parameters: Elastic parameters n, G_r, ν (or K_r) can be determined from results of either unloading or seismic tests. Alternatively, the tangent to the q versus ε_q plot from a drained shear test at the origin can be used to obtain the elastic bulk modulus by fitting it against observed undrained effective stress paths. A typical value of Poisson's ratio can also be used together with measured shear modulus. These latter procedures however, often give substantially smaller values for the elastic moduli compared to values obtained by unloading or seismic tests. This may be due to the development of some plastic strain at points where the slope of the tangent is measured, since identifying the tangent at the origin of the q versus ε_q curve is often difficult.

Steady state parameters: Determination of the position of the ultimate (steady) state line is probably one of the most difficult parts of the calibration procedure of all critical state models for sand. In the model by Imam, the exact position of the line may not significantly affect the predicted response at the small and medium ranges of strain. This is because in this model, the ultimate state line characterizes the behavior at large strains, and other model parameters account for the earlier stages of shearing. A linear $e - \ln p$ relationship is used for sand.

Imam notes that when determining model parameters using individual test results, some adjustments often need to be made in order to achieve the "best fit" to a range of experimental results. This is because experimental results often show some scatter, and model parameters should be selected such that predictions conform to an overall average behavior.

Imam (1999) describes the method of determining the model parameters. The model has been calibrated for Ottawa sand using test data from Sasitharan et al. (1994) and Skopek (1994).

7.3.4 Model Performance

Imam's model was used to predict the response of very loose saturated and dry Ottawa sand in undrained and drained loading conditions along a number of stress paths in the triaxial apparatus. The drained and undrained behavior of Toyoura sand in triaxial compression and triaxial extension was also predicted. A wide range of void ratios and consolidation stresses were covered.

Details of the results of the model predictions can be found in Imam (1999). In general, the model was able to predict the drained and undrained behavior of sands over a wide range of pressures and void ratios using a single set of parameters. A unique ultimate state line was also used for model predictions.

7.3.5 Summary

In summary, a constitutive model for sand based on the concept of critical state soil mechanics developed by Imam (1999) was presented. Model elements, strength, and deformability parameters conform to well-established and widely comprehended concepts related to the behavior of sand. Through the dependency of the stress ratio at the peak of the yield surface, the effects of void ratio, consolidation pressure, and direction of loading on yielding stresses of sand are accounted for.

Unlike the common simplification of using a constant stress ratio at zero dilatancy in the stress-dilatancy relationship of sand, a variable stress ratio was used in the formulation of this model, which was related to mean normal stress and void ratio. The relationship was obtained from measuring the variation of the stress ratio at phase transformation at different soil states. This dependency could be derived directly from Rowe's (1962) stress-dilatancy relationship.

Comparison of model predictions and observed behavior of Ottawa and Toyoura sands showed that the model is able to predict drained and undrained behavior of sands over a wide range of pressures and void ratios.

7.4 MODELING THE CONSTITUTIVE BEHAVIOR OF LOOSE GASSY SAND

7.4.1 The Model

The constitutive model proposed by Imam (1999), described in the previous sections, predicts the behavior of loose saturated sands, especially those susceptible to liquefaction. A simplified version of the model enables prediction of triaxial compression tests results only. This version was modified to take into account the effects of gas. The modification involved incorporating in Equation [7.26]. After one increment of model prediction, the results (the effective mean normal stress, change in normal stress, and void ratio) were input into the modification (Equation [7.26]). Hilf's analysis as presented in Equation [7.26] was used to calculate the change in void ratio and degree of saturation as a result of the change in pressure. The new void ratio was inputted back to the model and the process was repeated.

7.4.2 Model Performance

a) Modeling the Effect of Gas

The modified model was used to predict the effect of degree of saturation on the undrained behavior of loose sand. The original model by Imam was calibrated for Ottawa sand using test results from Sasitharan (1994) and Skopek (1994); the resulting calibration parameters were used in the modified model to test the effect of gas. The parameters are given in Table 7.1. A series of model predictions were made with a fixed void ratio of 0.80 and a fixed consolidation pressure of 300 kPa. The initial degree of saturation was varied from 95% to 70%. A saturated test was also included as a reference.

Figures 7.9 and 7.10 present the results of the model predictions for various degrees of saturation. The stress strain curves (Figure 7.9 (a)) show that samples with higher degrees of saturation strain softened but as the degree of saturation decreased below about 90%, the samples began showing a strain hardening behavior. The effective stress paths, presented in Figure 7.9 (b), showed similar results. The saturated specimen experienced complete strain softening. As the degree of saturation decreased from 100% to 95%, a quasi-steady state behavior was observed. In a quasi-steady state response, the sample strain softens to some minimum (called phase transformation) and then, with increasing strain, begins to strain harden. The sample with 90% degree of saturation still experienced a fair amount of strain softening before subsequent hardening. The stress strain curves and the stress paths for this model prediction showed that flow liquefaction may occur for samples with degrees of saturation greater than about 85%. For samples with degrees of saturation less than 85%, the potential of flow liquefaction was low.

Figure 7.10 (a) presents a plot of void ratio versus effective mean normal stress. As expected, the void ratio of the specimens in the saturated test did not change, because of the condition of no drainage. However, the gassy samples decreased in void ratio as the effective mean normal stress decreased. The lower the initial degree of saturation, the greater the decrease in void ratio over the same increment of effective stress decrease. This was partially due to the increased compressibility of the samples with low degrees of saturation. As the phase transformation point was reached, the effective mean normal stress began to rise; the void ratio of the gassy samples also increased after the phase transformation point. The increase in void ratio showed a smaller change in void ratio over effective mean normal stress than the decrease (i.e. it became more gradual). The laboratory results of the gassy specimens also showed that if there was an increase in void ratio after an initial decrease, then the increase was more gradual.

Figure 7.10 (b) shows the degree of saturation versus effective mean normal stress. The initial degrees of saturation ranged from 70% to 95%. In all samples, the degree of saturation increased slightly with decreasing effective mean normal stress. The increase was due to a small increase in pore pressure. Samples with lower initial degrees of saturation showed a greater increase in saturation over the same interval of effective mean normal stress. As the phase transformation point was reached and the effective mean normal stress began to decrease, the degree of saturation decreased at a more dramatic rate.

The modified model was able to account for the effects of gas in the behavior of loose sands. The modification to the constitutive model developed by Imam (1999) enabled the behavior of loose gassy sand to be captured and predicted.

b) Modeling the Collapse Behavior of Loose Saturated Ottawa Sand

The results of undrained saturated triaxial compression tests were predicted in order to calibrate the model. The model parameters obtained from saturated tests are shown in Table 7.1. Figures 7.11 and 7.12 present the test results along with the model predictions.

Figures 7.11 and 7.12 show that the model predicted the observed response well. The peak deviator stress and the subsequent strain softening characteristics of the laboratory tests were matched by the model. The final state (or steady state) was also predicted well. The laboratory tests, however, showed a small increase in effective mean normal stress at the beginning of loading that was not predicted by the model. This difference between the predicted and observed response at the beginning of loading is not considered significant.

c) Modeling the Collapse Behavior of Loose Gassy Ottawa Sand

The modified model was used to predict the behavior of samples of loose gassy sand tested in undrained triaxial compression. The predicted behavior of three typical gassy tests was compared to the observed behavior.

Figures 7.13 and 7.14 show the model predictions for a strain softening gassy sample. The model was able to predict the observed response very well. The peak and final points of the stress strain curves and effective stress paths for the prediction matched the tests results. However, similar to the saturated results, the model was unable to capture the small increase in effective mean normal stress, which was observed at the initial stages of loading. Figure 7.14 (a) shows the change in void ratio with effective mean normal stress. The degree of saturation is plotted against the effective mean normal stress in Figure 7.14 (b). These figures show that the model predicted both the void ratio and degree of saturation well. The predicted results of a typical strain softening gassy sample had good agreement with the observed behavior.

A gassy specimen, which displayed a quasi-steady state response to undrained loading, was modeled in Figures 7.15 and 7.16. The stress strain response and the effective stress paths are shown in Figure 7.15. As can be seen from this figure, the peak and final stress points predicted by the model were approximately the same as the laboratory test results. The predicted response matched the observed behavior reasonably well. In both responses, the sample reached a peak and then experienced subsequent strain softening. Changes in void ratio can be observed in Figure 7.16 (a). The match between the model and laboratory results was acceptable. Although, both results showed a decrease in void ratio with decreasing effective stress, the model results decreased at a faster rate and tended towards a lower void ratio. Figure 7.16 (b) shows the predicted and observed degree of saturation behavior. The model and laboratory results corresponded with both results tending towards a similar final degree of saturation, with an increase in saturation upon decreasing effective mean normal stress. A typical gassy sample, displaying a quasi-steady state response to loading, was predicted with reasonable accuracy by the model.

Finally, Figures 7.17 and 7.18 present the results of a strain hardening gassy sample predicted using the modified model. The stress strain curves in Figure

7.17(a) show that the observed behavior was somewhat different from the model prediction. The observed response showed a continual increase in deviator stress with increasing axial strain while the predicted response showed an increase in deviator stress until approximately 4% strain, where the deviator stress leveled off. The effective stress paths (Figure 7.17(b)) also showed a different observed and predicted response. The laboratory results showed an increase in effective mean normal stress while the model results showed an initial small decrease in effective mean normal stress and then a subsequent increase. The stress paths showed that the model and laboratory results approached a similar end point. The changes in void ratio are shown in Figure 7.18(a). Although the model and laboratory results were not a perfect match, the general trend of both results was the same. The model showed an initial decrease in void ratio followed by an increase. The laboratory results also showed an initial decrease in void ratio followed by an increase. In addition, the laboratory and model results tended toward the same void ratio. The degree of saturation predictions shown in Figure 7.18(b) also exhibited a response similar to the observed behavior. In both cases the degree of saturation initially increased and then decreased. Again, the model and laboratory results tended toward a similar final degree of saturation. The final state and the general trend of the strain hardening gassy samples was predicted well using the modified model. There were, however, some differences between the path followed by the model and laboratory results to get to the final state.

d) Modeling the Effect of Gas Characteristics

In Section 5.6.5, the effect of the gas characteristics on the potential for flow liquefaction was discussed. The modified model described in this chapter was used to confirm the differences in behavior between a soluble gas, such as carbon dioxide (CO_2) and a less soluble gas such as methane (CH_4). The model parameters are listed in Table 7.1. The Henry's coefficient for methane was taken to be one order of magnitude less than that for carbon dioxide.

The results of the predictions are shown in Figures 7.19 and 7.20. The stress strain curves and effective stress paths show that as the deviator load is applied, the carbon dioxide gas goes into solution more rapidly than methane, therefore, pore pressures built up quicker and the effective stress drop is lower. The undrained shear strength, or the minimum stress, was lower for the sample containing carbon dioxide gas. Figure 7.20 (a) shows that the void ratio decreased more rapidly in the sample containing methane, and reached a lower value than the sample containing carbon dioxide. In Figure 7.20(b) the saturation behavior reveals that the carbon dioxide gas went into solution more rapidly thereby resulting in slightly lower peak degree of saturation. These results indicate that for two similar samples, the one containing carbon dioxide gas would be slightly more susceptible to liquefaction. In other words, using carbon dioxide gas in the laboratory to determine the liquefaction potential of loose gassy sand (which in nature usually contains methane gas) leads to a slightly conservative liquefaction assessment.

7.4.3 Model Performance and Limitations

Overall, the modified model performed well. It appears that specimen end effects may have influenced the pore pressures measured in the laboratory, and therefore higher pore pressures could have existed in the middle of the specimen. The end effects, combined with the presence of gas, could have created a small time lag between the measured and actual pore pressures. An unequal pore pressure distribution and a time lag would have the effect of shifting the laboratory stress path slightly to the left, closer to the model predicted stress path. The influence, or stress path shift, would increase with greater gas content, and may partially explain why the model did not predict as well the response of specimens with higher gas contents.

The significant shortcoming observed from comparison of laboratory results with model predictions was the inability of the model to predict the slight increase in effective mean normal stress that was observed in the initial stages of all the undrained triaxial tests.

This increase in effective stress was most noticeable when looking at the effective stress paths. The samples with lower initial degrees of saturation (the strain hardening samples) exhibited a greater increase in effective mean normal stress. The initial increase in mean normal effective stress was because no pore pressures developed at the beginning of loading. Probably, no pore pressures developed because as the initial load was applied, no particle rearrangement took place due to the bubbles and their meniscus taking a small amount of load. A similar behavior has been observed with the bonded water of clay particles as noted by Schumann (1994). Hence, the model did not predict the behavior of strain hardening samples as well as it predicted the behavior of strain softening samples.

A second shortcoming was the assumption that surface tension did not influence the gassy specimen responses. The assumption that surface tension affects could be ignored was inherent in Hilf's analysis presented in Section 7.2.3. Satisfactory results have been obtained using Hilf's analysis, without the addition of complicated surface tension influences. However, if surface tension affects were accounted for, it would be expected that the predicted pore pressures would be slightly lower and therefore the model and laboratory results would have a greater discrepancy.

A third shortcoming was that the model was intentionally formulated for the equilibrium behavior of gassy samples and therefore, did not take into account the "real" transient response. To model the transient response would be significantly more difficult. Since the model was able to predict the response within a reasonable degree of accuracy, the immediate objectives of this thesis were satisfied. However, future work might include modifying the model to account for the transient response of gassy sands.

7.5 SUMMARY AND CONCLUSIONS

The results of this modeling program shows that the theoretical behavior of loose gassy sand can be investigated with the use of a constitutive model.

The equilibrium behavior of gassy soils in response to an application of total stress is governed by the compressibility of the free gas and the solubility of the gas in the pore liquid. Boyle's and Henry's laws govern these physical processes and from these laws the theoretical compressibility of a liquid/gas can be developed. The compressibility of a liquid/gas mixture is used in a procedure developed by Hilf (1948) to calculate the pore pressure change in gassy or unsaturated soils subjected to an applied total stress. Hilf's analysis relates the change volume due to the compression (and solution) of gas. This simple representation of gas response was used to modify an existing constitutive model developed by Imam (1999) to account for the presence of gas.

Although a number of constitutive models have been developed to predict the behavior of saturated sands, few focussed on the collapse behavior of loose sands. The constitutive model developed by Imam (1999), focuses on assessing the liquefaction susceptibility of loose sands over a wide range of states and loading conditions. The model was formulated based on critical state soil mechanics. Model elements, strength, and deformability parameters conform to well-established and widely comprehended concepts related to the behavior of sand. The dependency of the stress ratio at peak on the yield surface accounts for the effects of void ratio, consolidation pressure, and direction of loading on the yielding stresses. A variable stress ratio, related to mean normal stress and void ratio, is used in the model formulation. The model is able to predict the observed behavior of sands in drained and undrained loading over a wide range of pressures and void ratios.

The model developed by Imam (1999) was modified to take into account the behavior of gassy sands. The modification was achieved by introducing the compressibility and solubility of the pore gas and liquids, as described by Hilf. The modified model was used to predict the effect of degree of saturation on the undrained behavior of loose sand. The laboratory saturated and gassy tests were also modeled, in addition to the effect of gas characteristics. The model performed well and showed that as degree of saturation decreases, the susceptibility to liquefaction also decreases. Predicted responses of the saturated and gassy test results, which showed a strain softening behavior, matched the observed behavior well. The predictions of gassy test results that exhibited a strain hardening behavior were not as accurate, however, the general trend of an increase in void ratio and decrease in degree of saturation was predicted.

The modified model was also used to confirm that a sample containing a more soluble gas (i.e. carbon dioxide as opposed to methane) would show a greater susceptibility to liquefaction; hence, laboratory tests which use carbon dioxide gas to represent sediments containing methane, will lead to conservative liquefaction predictions.

The major shortcoming of the modified constitutive model was the inability of the model to predict the slight increase in effective mean normal stress that was observed in the initial stages of all the undrained triaxial tests. This resulted in some inaccuracy in the prediction of strain hardening gassy samples.

Table 7.1 - Model parameters used in predictions for Ottawa sand. All unit dependent parameters are given assuming that (p) is substituted in the equations in terms of kPa, except where stated otherwise.

Parameter Type	Parameter name	from Imam (1999)	from this study
Peak state	k_p	1.6	1.8
	e_μ	0.76	0.8
	a_p		
Stress-dilatancy	φ_{cv}	28.5	37
	k_{PT}	1	1
	a_{PT}		
Failure	k_f	0.75	0.75
Compression	β	0.012	0.02
Elastic	G_r	500	500
	K_r	1000	1000
	n	0.55	0.55
Ultimate State Line	$e_{ss} =$	$0.867-0.0167\ln p_{ss}$	$0.92-0.0159\ln p_{ss}$

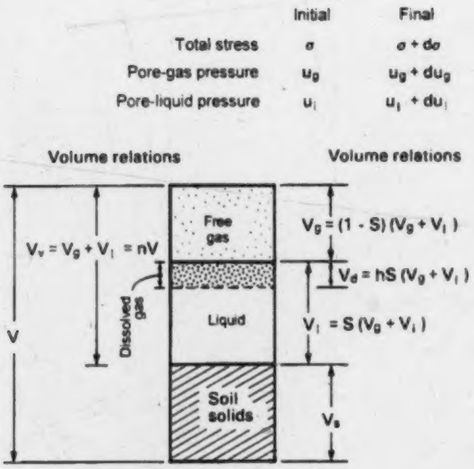
Initial
Final
Total stress
σ
$\sigma + d\sigma$
Pore-gas pressure
u_g
$u_g + du_g$
Pore-liquid pressure
u_l
$u_l + du_l$
Volume relations
Volume relations
$V_v = V_g + V_l = nV$
V
Dissolved gas
Free gas
Liquid
Soil solids
$V_g = (1 - S)(V_g + V_l)$
$V_d = hS(V_g + V_l)$
$V_l = S(V_g + V_l)$
V_s

Figure 7.1 - Volumetric composition of the pore fluid in an unsaturated (gassy) soil (modified from Fredlund and Rahardjo 1993).

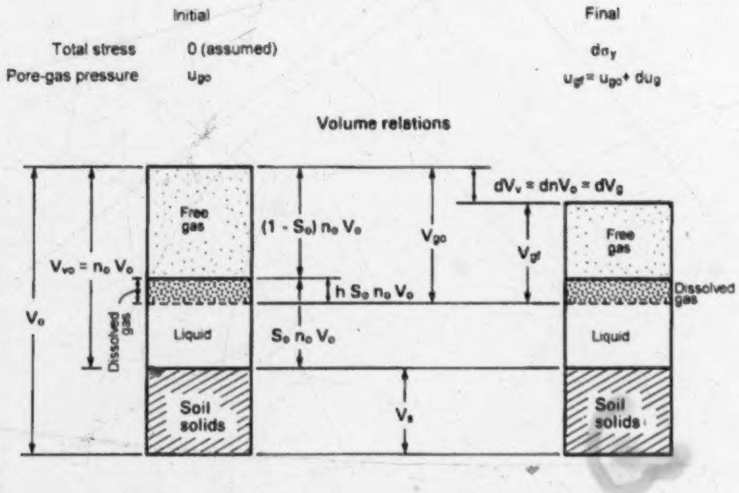
Initial
Final
Total stress
0 (assumed)
$d\sigma_y$
Pore-gas pressure
u_{go}
$u_{gf} = u_{go} + du_g$
Volume relations
$dV_v = dnV_o = dV_g$
Free gas
$(1 - S_o)\, n_o\, V_o$
V_{go}
V_{gf}
Free gas
$V_{vo} = n_o\, V_o$
$h\, S_o\, n_o\, V_o$
Dissolved gas
V_o
Dissolved gas
Liquid
$S_o\, n_o\, V_o$
Liquid
Soil solids
V_s
Soil solids

Figure 7.2 - Initial and final pressure and volume conditions considered in Hilf's analysis (modified from Fredlund and Rahardjo 1993).

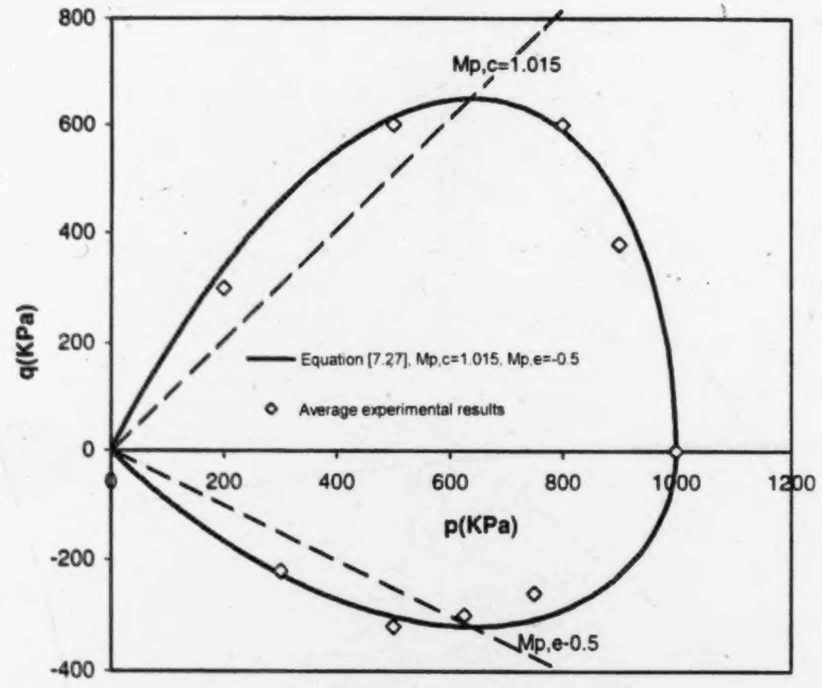

Figure 7.3 - Yield surface with reduced friction angle at peak in extension, compared with experimental yield stresses (modified from Imam 1999).

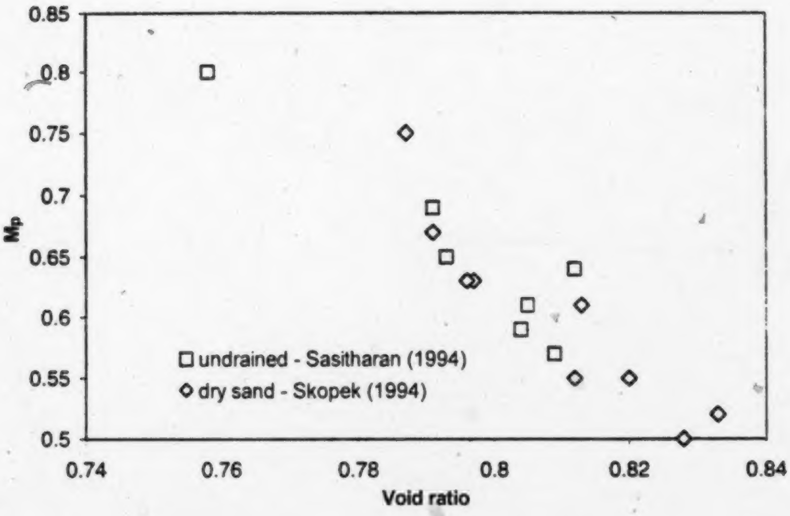

Figure 7.4 – Variation of stress ratio at peak (Mp) with void ratio obtained from drained constant deviator stress tests and undrained triaxial compression tests (modified from Imam 1999).

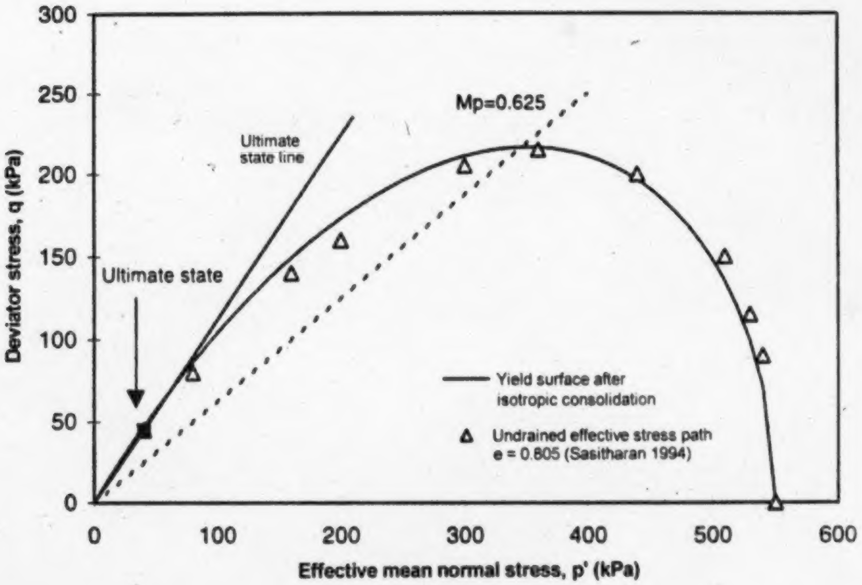

Figure 7.5 - Comparison of the undrained effective stress path (UESP) with the shape of the yield surface for a sample of Ottawa sand with a void ratio of 0.805 consolidated to 550 kPa (modified from Imam 1999).

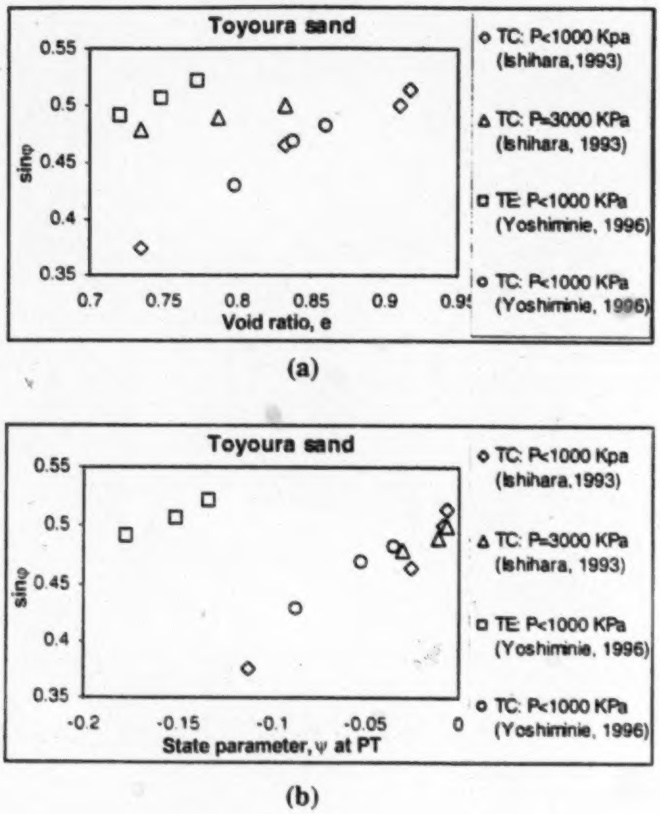

Figure 7.6 - Correlation of the friction angle at phase transformation (PT) with void ratio and state parameter (modified from Imam 1999).

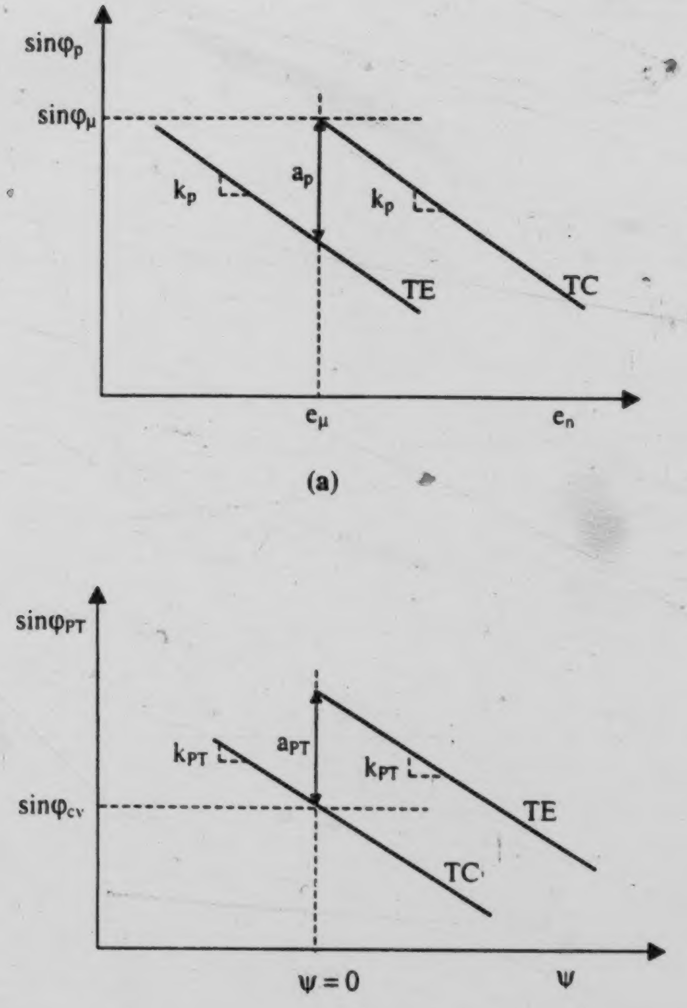
sinφ$_p$
sinφ$_μ$
k$_p$
a$_p$
k$_p$
TE
TC
e$_μ$
e$_n$
sinφ$_{PT}$
k$_{PT}$
a$_{PT}$
k$_{PT}$
sinφ$_{cv}$
TE
TC
ψ = 0
ψ

(a)

(b)

Figure 7.7 - Definition of model parameters used to determine friction angles of sand: (a) at the peak of the yield surface (b) at phase transformation (modified from Imam 1999).

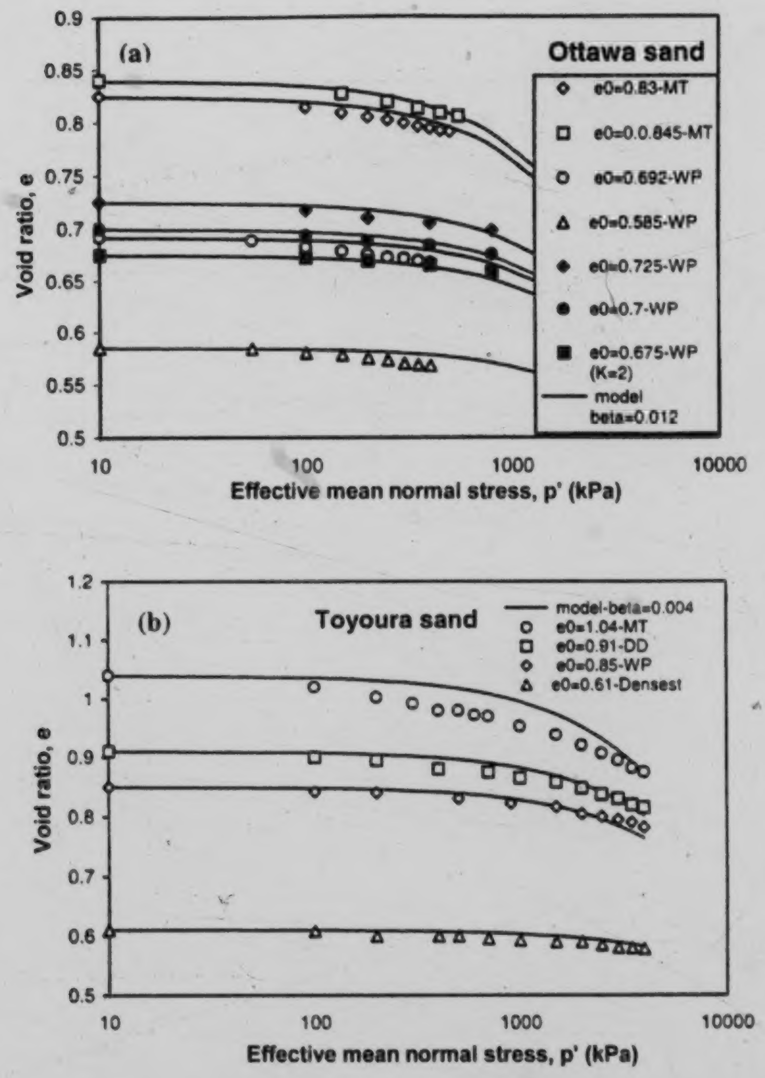

Figure 7.8 - Determination of the compressibility parameter β (Pestana and Whittle 1995) using compression data on Ottawa and Toyoura sands. Samples were prepared using moist tamping (MT), water pluviation (WP) and dry deposition (DD) methods (modified from Imam 1999).

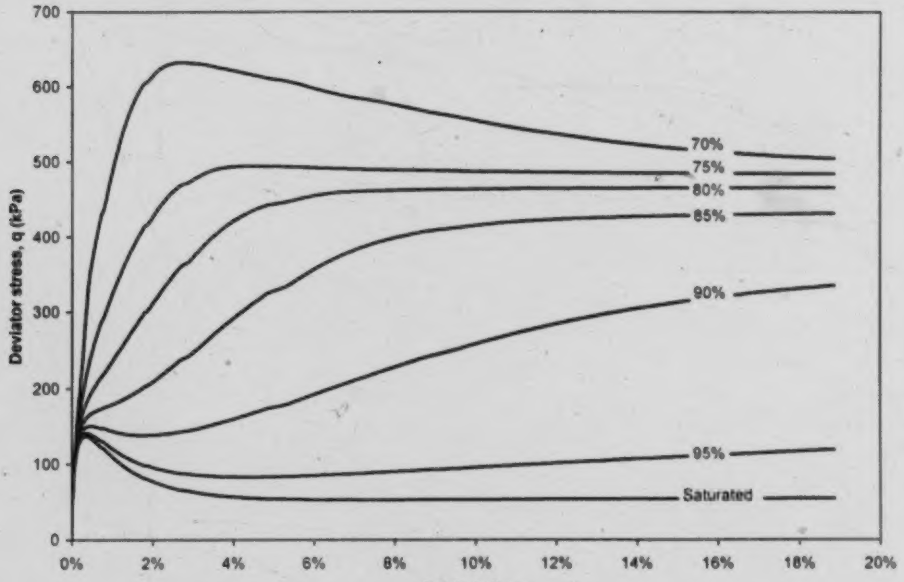

(a) Stress strain curves

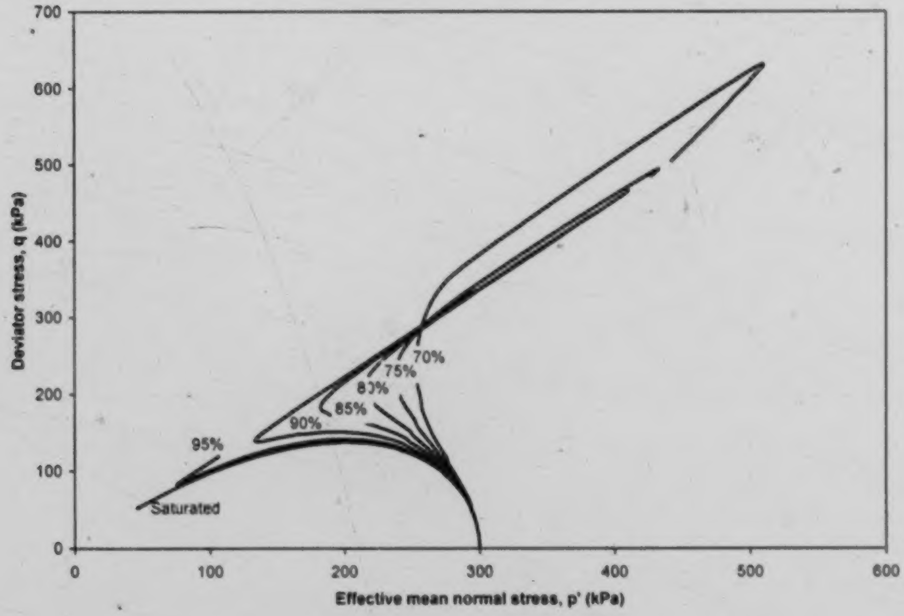

(b) Effective stress paths

Figure 7.9 – Model predictions of saturated and gassy undrained triaxial compression tests with void ratios of 0.80 and consolidation pressures of 300 kPa.

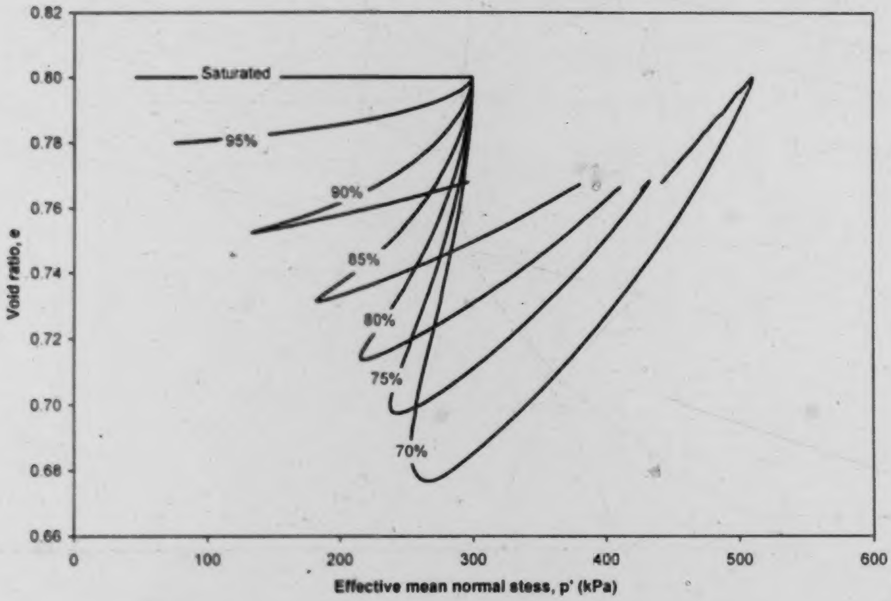

(a) Void ratio versus effective mean normal stress

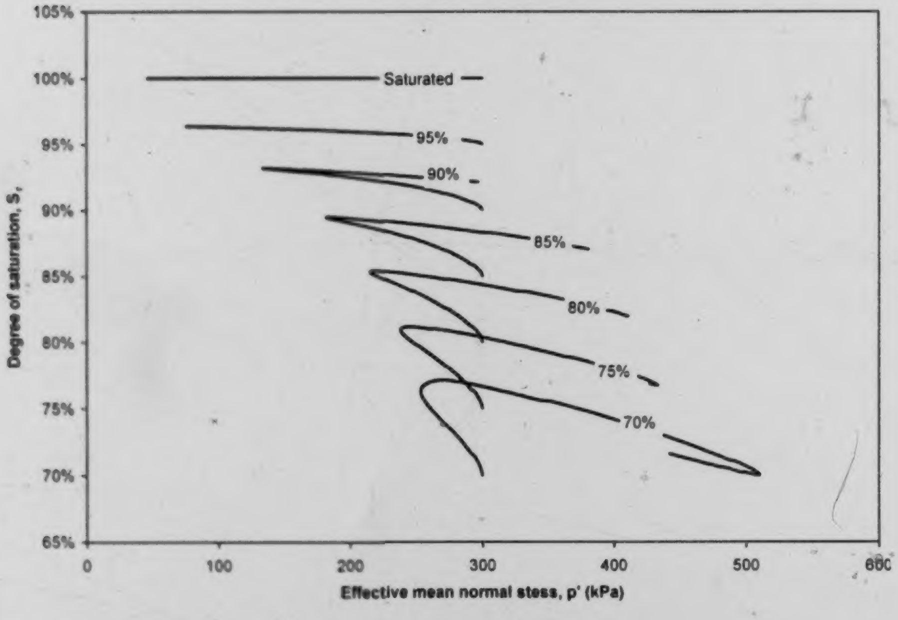

(b) Degree of saturation versus effective mean normal stress

Figure 7.10 - Model predictions of saturated and gassy undrained triaxial compression tests with void ratios of 0.80 and consolidation pressures of 300 kPa.

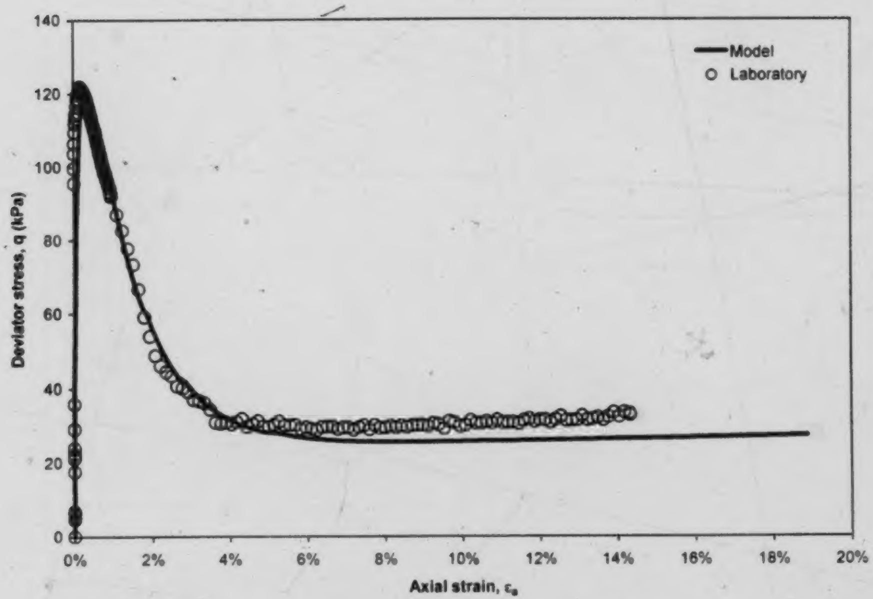

(a) Stress strain curves

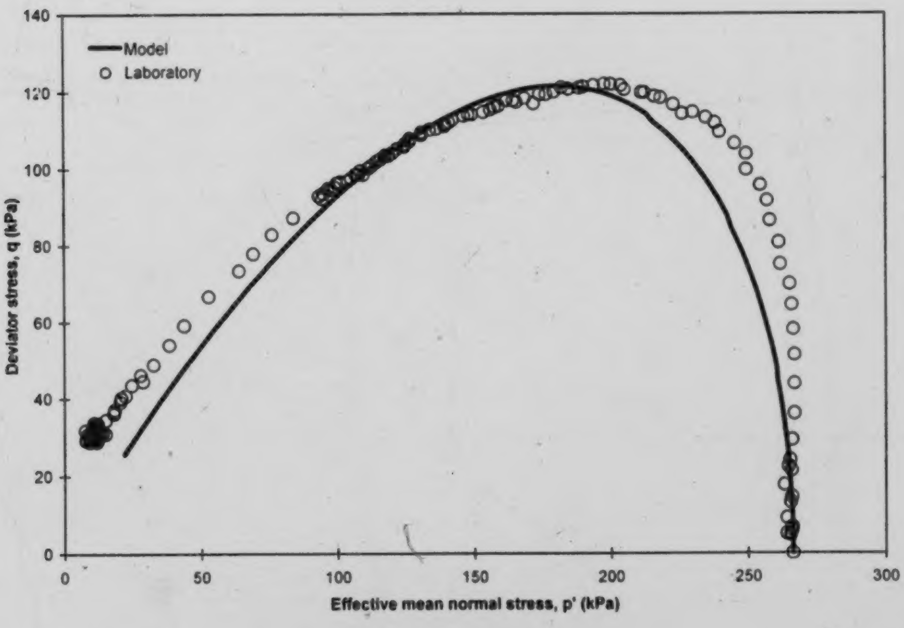

(b) Effective stress paths

Figure 7.11 - Predicted and observed response for Sample #11, saturated, consolidated undrained with a void ratio of 0.89 and a consolidation pressure of 266 kPa.

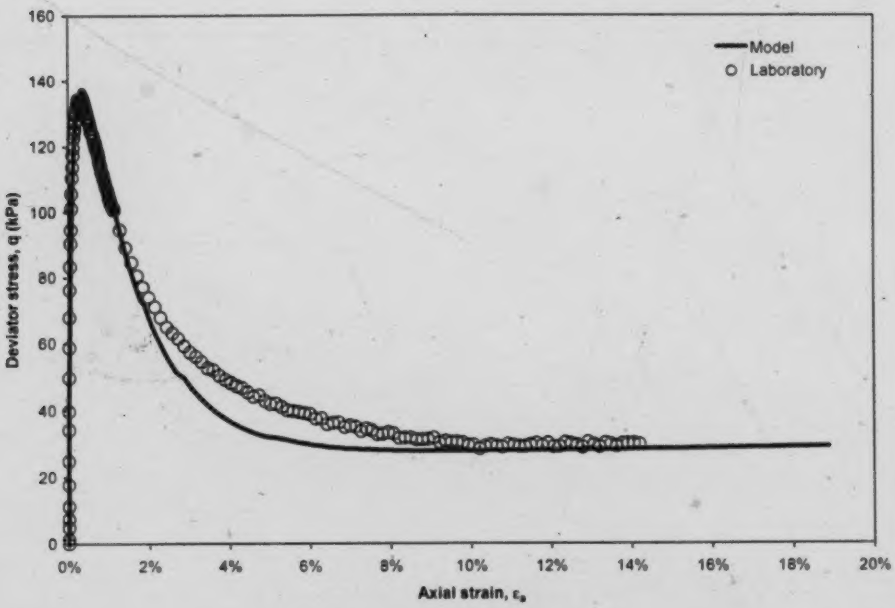

(a) Stress strain curves

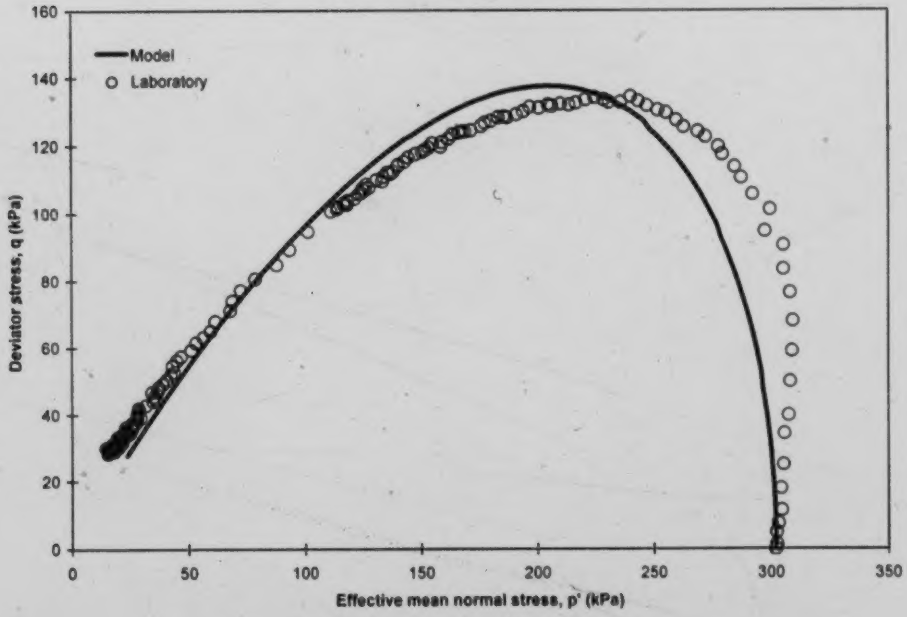

(b) Effective Stress paths

Figure 7.12 - Predicted and observed response for Sample #12, saturated, consolidated undrained with a void ratio of 0.91 and a consolidation pressure of 302 kPa.

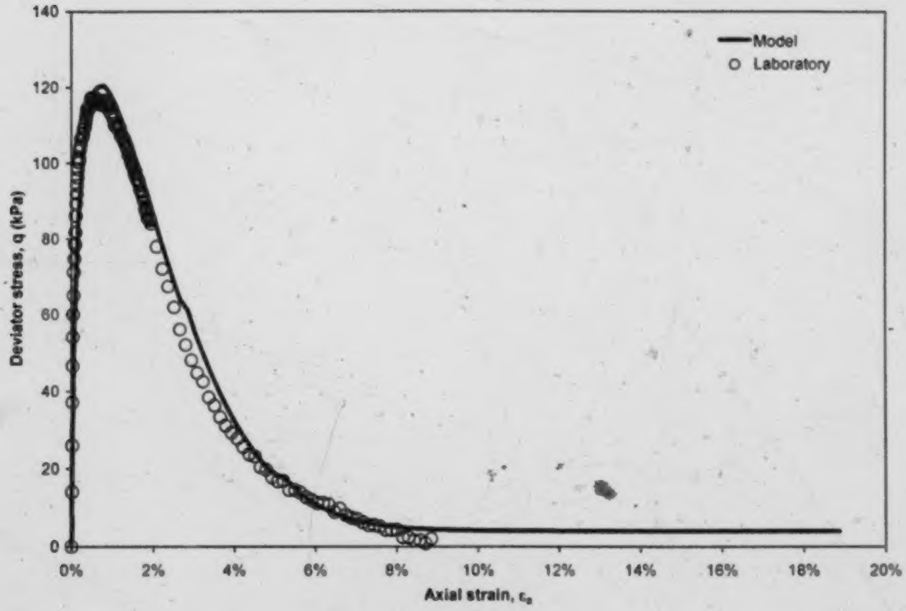

(a) Stress strain curves

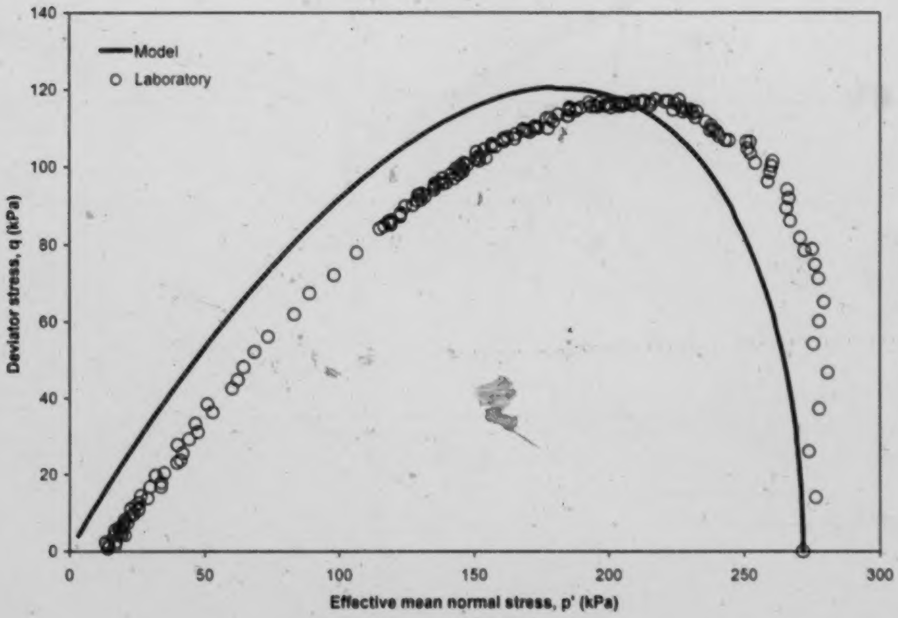

(b) Effective stress paths

Figure 7.13 - Predicted and observed response for Sample #25, gassy, consolidated undrained with a void ratio of 0.85, a consolidation pressure of 272 kPa, and an initial degree of saturation of 91%.

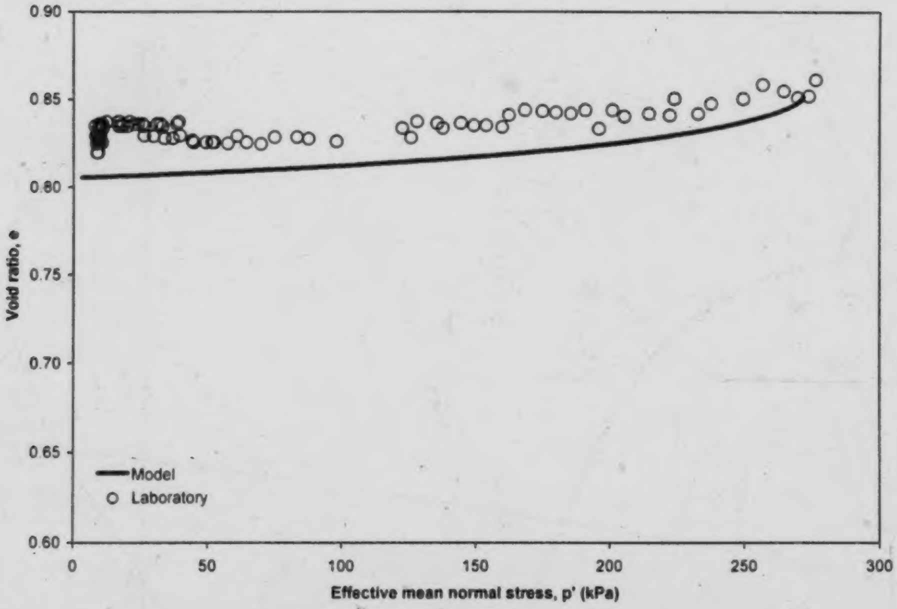

(a) Void ratio versus effective mean normal stress

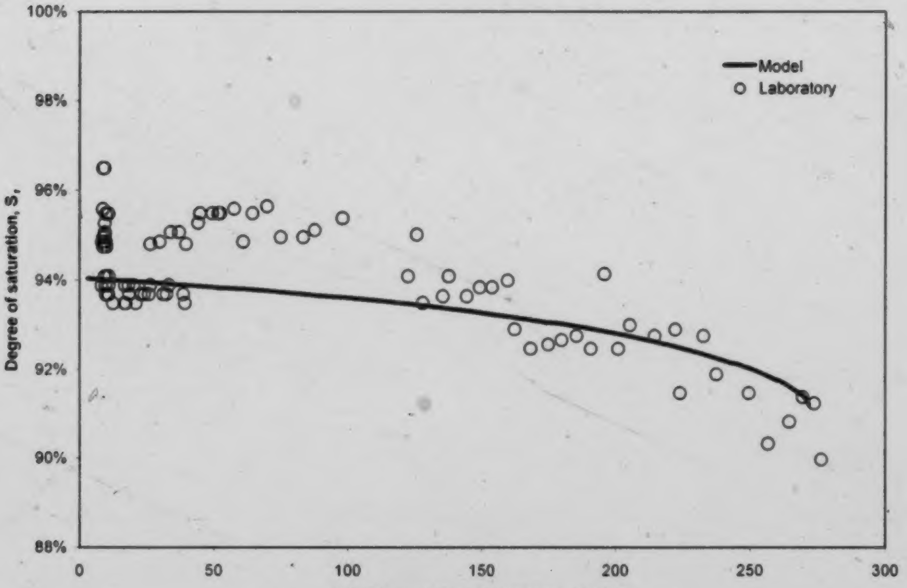

(b) Degree of saturation versus effective mean normal stress

Figure 7.14 - Predicted and observed response for Sample #25, gassy, consolidated undrained with a void ratio of 0.85, a consolidation pressure of 272 kPa, and an initial degree of saturation of 91%.

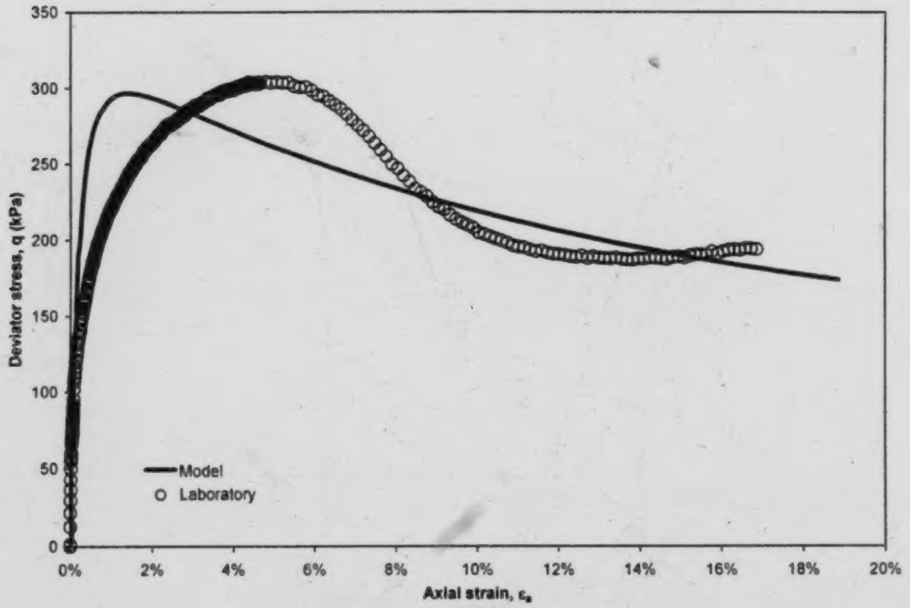

(a) Stress strain curves

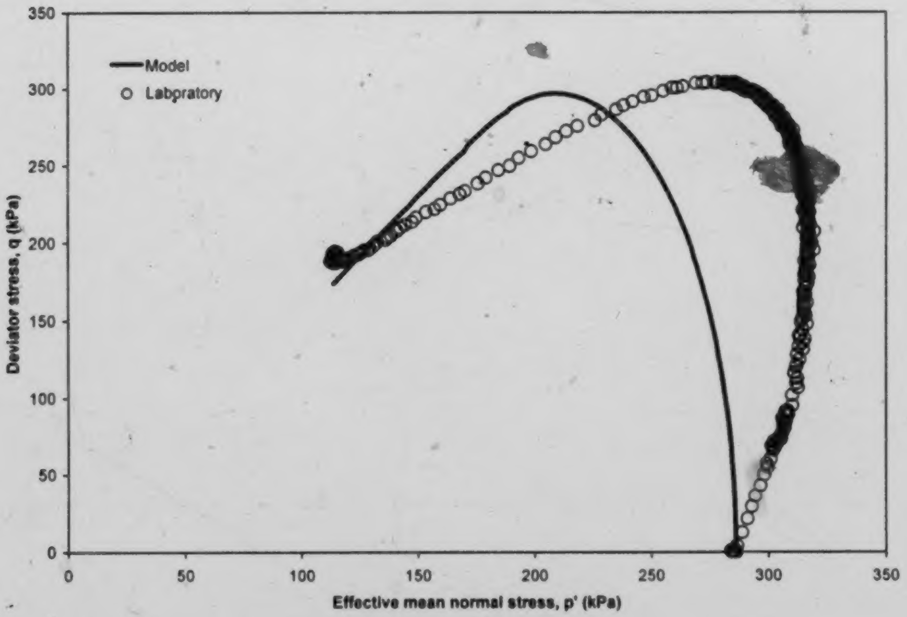

(b) Effective stress paths

Figure 7.15 - Predicted and observed response for Sample #8, gassy, consolidated undrained with a void ratio of 0.92, a consolidation pressure of 286 kPa, and an initial degree of saturation of 80%.

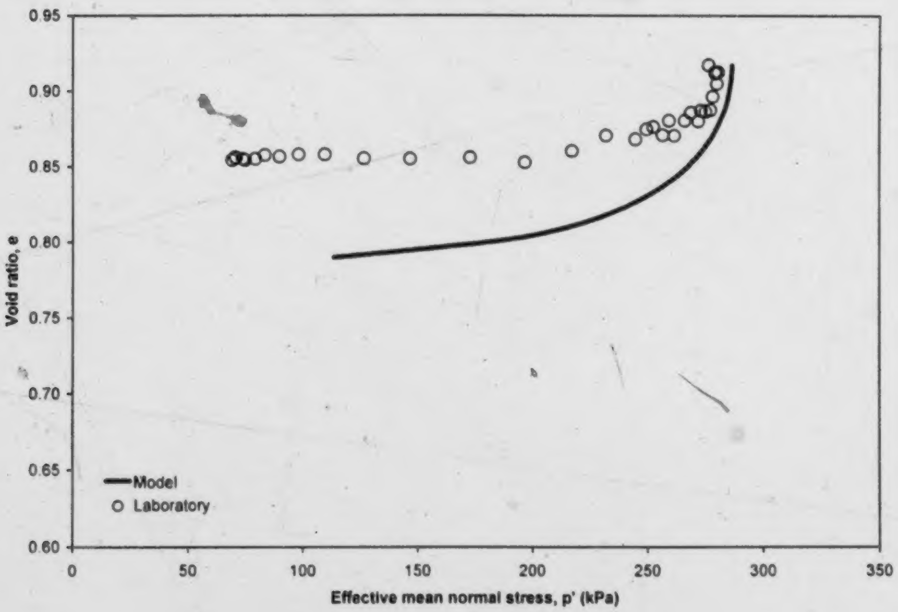

(a) Void ratio versus effective mean normal stress

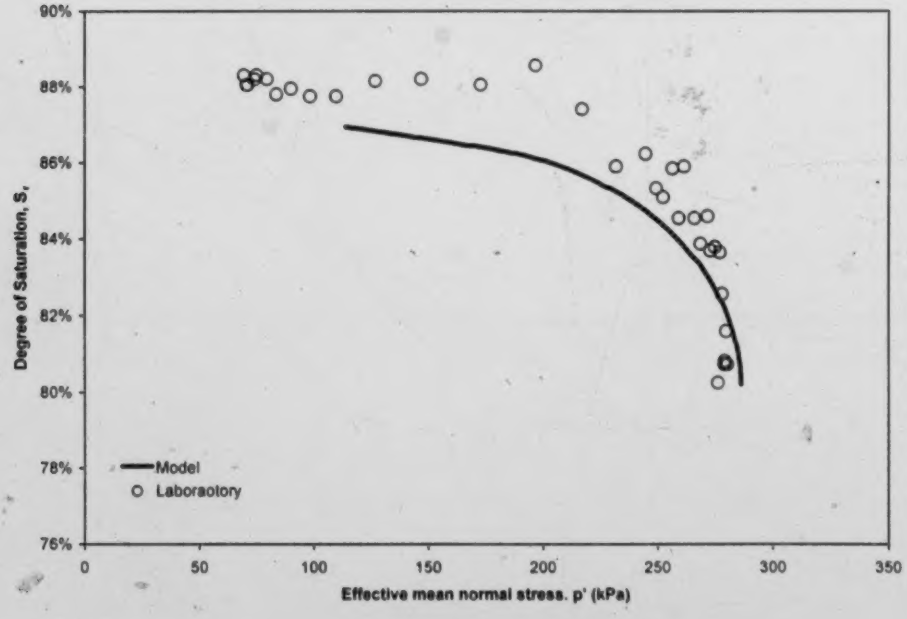

(b) Degree of saturation versus effective mean normal stress

Figure 7.16 - Predicted and observed response for Sample #8, gassy, consolidated undrained with a void ratio of 0.92, a consolidation pressure of 286 kPa, and an initial degree of saturation of 80%.

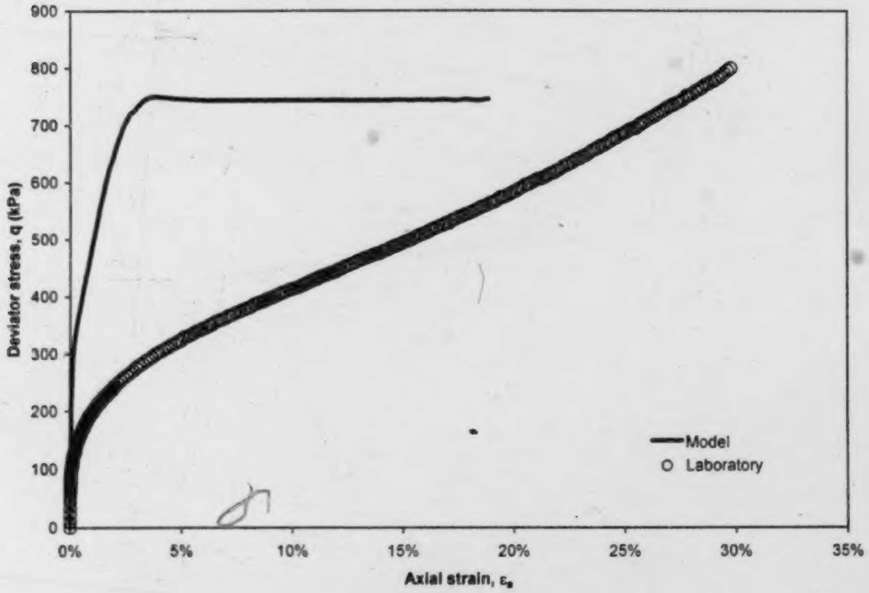

(a) Stress strain curves

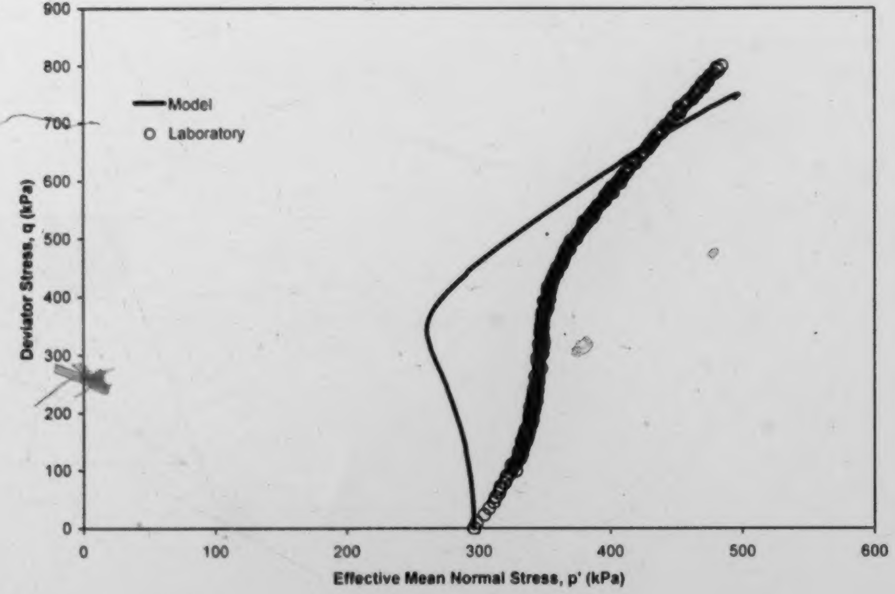

(b) Effective stress paths

Figure 7.17 - Predicted and observed response for Sample #21, gassy, consolidated undrained with a void ratio of 0.90, a consolidation pressure of 296 kPa, and an initial degree of saturation of 80%.

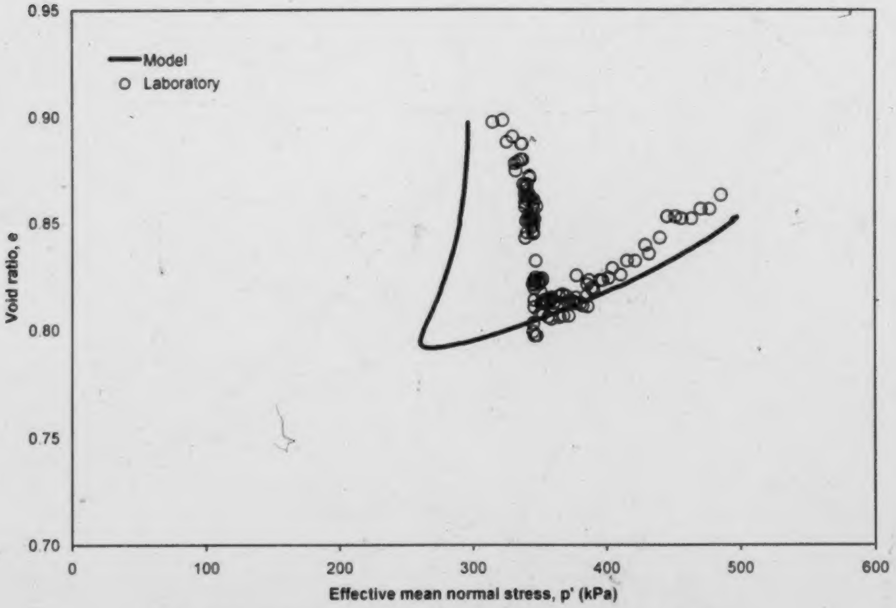

(a) Void ratio versus effective mean normal stress

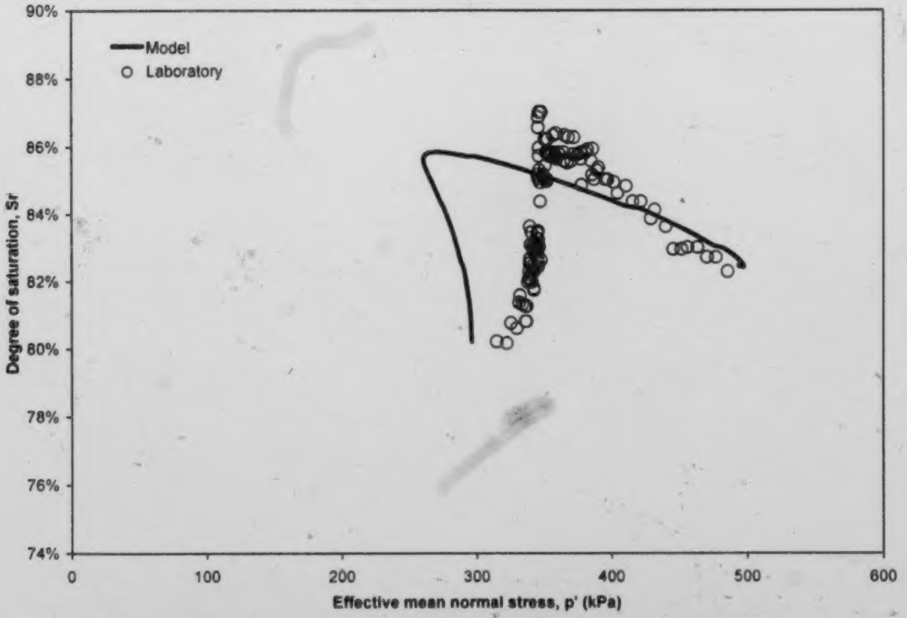

(b) Degree of saturation versus effective mean normal stress

Figure 7.18 - Predicted and observed response for Sample #21, gassy, consolidated undrained with a void ratio of 0.90, a consolidation pressure of 296 kPa, and an initial degree of saturation of 80%.

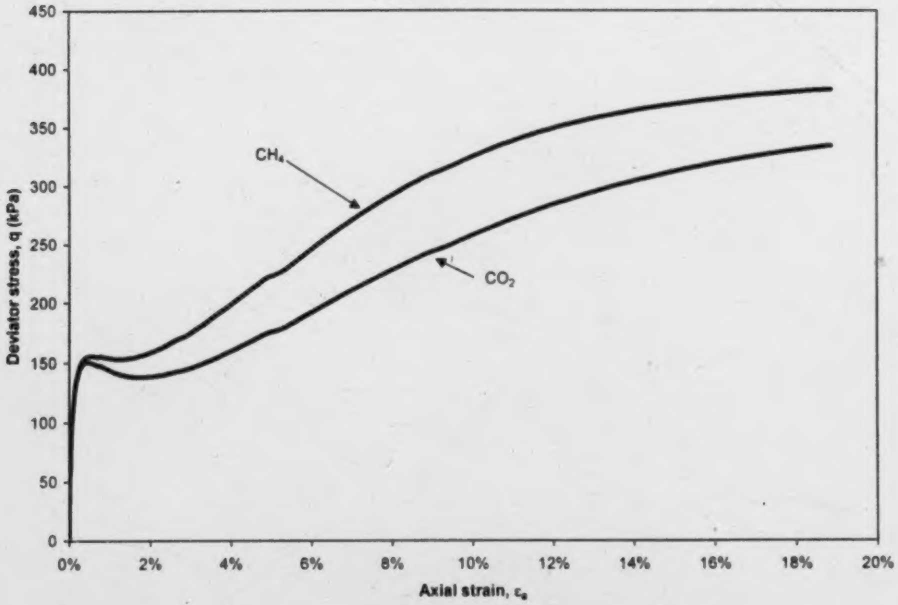

(a) Stress strain curves

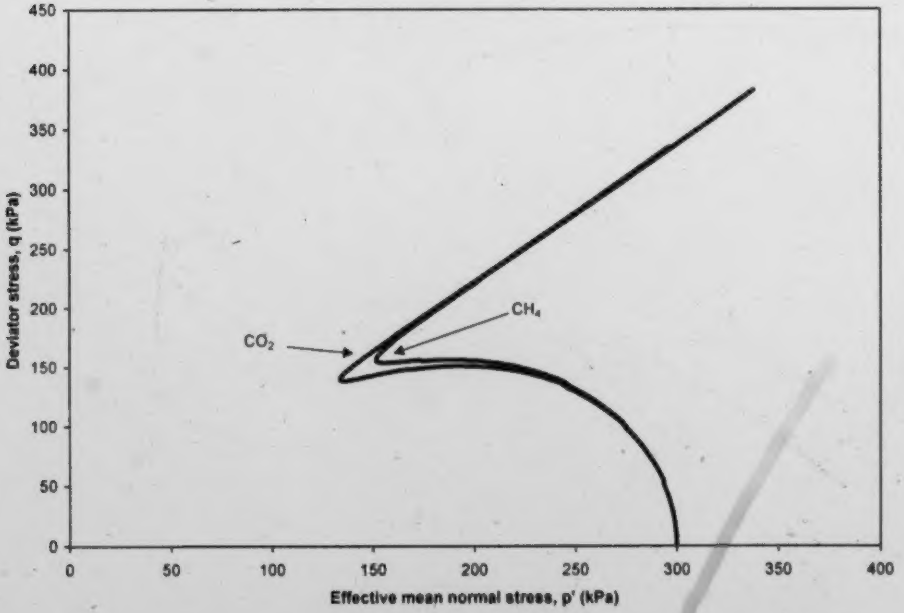

(b) Effective stress paths

Figure 7.19 - Model predictions of gassy undrained triaxial compression tests with consolidation pressures of 300 kPa, initial void ratios of 0.80, and initial degree of saturations of 90%.

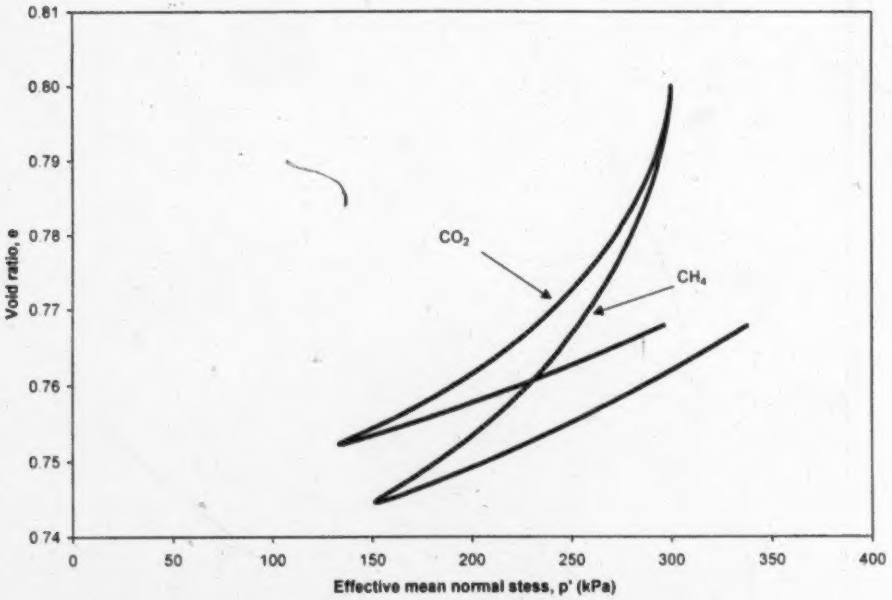

(a) Void ratio versus effective mean normal stress

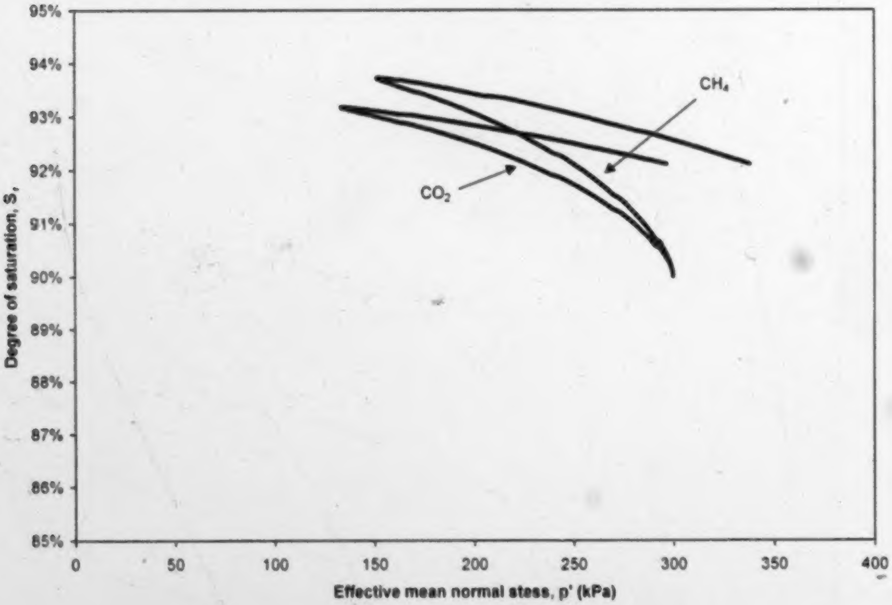

(b) Degree of saturation versus effective mean normal stress

Figure 7.20 - Model predictions of gassy undrained triaxial compression tests with consolidation pressures of 300 kPa, initial void ratios of 0.80, and initial degree of saturations of 90%.

CHAPTER 8

GENERAL DISCUSSIONS AND CONCLUSIONS

8.1 OVERVIEW

Gas can be found in many soils, both on land an on the ocean bottom, but is most common in seabed soils. Gas charged sediments are known to be widely distributed throughout the world's oceans, and occurrences have been reported in coastal and estuarine regions, across the continental shelves, and within deep ocean basins.

The presence of gas in soils will affect the engineering properties and behavior of the soil by altering the shear strength, settlement characteristics, and potential for flow or cyclic liquefaction. Gas found in seabed soils will affect marine geophysical surveys, foundation design, drilling procedures, slope stability, and may even have some environmental effects. This thesis focuses on the effect of gas on the stability of submarine slopes by examining how the presence of gas influences the resistance of loose soils to liquefaction.

Many instabilities in cohesionless sediments are as a result of liquefaction flow slides. Many liquefaction events, both flow and cyclic, have occurred in submarine slopes. Two submarine liquefaction slides were discussed in more detail (Chapter 1); one being a flow liquefaction failure in the Fraser River delta, British Columbia, and the other a cyclic liquefaction failure in the Klamath River delta, California. These case histories highlighted the effect that gas has on liquefaction failures. In both cases, the presence of gas affected the soil's engineering properties and possibly contributed to the liquefaction failure.

The objective of this thesis was to determine how the presence of gas affects the behavior of loose soils subjected to loading. Specifically could a loose gassy sand strain soften under shear and experience flow liquefaction, and/or cyclic soften and experience cyclic liquefaction.

8.2 GASSY SOILS

Gassy soils are characterized as having a large amount of dissolved gas in their pore fluid. Gassy soils are often confused with unsaturated soils, but the two types of soils are different in their behavior. A gassy soil, when subjected to a decrease in total stress, near or below the liquid gas saturation pressure, exhibits very little decrease in pore pressure. In contrast, an unsaturated soil, when subjected to a decrease in total stress decreases in pore pressure.

Gasses found in soils include carbon dioxide, hydrogen sulfide, ethane, and methane; however only methane is really found in any significant quantity. These gasses may originate from biogenic (bacterial activity) or petrogenic (organic precursors) processes. Gas may also originate form volcanic and hydrothermal sources, or may be primordial ("deep earth") gas, or may result from the destabilization of gas hydrates.

Previously published research has examined gas in dense sand such as the Athabasca soil sands, or soft fine-grained soils such as marine muds. Previous research has focused on sample disturbance, equilibrium effects, shear strength, the effect of large bubbles on consolidation, and acoustics. Fieldwork on gassy soils has concentrated on modifying samplers and probes to detect and sample gassy sediments and pore fluids, and developing new methods for calculating in situ gas contents. A research program currently underway at Oxford is examining the strength of fine-grained soils containing natural gas producing bacteria.

To date, there appears to be no published research work that studies the effect of gas on the geotechnical behavior of loose sand.

8.3 LABORATORY PROGRAM

A laboratory program, consisting of specialized triaxial testing, was undertaken to meet the thesis objectives. Two different triaxial systems were used for the monotonic and cyclic testing (Chapter 2).

Perhaps the most challenging aspect of the equipment design (Chapter 3) was determining a method to measure the gas content of the specimen during testing. Several methods were considered including measuring the sample volume change from the cell fluid, determining the sample volume change from radial strain gauge measurements, and using bender elements to measure compression wave attenuation. These methods had many shortcomings when applied to the specific requirements of this laboratory program. An innovative method for measuring the gas content using time domain reflectometry was developed. The triaxial apparatus was modified to include a time domain reflectometry mini-probe in the base, enabling the measurement of apparent dielectric constant. Through a series of calibration curves, developed from laboratory tests, the volumetric water content and degree of saturation could be determined. The time domain reflectometry mini-probe was able to achieve the required level of accuracy, was simple to use, and inexpensive to build.

A specified testing procedure was followed in the laboratory program (Chapter 4). Test specimens were prepared using the moist tamping technique. Specimens prepared by this method are more susceptible to flow liquefaction when tested in triaxial compression than specimens prepared other common methods. Under cyclic loading, specimens prepared by the moist tamping technique exhibited a higher resistance to cyclic liquefaction.

The prepared specimens were consolidated by reducing the back pressure, while maintaining a constant cell pressure. This allowed the carbon dioxide gas to come out of solution.

8.4 FLOW LIQUEFACTION POTENTIAL OF LOOSE GASSY SAND

Monotonic triaxial compression tests were performed on saturated and gassy specimens to determine the effects of gas on the propensity for loose sand to strain soften and experience flow liquefaction (Chapter 5).

Based on the results of the monotonic laboratory program a number of conclusions are noted.

- Tests performed on saturated specimens showed that if loose saturated specimens were tested in undrained conditions they responded in a strain softening manner, but if they were tested in drained conditions they responded in a strain hardening manner.
- Tests performed on gassy specimens showed that they responded in a strain softening manner if the specimen had a high initial degree of saturation and a high initial void ratio, or an initial degree of saturation less than about 88% but a very high void ratio.
- Tests performed on gassy specimens responded in a strain hardening manner if the initial degree of saturation was less than about 88% and the void ratio was not extremely high, or if the degree of saturation was less than about 80% regardless of void ratio.

The results of the monotonic laboratory program were evaluated using the framework of critical state soil mechanics. This framework uses the state boundary surface, which is a unique surface that relates deviator stress, effective mean normal stress, and void ratio.

The shape of the state boundary surface can be approximated by a straight line in deviator stress – effective mean normal stress space and a straight line in void ratio – logarithm effective mean normal stress space. The parameters representing these lines for Ottawa sand were determined from the laboratory program and can be summarized as:

$M = 1.50$
$s = 0.8$

for $p' < 250$ kPa	for $p' > 250$ kPa
$\lambda = 0.0159$	$\lambda = 0.153$
$\Gamma = 0.92$	$\Gamma = 1.68$

The potential for flow liquefaction of loose gassy sand will depend on the soil state (density, initial consolidation stress, and soil structure) and grain characteristics. Mode and rate of shearing will also influence the liquefaction potential of a specimen.

The effect of these variables on the static (flow) liquefaction resistance are as follows.

- As the density increases the potential for liquefaction increases.
- If the initial confining pressure is increased, then the potential for liquefaction will also increase.
- In laboratory specimens, soil structure is induced by the method of sample preparation. The use of the moist tamping technique to prepare the laboratory specimens results in the highest propensity to liquefy when compared with other specimen preparation techniques.
- Perhaps the most important grain characteristics is the presence of fines. A sand containing fines has a higher potential for liquefaction than a sand with no fines.
- Triaxial compression, the most commonly used laboratory shearing mode, gives the highest undrained shear strength and the lowest brittleness for a given relative density. When compared with a simple shear mode of shearing, which best

matches observed field performances, specimens tested in triaxial compression result in an unconservative judgement for flow liquefaction problems.

To meet the objectives of the laboratory program, it was necessary to eliminate many of the variables affecting the potential for flow liquefaction. Most variables were eliminated by using the same values and test methods for all the specimens tested. In this manner, the effects of initial consolidation stress, soil structure, grain characteristics, and rate and mode of shearing were eliminated from this program. The effects of density were minimized by preparing all specimens to a very loose to loose state.

For the specialized case of gassy specimens, the liquefaction potential also depends on the degree of saturation and the gas and pore fluid characteristics. The objective of the monotonic triaxial testing was to determine the effect of gas on the flow liquefaction resistance of loose sand. The laboratory results showed that the presence of gas moves the state boundary surface up in void ratio – logarithmic effective mean normal stress projection. A higher state boundary surface means that either a higher void ratio or a higher effective mean normal stress is necessary to trigger collapse. The laboratory results also showed that for a given density, the potential for flow liquefaction of a gassy sand is lower than a saturated sand. However, the results also showed that liquefaction can occur in gassy soils provided they are loose enough and the initial degree of saturation is high enough. The test results showed that liquefaction is possible for specimens with initial degrees of saturation less than 88% only if they are very loose and essentially impossible for specimens with initial degrees of saturation less than 80%.

The main conclusion of the laboratory work was that if specimens of Ottawa sand are sufficiently loose and if the initial degree of saturation is sufficiently high (in this case, greater than about 88%), then the specimens tested in triaxial compression can strain soften under shear and experience flow liquefaction.

8.5 CYCLIC LIQUEFACTION RESISTANCE OF LOOSE GASSY SAND

Cyclic triaxial tests were performed on saturated and gassy specimens to determine the effects of gas on the propensity for loose sand to cyclic soften and experience cyclic liquefaction (Chapter 6).

The results of the laboratory tests show that all specimens, saturated and gassy, when subjected to cyclic loading reached essentially zero effective confining pressure, and experienced cyclic liquefaction.

The resistance of a soil to cyclic loading is influenced by the applied shear stress as well as the soil state (void ratio, effective confining pressure, and soil structure) and grain characteristics. In addition to soil state and grain characteristics, the soil's resistance to cyclic loading will be affected by the loading intensity, duration, and frequency. These factors are summarized below:

- A high initial effective consolidation stress will decrease the resistance of a specimen to cyclic liquefaction. The effects of different consolidation stresses are more pronounced for denser specimens.
- The cyclic liquefaction resistance increases with increasing relative density.
- Soil structure in laboratory specimens is induced by the method of specimen preparation. Specimens prepared using the moist tamping technique have a higher resistance to cyclic loading than specimens of the same density prepared by different specimen preparation methods.
- Similar to static liquefaction, one of the most important grain characteristics is the presence of fines. A sandy soil containing fines will have a higher resistance to cyclic liquefaction than a sandy soil with no fines.
- The effects of loading intensity and duration are represented by the cyclic resistance ratio and number of cycles to failure, respectively. The effect of loading frequency on the cyclic resistance is minimal when confined to the commonly used range of testing frequencies.

Similar to the monotonic testing program, it was necessary to eliminate many of the variables affecting the cyclic resistance as possible. Most variables were eliminated by using the same values and methods for all the specimens tested. In this manner, the effects of initial consolidation stress, soil structure, and grain characteristics were eliminated. The effects of density were minimized by preparing all specimens to a loose to medium dense state.

In the case of gassy specimens, the resistance to liquefaction will also be affected by the initial degree of saturation. Determining the effect of gas on the cyclic liquefaction resistance of loose sand was the objective of the cyclic triaxial laboratory program. The results of the laboratory program showed that the presence of gas increased the resistance to cyclic loading by 200 to 300 percent. The results showed that when the gassy specimens were subjected to a deviatoric stress that was not very close to the monotonic failure envelope, then liquefaction did not occur. In other words, liquefaction either occurred in a few cycles or not at all. During loading, the gassy samples increased in both density and degree of saturation. The results of the cyclic triaxial tests were compared to the limiting line proposed by Seed et al. (1985). The comparison showed that the cyclic resistance of the saturated and gassy tests, when the final gas content and degree of saturation was used, were very similar to the cyclic resistance which would be predicted by using the limiting line. This observation lead to a method to predict the increased resistance of the gassy specimens using the limiting line proposed by Seed et al. (1985) as well as curves produced from the laboratory data. This proposed method to calculate the resistance to cyclic liquefaction of gassy samples was successfully applied to the CANLEX gassy sample data.

The main conclusion of the cyclic laboratory work was that the presence of gas will increase the resistance of loose Ottawa sand specimens to cyclic liquefaction.

8.6 MODELING THE CONSTITUTIVE BEHAVIOR OF LOOSE GASSY SAND

The theoretical behavior of loose gassy sand was investigated with the use of a constitutive model (Chapter 7). The model that was used to predict the behavior of the gassy soils was modified from an existing constitutive model developed by Imam (1999). Imam's model focused on assessing the liquefaction susceptibility of loose sands over a wide range of states and loading conditions. The model was formulated based on critical state soil mechanics. The model elements, strength, and deformability parameters conform to well-established and widely comprehended concepts related to the behavior of soils.

Imam's model was modified to take into account the compressibility and solubility of the pore gas and liquids. Hilf's (1948) equation, which calculates the pore pressure change in a gassy or unsaturated soil subjected to an applied total stress, was added into the model formulation. Only two additional parameters were required to modify the model; the initial degree of saturation and the coefficient of volumetric solubility (Henry's constant) of the gas used.

The modified model was used to predict the effect of gas on the undrained static behavior of loose sand. The laboratory results of the saturated specimens were modeled and the predicted and observed behaviors were found to agree well. Results from the gassy specimens were also predicted and again the model prediction matched the test results. The model confirmed that gas has the effect of decreasing the susceptibility to flow liquefaction. In addition, the model confirmed that specimens containing a more soluble gas (i.e. carbon dioxide as opposed to methane) would be more susceptible to liquefaction.

The major shortcoming of the modified model was the inability of the model to predict the slight increase in effective mean normal stress that is observed in the initial stages of all the undrained triaxial tests. This shortcoming resulted in some differences between the predicted and observed behavior of the strain hardening specimens. However, in general, the model performance was excellent.

8.7 GUIDELINES FOR EVALUATING LIQUEFACTION POTENTIAL OF LOOSE GASSY SAND

8.7.1 Potential for Flow Liquefaction

The potential for flow liquefaction of a saturated sand will depend on the soil state and grain characteristics, as well as the mode and rate of shear. The potential for flow liquefaction of a gassy sand will depend on the same parameters as a saturated sand with the addition of the degree of saturation and to some extent the gas characteristics. Based on previous work and results from the constitutive model, it appears that gas characteristics (i.e. carbon dioxide as opposed to methane) will have a minimal effect.

Based on the results of this laboratory program, a plot of void ratio versus degree of saturation was produced (Figure 8.1). This plot shows the zone of potential liquefaction of Ottawa sand. When the void ratio is very high (the specimen is sufficiently loose) and the initial degree of saturation is greater than about 80%, the soil could be susceptible to flow liquefaction.

Figure 8.1 was produced from the laboratory test results combined with engineering judgement, and therefore is only intended to be used as a guideline only, appreciating that the tests results are under controlled conditions using Ottawa sand with carbon dioxide gas, prepared with the moist tamping method, in triaxial compression loading.

8.7.2 Potential for Cyclic Liquefaction

The resistance of a saturated sand to cyclic loading is influenced by the applied shear stress as well as the soil state and grain characteristics. Gassy soils subjected to cyclic loading will be influenced by the same factors as saturated soils, but will also be affected by the initial degree of saturation and gas characteristics. The constitutive model showed that gas characteristics had a minimal affect on the potential for flow liquefaction. Therefore, is it assumed that the type of gas (i.e. carbon dioxide or methane) will not have a significant affect on the resistance of the soil to cyclic liquefaction.

Based on the results of the cyclic triaxial tests, a method to predict the cyclic resistance ratio of loose gassy sand is presented. To use the method, the cyclic resistance is first predicted from the initial relative density of the soil, using Figure 8.2. Figure 8.2, which is a plot of the cyclic resistance ratio normalized to simple shear versus the relative density, was developed from the Seed et al. (1985) limiting line. The next step in the method is to use Figure 8.3 to determine the increase in cyclic resistance ratio as a function of the initial degree of saturation. Figure 8.3 was developed from the laboratory test results. The final step in the process is to add the increase in cyclic resistance ratio due to the presence of gas, to the initial cyclic resistance ratio obtained from Figure 8.2, to get the final cyclic resistance ratio. This cyclic resistance ratio is the resistance of the gassy soil to cyclic loading.

The procedure for evaluating the cyclic resistance of loose gassy sand was based on laboratory tests of loose to medium dense Ottawa sand prepared using the moist tamping method. The method was based on limited data and is intended to be used as a guideline only.

8.7.3 Cautionary Notes

The methods and guidelines presented above for determining the potential for flow liquefaction and the resistance to cyclic liquefaction were developed under controlled laboratory conditions. The guidelines were based on the laboratory results and engineering judgement. Caution should be used when applying these methods to dense specimens, specimens consolidated to effective stresses other than 300 kPa, anistropically consolidated specimens, structured specimens, specimens prepared by a method other than moist tamping, specimens containing fines or specimens not made of Ottawa sand, and specimens prepared with a gas other than carbon dioxide. For the flow liquefaction guidelines, caution should be used for specimens sheared in any mode other than triaxial compression. For the cyclic liquefaction method, the mode of shearing used should be correctly normalized to the simple shear method.

8.8 CONTRIBUTIONS

The research work presented in this thesis has made a contribution to the field of geotechnical engineering. It is the first research program that studied the behavior of loose gassy sands. The results from this research will contribute to the fundamental understanding of the behavior of both saturated and gassy soils. Valuable insight into the effect of gas on the flow and cyclic liquefaction of loose sands has been gained. The results of the laboratory and numerical work have industrial applications, particularly in the offshore industries. Applications may include improved foundation design for port facilities, bridge piers, and offshore structures. An improved understanding of submarine slope stability could potentially enhance the reliability of submarine cable crossings and improve dredging operations. Industries involved in offshore structures, dredging operations, and submarine pipelines could benefit from the results of this research.

8.9 RECOMMENDATIONS FOR FUTURE WORK

This thesis shows that understanding the effect of gas on soil behavior is a complex problem. Clearly more research is needed to fully understand the implications of gas on soil behavior and soil engineering properties.

8.9.1 Liquefaction of Gassy Soils

Although the effect of gas on the liquefaction resistance of a soil was studied in this program, further research is needed to investigate how factors such as confining pressure, grain characteristics, and mode of shearing affect the behavior of loose gassy soils. It would be useful to investigate these factors under both static and cyclic loading. Further laboratory work could be combined with the development of a constitutive model to predict the cyclic response of gassy sands. Incorporating the static and cyclic constitutive models into a numerical model would allow the prediction of gassy soils in conditions such as the stability of submarine slopes subjected to dredging operations, storm loading, or earthquake loading. The aim of further laboratory and modeling work would be to produce guidelines and recommendations for evaluating the flow and cyclic liquefaction risk of gassy soils.

The laboratory and numerical work should be complimented by field research. Further work might include in situ testing equipment to identify gas and quantify the type, amount, and variability of the gas. It would be desirable to perform in situ testing that does not require samples in addition to the more traditional soil sampling. Characterization of the in situ geotechnical properties of gassy soils would also be beneficial. The aim of the field program would be to incorporate the findings, along with the laboratory and numerical work, into a framework to analysis the potential for liquefaction of gassy soils. The framework should be risk based; similar to what has been developed recently for saturated soils. By presenting the results in a risk based framework, the recommendations for determining the liquefaction of gassy soils could be linked together with the recommendations for determining the liquefaction of saturated soils. Practitioners would then be able to easily identify the risk of liquefaction for both types of soil and perform simple calculations to determine if further work is required.

Research into the transient nature of gassy soils is also recommended, specifically, rate effects and the influence of solubility on the response of gassy soils. For example, under the influence of a cyclic load, the frequency of the loading will affect the response. If the frequency is very fast, such as an earthquake, the solubility of the gas might make very little difference; even a highly soluble gas might not have enough time to dissolve. However, under loading conditions such as storm waves, the frequency of loading is significantly slower, and therefore the solubility of the gas may make a large difference in soil response. Similarly, the rate of static loading will also influence the soil's response. Under the influence of a slowly applied load such as tidal drawdown, the solubility of the gas in solution will make a difference. For example, the higher the solubility the quicker the response and therefore the greater the loss of strength.

8.9.2 Geotechnical Properties of Gassy Sands

In addition to the research required on the liquefaction of gassy soils, further work is also recommended in studying the geotechnical properties of gassy sands. Previous research on gassy soils has focused on fine grained soils, and little is know about the geotechnical properties of coarse grained soils containing gas. Possible research into the strength and settlement characteristics of gassy sands, as well as the effect of gas on the permeability of both loose and dense sands, would be beneficial. Understanding the geotechnical properties of gassy sands would improve the design of foundations for offshore and nearshore structures and the design of trenches for submarine cables.

8.10 FINAL REMARKS

Many liquefaction events have occurred in submarine slopes know to contain gas. The objectives of this thesis were to determine how the presence of gas affects the potential for flow and/or cyclic liquefaction. The effect of gas on liquefaction of loose sand is an important topic, which contributes to the fundamental understanding of soil mechanics and has industrial applications, particularly in the offshore industries.

Guidelines were developed for evaluating the potential for flow liquefaction of loose sand soils based on initial degree of saturation and initial density. Guidelines were also recommended for evaluating the resistance to cyclic liquefaction, again based on the initial degree of saturation and density. The guidelines are preliminary and further work is required to generalize them for a broader range of soil and loading conditions. This research also resulted in the development of a constitutive model that captures the behavior of gassy sands subjected to static loading. The model was formulated by modifying an existing constitutive model with simple gas laws. The constitutive model can be used to predict the behavior of gassy soils over a wide range of soil and loading conditions. It can also be used in conjunction with the guidelines mentioned above to predict the potential for flow liquefaction.

By integrating monotonic and cyclic laboratory results with a constitutive model, this thesis has fulfilled its objective of advancing our understanding of the effect that gas has on the liquefaction of loose sands.

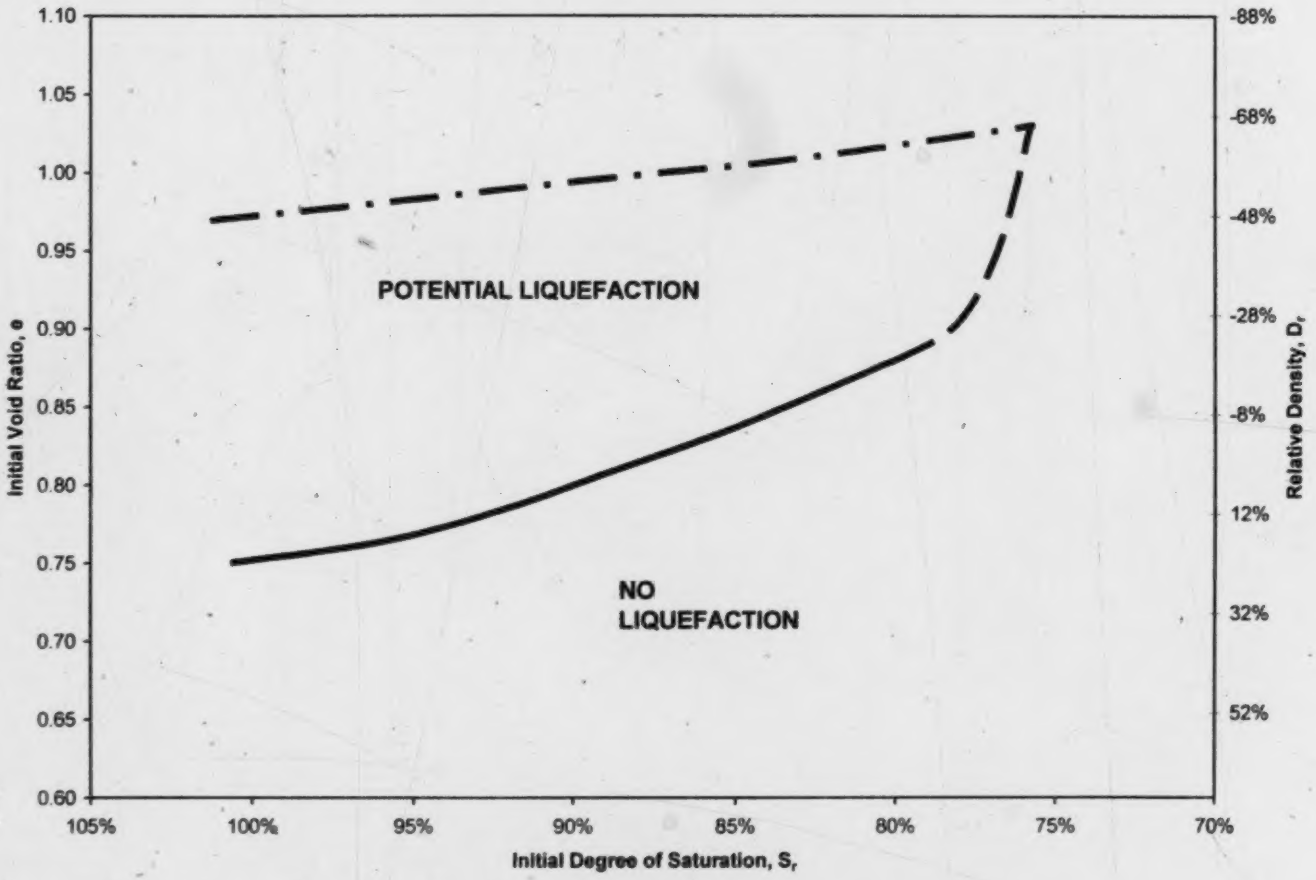

Figure 8.1 - Potential for flow liquefaction of Ottawa sand.

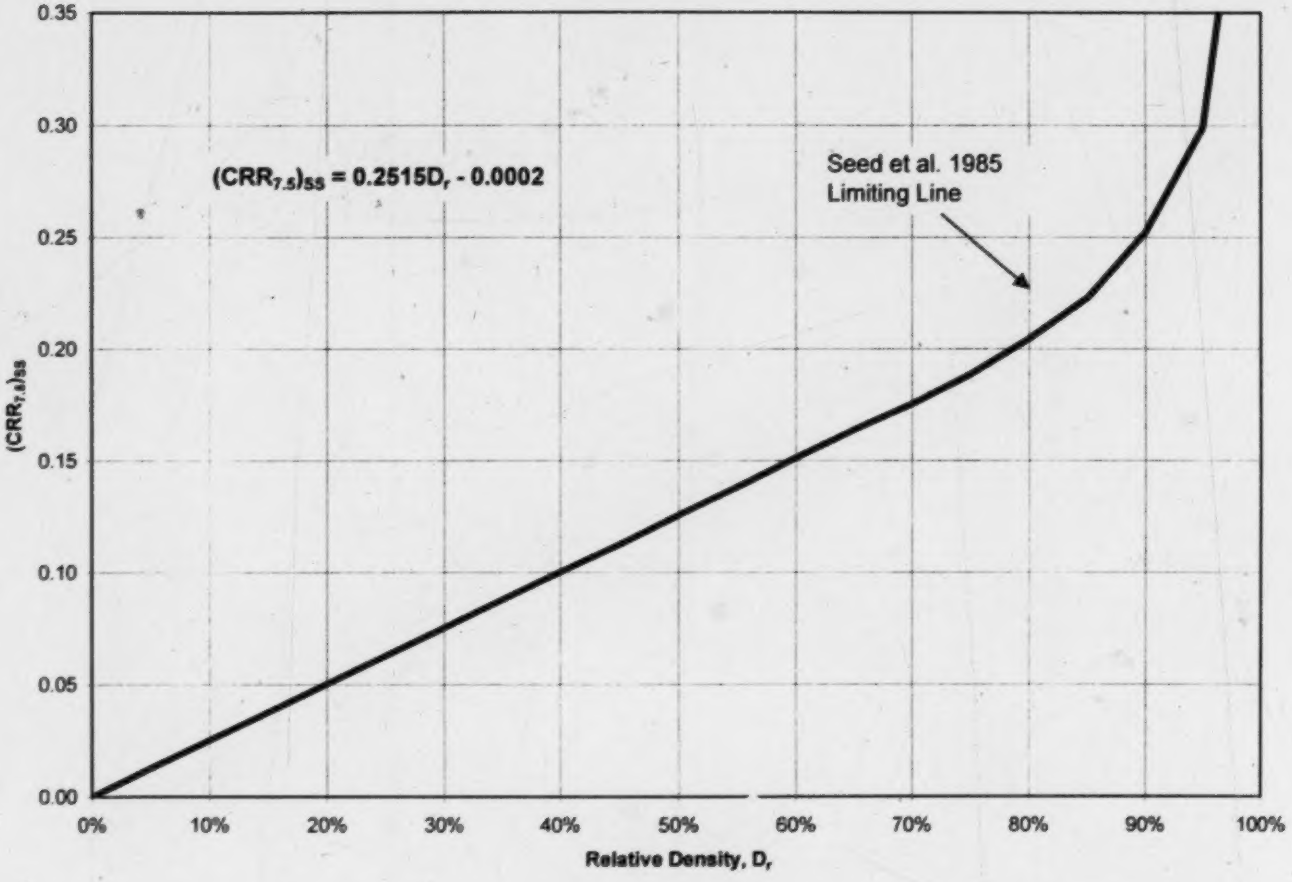

Figure 8.2 - Cyclic resistance ratio versus relative density, based on Seed et al. (1985) limiting line.

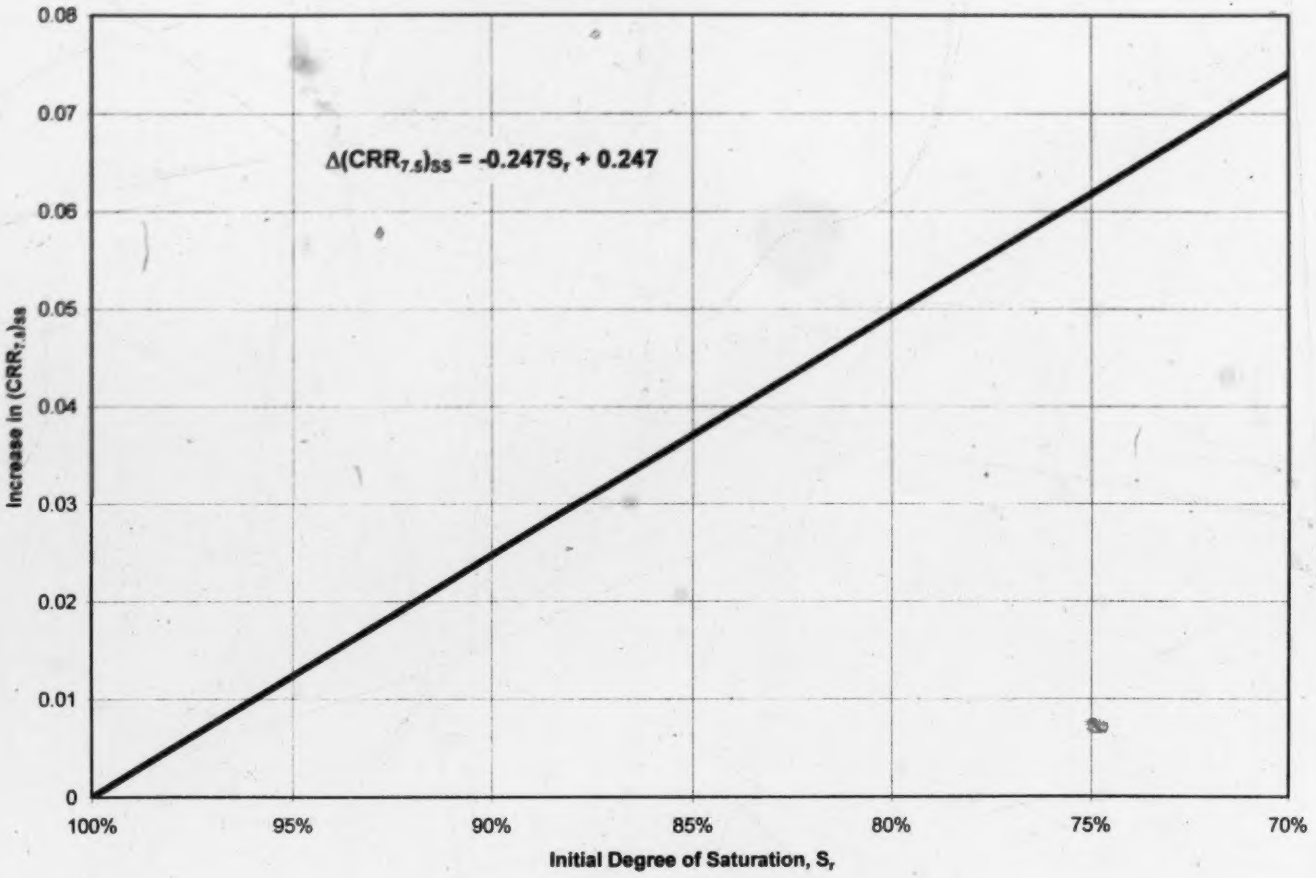

Figure 8.3 – Increase in cyclic resistance ratio versus initial degree of saturation for loose Ottawa sand.

REFERENCES

LIST OF REFERENCES

Ag, A. 1994. Consolidation and permeability behavior of high porosity Baltic seabed sediments. MS Thesis, University of Rhode Island.

Albert, D.B., Martens, C.S., and Alperin, M.J. 1998. Biogeochemical process controlling methane in gassy coastal sediments II. Groundwater flow control of acoustic turbidity in Eckernförde Bay sediments. Continental Shelf Research, **18**: 1771-1793.

Anderson, A.L., Abegg, F., Hawkins, J.A., Duncan, M.E., and Lyons, A.P. 1998. Bubble populations and acoustic interaction with the gassy seafloor of Eckernförde Bay. Continental Shelf Research, **18**: 1807-1838.

Andresen, A. and Bjerrum, L. 1968. Slides in subaqueous slopes in loose sand and silt. Norwegian Geotechnical Institute, Publication No. 81, pp. 1-9.

Andresen, A., and Bjerrum, L. 1967. Slides in subaqueous slopes in loose sand and silt. *In* Marine geotechnique. *Edited by* A.F. Richards. University of Illinois Press. Urbana, Ill., pp. 221-239.

Andrews, J.R. 1994. Time domain reflectometry. Symposium and Workshop on Time Domain Reflectometry in Environmental, Infrastructure, and Mining Applications, Evanston, Illinois, September 7-9, 1994, pp. 4-13.

Been, K., Jefferies, M.G., and Hachey, J. 1991. The critical state of sand. Géotechnique, **41**: 365-381.

Bishop, A.W. 1971. Shear strength parameters for undisturbed and remolded soil specimens. Roscoe Memorial Symposium, Cambridge University, pp. 3-58.

Bjerrum, L. 1971. Subaqueous slope failures in Norwegian fjords. Norwegian Geotechnical Institute Publication No. 88, pp. 1-8.

Bohl, H. and Roth, K. 1994. Evaluation of dielectric mixing models to describe the θ(ε) – relation. Symposium and Workshop on Time Domain Reflectometry in Environmental, Infrastructure, and Mining Applications, Evanston, Illinois, September 7-9, 1994, pp. 309-319.

Brandes, H.G., Silva, A.J., Ag, A., and Veyera, G.E. 1996. Consolidation and permeability characteristics of high porosity surficial sediments in Eckernförde Bay. Geomarine Letters, **16**(3): 175-181.

Breck, D.W. 1974. Zeolite molecular sieves: structure, chemistry, and use. Chichester: Wiley

Briggs, K.B., Jackson, P.D., Hoyler, R.J., Flint, R.C., Sandidge, J.C., and Young, D.K. 1998. Two-dimensional variability in sediment porosity, density, and electrical resistivity in Eckernförde Bay sediments. Continental Shelf Research, **18**: 1939-1964.

Brogan, D. 1995. The strength behavior of Baltic Sea sediments. MS Thesis, University of Rhode Island.

Bussman, I. And Suess, E. 1998. Groundwater seepage in Eckernförde Bay (Western Baltic Sea): effect on methane and salinity distribution of the water column. Continental Shelf Research, **18**: 1795-1806.

Casagrande, A. 1976. Liquefaction and cyclic deformation of sands – A critical review. Harvard Soil Mechanics Series No. 88, Harvard University, Cambridge, Massitusis.

Castro, G. 1969. Liquefaction of sand. Harvard Soil Mechanics Series No. 81, 112 pages.

Chan, C.K. 1981. An electropneumatic cyclic loading system. Geotechnical Testing Journal, ASTM, **4**(4): 183-187.

Chan, C.K. and Mulilus, J.P. 1976. Pnematic sinusoidal loading system. Journal of the Geotechnical Engineering Division, ASCE, **102**(3): 277-282.

Chang, N.Y., Yey, S.T., and Kaufman, L.P. 1982. Liquefaction potential of clean an silty sands. Proceedings of Third Microzonation Conference, Seattle, Washington, pp. 1018-1032.

Chillarige, A.V. 1995. Liquefaction and seabed instability in the Fraser River delta. Ph.D. Thesis, University of Alberta, Edmonton, Alberta, Canada, 194 pages.

Chillarige, A.V., Robertson, P.K., Morgenstern, N.R., and Christian, H.A. 1997a. Evaluation of the in situ state of Fraser River sand. Canadian Geotechnical Journal, **34** (4): 510-519.

Chillarige, A.V., Robertson, P.K., Morgenstern, N.R., and Christian, H.A. 1997b. Seabed instability due to flow liquefaction in the Fraser River delta. Canadian Geotechnical Journal, **34**(4): 520-533.

Christian, H.A. 1998. Personal Communications.

Christian, H.A. and Cranston, R.E. 1997. A methodology for detecting free gas in marine sediments. Canadian Geotechnical Journal, **34**(2): 293-304.

Christian, H.A., Mosher, D.C., Mulder, T., Barrie, J.V., and Courtney, R.C. 1997a. Geomorphology and potential slope instability on the Fraser River delta foreslop, Vancouver, British Columbia. Canadian Geotechnical Journal, **34**(3): 432-446.

Christian, H.A., Woeller, D.J., Robertson, P.K., and Courtney, R.C. 1997b. Site investigations to evaluate flow liquefaction slides at sand heads, Fraser River delta. Canadian Geotechnical Journal, **34**(3): 384-397.

Coleman, J.M., Suhayda, J.N., Whelan, T. III, and Wright, L.D. 1974. Mass movement of Mississippi River delta sediments. Trans. Gulf Coast Association, Geol. Society, XXIV: 49-68.

Conn, P. and Arthur, J. 1990. Safey in offshore drilling: the role of shallow gas surveys. *Editors*: D.A. Ardus and C.D. Green, Kluwer Academic Publishers, Dordrecht, pp. 235-256.

D'Appolonia. 1981. ENEL VI and VIII Nuclear Power Plant, Alto Lazio, Italy. Report on Site Performance, July 1978 through December 1980, Unpublished Report, Project 77-500.

Dando, P.R. and Hovland, M. 1992. Environmental effects of submarine seeping gas. Continental Shelf Research, **12**(10): 1197-1127.

Dando, P.R., Austen, M., Burke, R., Kendall, M.A., Kennicutt II, M.C., Judd, A.G., Moore, D.C., O'Hara, S.C.M., Schmaljohann, R., Southward, R., and Southward, A.J. 1991. The ecology of a North sea pockmark with an active methane seep. Marine Ecology Progress Series, **70**: 49-63.

Davis, J.L. and Annan, A.P. 1977. Electromagnetic detection of soil moisture: Progress report I. Canadian Journal of Remote Sensing, **3**(1): 76-86.

Denk, E.W., Dunlap, W.A., Bryant, W.R., Milberger, L.J., Whelan, T.J. 1981. A pressurized core barrel for sampling gas-charged marine sediments. Proceedings of the 13th Annual Offshore Technology Conference, Houston, Texas, May 4-7, 1981, pp. 43-52.

Dill, R.F. 1964. Sedimentation and erosion in Scripps Submarine Canyon Head. *In* Papers in marine geology (Shepard Commemorative Volume). *Edited by* R.L. Miller. Macmillan Publication, New York, pp. 23-41.

Dirksen, C. and Dasberg, S. 1993. Improved calibration of time domain reflectometry soil water content measurements. Soil Science Society of America Journal, **57**(3): 660-667.

Dobson, M.C., Ulaby, R.T., Hallikainen, M.T. and El-Rayes, M.A. 1985. Microwave dielectric behaviour of wet soil – Part II: Dielectric mixing models. IEEE Trans. Geosci. Remote Sensing, Vol. **Ge-32**(1): 35-46.

Dorsey, N.E. 1940. Properties of ordinary water-substances. American Chemical Society, Mono. Series, New York, Reinhold, 673 pages.

Duffy, S.M., Wheeler, S.J., and Bennell, J.D. 1994. Shear modulus of kaolin containing methane bubbles. ASCE Journal of Geotechnical Engineering, **120**(5): 781-797.

Dusseault, M.B. 1977. The geotechnical characteristics of the Athabasca oil sands. Ph.D. Thesis, Department of Civil Engineering, University of Alberta, 472 pages.

Dusseault, M.B. 1979. Undrained volume and stress change behavior of unsaturated very dense sands. Canadian Geotechnical Journal, **16**(4): 627-640.

Dusseault, M.B. 1980. Sample disturbance in Athabasca oil sands. Canadian Petroleum Technology, **9**(2): 85-92.

Dusseault, M.B. and Morgenstern, N.R. 1978a. Characteristics of natural slopes in the Athabasca oil sands. Canadian Geotechnical Journal, **15**(2): 202-215.

Dusseault, M.B. and Morgenstern, N.R. 1978b. Shear strength of Athabasca oil sands. Canadian Geotechnical Journal, **15**(2): 216-238.

Dusseault, M.B. and von Domselaar, H.R. 1982. Uncemented gaseous sand sampling. Proceedings of the Conference Updating Surface Sampling of Soils and Laboratory and In Situ Testing, Santa Barbara, California, pp. 57-73.

Ells, S.C. 1926. Bituminous sands of Northern Alberta; Occurrence and economic possibilities; Report on investigations to end of 1924. Canada Mines Branch Report 632, 239 pages.

Esrig, M. and Kirby, R.C. 1977. Implications of gas content for prediction the stability of submarine slopes. Marine Geotechnology, **2**(2): 81-100.

Evans, C.D.R. 1988. Acoustic turbidity in Quaternary sediments from Hong Kong waters. British Geological Survey, Marine Report 88/44.C, submitted to Geotechnical Control Office, Hong Kong, 67 pp.

Fannin, N.G.T. 1980. The use of regional geological surveys in the North Sea and adjacent areas in the recognition of offshore hazards. *In*: Offshore site investigation, *Edited by*: D.A. Ardus, Graham and Trotman, London, pp. 5-21.

Field, M.E. 1984. The submarine landslide of 1980 off northern California. *In* Highlights in Marine Research of the U.S. Geological Survey. *Editor* S.H. Clarke. U.S. Geological Survey, Circ, **938**: 65-72.

Field, M.E. and Jennings, A.E. 1987. Seafloor gas seeps triggered by a northern California earthquake. Marine Geology, **77**: 39-51.

Field, M.E., Clarke, S.H.Jr., and White, M.W. 1980. Geology and geologic hazards of offshore Eel River Basin, northern California continental margin. U.S. Geological Survey Open-File Report 80-1080, 80 pages.

Field, M.E., Gardner, J.V., Jennings, A.E., and Edwards, B.D. 1982. Earthquake-induced sediment failures on a 0.25° slope, Klamath River delta, California. Geology, **10**: 542-546.

Floodgate, G.D. and Judd, A.G. 1992. The origins of shallow gas. Continental Shelf Research, **12**(10): 1145-1156.

Fredlund, D.G. 1979. Second Canadian Geotechnical Colloquium: Appropriate concepts and technology for unsaturated soil. Canadian Geotechnical Journal, **16**(1): 121-139.

Fredlund, D.G. and Rahardjo, H. 1993. Soil mechanics for unsaturated soils. John Wiley & Sons, Inc., New York, New York.

Gardner, T.N. and Goringe, M.J. 1988. The measurement of gas bubble size distributions in a three phase laboratory gassy soil. Geotechnical Testing Journal, **11**(1): 49-55.

Greene, H.G., Gardner-Taggart, J., Ledbetter, M.T., Barminski, R., Chase, T.E., Hicks, K.R., and Baxter, C. 1991. Offshore and onshore liquefaction at Moss landing spit, central California – Result of the October 17, 1989, Loma Prieta earthquake. Geology, **19**: 945-949.

Grozic, E.M. 1997. Laboratory measurement of unfrozen water content using time domain reflectometry. M.Eng. Report, University of Alberta, Edmonton, Alberta.

Grozic, J.L., Robertson, P.K., and Morgenstern, N.R. 1999. The behavior of loose gassy sand. Canadian Geotechnical Journal, accepted for publication.

Hardy, R.M. and Hemstock, R.A. 1963. Shearing strength characteristics of Athabasca oil sands. K.A. Clark Volume, Research Council of Alberta, Information Series No. 45, p. 109.

Heezen, B.C. and Ewing, M. 1952. Turbidity currents and submarine slumps and the Grand Banks earthquake. American Journal of Science, **250**: 849-873.

Heezen, B.C. and Ewing, M. 1965. Orleansville earthquake and turbidity currents. American Association of Petroleum Geologists Bulletin, **39**: 2505-2514.

Hilf, J.W. 1948. Estimating construction pore pressures in rolled earth dams. Proceedings of the 2nd International Conference on Soil Mechanics and Foundation Engineering, Rotterdam, The Netherlands, 1948, Vol. 3, pp. 234-240.

Holish, L.L. and Hendron, D.H. 1975. Liquefaction considerations for two submerged essential service cooling ponds. *In* 1975 Structural design of nuclear power plant facilities, Vol. 1-B, New York. American Society for Testing and Materials, pp. 897-931.

Hoskins, E.G. and Griffiths, J.R. 1971. Hydrocarbon potential of northern and central Callifornia offshore. In: Future Petroleum Provinces of the United States; their Geology and Potential, American Association of Petroleum Geologists Memoir 15, Vol. 1, pp. 212-228.

Houtz, R.E. and Wellman, H.W. 1962. Turbidity current at Kadavu Passage, Fiji. Geological Magazine, **99**: 57-62.

Hovland, M. 1992. Pockmarks and gas-charged sediments in the eastern Skagerrak. Continental Shelf Research, **12**(10): 1111-1119.

Hovland, M. and Judd, A.G. 1988. Seabed pockmarks and seepages: impact on geology, biology and the marine environment. Graham and Trotman, London, 293 pp.

Hovland, N. and Thomsen, E. 1989. Hydrocarbon-based communities in the North Sea? Sarsia, **74**:29-42.

Imam, S.M.R. 1999. Modeling the constitutive behavior of sand for the analysis of static liquefaction. Ph.D. Thesis, University of Alberta, Edmonton, Alberta, 326 pages.

Ishibashi, I. 1985. Effect of grain characteristics on liquefaction potential – In search of standard sand for cyclic strength. Geotechnical Testing Journal, **8** (3): 137-139.

Ishihara, K. 1993. Liquefaction and flow failure during earthquakes. The 33rd Rankine Lecture. Géotechnique, **43**(3): 351-415.

Ishihara, K. and Koseki, J. 1989. Cyclic shear strength of fines-containing sands. In Earthquake Geotechnical Engineering, Discussion Session on Influence of Local Conditions on Seismic Response, Proceedings of the 12th International Conference on Soil Mechanics and Foundation Engineering, Rio de Janeiro. A.A. Balkema, Amsterdam, pp. 101-106.

Ishihara, K., Verdugo, R., and Acacio, A.A. 1991. Characterization of cyclic behavior of sand and post-seismic stability analysis. Proceedings of the IX Asian Regional Conference on Soil Mechanics and Foundation Engineering, Bangkok, Thailand, Vol. 2, pp. 17-40.

Jackson, D.R., Williams, K.L., Wever, T.F., Friedrichs, C.T., and Wright, L.D. 1998. Sonar evidence for methane ebullition in Eckfernförde Bay. Continental Shelf Research, 1893-1915.

Janda, S.R. and Nolan, K.M. 1979. Stream sediment discharge in northwestern California. *In*: Guidebook for Fieldtrip to Observe Natural and Management-related Erosion in Franciscan Terrane of Northern California. San Jose, Geological Society of America Cordilleran Section, Vol. 4, pp. 1-27.

Jefferies, M.G. 1993. Nor-Sand: a simple critical state model for sand. Géotechnique. **43**(1): 91-103.

Johnston, W.A. 1921. Sedimentation of the Fraser River delta. Geological Survey of Canada Memorandum 125, 46 pages.

Judd, A.G. and Hovland, M. 1992. The evidence of shallow gas in marine sediments. Continental Shelf Research, **12**(10): 1081-1095.

Kenyon, P.M. and Turcotte, D.L. 1985. Morphology of a delta prograding by bulk sediment transport. Geological Survey of America Bulletin, **96**: 1457-1465.

Knight, J.H. 1991. Letter to the editor – discussion of "the spatial sensitivity of time domain reflectometry" by J.M. Baker and R.J. Lascano. Soil Science, **151**(3): 254-255.

Konrad, J.M. 1993. Undrained response of loosely compacted sands during monotonic and cyclic compression tests. Géotechnique, **43**(1): 69-89.

Koppejan, A.W., Van Wamelan, B.M., and Weinberg, L.J.H. 1948. Coastal flow slides in the Dutch province of Zeeland. Proceedings of the 2nd International Conference on Soil Mechanics and Foundation Engineering, Rotterdam, Vol. 5, pp. 89-96.

Kostaschuk, R.A., Luternauer, J.L., McKenna, G.T., and Moslow, T.F. 1992. Sediment transport in a submarine channel system: Fraser River delta, Canada. Journal of Sedimentary Petrology, **62**(2): 273-282..

Kraft, L.M., Jr., Gavin, T.M., and Bruton, J.C. 1992. Submarine flowslide in Puget Sound. Journal of Geotechnical Engineering, ASCE, **118**: 1577-1591.

Kramer, S.L. 1988. Triggering of liquefaction flow slides in coastal soil deposits. Engineering Geology, **26**: 17-31.

Kuerbis, R. and Vaid, Y.P. 1988. Sand sample preparation – the slurry deposition method. Soils and Foundations, **28**(4): 107-118.

Ladd, R.S. 1978. Preparing test specimens using undercompaction. Geotechnical Testing Journal, **1**(1): 16-23.

Lade, P.V. and Yamamuro, J.A. 1997. Effects of nonplastic fines on static liquefaction of sands. Canadian Geotechnical Journal, **34**(6): 918-928.

Lajoie, K.R. and Keefer, D.K. 1981. Investigations of the November 1980 earthquake in Humboldt County, California: U.S. Geological Survey Open-File Report 81-397, 20 pages.

Lambe, T.W. 1951. Soil testing for engineers. John Wiley & Sons, Inc., New York, New York.

Langseth, M.G. and Moore, J.C. 1990. Fluids in accretionary prisms. EOS, **71**: 245-246.

Lashof, D.A. and Ahuja, D.R. 1990. Relative contribution of greenhouse gas emissions to global warming. Nature, **344**:529-531.

Lavoie, D.M., Lavoie, D.L., Pittenger, H.A., and Bennett, R.H. 1996. Bulk sediment properties interpreted in light of qualitative and quantitative microfabric analysis. Geomarine Letters, **16**(3): 226-231.

Lefebvre, M.E. 1997. The feasibility of coaxial time domain reflectometry as an insitu site characterization tool for determining the moisture content of mine tailings. M.Sc. Thesis, University of Alberta, Edmonton, Alberta.

Long, D. 1992. Devensian Late-glacial gas escape in the central North Sea. Continental Shelf Research, **12**(10): 1097-1110.

Lord, T. 1998. Personal communications.

Luternauer, J.L. 1980. Genesis of morphologic features on the western delta front of the Fraser River, British Columbia. *In* The Coastlines of Canada. *Edited by* S.B. McCann. Geological Survey of Canada, Paper 80-10, pp. 381-396.

Luternauer, J.L. and Finn, W.D.L. 1983. Stability of the Fraser River delta front. Canadian Geotechnical Journal, **20**: 603-616.

MacDonald, I.R., Reilly II, J.F., Guinasso, Jr, N.L. Brooks, J.M., Carney, R.S., Bryant, W.A., and Bright, T.J. 1990. Chemosynthetic mussels at brine-filled pockmark in the Northern Gulf of Mexico. Science, **248**: 1096-1099.

Marcuson, W.F., III, and Gilbert, P.A. 1972. Earthquake liquefaction potential at Patoka Dam, Indiana. Army Engineer Waterways Experimental Station, Miscellaneous Paper S-72-42, 62 pages.

Martens, C.S., Albert, D.B., and Alperin, M.J. 1998. Biochemical processes controlling methane in gassy coastal sediments I. A model coupling organic matter flux to gas production, oxidation, and transport. Continental Shelf Research, **18**: 1741-1770.

Mathews, W.H. and Shepard, F.P. 1962. Sedimentation of the Fraser River delta, British Columbia. The Bulletin of the American Association of Petroleum Geologists, **46**(8): 1416-1438.

McKenna, G.T., and Luternauer, J.L. 1987. First documented failure at the Fraser River Delta front, British Columbia. *In* Current research, part A. Geological Survey of Canada, Paper 87-1A, pp. 919-924.

McKenna, G.T., Luternauer, J.L., and Kostaschuk, R.A. 1992. Large-scale mass-wasting events of the Fraser River delta front near Sand Heads, British Columbia. Canadian Geotechnical Journal, **29**: 151-156.

Mernard, H.W. 1964. Marine geology of the Pacific. McGraw-Hill Book Company, New York.

Miura, S. and Toki, S. 1982. A sample preparation method and its effect on static and cyclic deformation-strength properties of sand. Soils and Foundations, **22**(1): 61-77.

Miura, S., Toki, S. and Tanisawa, F. 1984. Cone penetration characteristics and its correlation to static and cyclic deformation – strength behaviors of anisotropic sand. Soils and Foundations, **24**(2): 58-74.

Monahan, P.A., Luternauer, J.L., and Barrie, J.V. 1993. A delta plain sheet sand in the Fraser River delta, British Columbia, Canada. Quaternary International, **20**: 27-38.

Morgenstern, N.R. 1967. Submarine slumping and the initiation of turbidity currents. *In* Marine geotechnique. *Edited by* A.F. Richards. University of Illinois Press, Urbana, Ill., pp. 189-210.

Morgenstern, N.R. 1995. Personal Communications.

Morgenstern, N.R. 1998. Personal communications.

Morrison, K.I. 1984. Case history of very large submarine landslide, Kitimat, British Columbia. *In* Proceedings of the 4th International Symposium on Landslides, Toronto, Ontario, Vol. 2, pp. 337-342.

Nageswaran, S. 1983. Effect of gas bubbles on the sea-bed behavior. Ph.D. thesis, Oxford University, Oxford, England.

Nittrouer, C.A., Lopez, G.R., Wright, L.D., Bently, S.J., D'Andrea, A.F., Friedrichs, C.T. Craig, N.I., and Sommerfield, C.K. 1998. Oceanographic processes and the preservation of sedimentary structure in Eckernförde Bay, Baltic Sea. Continental Shelf Research, **18**: 1689-1714.

O'Connor, K.M., Dowding, C.H., Herkelrath, W.N., Greene, J., Huston, D.R., Norland, M.R., Ogle, J.W., and Van Eeckhhout, E. 1994. Introduction. Symposium and Workshop on Time Domain Reflectometry in Environmental, Infrastructure, and Mining Applications, Evanston, Illinois, September 7-9, 1994, pp. 2-3.

Papatheodorou, G. and Ferentinos, G. 1997. Submarine and coastal sediment failure triggered by the 1995, Ms=6.5 Aegion earthquake, Gulf of Corinth, Greece. Marine Geology, **137**: 287-304.

Parkes, R.J., Cragg, B.A., Fry, J.C., Herbert, R.A., and Wimpenny, J.T. 1990. Bacterial biomass and activity in deep sediment layers from the Peru margin. Philosophical Transactions of the Royal Society of London, **A331**, 139-153.

Peacock, W.H. and Seed, H.B. 1968. Sand liquefaction under cyclic loading simple shear conditions. Journal of Soils Mechanics and Foundations ASCE, **94**(3): 689-708.

Perissiratis, G., Mitropoulos, D., and Angelopoulos, J. 1984. The role of earthquakes in inducing sediment mass movements in the eastern Corinthiacos Gulf: An example from February 24 – March 4, 1981 activity. Marine Geology, **55**: 35-45.

Pestana, J.M. and Whittle, J.A. 1995. Compression model for cohesionless soils. Géotechnique, **45**(4): 611-631.

Premchitt, J., Rad, N.S., To, P., Shaw, R., and James, J.W.C. 1992. A study of gas in marine sediments in Hong Kong. Continental Shelf Research, **12**(10): 1251-1264.

Prior, D.B., Doyle, E.H., and Kaluza, M.J. 1989. Evidence for sediment eruption on deep sea floor. Gulf of Mexico Science, **243**: 517-519.

Rad, N.S. and Lunne, T. 1994. Gas in Soil. I: Detection and n-profiling. Journal of Geotechnical Engineering, **120**(4): 697-715.

Rad, N.S., Lunne, T., Tjelta, T.I., and Eide, A. 1989. A new soil investigation tool for detection of shallow gas. Proceedings of the Conference on Shallow Gas and Leaky Reservoirs, Stavenger, Norway.

Rad, N.S., Vianna, A.J.D., and Berre, T. 1994. Gas in soils. II: Effect of gas on undrained static and cyclic strength of sand. Journal of Geotechnical Engineering, **120**(4): 716-737.

Rau, G. and Chaney, R.C. 1988. Triaxial testing of marine sediments with high gas contents. *In* Advanced triaxial testing of soil and rock. *Editors* Donaghe, R.T., Chaney, R.C., and Silber, M.L. ASTM STP 977, Philadelphia, pp. 338-352.

Real, C.R., Toppozada, T.R., and Parke, D.L. 1978. Earthquake epicenter map of California, showing events from 1900 – 1974 equal to or greater than magnitude 4.0 or intensity V. California Resources Agency, Department of Conservation, Open-File Report 78-4 SAC, scale 1:1,000,000.

Richardson, M.D. and Davis, A.M. 1998. Modeling methane-rich sediments of Eckernförde Bay. Continental Shelf Research, **18**: 1671-1688.

Robertson, P.K. 1994. Suggested terminology for liquefaction. Proceedings of the 47th Canadian Geotechnical Conference, Halifax, N.S. CGS. September 1994 pp. 277-286.

Robertson, P.K. 1998. Personal Communications.

Robertson, P.K. and Wride, C.E. 1998. Evaluating cyclic liquefaction potential using the cone penetration test. Canadian Geotechnical Journal, **35**(3): 442-459.

Robertson, P.K., Wride, C.E., List B,R., Atukorala U., Biggar, K.W., Byrne, P.M., Campanella, R.G., Cathro, D.C., Chan, D.H., Czajewski, K., Finn, W.D.L., Gu, W.H., Hammamji, Y., Hofmann, B.A., Howie, J.A., Hughes, J., Imrie, A.S., Konrad, J.-M., Küpper, A., Law, T., Lord, E.R.F., Monahan, P.A., Morgenstern, N.R., Phillips, R., Piché, R., Plewes, H.D., Scott, D., Sego, D.C., Sobkowicz, J., Stewart, R.A., Tan, S., Vaid, Y.P., Watts, B.D., Woeller, D.J., Youd, T.L. and Zavodni, Z. 1999. The CANLEX project: summary and conclusions. Canadian Geotechnical Journal. In Press.

Roscoe, K.H., Schofield, A.N. and Wroth, C.P. 1958. On yielding of soils. Géotechnique, **8**: 22-53.

Roth, K., Schulin, R., Fluhler, H., and Attinger, W. 1990. Calibration of time domain reflectometry for water content measurement using a composite dielectric approach. Water Resources Research, **26**(10): 2267-2273.

Rowe, P.W. 1962. The stress-dilatancy relation for static equilibrium of an assembly of particles in contact. Proc. Of the Roy. Soc. A269: 500-527.

Rowe, P.W. 1969. The relation between shear strength of sands in triaxial compression, plane strain and direct shear. Géotechnique, **19**(1): 75-86.

Sasitharan, S. 1994. Collapse behavior of very loose sand. Ph.D. Thesis, University of Alberta, Alberta, Canada.

Sasitharan, S., Robertson, P.K., Sego, D.C., and Morgenstern, N.R. 1994. State boundary surface for very loose sand and its practical implications. Canadian Geotechnical Journal, **31**(3): 321-334.

Schubel, J.S. 1974. Gas bubbles and the acoustically impenetrable, or turbid, character of some estuarine sediments. *In* Natural Gasses in Marine Sediments. *Editor* I.R. Kaplan. Plenum Press, NY, pp. 275-298.

Schumann, I. 1992. Fundamentos de um modelo de comportamento de solos argilosos saturados, D.Sc. Thesis, Universidade Federal do Rio de Janeiro (UFRJ/COPPE), Rio de Janeiro, Brasil.

Schwarz, H.U. 1982. Subaqueous slope failures – experiments and modern occurrences. *In* Contributions to sedimentology. *Edited by* F. Fuchtbauer, A.P. Lisitzyn, J.D. Milliman, and E. Seibold. Stuttgart.

Seed, H.B. 1968. Landslides during earthquakes due to soil liquefaction. Journal of the Soil Mechanics and Foundations Division, ASCE, **94**: 1053-1122.

Seed, H.B., Tokimatsu, K., Harder, L.F., and Chung, R. 1985. Influence of SPT procedures in soil liquefaction resistance evaluations. Journal of Geotechnical Engineering, ASCE, **111**(12): 1425-1445.

Seed, H.B. and Harder, L.F. 1990. SPT-based analysis of cyclic pore pressure generation and undrained residual strength. Seed Memorial Symposium, pp. 351-376.

Sills, G.C. 1988. Triaxial testing of gassy sand, Report of test programme for Statoil. Department of Engineering Science, Oxford University, Oxford, England.

Sills, G.C. and Nageswaran, S. 1984. Compressibility of gassy soils. *In* Proceedings of Oceanology International, Society for Underwater Technology, Brighton, England, pp. OI 2.6/1-18.

Sills, G.C. and Wheeler, S.J. 1992. The significance of gas for offshore operations. Continental Shelf Research, **12**(10): 1239-1250.

Sills, G.C., 1997. Personal Communications.

Sills, G.C., Wheeler, S.J., Thomas, S.D., and Gardner, T.N. 1991. Behaviour of offshore soils containing gas bubbles. Géotechnique, **41**(2): 227-241.

Silva, A.J. and Brandes, H.G. 1998. Geotechnical properties and behavior of high-porosity, organic-rich sediments in Eckernförde Bay, Germany. Continental Shelf Research, **18**: 1917-1938.

Silva, A.J., Brandes, H.G., Veyera, G.E. 1996. Geotechnical characterization of surficial high-porosity sediments in Eckernförde Bay. Geomarine Letters, **16**(3): 167-174.

Silver, M.L., Tatsuoka, F., Phukunhaphan, A., and Avramidis, A.S. 1980. Cyclic undrained strength of sand by triaxial test and simple shear test. Proceedings of the 7th World Conference on Earthquake Engineering, Istanbul, Vol. 3, pp. 281-288.

Silvis, F. and de Groot, M.B. 1995. Flow slides in the Netherlands: experience and engineering practice. Canadian Geotechnical Journal, **32**: 1086-1092.

Skopek, P. 1994. Collapse behavior of very loose dry sand. Ph.D. Thesis, University of Alberta, 1994, 106 pages.

Sladen, J.A., D'Hollander, R.D., and Krahn, J. 1985. The liquefaction of sands, a collapse surface approach. Canadian Geotechnical Journal, **22**: 564-578.

Slowey, N.C., Bryant, W.R., Lambert, D.N. 1996. Comparison of high-resolution seismic profiles and the geoacoustic properties of Eckernförde Bay sediments. Geomarine Letters, **16**(3): 240-248.

Smith, K.A. and Mullins, C.E. (Eds.). 1991. Soil analysis: Physical methods. Marcel Dekker, New York, N.Y., 620 pp.

Sobkowicz, J.C. 1982. The mechanics of gassy sediments. Ph.D. thesis, University of Alberta, Alberta, Canada.

Sobkowicz, J.C. and Morgenstern, N.R. 1984. The undrained equilibrium behavior of gassy sediments. Canadian Geotechnical Journal, **21**: 439-448.

Sobkowicz, J.C. and Morgenstern, N.R. 1987. An experimental investigation of transient pore pressure behavior in soils due to gas exsolution. Proceedings of the International Symposium on Prediction and Performance in Geotechnical Engineering, Calgary, Alberta, Canada, pp. 267-275.

Stoll, R.D. and Bautista, E.O. 1998. Using the Biot theory to establish a baseline geoacoustic model for seafloor sediments. Continental Shelf Research, **18**: 1839-1857.

Tatsuoka, F., Muramatsu, M., and Sasaki, T. 1982. Cyclic undrained stress-strain behavior of dense sands by torsional simple shear test. Soils and Foundations, **22**(2): 55-70.

Tatsuoka, F., Toki, S., Miura, S., Kato, H., Okamoto, M., Yamada, S., Yasuda, S., Tanizawa, F. 1986. Some factors affecting cyclic undrained triaxial strength of sand. Soils and Foundations, **26**(3): 99-116.

Terzaghi, K. 1956. Varieties of submarine slope failures. Proceedings, 8th Texas Conference on Soils and Foundation Engineering, University of Texas, Austin, pp. 1-41.

Terzaghi, K. 1962. *Discussion* Sedimentation of the Fraser River delta, British Columbia. The Bulletin of the American Association of Petroleum Geologists, **46**(8): 1438-1443.

Thomas, J. 1992. Static, cyclic, and post liquefaction undrained behaviour of Fraser River sand. M.A.S. The University of British Columbia, 117 pages.

Thomas, S.D. 1987. The consolidation behaviour of gassy soil. Ph.D. Thesis, Oxford University.

Toki, S., Tatsuoka, F., Miura, S., Yoshimi, Y., Yasuda, S., and Makihara, Y. 1986. Cyclic undrained triaxial strength of sand by a cooperative test program. Soils and Foundations, **26**(3): 117-128.

Tokimatsu, K. and Yoshimi, Y. 1983. Empirical correlation of soil liquefaction based on SPT N-value and fines content. Soils and Foundations, **23**(4): 56-74.

Topp, G.C., Davis, J.L., and Annan, A.P. 1980. Electromagnetic determination of soil water content: measurements in coaxial triaxial lines. Water Resources Research, **16**(3): 574-582.

Topp, G.C., Davis, J.L., and Annan, A.P. 1982. Electromagnetic determination of soil water content using TDR: I. Applications to wetting fronts and steep gradients. Soil Science Society of America Journal, **46**: 672-678.

Verdugo, R. and Ishihara, K. 1996. The steady state of sandy soils. Soils and Foundations, **36**(2): 81-91.

Vogel, T.M., Oremland, R.S., and Kvenvolden, K.A. 1982. Low-temperature formation of hydrocarbon gases in San Francisco Bay sediment (California, USA). Chemical Geology, **37**: 289-298.

Welday, E.E. and Williams, J.W. 1975. Offshore surficial geology of California. California Division of Mines and Geology Map Sheet 2, scale 1:500,000.

Wever, T.F., Abegg, F., Fiedler, H.M., Fechner, G., and Stender, I.H. 1998. Shallow gas in the muddy sediments of Eckernförde Bay. Continental Shelf Research, **18**: 1715-1739.

Wheeler, S.J. 1986. The stress-strain behavior of soils containing gas bubbles. Ph.D. thesis, Oxford University, Oxford, England.

Wheeler, S.J. 1988a. A conceptual model for soils containing large gas bubbles. Géotechnique, **38**: 389-397.

Wheeler, S.J. 1988b. The undrained shear strength of soils containing large gas bubbles. Géotechnique, **38**: 399-413.

Wheeler, S.J. 1991. An alternative framework for unsaturated soil behaviour. Géotechnique, **41**: 257-261.

Wheeler, S.J. and Gardner, T.N. 1989. Elastic moduli of soils containing large gas bubbles. Géotechnique, **39**(2): 333-342.

Wheeler, S.J. and Sivakumar, V. 1995. An elasto-plastic critical state framework for unsaturated soil. Géotechnique, **45**(1): 35-53.

Wheeler, S.J., Sills, G.C., Sham, W.K., Duffy, S.M., and Boden, D.G. 1991. The influence of shallow gas on geotechnical properties. Journal of the Society of Underwater Technology, **17**: 11-16.

Whelan, T. III, Coleman, J.M., and Suhayda, J.N. 1975. The geochemistry of recent Mississippi River delta sediments: Gas concentration and sediment stability. Proceedings of the Offshore Technology Conference; OTC 2342, Houston, Texas, pp. 71-77.

Whelan, T. III, Coleman, J.M., Suhayda, J.N., and Roberts, N.H. 1977. Acoustical penetration and shear strength in gas charged sediments. *In* Marine Geotechnology, Vol. 2, Marine Slope Stability. *Edited by* A.F. Richards. Elsevier, Amsterdam, The Netherlands, pp. 147-159.

Whelan, T. III, Ishmael, J.T., and Rainey, G.B. 1978. Gas-sediment interactions in Mississippi Delta sediments. *In* Proceedings of the Offshore Technology Conference; OTC 3166, Houston, Texas, pp. 1029-1032.

Whiticar, M. 1982. The presence of methane bubbles in the acoustically turbid sediments of Eckernförde Bay, Baltic Sea. *In* The Dynamic Environment of the Ocean Floor. *Editors* Fanning, K.A., Manheim, F.T. Lexinton Books, Lexington, MA, pp. 192-235.

Wilkens, R.H. and Richardson, M.D. 1998. The influence of gas bubbles on sediment acoustic properties: in situ, laboratory, and theoretical results from Eckfernförde Bay, Baltic Sea, Germany. Continental Shelf Research, **18**: 1859-1892.

Williams, J.P. and Sarginson, M. 1990. Signature – the future approach to reliable shallow gas detection. *In* Safety in offshore drilling: the role of shallow gas surveys. *Editors* D.A. Ardus and C.D. Green. Kluwer Academic Publishers, Dordrecht, pp. 235-256.

Wood, D.M. 1990. Soil behaviour and critical state soil mechanics. Cambridge University Press, Cambridge, pp. 179-188.

Wride, C.E. and Robertson, P.K. 1997a. CANLEX Introductory Data Review Report. January 1997, 90 pages.

Wride, C.E. and Robertson, P.K. 1997b. CANLEX Phase I and III Data Review Report. October 1997, 168 pages.

Xia, H. and Hu, T. 1991. Effects of saturation and back pressure on sand liquefaction. Journal of Geotechnical Engineering, ASCE, **117**(9): 1347-1362.

Yamamoto, S., Alcauskas, J.B., and Crozier, T.E. 1976. Solubility of methane in distilled water and seawater. J. Chemical and Engrg. Data, **21**(1): 78-80.

Yoshimi, Y. and Oh-oka, H. 1975. Influence of degree of shear stress reversal on the liquefaction potential of saturated sand. Soils and Foundations, **15**(3): 27-40.

Yoshimine, M. and Ishihara, K. 1998. Flow potential of sand during liquefaction. Soils and Foundations, **38**(3): 189-198.

Yoshimine, M., Ishihara, K., and Vargas, W. 1998. Effects of principal stress direction and intermediate principal stress on undrained shear behavior of sand. Soils and Foundations, **38**(3): 178-188.

Yoshimine, M., Robertson, P.K., and Wride, C.E. 1999. Undrained shear strength of clean sands. Accepted for publication in the Canadian Geotechnical Journal.

Youd, T.L. and Idriss, I.M. (Editors). 1998. Proceedings of the National Center for Earthquake Engineering Research (NCEER) Workshop on Evaluation of Liquefaction Resistance of Soils, Salt Lake City, Utah, January 1996. NCEER-97-0022.

Yuan, F., Bennell, J.D., and Davis, A.M. 1992. Acoustic and physical characteristics of gassy sediments in the western Irish Sea. Continental Shelf Research, **12**(10): 1121-1134.

Zegelin, S.J., White, I., and Jenkins, D.R. 1989. Improved field probes for soil water content and electrical conductivity measurement using time domain reflectometry. Water Resources Research, **25**(11): 2367-2376.

APPENDIX A

MONOTONIC TRIAXIAL TEST RESULTS

This appendix contains the test results for each monotonic triaxial test. The test results are presented in the order in which they were performed. A summary table of all tests is also included.

Table A.1 - Summary of monotonic triaxial test results.

Sample	Test Type		Initial p'	Initial Sr *		Void Ratio †	Response	Peak		Minimum		End of Test	
					Final			p'	q'	p'	q'	p'	q'
6	Saturated	CD	301.0	100%	100%	0.825	D					596.4	893.6
8	Gassy	CU	286.2	80%	88%	0.917	A	278.4	304.1	110.2	184.2		
9	Gassy	CU	295.2	72%	77%	1.066	D					374.0	548.3
10	Gassy	CU	258.6	91%	95%	0.986	A	195.1	155.7	37.5	75.3		
11	Saturated	CU	266.3	100%	100%	0.896	A	197.9	121.9	10.5	32.9		
12	Saturated	CU	302.1	100%	100%	0.910	A	240.3	134.4	17.0	29.8		
13	Gassy	CU	303.6	83%	90%	0.883	D					411.4	584.8
14	Gassy	CU	301.5	97%	104%	0.771	B	283.2	318.8	187.2	254.4	189.77	273.36
15	Gassy	CU	312.5	80%	84%	0.874	D					486.1	824.9
16	Gassy	CU	317.1	82%	87%	0.876	D					472.9	713.6
17	Gassy	CU	298.5	77%	81%	0.890	D					458.3	703.5
18	Gassy	CU	296.1	76%	75%	0.883	D					535.1	866.7
19	Saturated	CD	295.0	100%	100%	0.765	D					768.3	1427.5
20	Gassy	CU	300.7	86%	92%	0.872	D					318.6	499.6
21	Gassy	CU	296.3	80%	82%	0.897	D					484.7	799.6
22	Saturated	CU	301.4	100%	100%	0.733	A	191.0	137.1	12.9	49.7		
23	Saturated	CD	287.4	100%	100%	0.743	D					618.8	1005.9
24	Gassy	CU	283.9	97%	106%	0.835	A	236.3	133.9	-4.8	-11.6		
25	Gassy	CU	271.7	91%	96%	0.852	A	226.1	117.3	9.6	0.0		

* Initial degree of saturation is calculated from TDR data at the beginning of shear.

† Void ratio is at the beginning of shear.

Note: p' is the mean normal effective stress defined as $^1/_3\,(\sigma_1 + 2\sigma_3)$

q' is the deviator stress defined as $(\sigma_1 - \sigma_3)$

CU - Consolidated Undrained triaxial test

CD - Consolidated Drained triaxial test

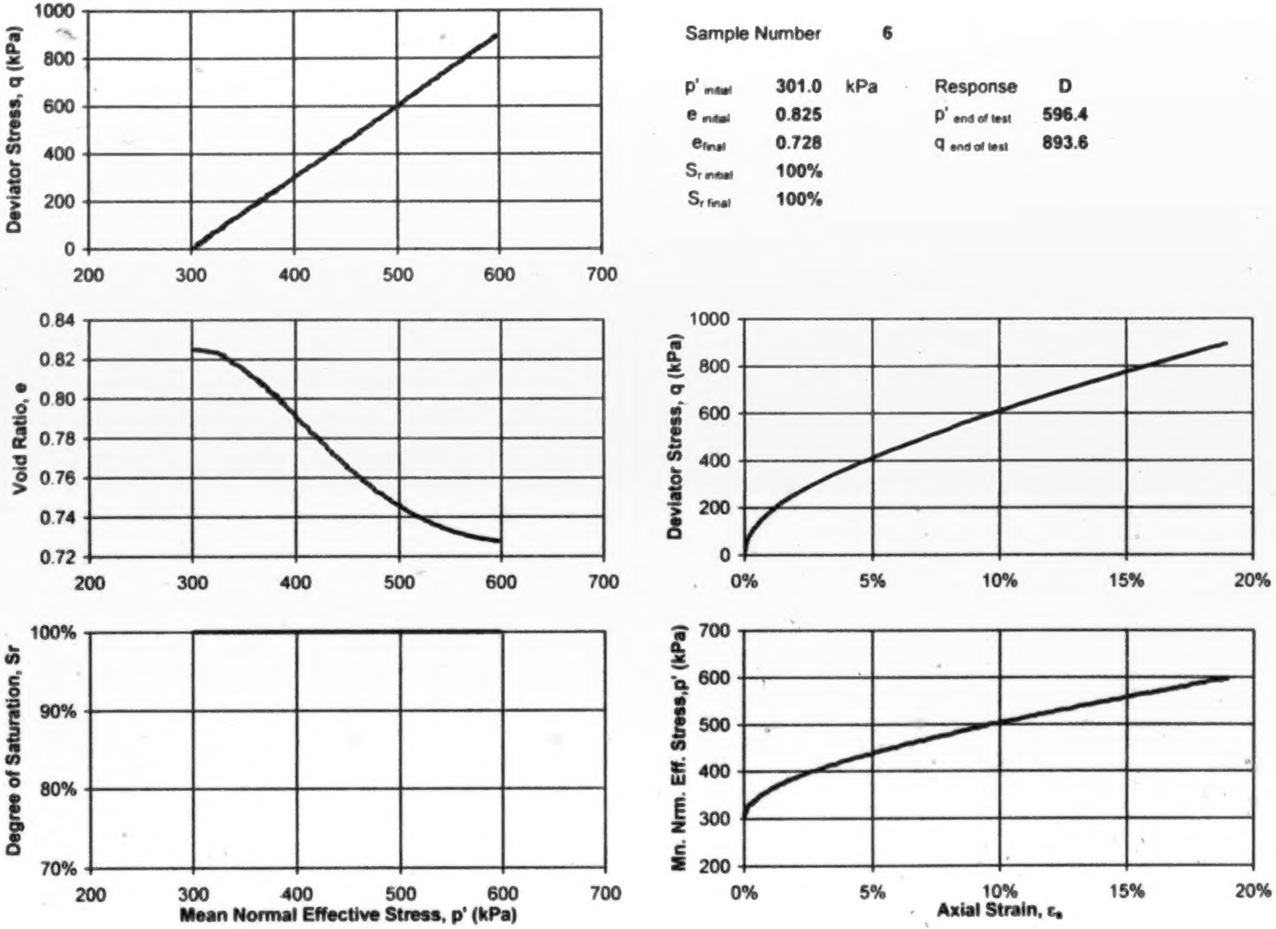

Sample Number 6

$p'_{initial}$	301.0 kPa	Response	D
$e_{initial}$	0.825	$p'_{end\ of\ test}$	596.4
e_{final}	0.728	$q_{end\ of\ test}$	893.6
$S_{r\ initial}$	100%		
$S_{r\ final}$	100%		

Figure A.1 - Sample #6, Saturated, CD.

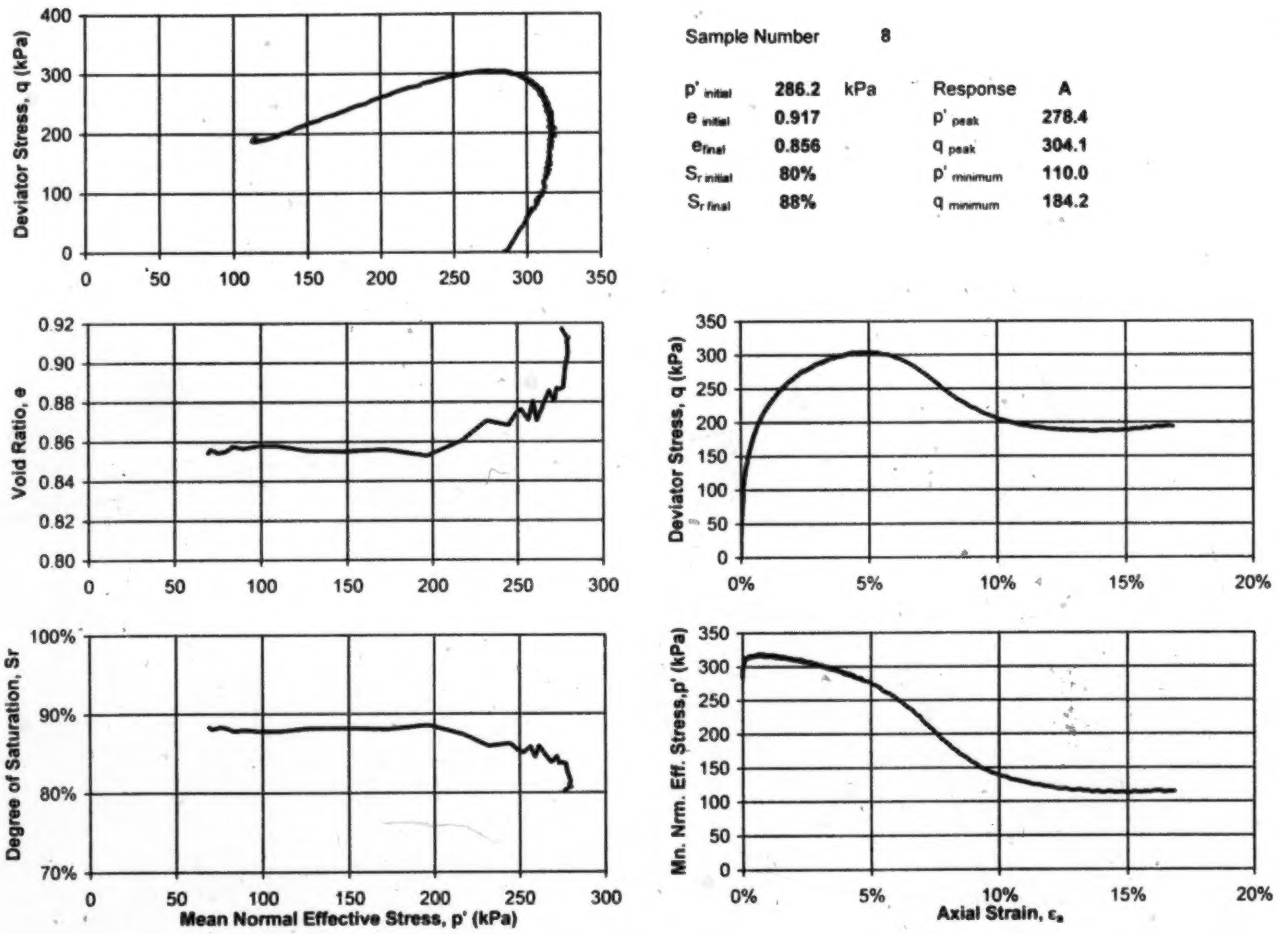

Sample Number 8

$p'_{initial}$	286.2	kPa	Response	A
$e_{initial}$	0.917		p'_{peak}	278.4
e_{final}	0.856		q_{peak}	304.1
$S_{r\,initial}$	80%		$p'_{minimum}$	110.0
$S_{r\,final}$	88%		$q_{minimum}$	184.2

Figure A.2 - Sample #8, Gassy, CU.

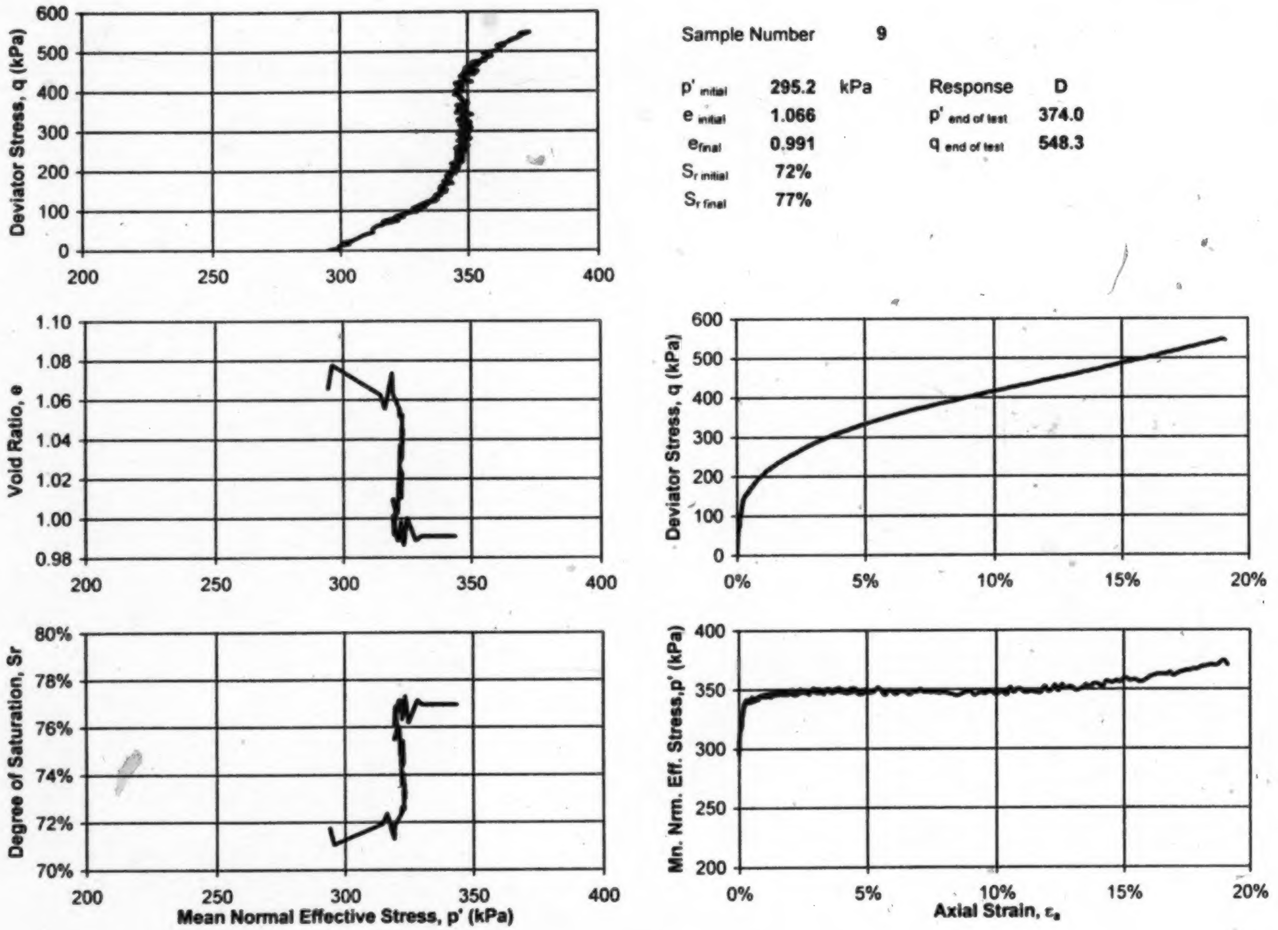

Sample Number 9

$p'_{initial}$	295.2	kPa	Response	D
$e_{initial}$	1.066		$p'_{end\ of\ test}$	374.0
e_{final}	0.991		$q_{end\ of\ test}$	548.3
$S_{r\ initial}$	72%			
$S_{r\ final}$	77%			

Figure A.3 - Sample #9, Gassy, CU.

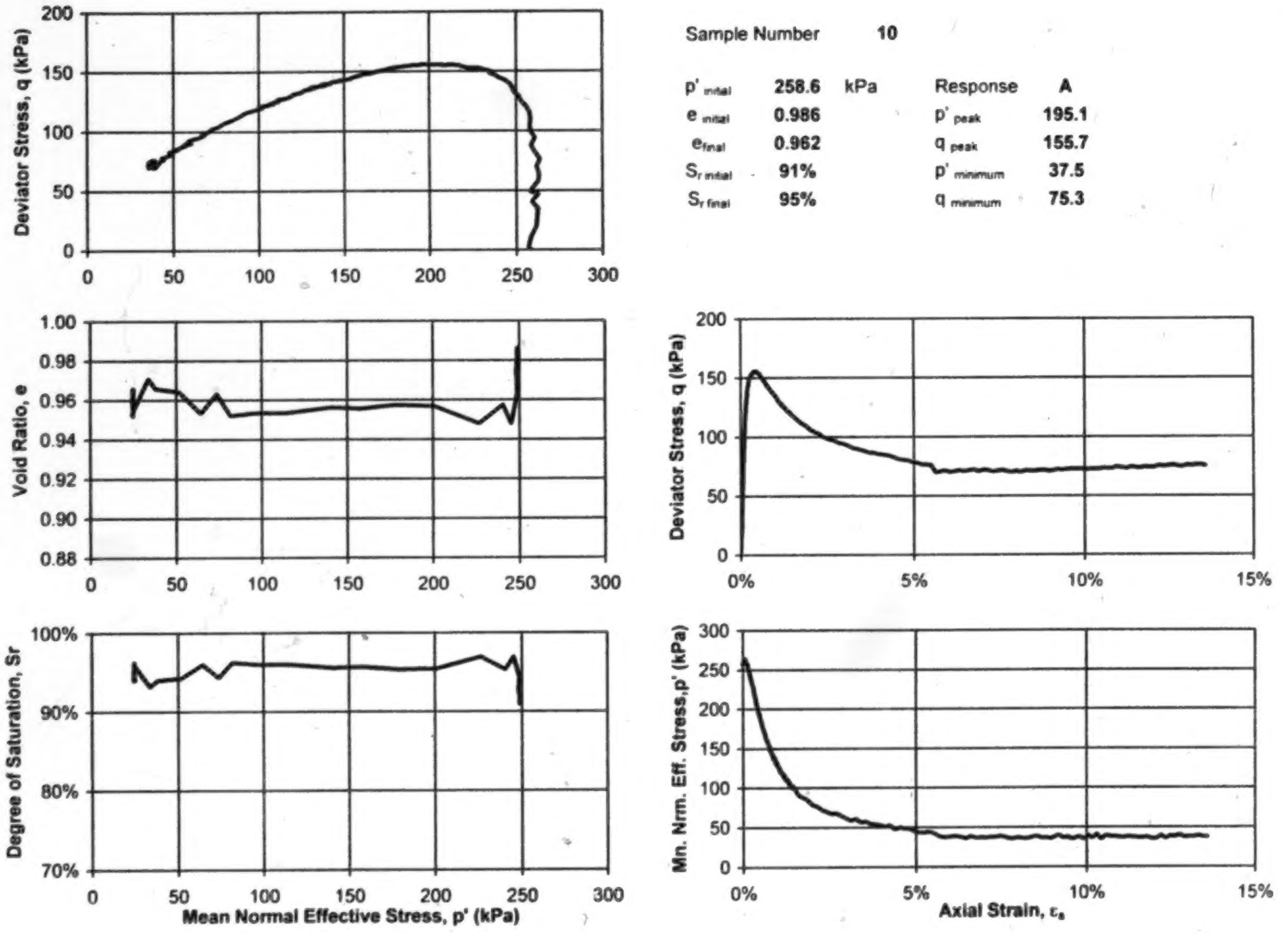

Sample Number 10

$p'_{initial}$	258.6	kPa	Response	A
$e_{initial}$	0.986		p'_{peak}	195.1
e_{final}	0.962		q_{peak}	155.7
$S_{r\,initial}$	91%		$p'_{minimum}$	37.5
$S_{r\,final}$	95%		$q_{minimum}$	75.3

Figure A.4 - Sample #10, Gassy, CU.

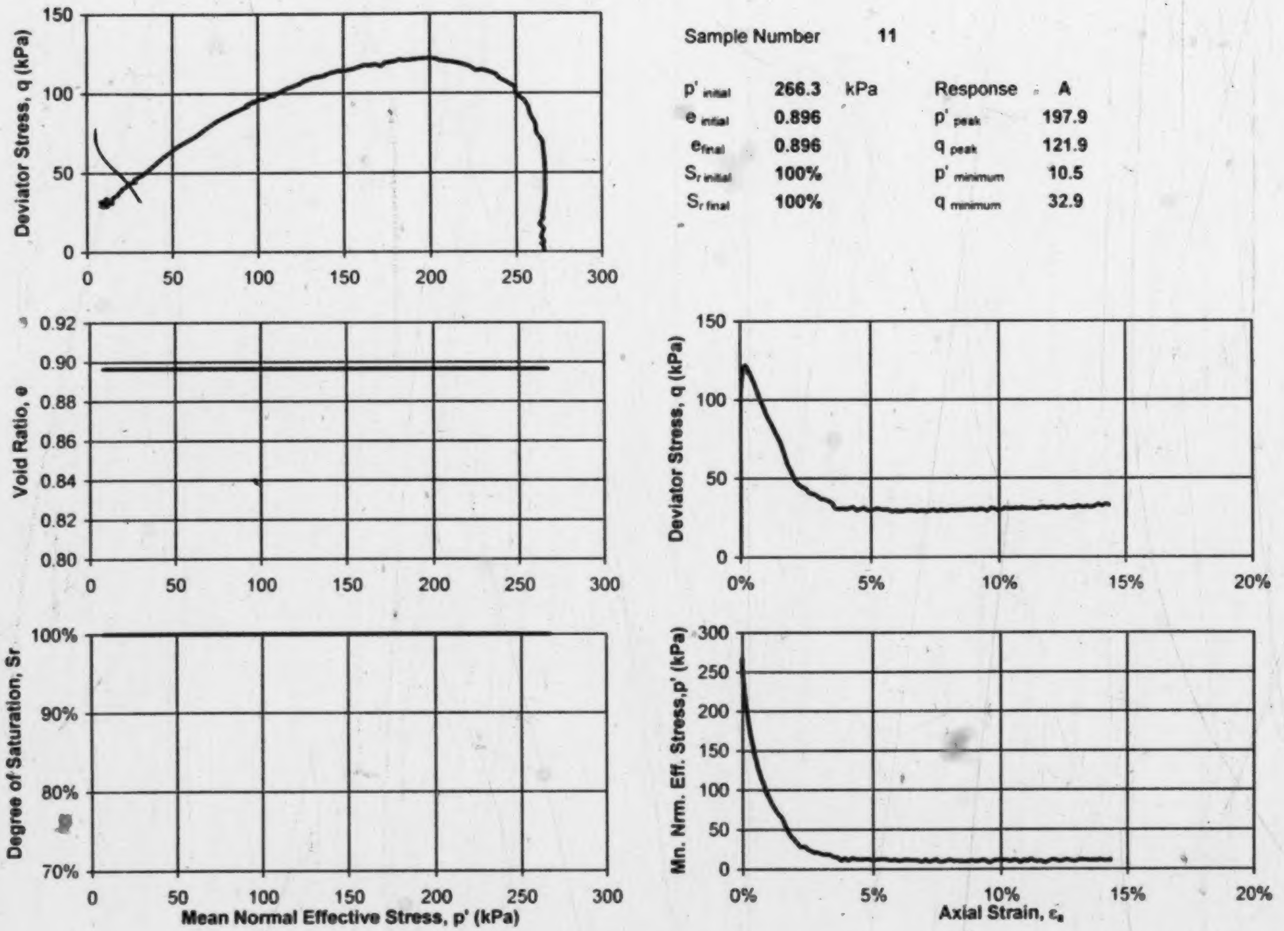

Sample Number 11

$p'_{initial}$	266.3	kPa	Response	A
$e_{initial}$	0.896		p'_{peak}	197.9
e_{final}	0.896		q_{peak}	121.9
$S_{r\,initial}$	100%		$p'_{minimum}$	10.5
$S_{r\,final}$	100%		$q_{minimum}$	32.9

Figure A.5 - Sample #11, Saturated, CU.

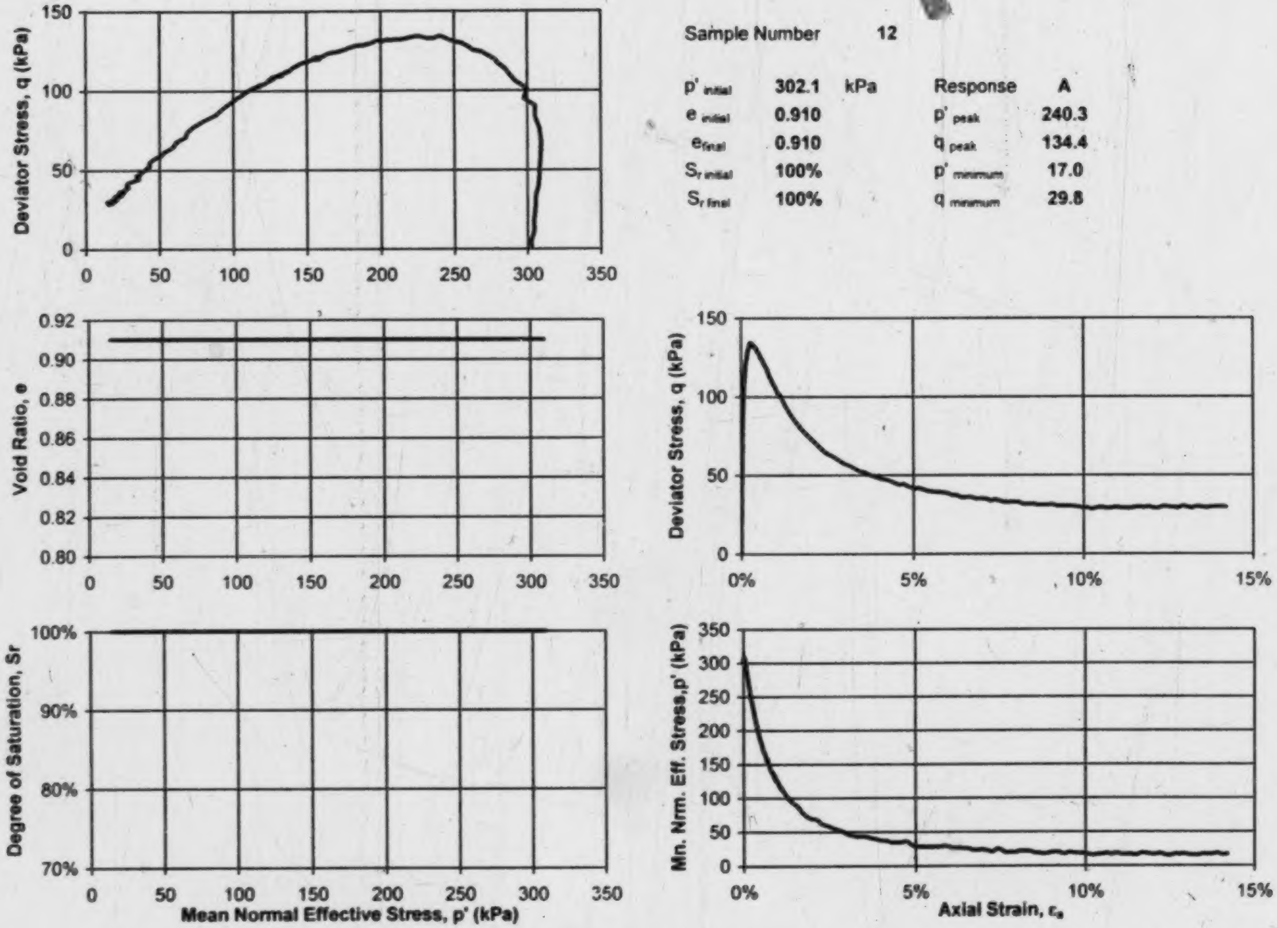

Sample Number	12			
$p'_{initial}$	302.1	kPa	Response	A
$e_{initial}$	0.910		p'_{peak}	240.3
e_{final}	0.910		q_{peak}	134.4
$S_{r\,initial}$	100%		$p'_{minimum}$	17.0
$S_{r\,final}$	100%		$q_{minimum}$	29.8

Figure A.6 - Sample #12, Saturated, CU.

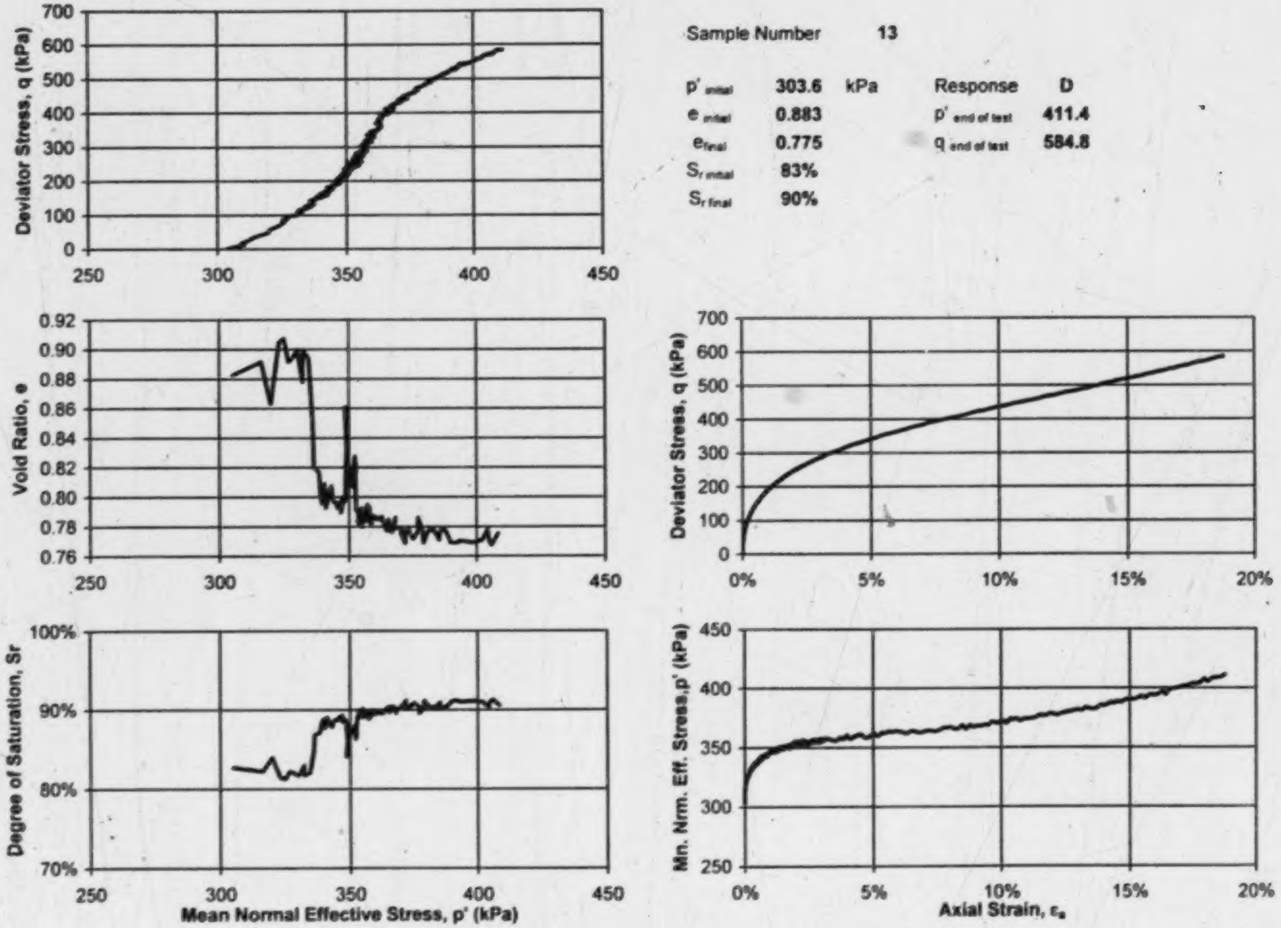

Sample Number	13			
$p'_{initial}$	303.6	kPa	Response	D
$e_{initial}$	0.883		$p'_{end\ of\ test}$	411.4
e_{final}	0.775		$q_{end\ of\ test}$	584.8
$S_{r\ initial}$	83%			
$S_{r\ final}$	90%			

Figure A.7 - Sample #13, Gassy, CU.

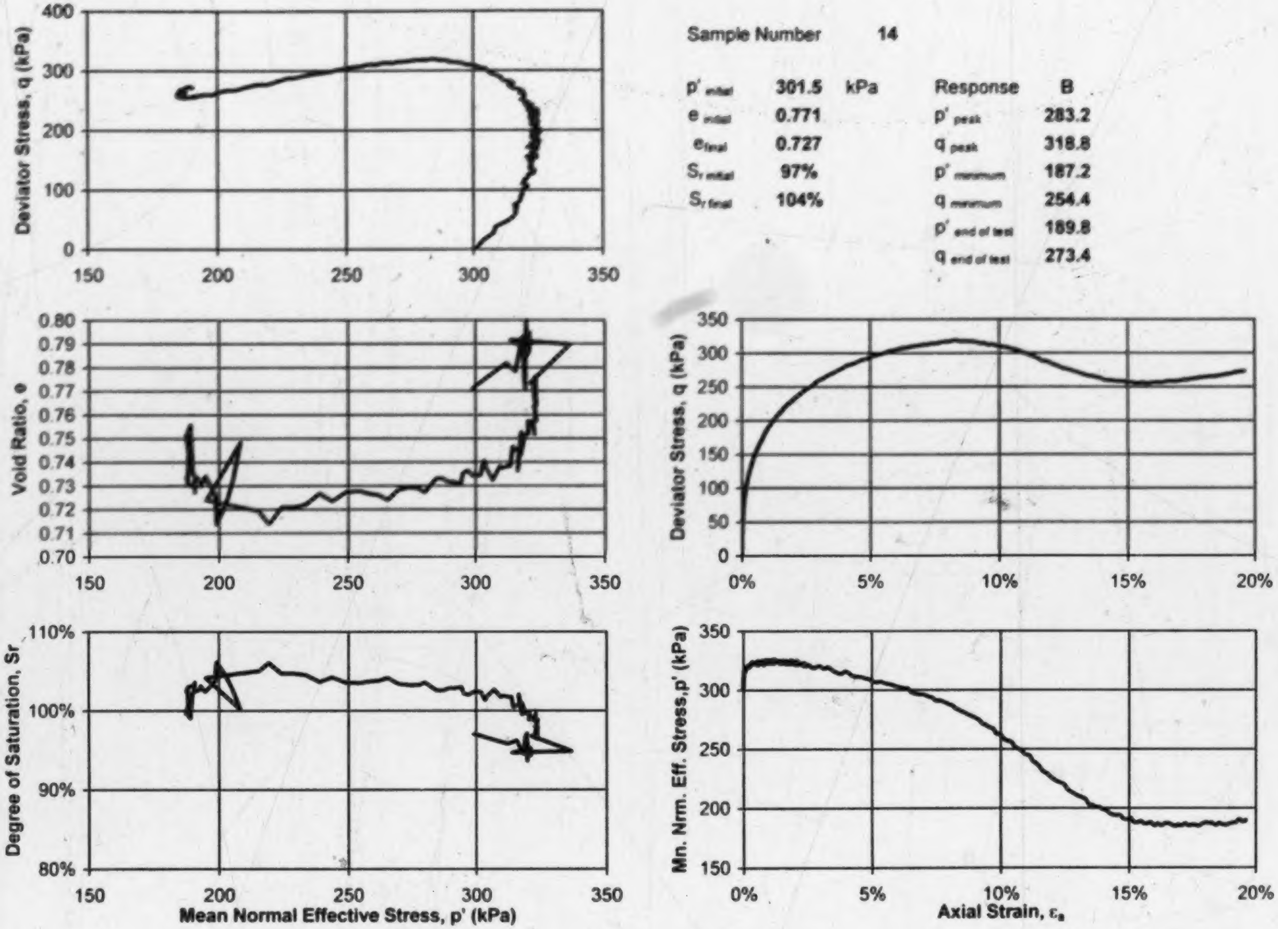

Figure A.8 - Sample #14, Gassy, CU.

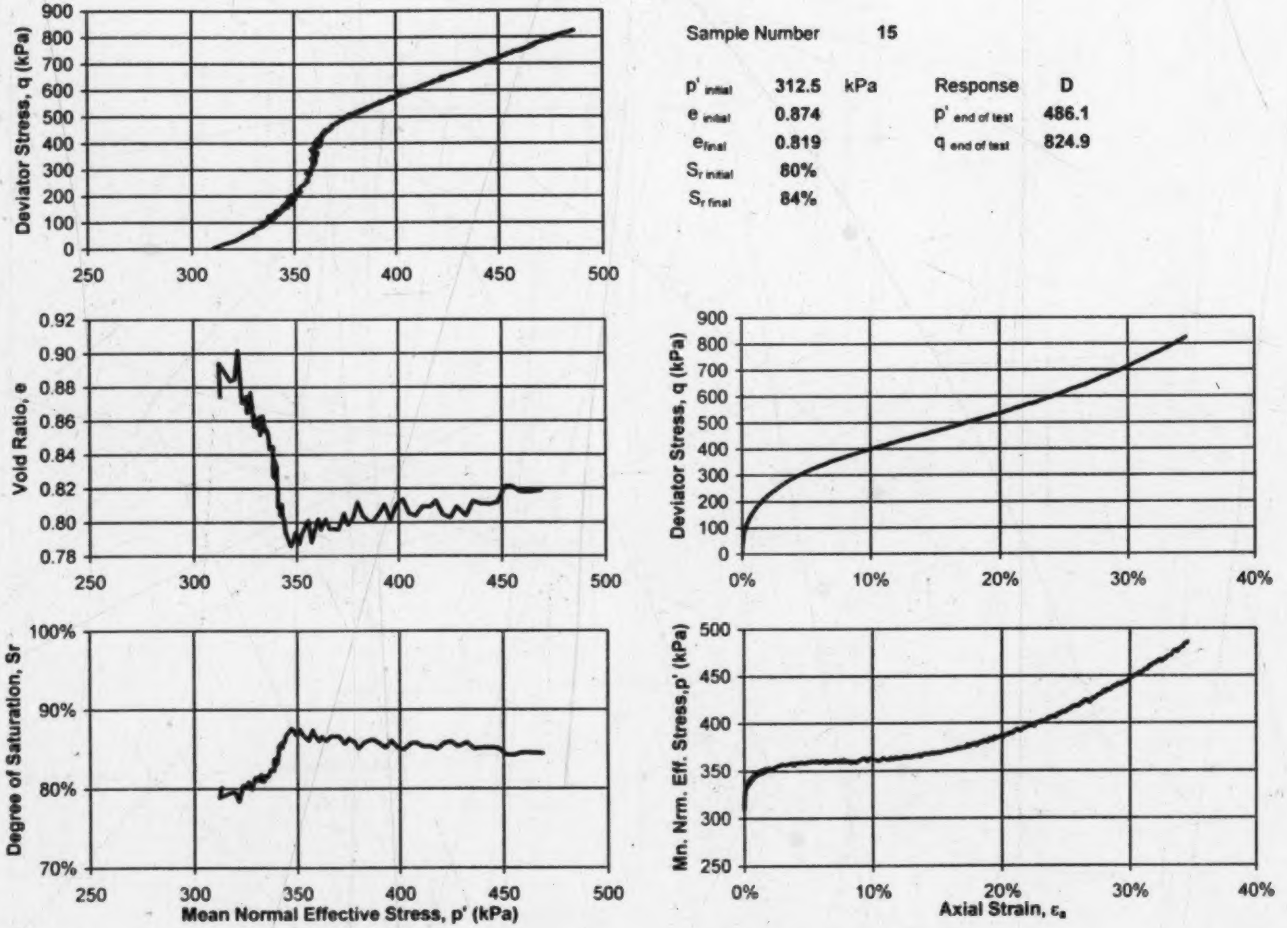

Sample Number 15

$p'_{initial}$	312.5	kPa	Response	D
$e_{initial}$	0.874		$p'_{end\ of\ test}$	486.1
e_{final}	0.819		$q_{end\ of\ test}$	824.9
$S_{r\ initial}$	80%			
$S_{r\ final}$	84%			

Figure A.9 - Sample #15, Gassy, CU.

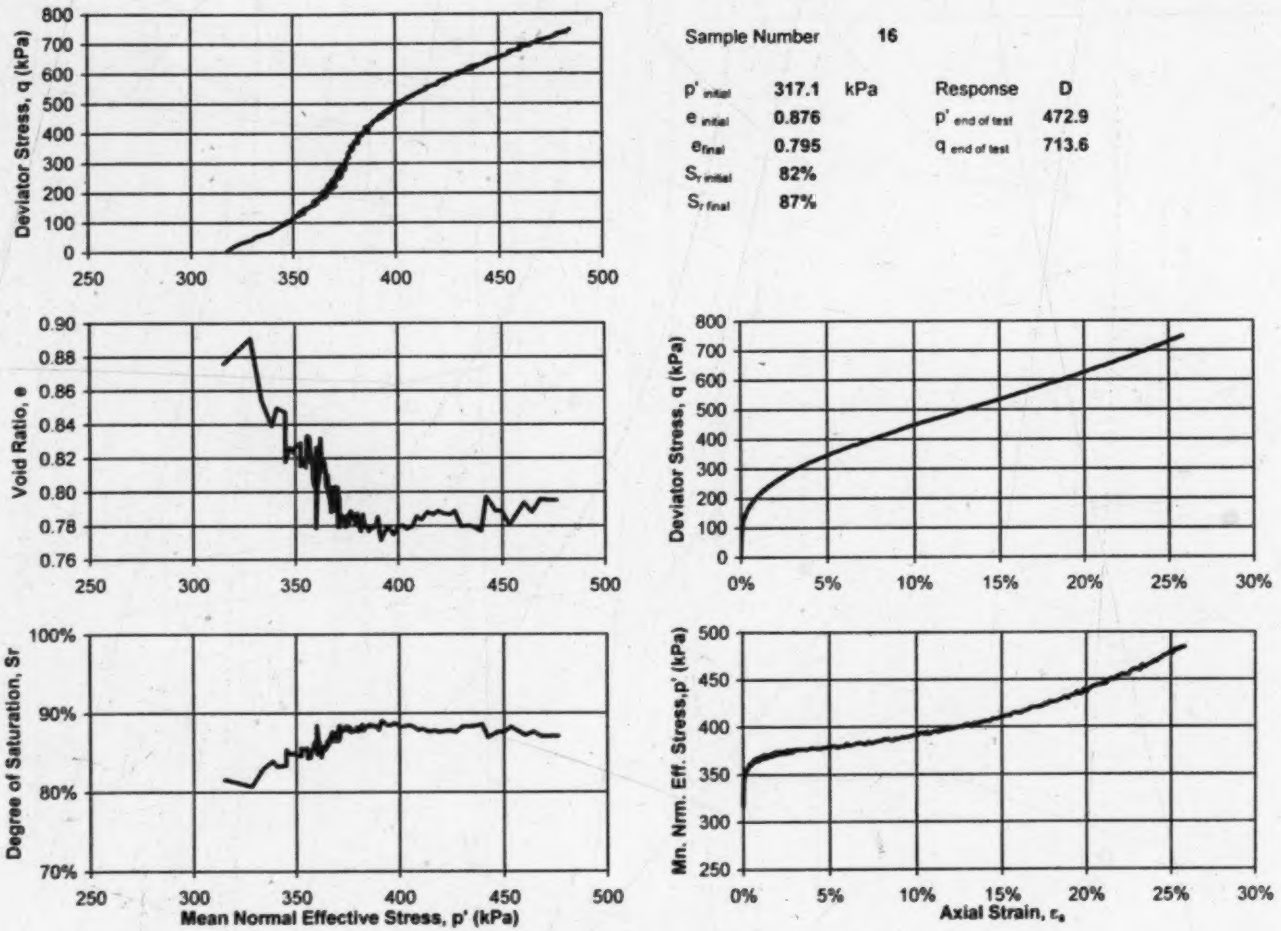

Sample Number 16

$p'_{initial}$	317.1	kPa	Response	D
$e_{initial}$	0.876		$p'_{end\ of\ test}$	472.9
e_{final}	0.795		$q_{end\ of\ test}$	713.6
$S_{r\ initial}$	82%			
$S_{r\ final}$	87%			

Figure A.10 - Sample #16, Gassy, CU.

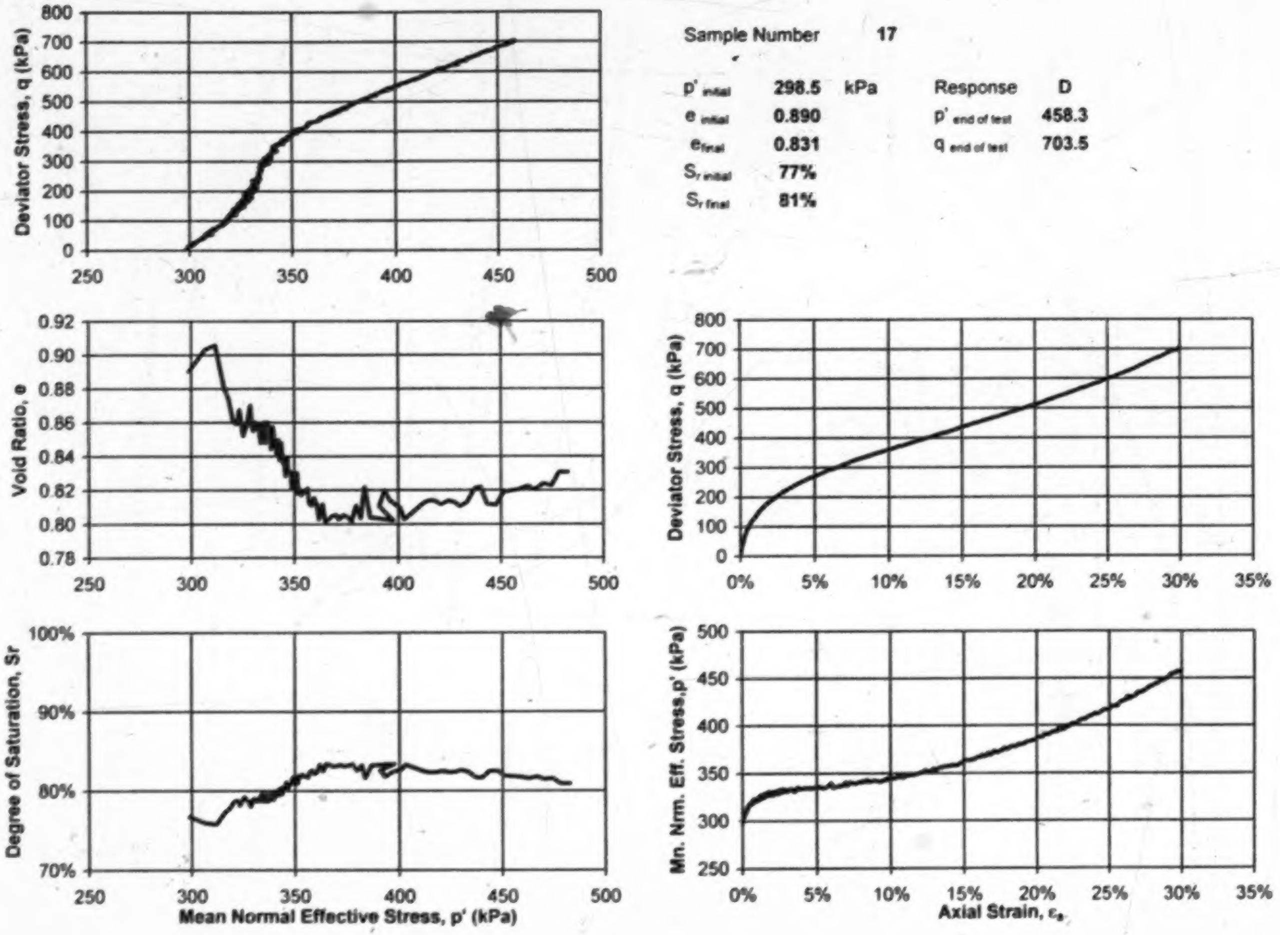

Sample Number 17

$p'_{initial}$	298.5	kPa	Response	D
$e_{initial}$	0.890		$p'_{end\ of\ test}$	458.3
e_{final}	0.831		$q_{end\ of\ test}$	703.5
$S_{r\ initial}$	77%			
$S_{r\ final}$	81%			

Figure A.11 - Sample #17, Gassy, CU.

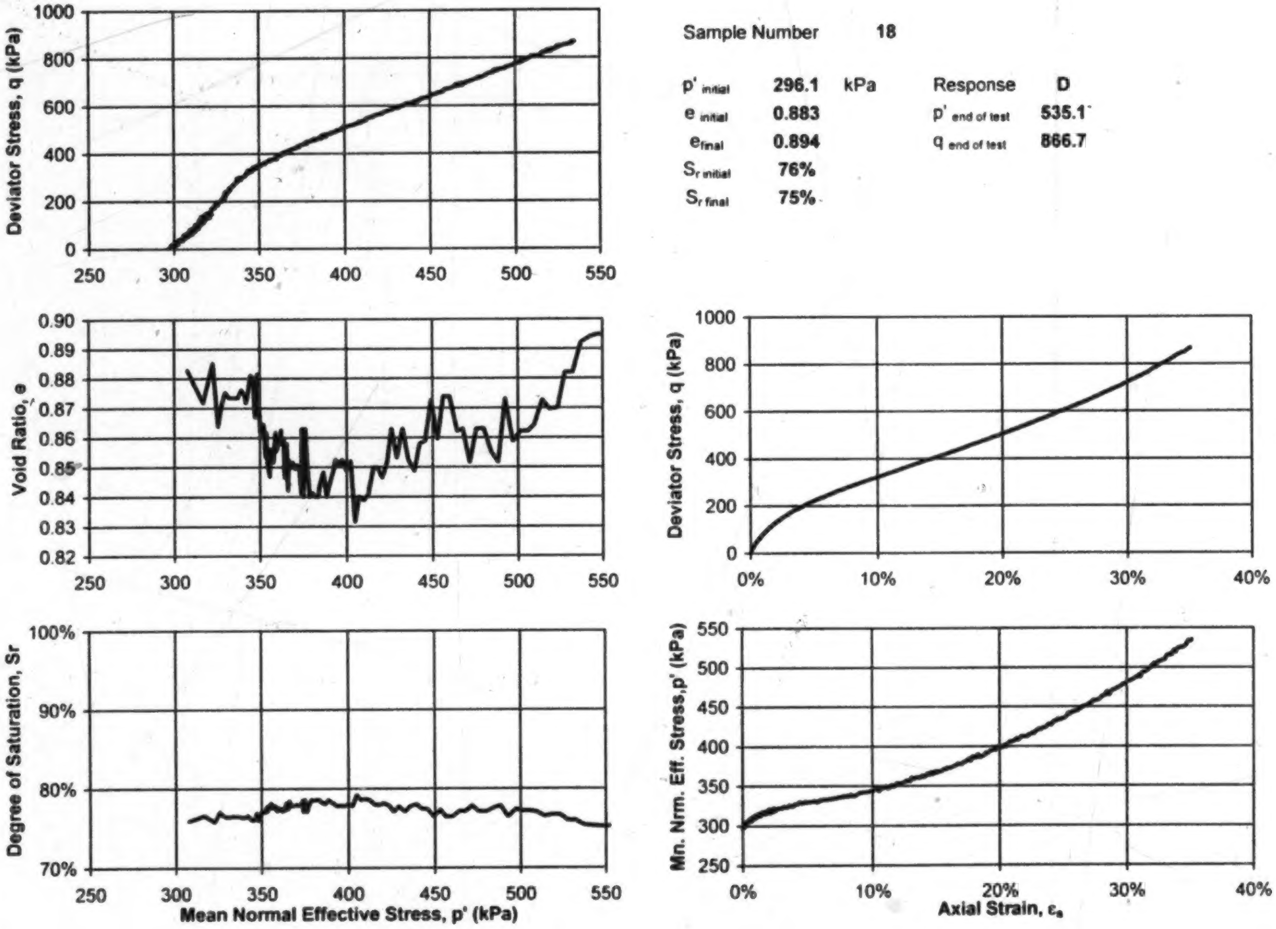

Sample Number	18			
$p'_{initial}$	296.1	kPa	Response	D
$e_{initial}$	0.883		$p'_{end\ of\ test}$	535.1
e_{final}	0.894		$q_{end\ of\ test}$	866.7
$S_{r\ initial}$	76%			
$S_{r\ final}$	75%			

Figure A.12 - Sample #18, Gassy, CU.

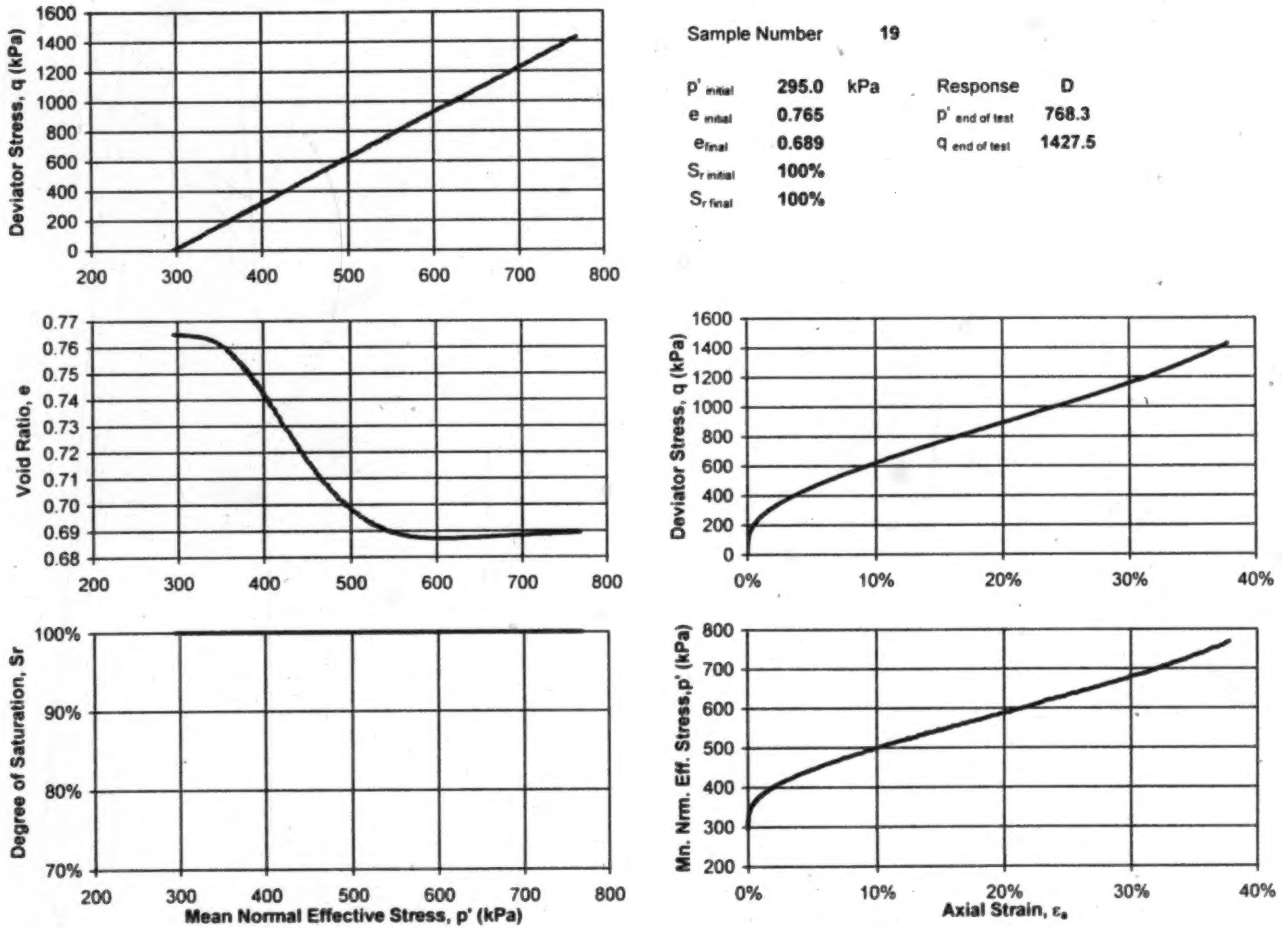

Sample Number	19			
$p'_{initial}$	295.0	kPa	Response	D
$e_{initial}$	0.765		$p'_{end\ of\ test}$	768.3
e_{final}	0.689		$q_{end\ of\ test}$	1427.5
$S_{r\ initial}$	100%			
$S_{r\ final}$	100%			

Figure A.13 - Sample #19, Saturated, CD.

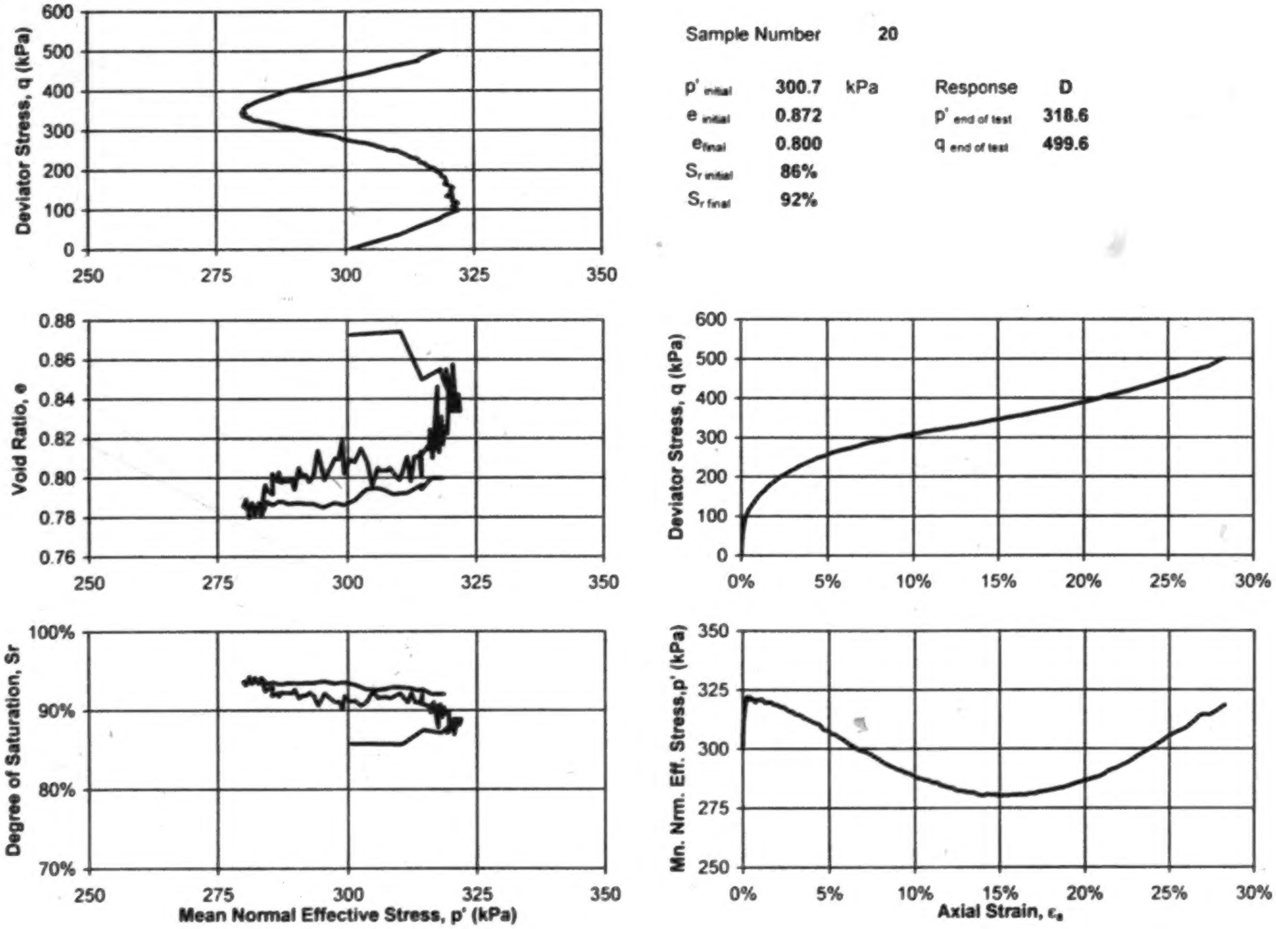

Sample Number 20

$p'_{initial}$	300.7	kPa	Response	D
$e_{initial}$	0.872		$p'_{end\ of\ test}$	318.6
e_{final}	0.800		$q_{end\ of\ test}$	499.6
$S_{r\ initial}$	86%			
$S_{r\ final}$	92%			

Figure A.14 - Sample #20, Gassy, CU.

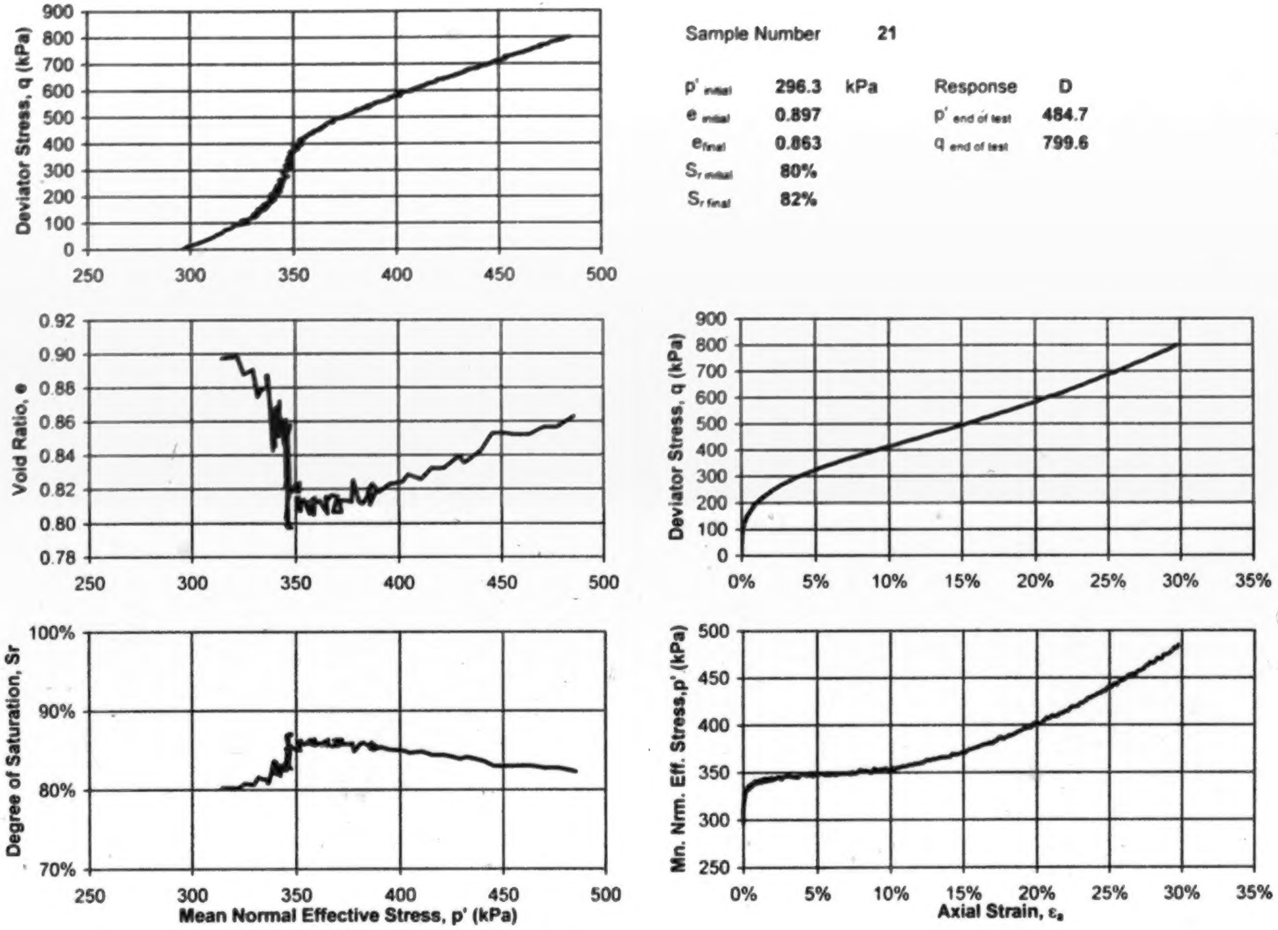

Sample Number 21

$p'_{initial}$	296.3	kPa	Response	D
$e_{initial}$	0.897		$p'_{end\ of\ test}$	484.7
e_{final}	0.863		$q_{end\ of\ test}$	799.6
$S_{r\ initial}$	80%			
$S_{r\ final}$	82%			

Figure A.15 - Sample #21, Gassy, CU.

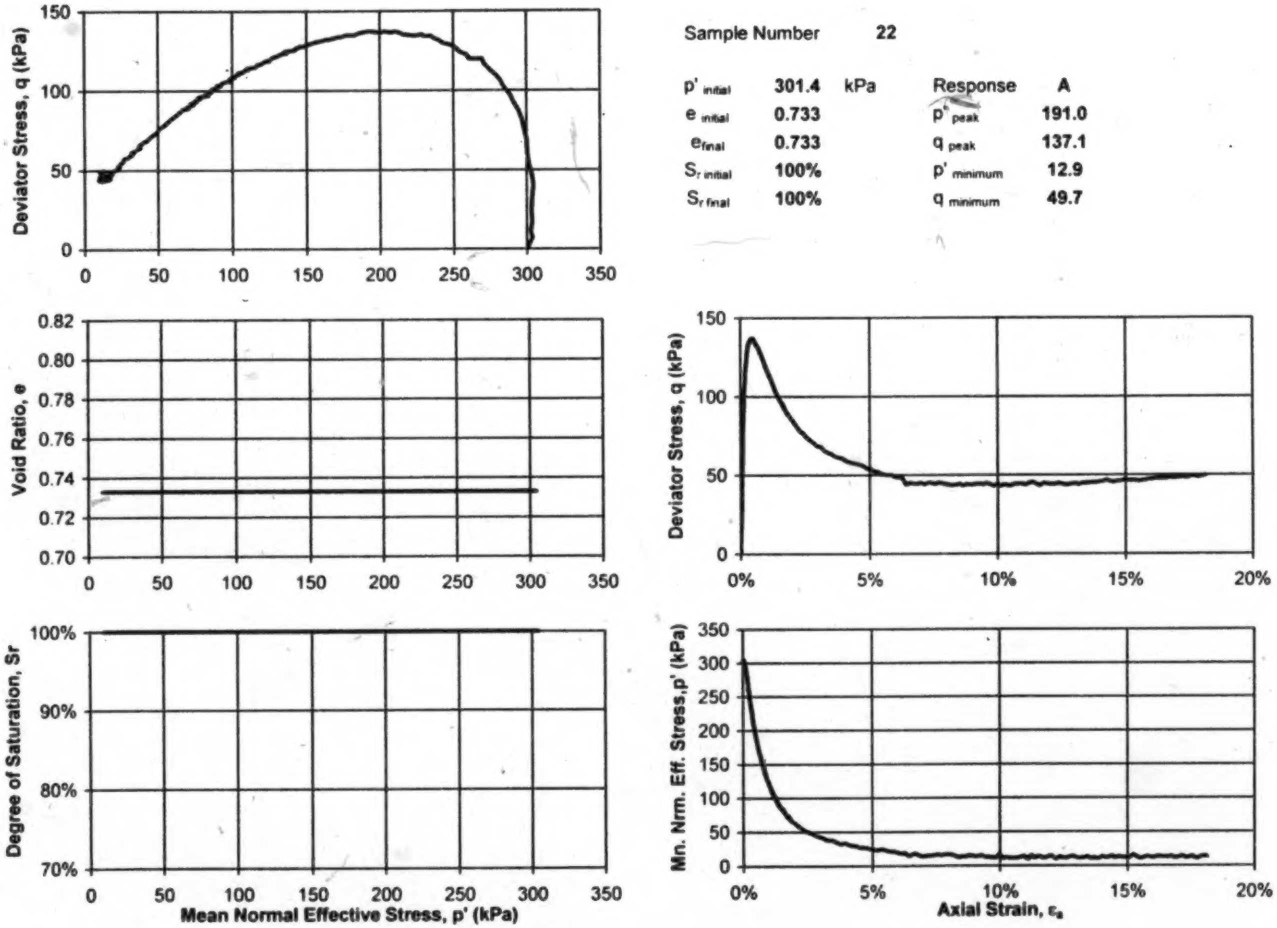

Sample Number	22			
$p'_{initial}$	301.4	kPa	Response	A
$e_{initial}$	0.733		p'_{peak}	191.0
e_{final}	0.733		q_{peak}	137.1
$S_{r\,initial}$	100%		$p'_{minimum}$	12.9
$S_{r\,final}$	100%		$q_{minimum}$	49.7

Figure A.16 - Sample #22, Saturated, CU.

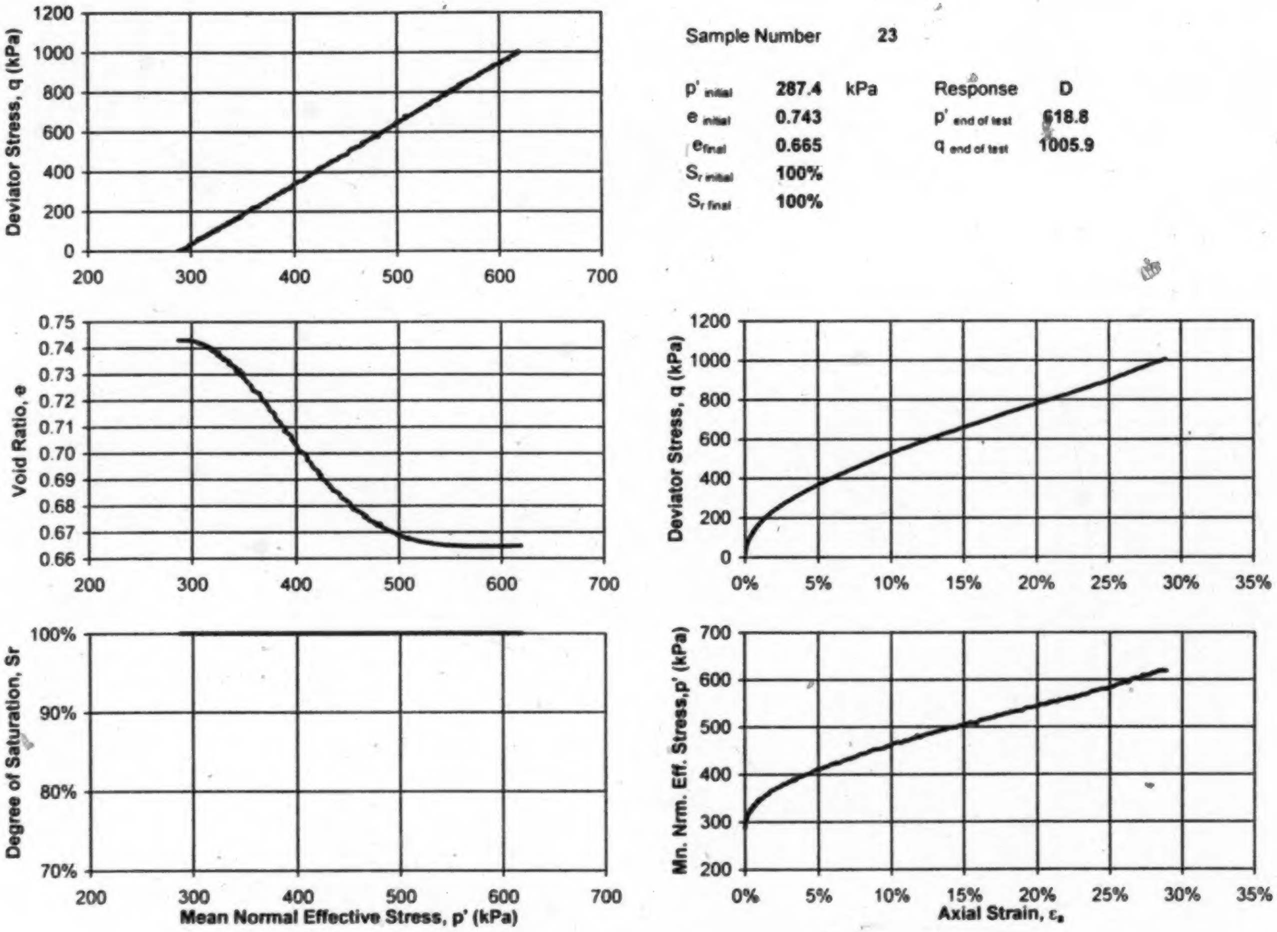

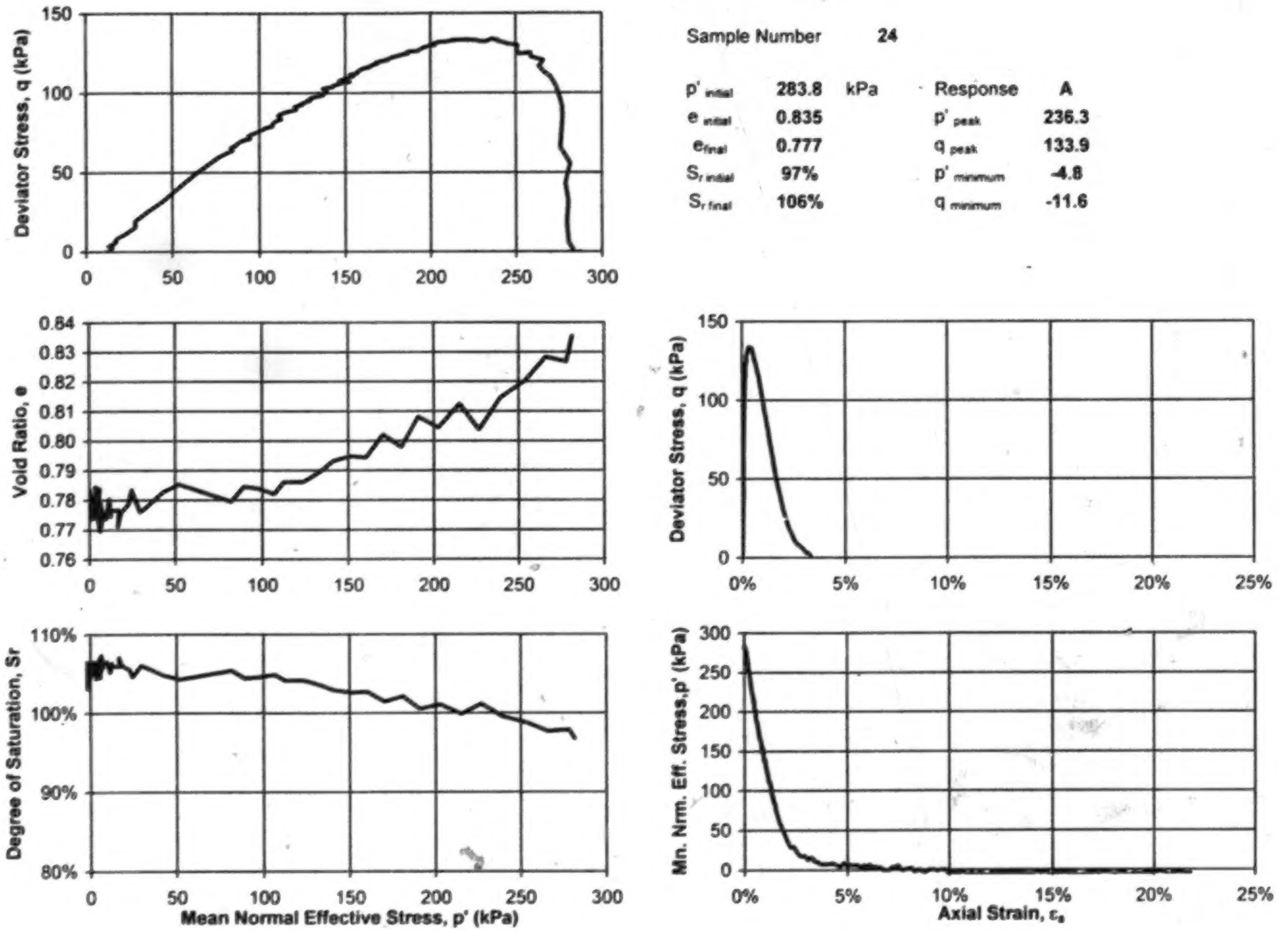

Sample Number 24

$p'_{initial}$	283.8	kPa	Response	A
$e_{initial}$	0.835		p'_{peak}	236.3
e_{final}	0.777		q_{peak}	133.9
$S_{r\,initial}$	97%		$p'_{minimum}$	-4.8
$S_{r\,final}$	106%		$q_{minimum}$	-11.6

Figure A.18 - Sample #24, Gassy, CU.

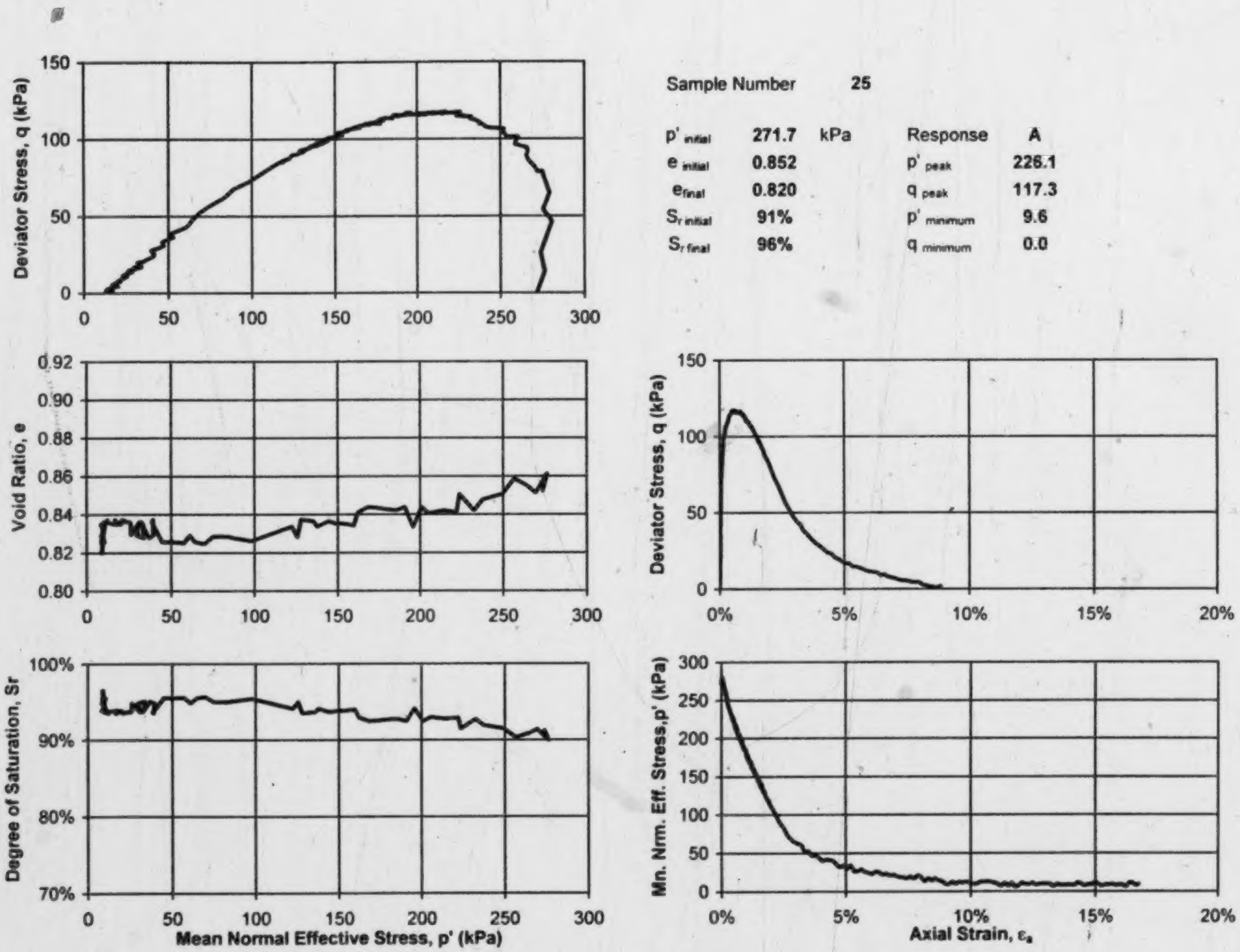

Sample Number 25

$p'_{initial}$	271.7	kPa	Response	A
$e_{initial}$	0.852		p'_{peak}	226.1
e_{final}	0.820		q_{peak}	117.3
$S_{r\,initial}$	91%		$p'_{minimum}$	9.6
$S_{r\,final}$	96%		$q_{minimum}$	0.0

Figure A.19 - Sample #25, Gassy, CU.

APPENDIX B

CYCLIC TRIAXIAL TEST RESULTS

This appendix contains the test results for each cyclic triaxial test. The test results are presented in the order in which they were performed. A summary table of all tests is also included.

Table B.1 - Summary of cyclic triaxial results.

Sample	Type	σ_{dp}' (kPa)	p' initial (kPa)	Period (Sec)	e* initial	e* final	Sr* initial	Sr* final	CRR $\sigma_d'/(2\sigma_3')$	N	M	Correction $CRR_M/CRR_{M=7.5}$	CRR_{tt} (M=7.5)	CRR_{SS} (M=7.5)
16	Saturated	55	300.5	12	0.736	0.736	100%		0.092	25	8.433	0.8744	0.105	0.073
18	Saturated	55	297.7	12	0.716	0.716	100%		0.092	1	4.944	1.6482	0.056	0.039
19	Saturated	55	296.4	12	0.713	0.713	100%		0.093	38	8.819	0.8313	0.112	0.078
20	Saturated	50	294.3	12	0.708	0.708	100%		0.085	34	8.665	0.8480	0.100	0.070
25	Saturated	60	296.3	14	0.706	0.706	100%		0.101	27	8.518	0.8646	0.117	0.082
28	Gassy	70	296.7	15	0.711	0.699	100%	103%	0.118	3	5.328	1.5017	0.079	0.055
32	Gassy	70	294.1	15	0.724	0.707	99%	103%	0.119	4	5.604	1.4117	0.084	0.059
33	Gassy	140	271.6	30	0.754	0.701	87%	94%	0.258	2	5.101	1.5851	0.163	0.114
36	Gassy	130	291.8	26	0.775	0.690	78%	86%	0.223	1	4.934	1.6521	0.135	0.094
37	Gassy	115	291.0	24	0.795	0.711	76%	84%	0.198	1	5.003	1.6239	0.122	0.085
38	Gassy	148	270.1	30	0.731	0.700	83%	86%	0.277	3	5.380	1.4841	0.186	0.131
39	Gassy	155	213.1	31	0.789	0.694	74%	83%	0.299	2	5.199	1.5478	0.193	0.135
40	Gassy	125	283.9	24	0.753	0.698	84%	90%	0.243	3	5.384	1.4826	0.164	0.115
41	Gassy	158	270.9	31	0.674	0.608	75%	82%	0.297	2	5.124	1.5762	0.188	0.132
42	Gassy	140	212.0	27	0.713	0.658	79%	85%	0.276	2	5.177	1.5563	0.177	0.124

* Void ratio and degree of saturation are calculated from TDR data.

Note: σ_{dp}' is the applied effective cyclic stress.
p' is the mean normal effective stress defined as $^1/_3\,(\sigma_1' + 2\sigma_3')$.
N is the number of cycles to failure.
M is the equivalent earthquake magnitude.
All specimens were tested undrained.

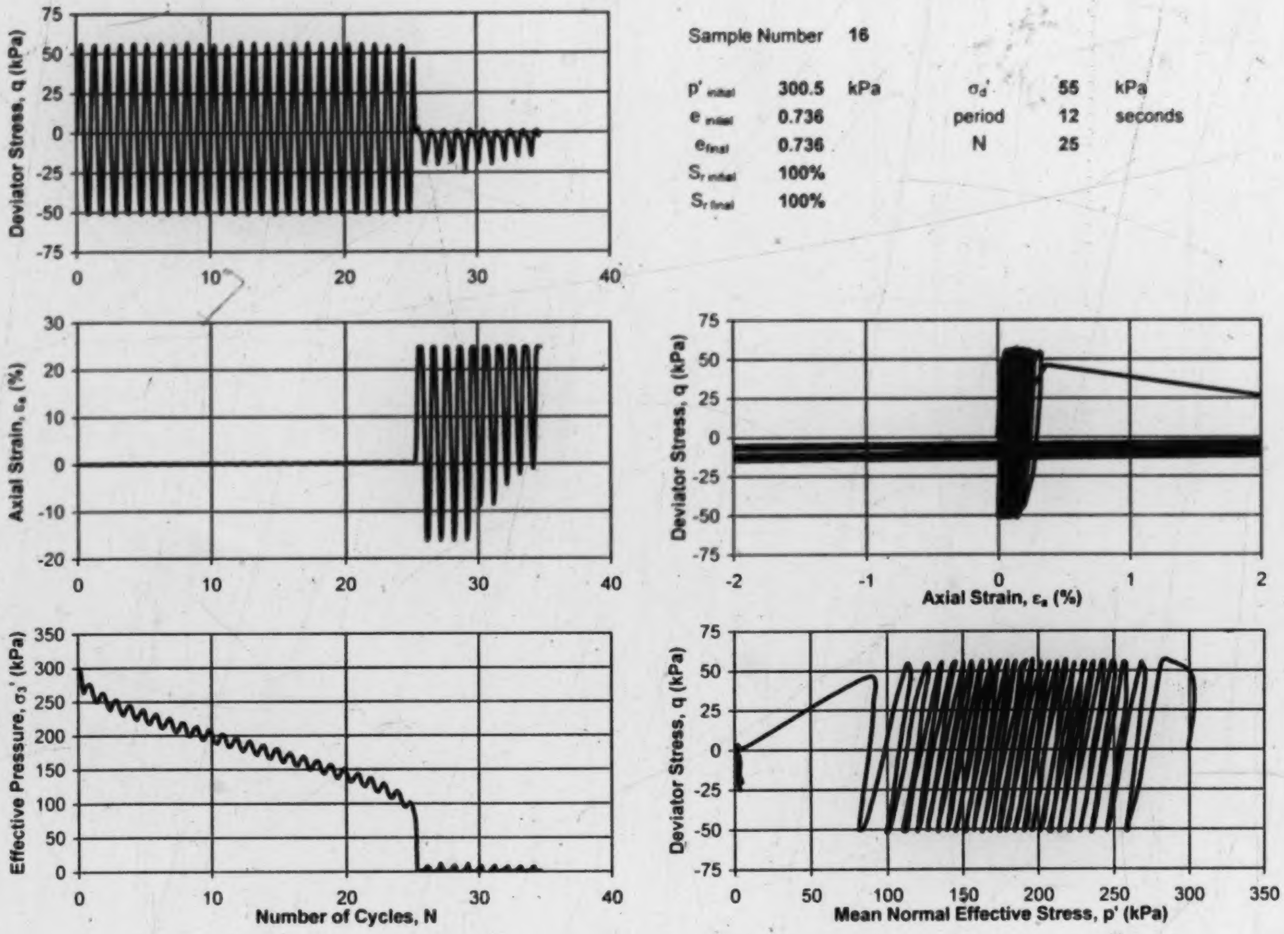

Sample Number 16

$p'_{initial}$	300.5	kPa	σ_d'	55	kPa
$e_{initial}$	0.736		period	12	seconds
e_{final}	0.736		N	25	
$S_{r\ initial}$	100%				
$S_{r\ final}$	100%				

Figure B.1 - Sample #16, Saturated.

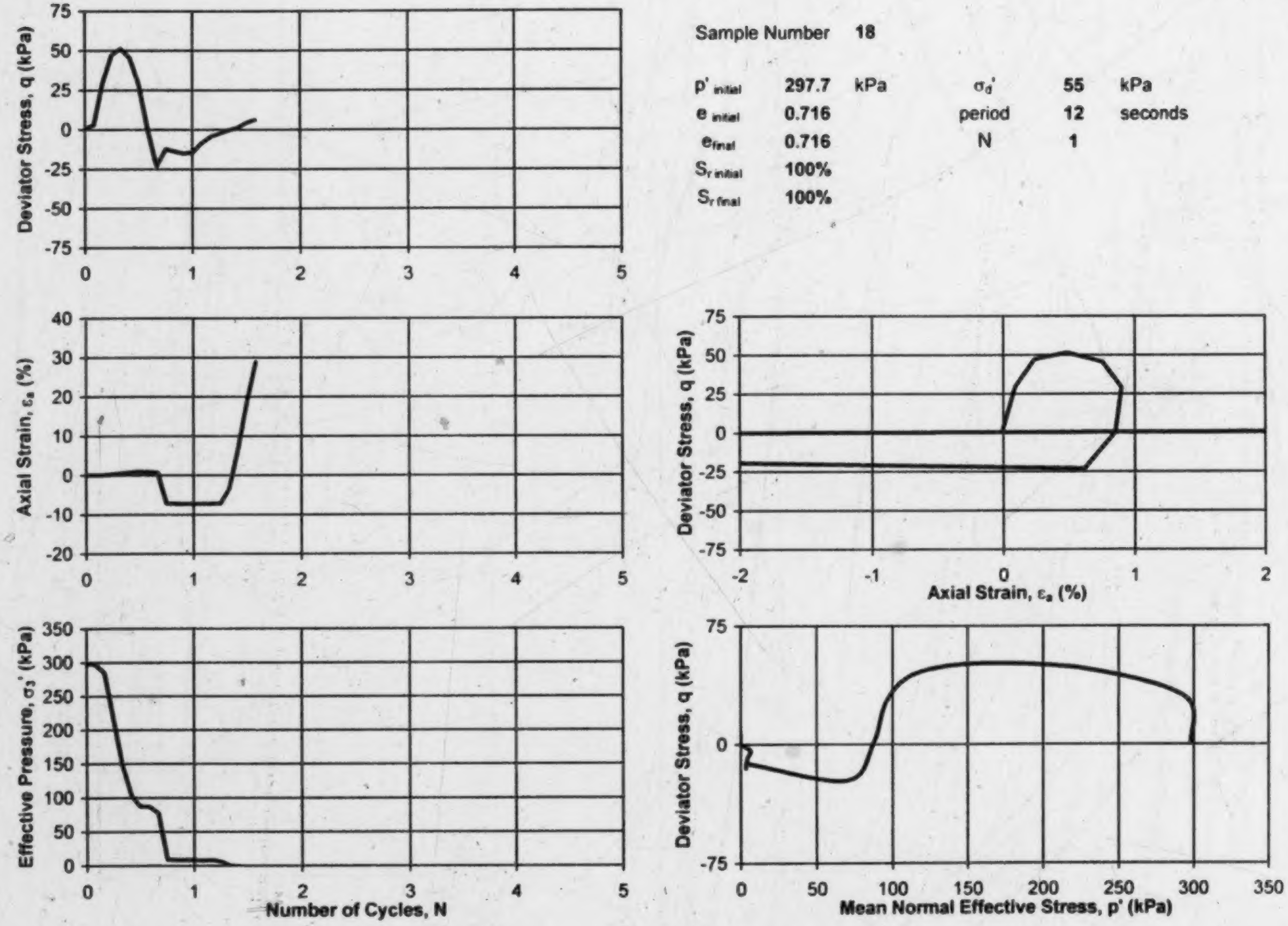

Sample Number 18

$p'_{initial}$	297.7	kPa	σ_d'	55	kPa
$e_{initial}$	0.716		period	12	seconds
e_{final}	0.716		N	1	
$S_{r\,initial}$	100%				
$S_{r\,final}$	100%				

Figure B.2 - Sample #18, Saturated.

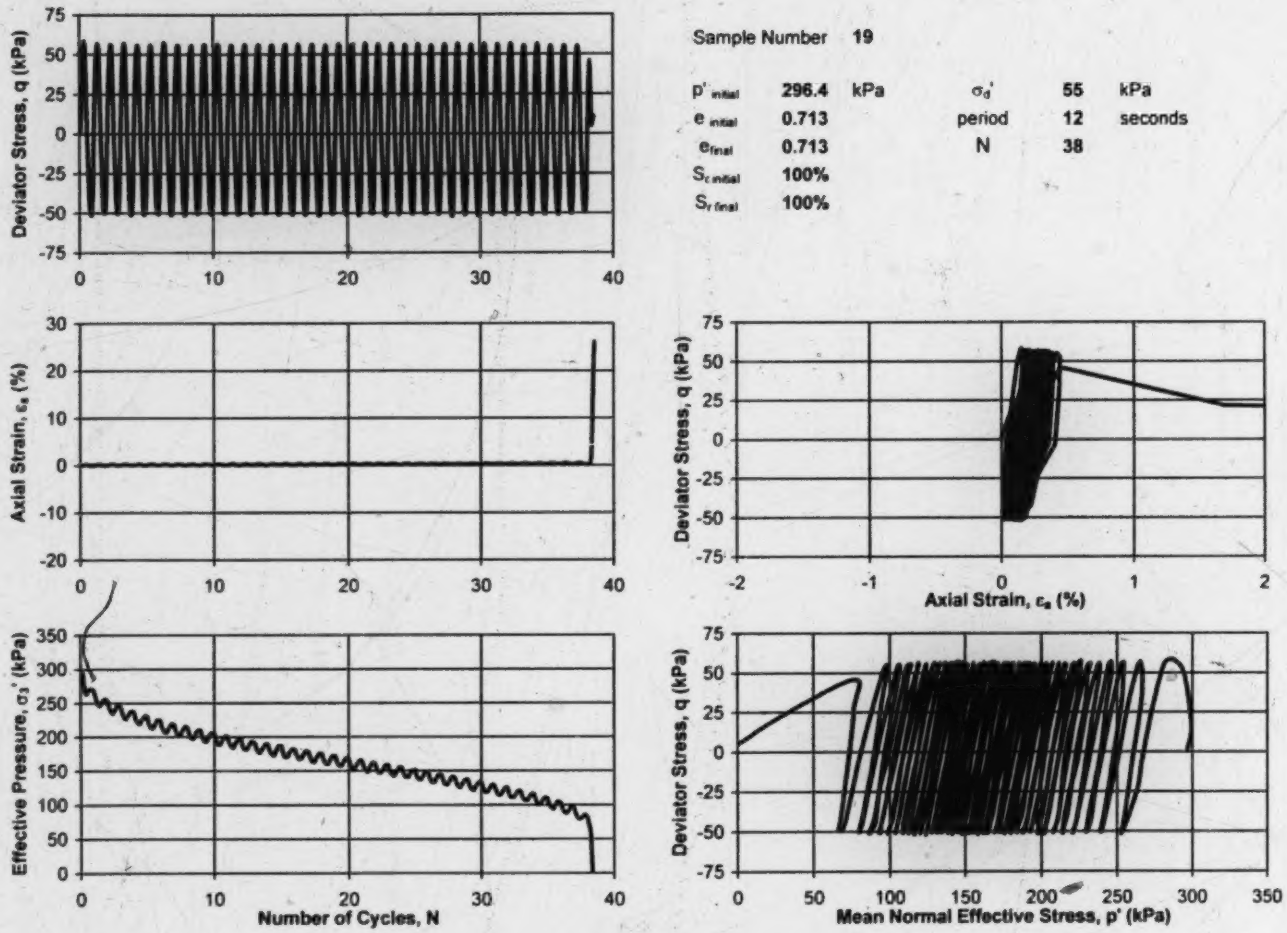

Sample Number 19

$p'_{initial}$	296.4	kPa	σ_d'	55	kPa
$e_{initial}$	0.713		period	12	seconds
e_{final}	0.713		N	38	
$S_{r\,initial}$	100%				
$S_{r\,final}$	100%				

Figure B.3 - Sample #19, Saturated.

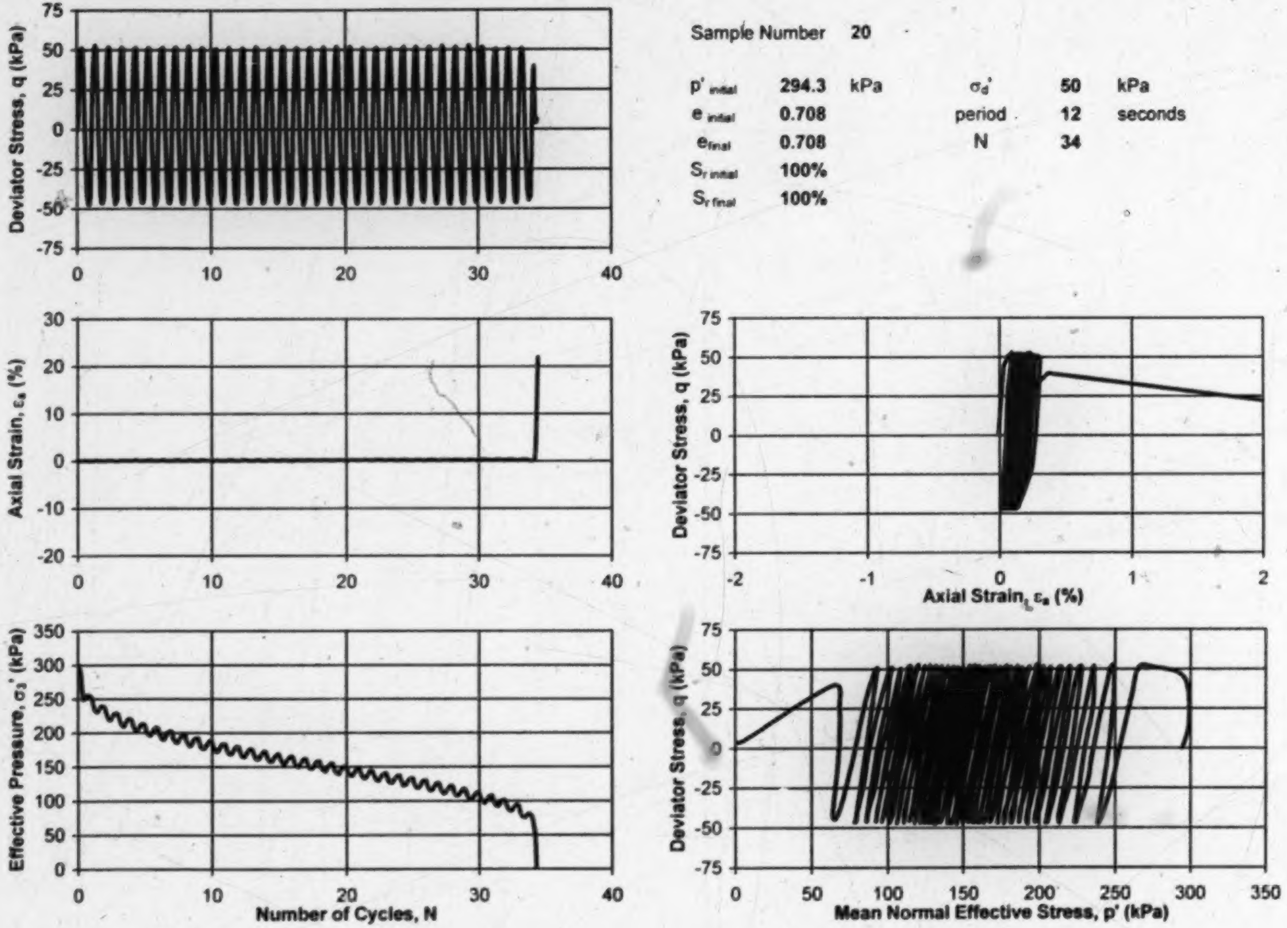

Sample Number 20

$p'_{initial}$	294.3	kPa	σ_d'	50	kPa
$e_{initial}$	0.708		period	12	seconds
e_{final}	0.708		N	34	
$S_{r\,initial}$	100%				
$S_{r\,final}$	100%				

Figure B.4 - Sample #20, Saturated.

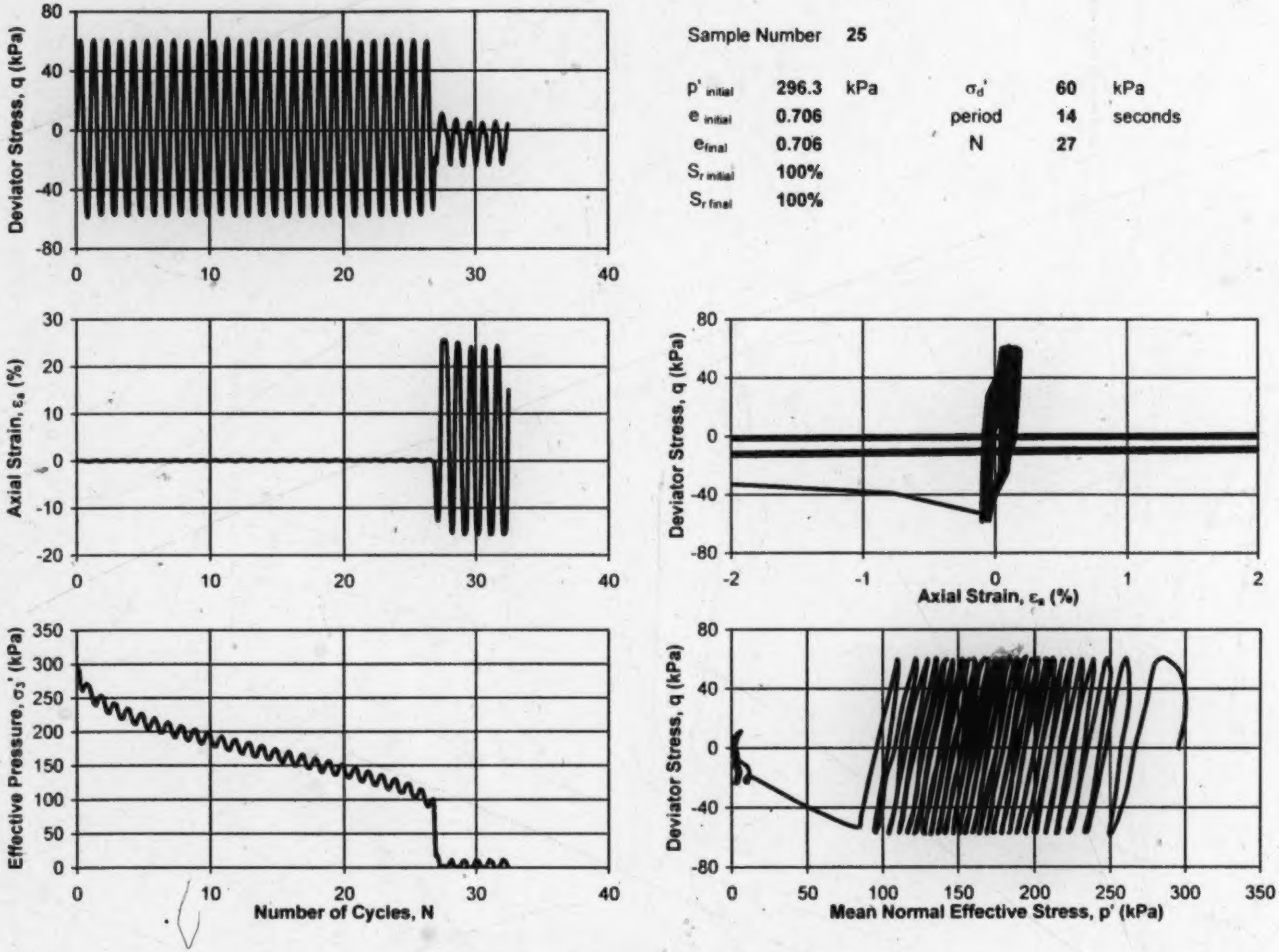

Sample Number 25

$p'_{initial}$	296.3	kPa	σ_d'	60	kPa
$e_{initial}$	0.706		period	14	seconds
e_{final}	0.706		N	27	
$S_{r\,initial}$	100%				
$S_{r\,final}$	100%				

Figure B.5 - Sample #25, Saturated.

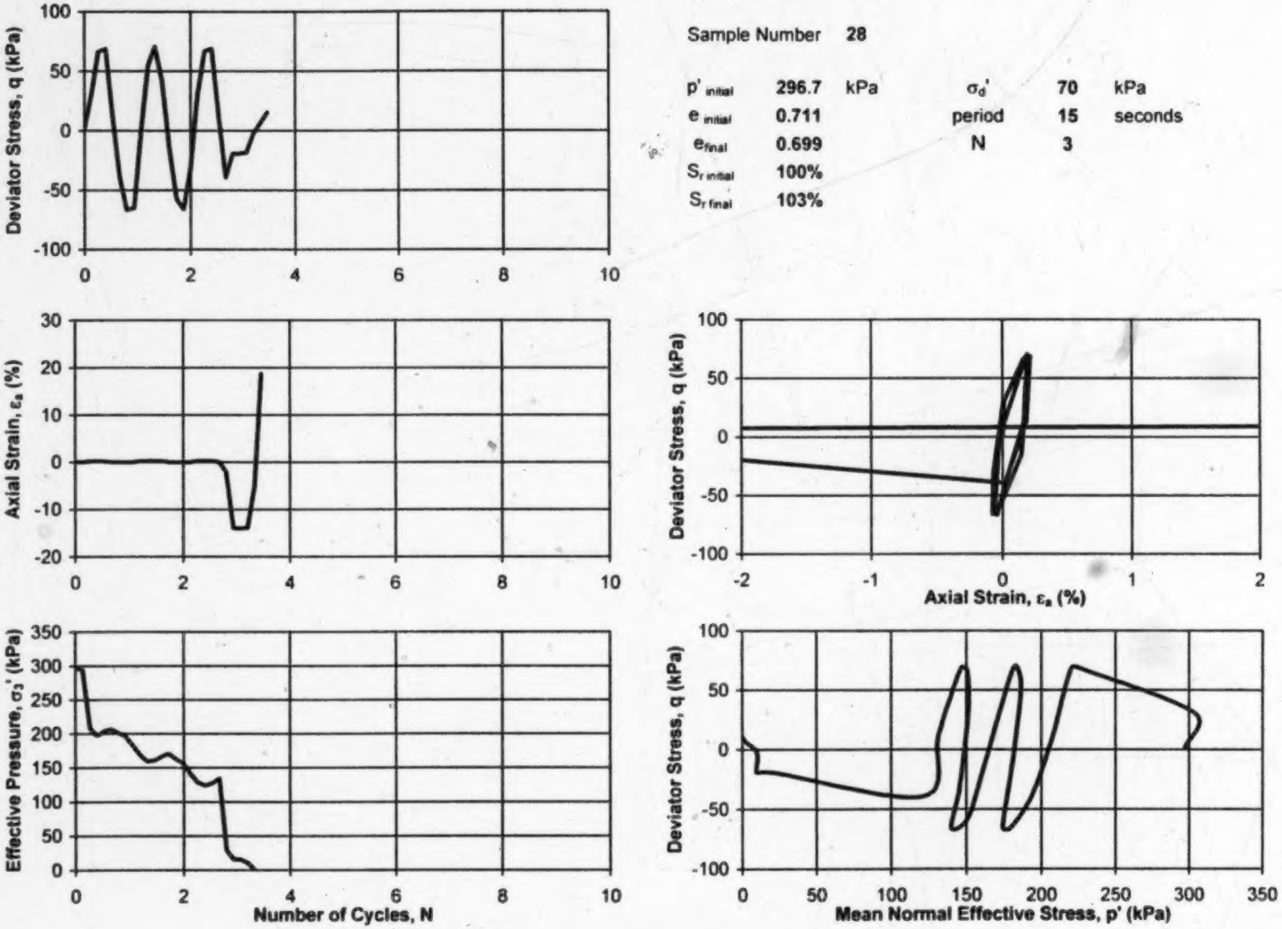

Sample Number 28

$p'_{initial}$	296.7	kPa	σ_d'	70	kPa
$e_{initial}$	0.711		period	15	seconds
e_{final}	0.699		N	3	
$S_{r\,initial}$	100%				
$S_{r\,final}$	103%				

Figure B.6 - Sample #28, Gassy.

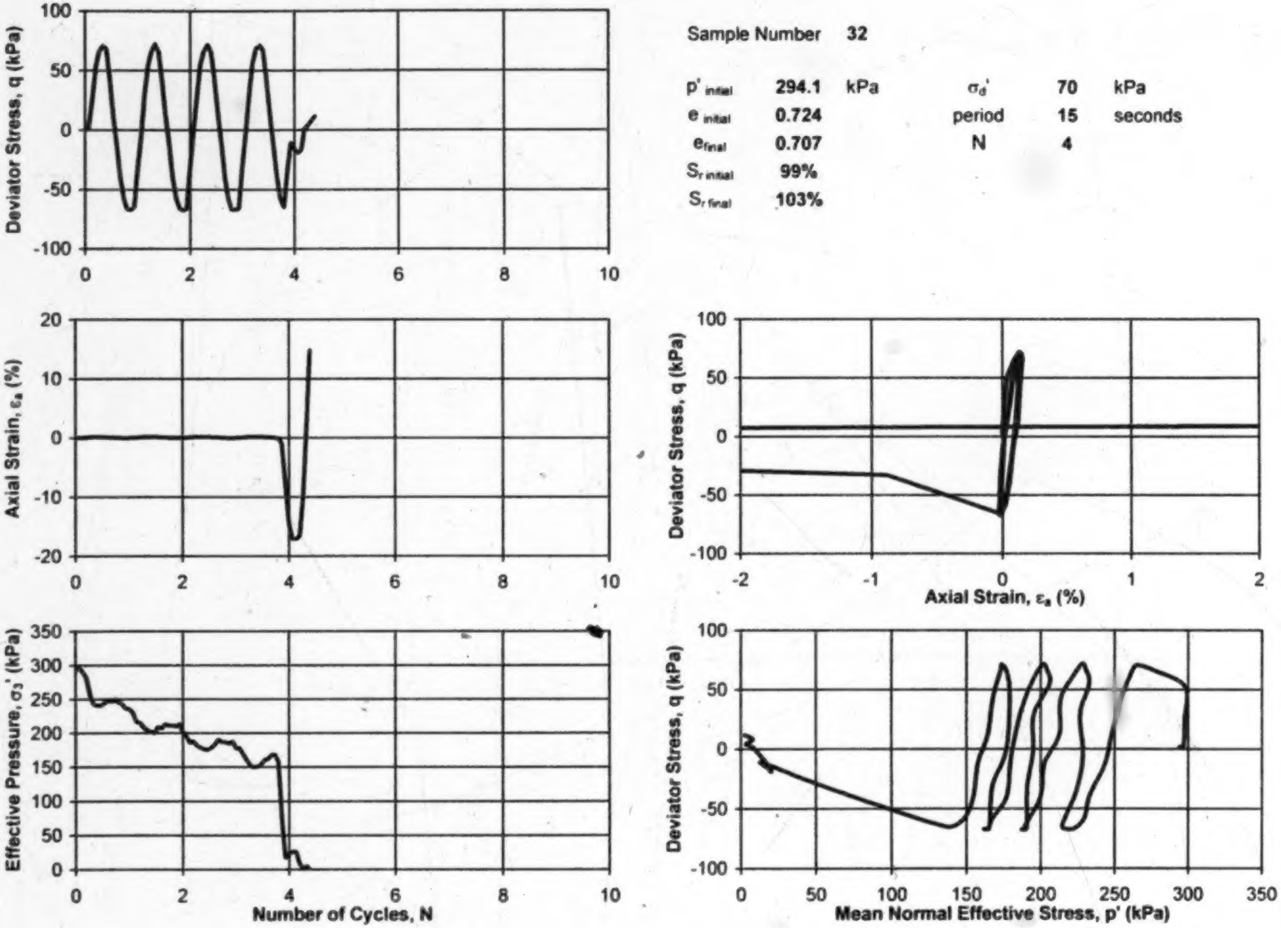

Sample Number 32

$p'_{initial}$	294.1	kPa	σ_d'	70	kPa
$e_{initial}$	0.724		period	15	seconds
e_{final}	0.707		N	4	
$S_{r\,initial}$	99%				
$S_{r\,final}$	103%				

Figure B.7 - Sample #32, Gassy.

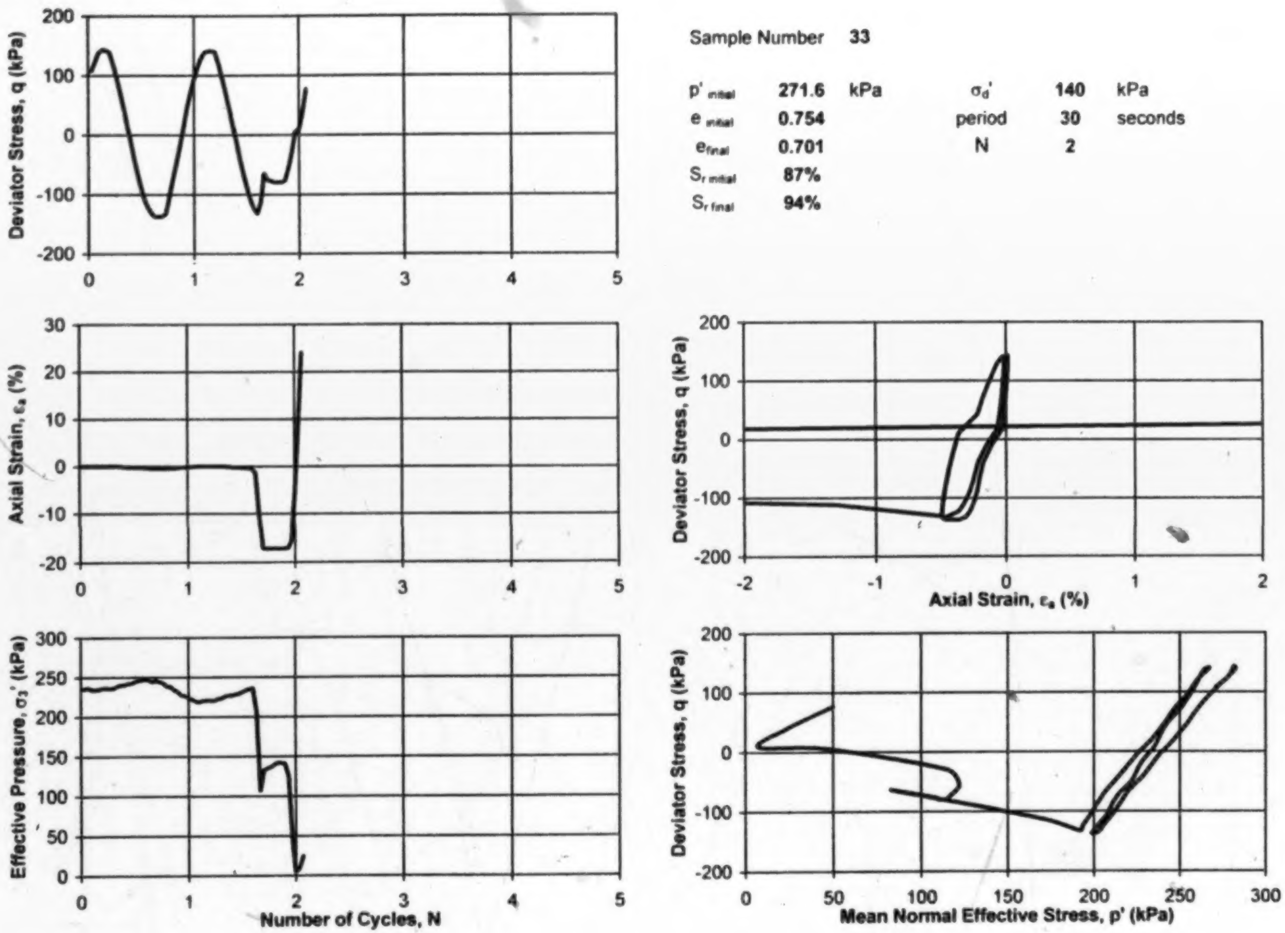

Sample Number 33

$p'_{initial}$	271.6	kPa	σ_d'	140	kPa
$e_{initial}$	0.754		period	30	seconds
e_{final}	0.701		N	2	
$S_{r\ initial}$	87%				
$S_{r\ final}$	94%				

Figure B.8 - Sample #33, Gassy.

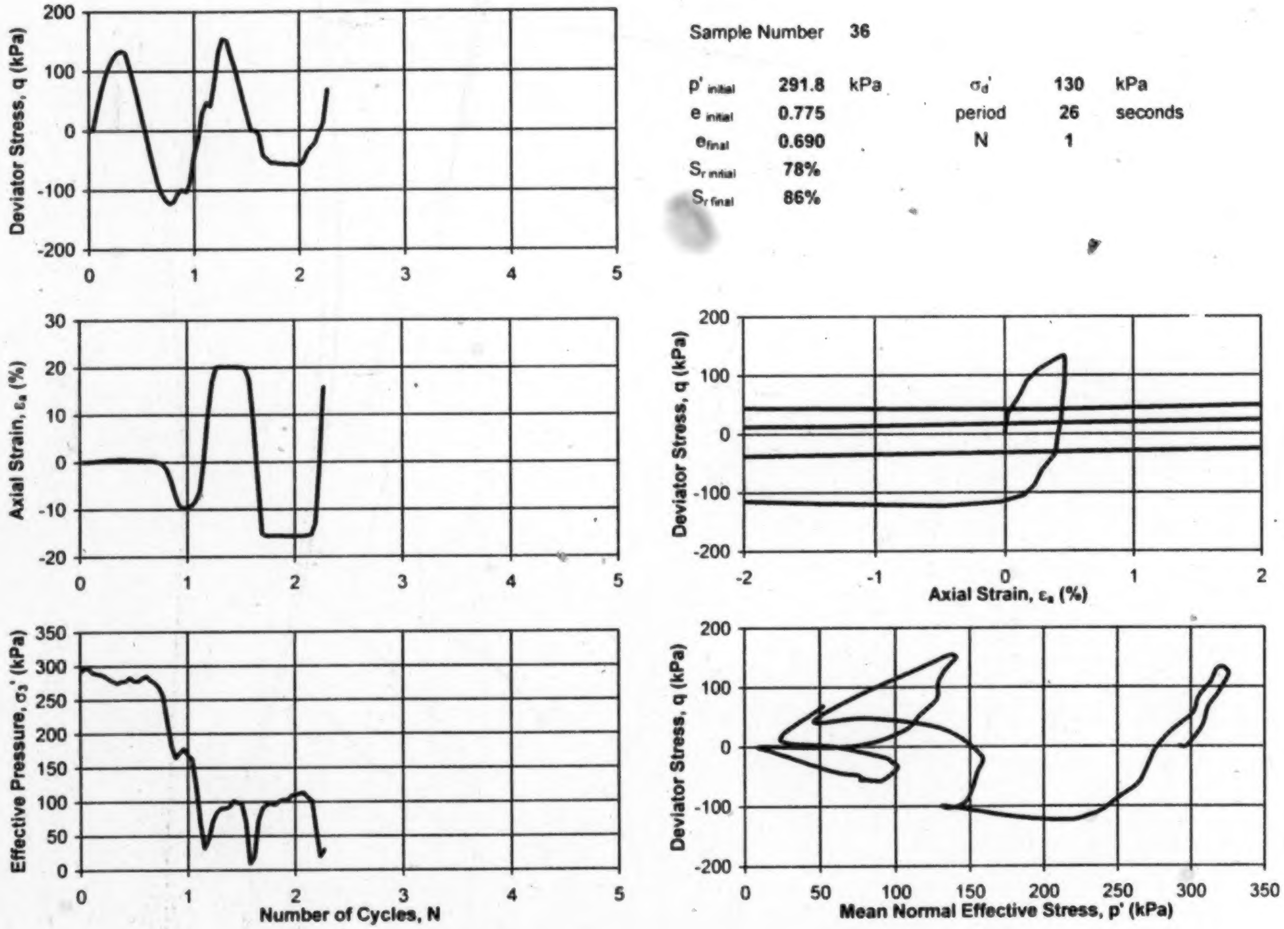

Sample Number 36

$p'_{initial}$	291.8	kPa	σ_d'	130	kPa
$e_{initial}$	0.775		period	26	seconds
e_{final}	0.690		N	1	
$S_{r\,initial}$	78%				
$S_{r\,final}$	86%				

Figure B.9 - Sample #36, Gassy.

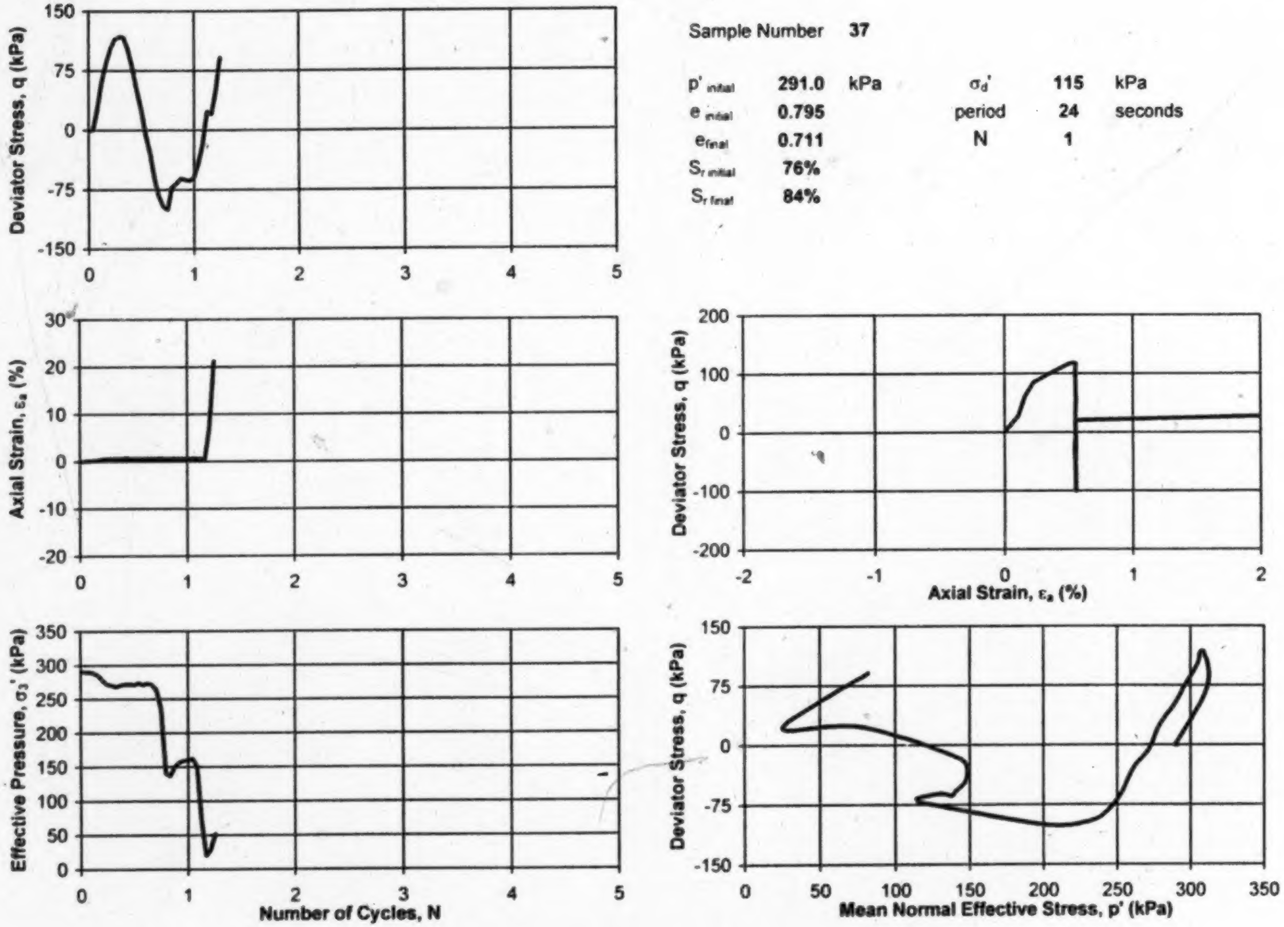

Sample Number 37

$p'_{initial}$	291.0	kPa	σ_d'	115	kPa
$e_{initial}$	0.795		period	24	seconds
e_{final}	0.711		N	1	
$S_{r\ initial}$	76%				
$S_{r\ final}$	84%				

Figure B.10 - Sample #37, Gassy.

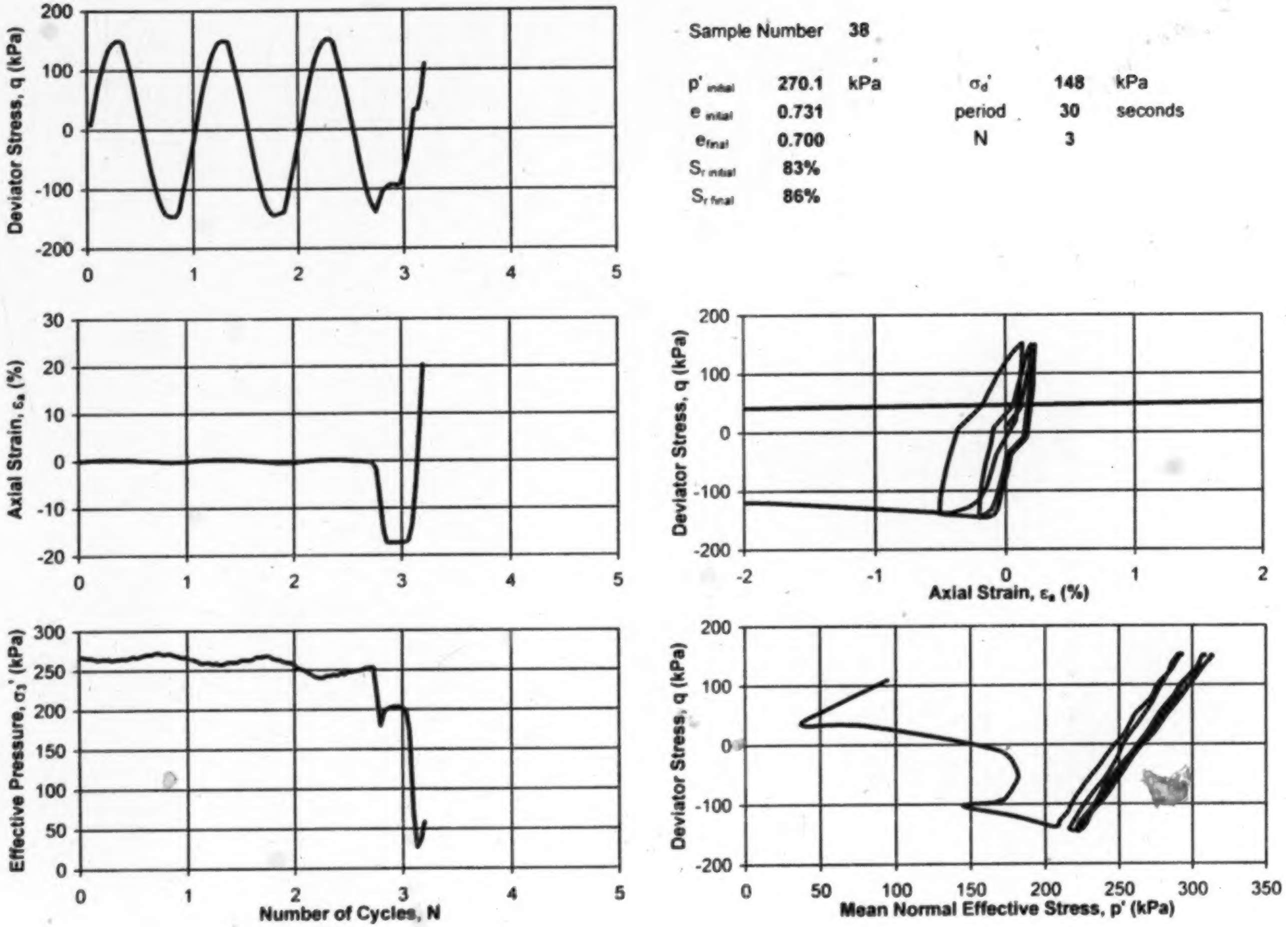

Sample Number 38

$p'_{initial}$	270.1	kPa	σ_d'	148	kPa
$e_{initial}$	0.731		period	30	seconds
e_{final}	0.700		N	3	
$S_{r\,initial}$	83%				
$S_{r\,final}$	86%				

Figure B.11 - Sample #38, Gassy.

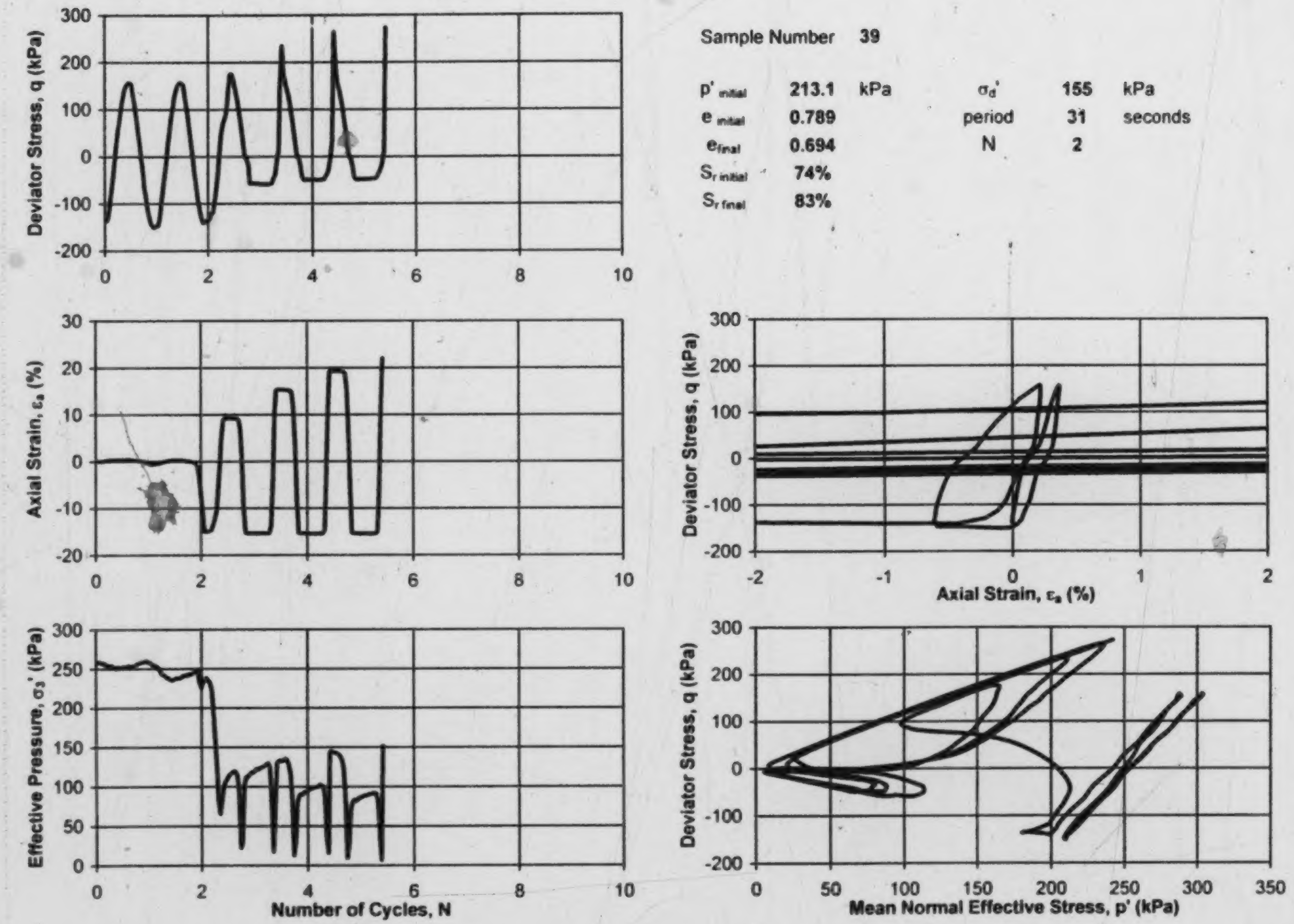

Sample Number 39

$p'_{initial}$	213.1	kPa	σ_d'	155	kPa
$e_{initial}$	0.789		period	31	seconds
e_{final}	0.694		N	2	
$S_{r\,initial}$	74%				
$S_{r\,final}$	83%				

Figure B.12 - Sample #39, Gassy.

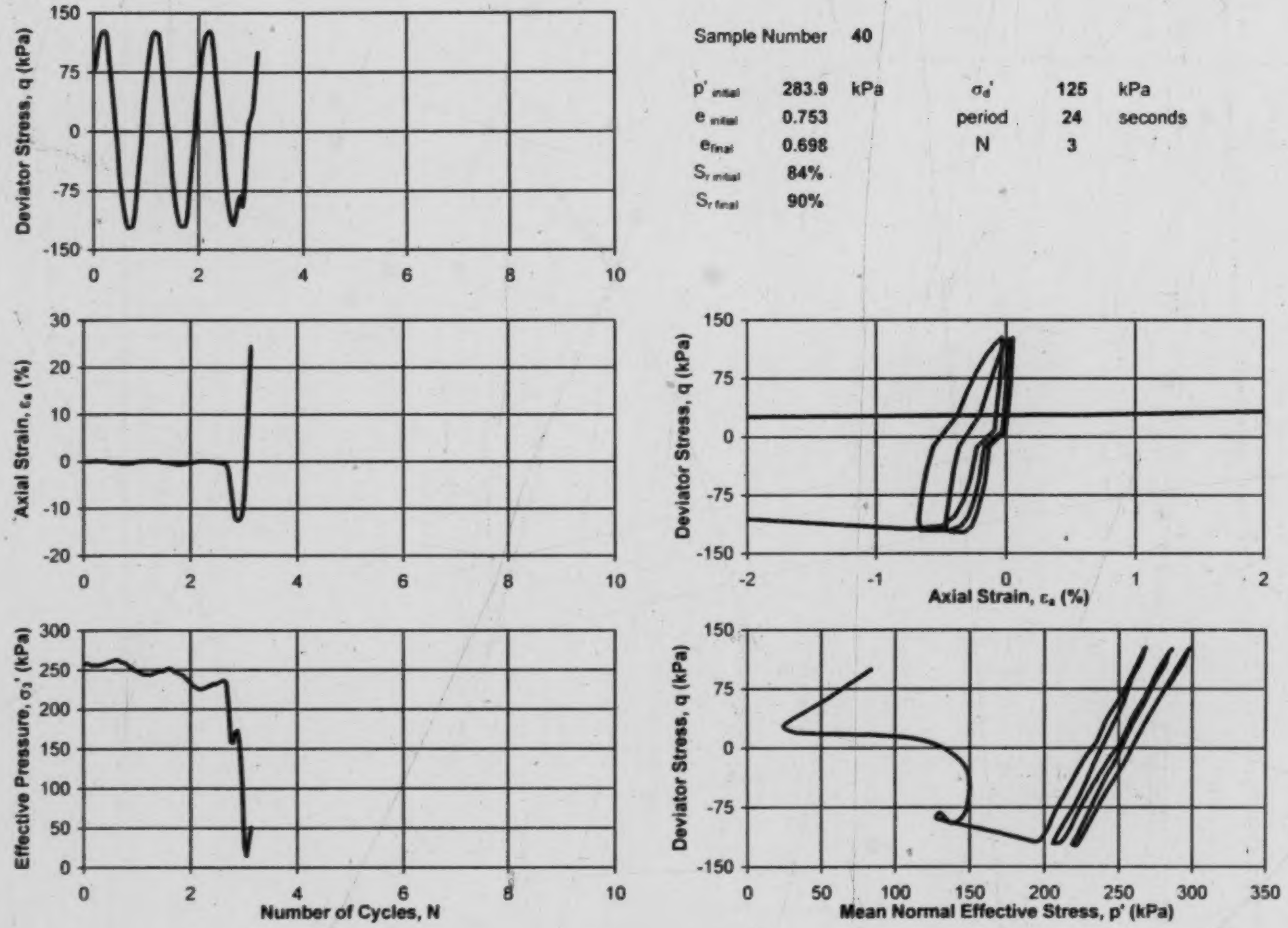

Sample Number 40

$p'_{initial}$	283.9	kPa	σ_d'	125	kPa
$e_{initial}$	0.753		period	24	seconds
e_{final}	0.698		N	3	
$S_{r\,initial}$	84%				
$S_{r\,final}$	90%				

Figure B.13 - Sample #40, Gassy.

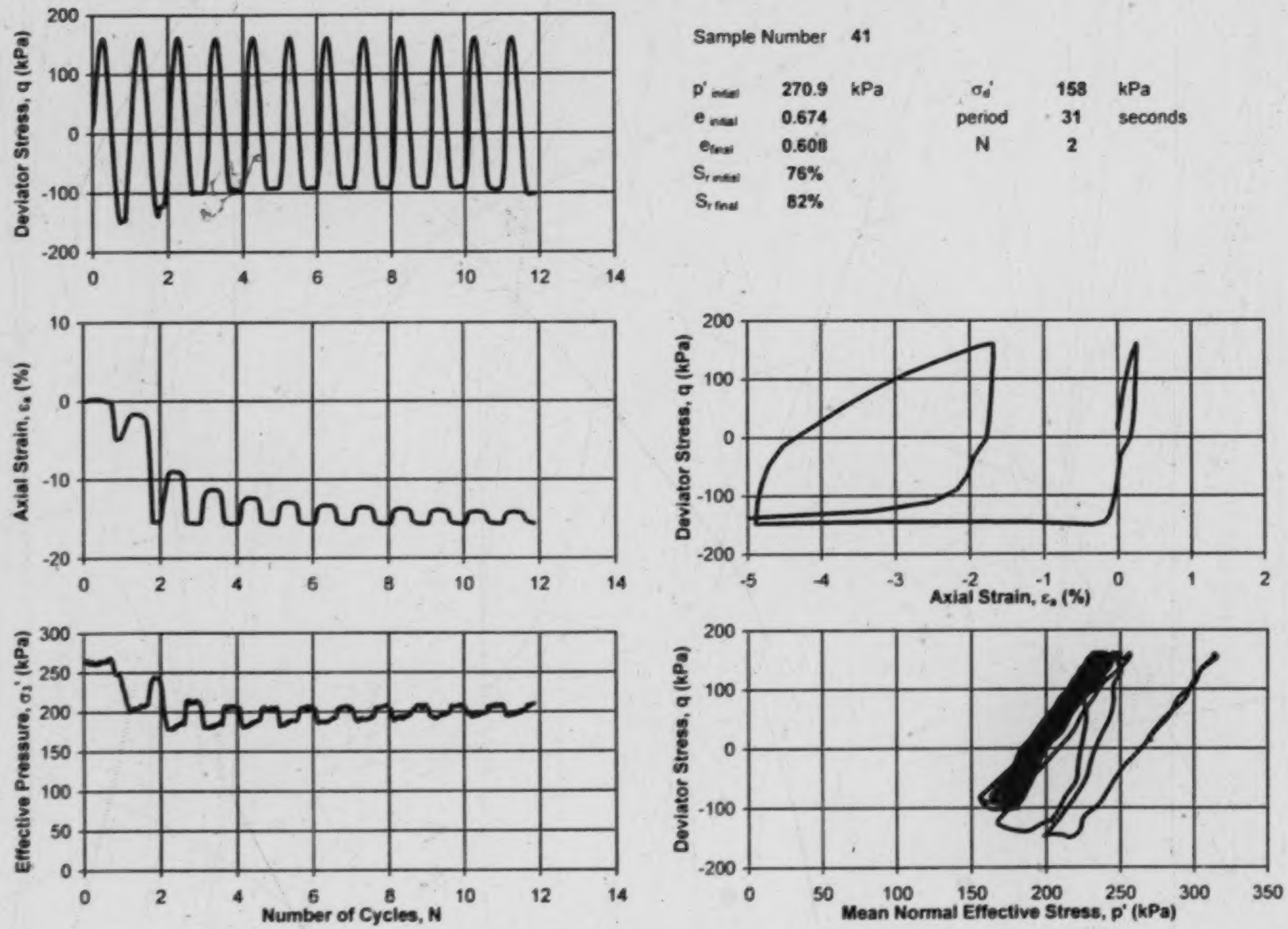

Sample Number 41

$p'_{initial}$	270.9	kPa	σ_d'	158	kPa
$e_{initial}$	0.674		period	31	seconds
e_{final}	0.608		N	2	
$S_{r\ initial}$	76%				
$S_{r\ final}$	82%				

Figure B.14 - Sample #41, Gassy.

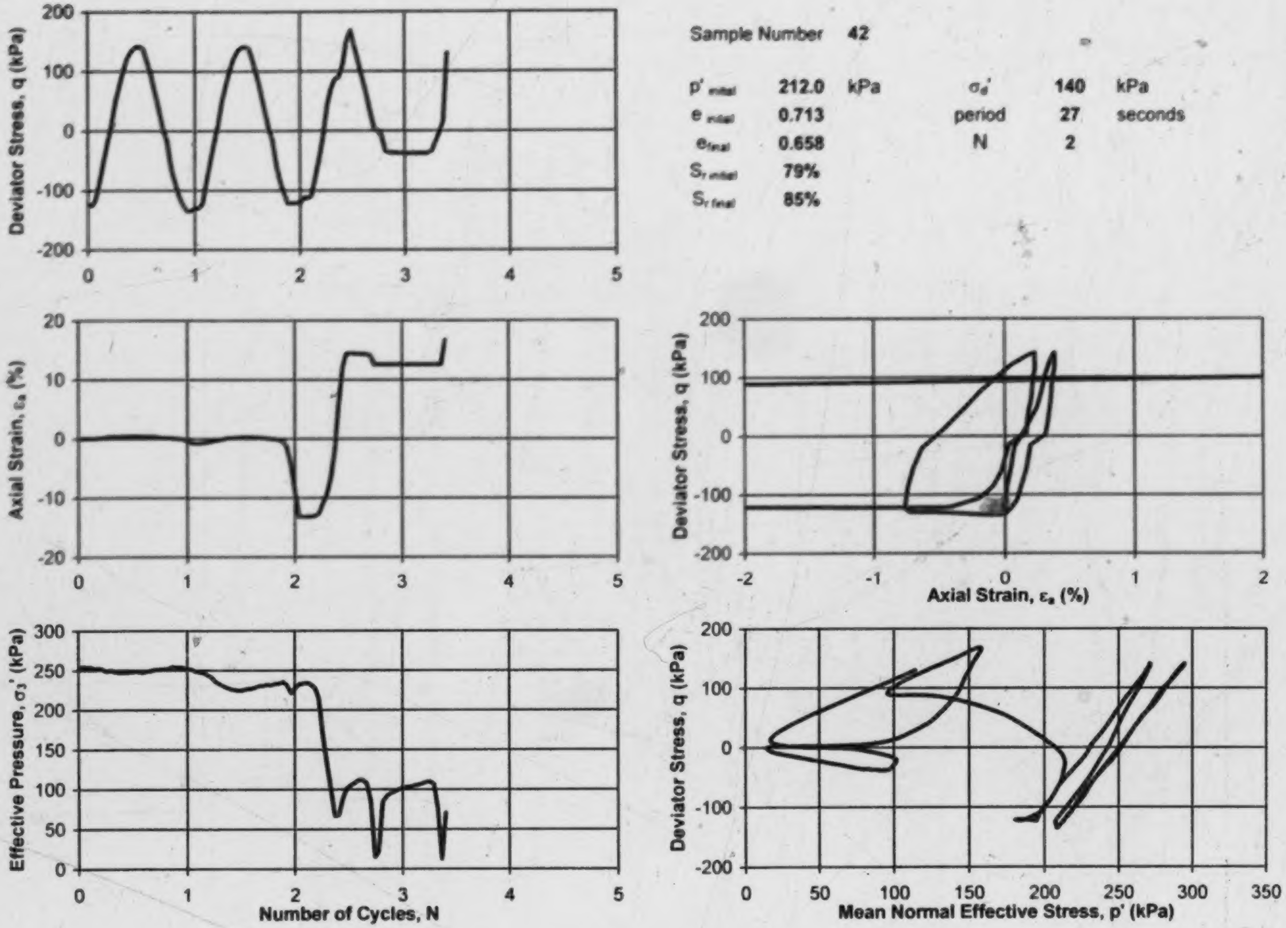

Sample Number 42

$p'_{initial}$	212.0	kPa	σ_d'	140	kPa
$e_{initial}$	0.713		period	27	seconds
e_{final}	0.658		N	2	
$S_{r\,initial}$	79%				
$S_{r\,final}$	85%				

Figure B.15 - Sample #42, Gassy.

APPENDIX C

CYCLIC TRIAXIAL TESTS THAT DID NOT FAIL

This appendix contains the test results for each cyclic triaxial test that did not fail under the first application of deviatoric stress. The tests were stopped after it appeared that failure would not occur; the specimens were then re-tested with a larger deviatoric stress. The test results are presented in the order in which they were performed. A summary table of all tests is also included.

Table C.1 - Summary of cyclic triaxial results for specimens that did not fail.

Sample #		Type	σ_{dp}' (kPa)	p' initial (kPa)	Period (Sec)	e initial	S_r initial	CRR $\sigma_d'/(2\sigma_3')$	N	Failure?
30	a	Gassy	70	298.6	14	0.81	74%	0.118	49	none
	b	Gassy	100	288.7	20	0.77	76%	0.172	14	none
	c	Gassy	140	279.6	28	0.77	76%	0.242	1	failed
38	a	Gassy	88	284.2	18	0.76	82%	0.155	13	none
	b	Gassy	98	251.1	20	0.74	83%	0.174	15	none
	c	Gassy	108	247.5	22	0.73	83%	0.196	13	none
	d	Gassy	118	292.9	24	0.73	83%	0.214	10	none
	e	Gassy	128	243.6	26	0.73	83%	0.234	6	none
	f	Gassy	138	305.2	28	0.73	83%	0.253	9	none
	g	Gassy	148	270.1	30	0.73	83%	0.277	3	failed
39	a	Gassy	92	295.6	20	0.89	67%	0.155	8	none
	b	Gassy	105	309.0	22	0.81	72%	0.185	4	none
	c	Gassy	115	287.7	24	0.81	73%	0.203	4	none
	d	Gassy	125	294.3	25	0.80	73%	0.222	5	none
	e	Gassy	135	265.3	27	0.80	73%	0.242	9	none
	f	Gassy	145	241.0	30	0.80	73%	0.268	14	none
	g	Gassy	155	213.1	31	0.79	74%	0.299	2	failed
40	a	Gassy	100	290.3	20	0.79	79%	0.172	9	none
	b	Gassy	110	224.3	22	0.75	84%	0.214	2	none
	c	Gassy	125	283.9	24	0.75	84%	0.243	3	failed
41	a	Gassy	125	295.2	24	0.74	71%	0.212	6	none
	b	Gassy	138	283.9	27	0.68	76%	0.263	3	none
	c	Gassy	148	242.8	29	0.68	76%	0.276	3	none
	d	Gassy	158	270.9	31	0.67	76%	0.297	2	failed
42	a	Gassy	115	293.7	23	0.76	75%	0.196	8	none
	b	Gassy	128	288.0	25	0.71	79%	0.256	3	none
	c	Gassy	140	212.0	27	0.71	79%	0.276	2	failed

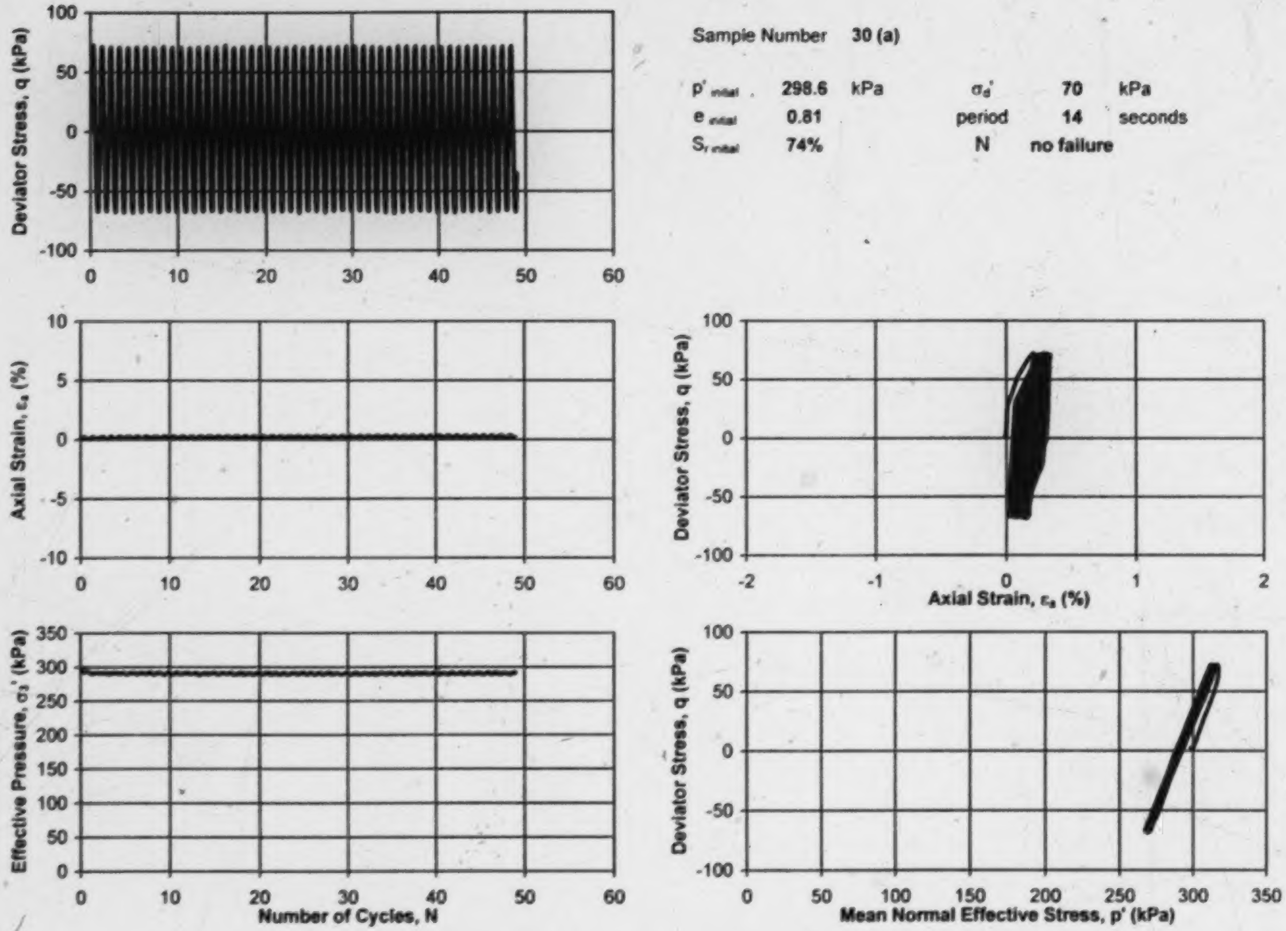

Sample Number	30 (a)				
$p'_{initial}$	298.6	kPa	σ_d'	70	kPa
$e_{initial}$	0.81		period	14	seconds
$S_{r\,initial}$	74%		N	no failure	

Figure C.1 - Sample #30 (a), Gassy.

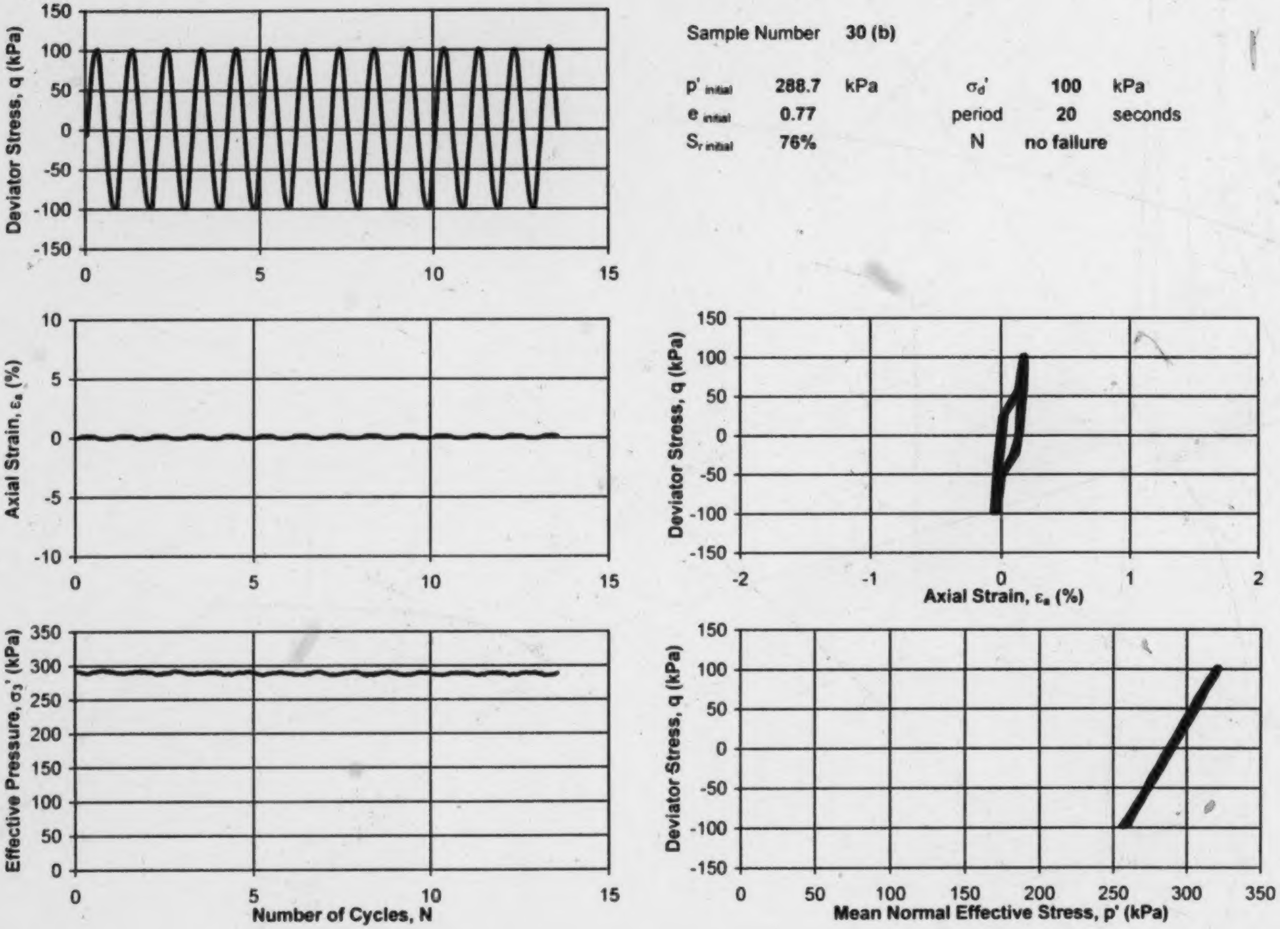

Sample Number 30 (b)

$p'_{initial}$	288.7	kPa	σ_d'	100	kPa
$e_{initial}$	0.77		period	20	seconds
$S_{r\ initial}$	76%		N	no failure	

Figure C.2 - Sample #30 (b), Gassy.

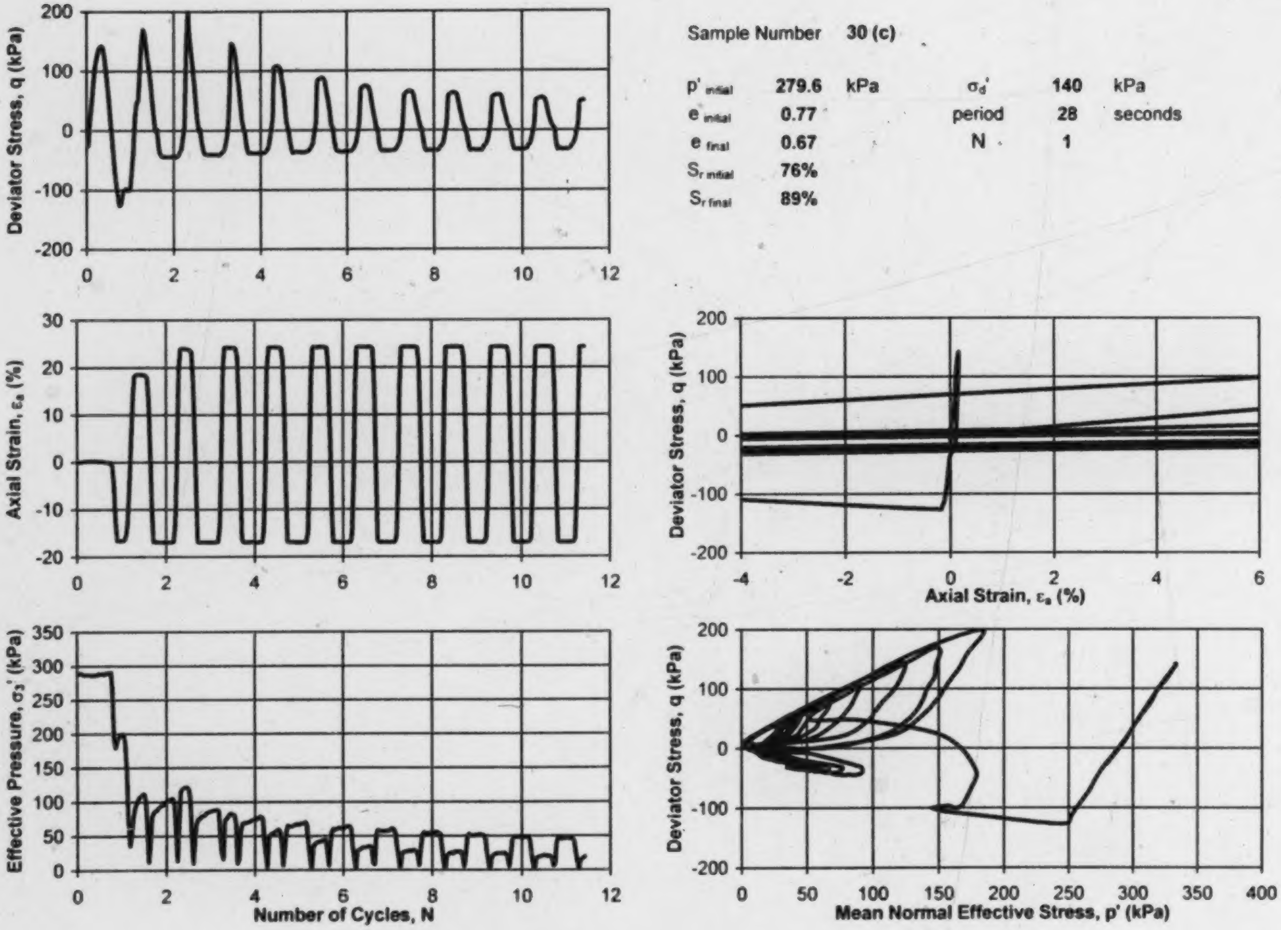

Sample Number	30 (c)				
$p'_{initial}$	279.6	kPa	σ_d'	140	kPa
$e_{initial}$	0.77		period	28	seconds
e_{final}	0.67		N	1	
$S_{r\,initial}$	76%				
$S_{r\,final}$	89%				

Figure C.3 - Sample #30 (c), Gassy.

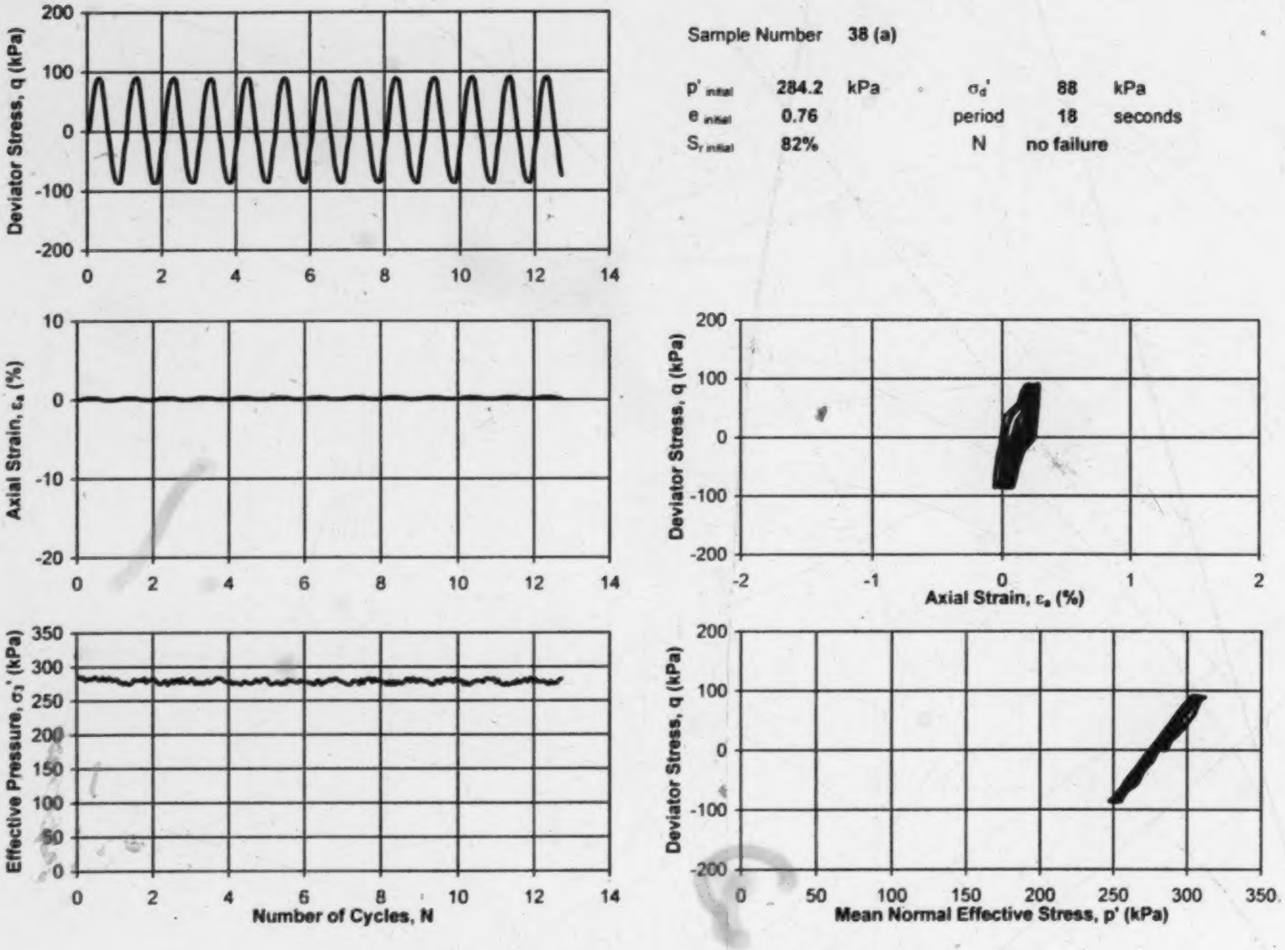

Sample Number	38 (a)				
$p'_{initial}$	284.2	kPa	σ_d'	88	kPa
$e_{initial}$	0.76		period	18	seconds
$S_{r\,initial}$	82%		N	no failure	

Figure C.4 - Sample #38 (a), Gassy.

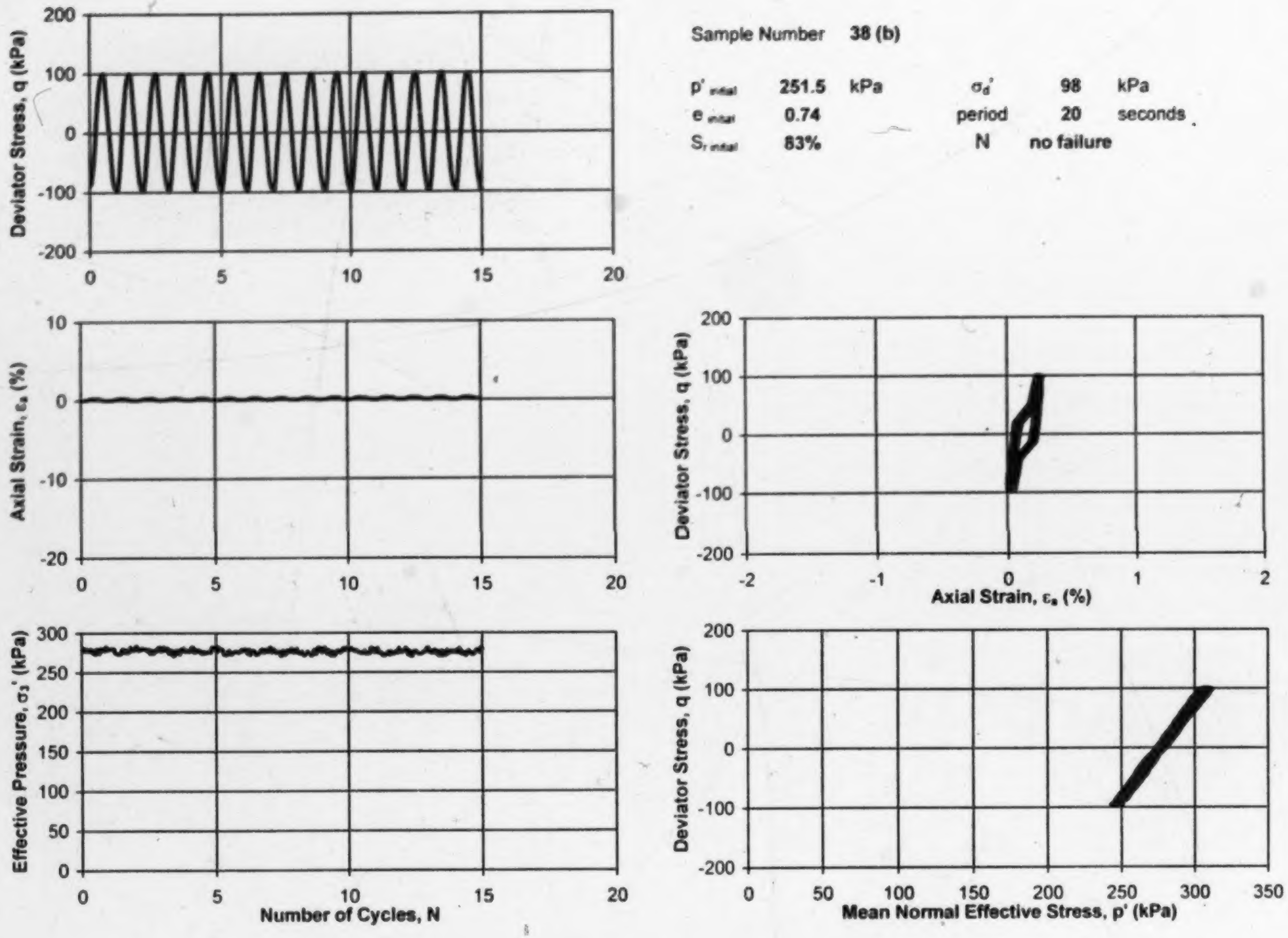

Sample Number 38 (b)

$p'_{initial}$	251.5	kPa	σ_d'	98	kPa
$e_{initial}$	0.74		period	20	seconds
$S_{r\,initial}$	83%		N	no failure	

Figure C.5 - Sample #38 (b), Gassy.

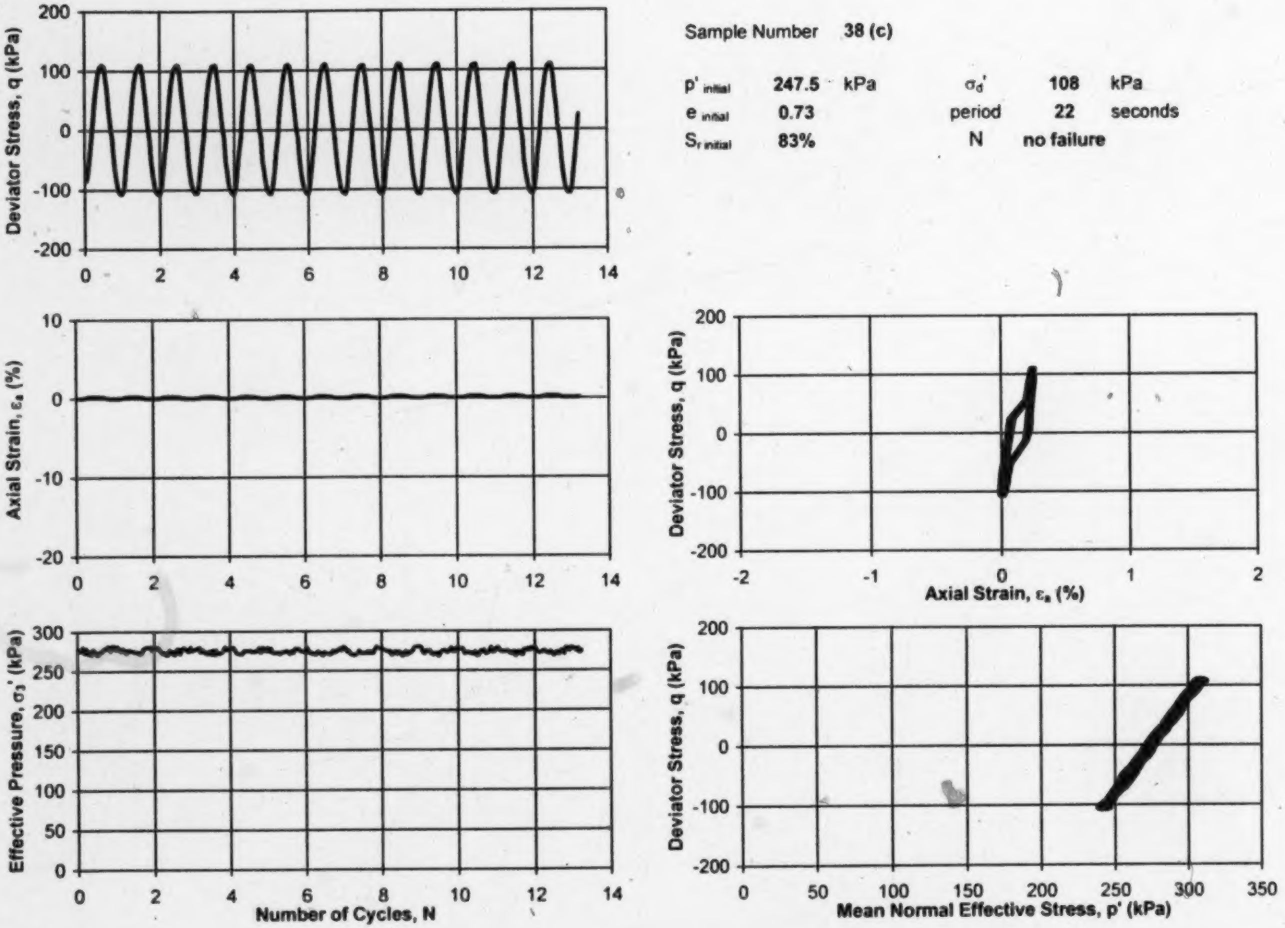

Sample Number 38 (c)

$p'_{initial}$	247.5	kPa	σ_d'	108	kPa
$e_{initial}$	0.73		period	22	seconds
$S_{r\,initial}$	83%		N	no failure	

Figure C.6 - Sample #38 (c), Gassy.

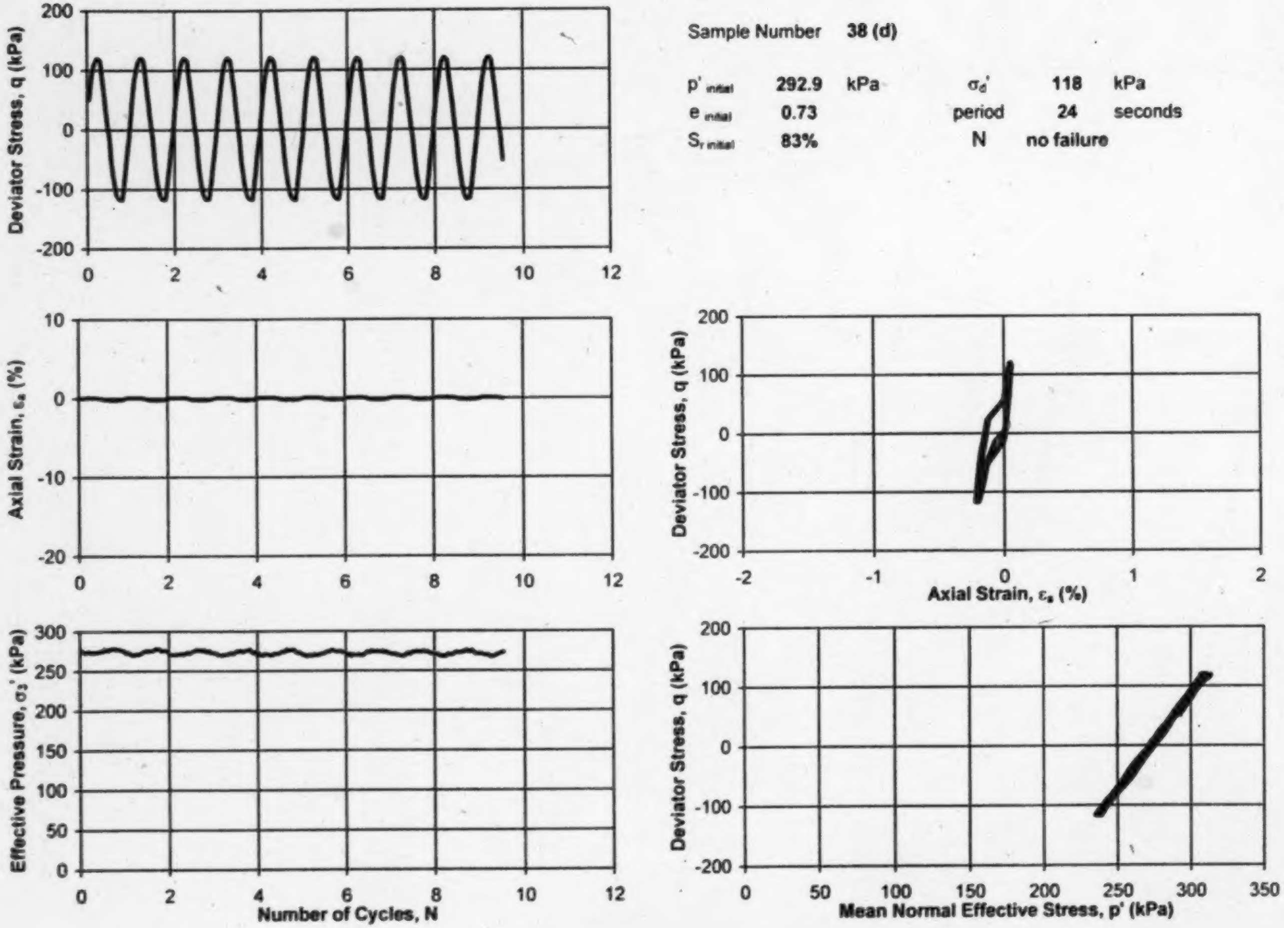

Sample Number 38 (d)

$p'_{initial}$	292.9	kPa	σ_d'	118	kPa
$e_{initial}$	0.73		period	24	seconds
$S_{r\,initial}$	83%		N	no failure	

Figure C.7 - Sample #38 (d), Gassy.

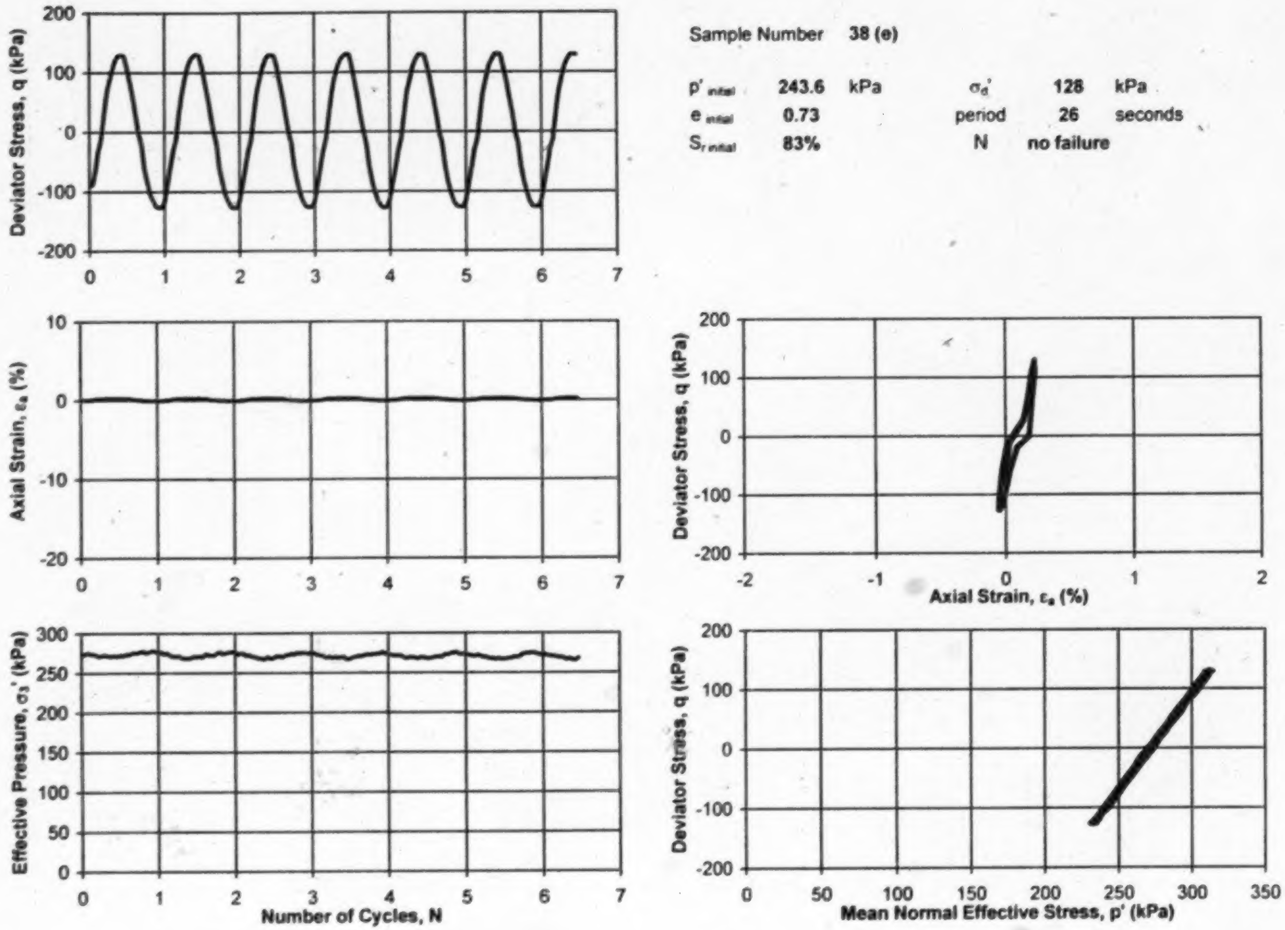

Sample Number 38 (e)

$p'_{initial}$	243.6	kPa	σ_d'	128	kPa
$e_{initial}$	0.73		period	26	seconds
$S_{r\,initial}$	83%		N	no failure	

Figure C.8 - Sample #38 (e), Gassy.

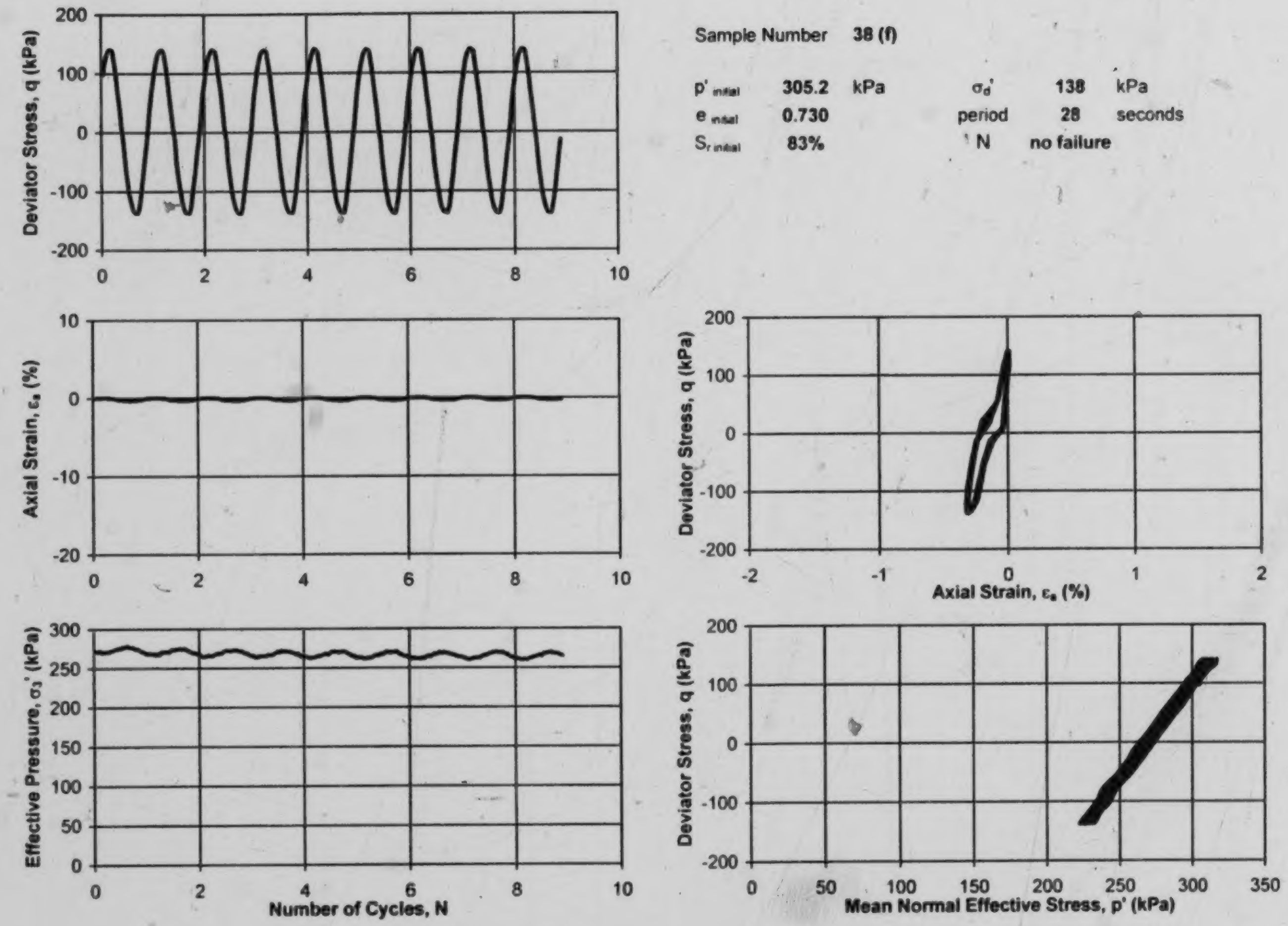

Sample Number 38 (f)

$p'_{initial}$	305.2	kPa	σ_d'	138	kPa
$e_{initial}$	0.730		period	28	seconds
$S_{r\,initial}$	83%		N	no failure	

Figure C.9 - Sample #38 (f), Gassy.

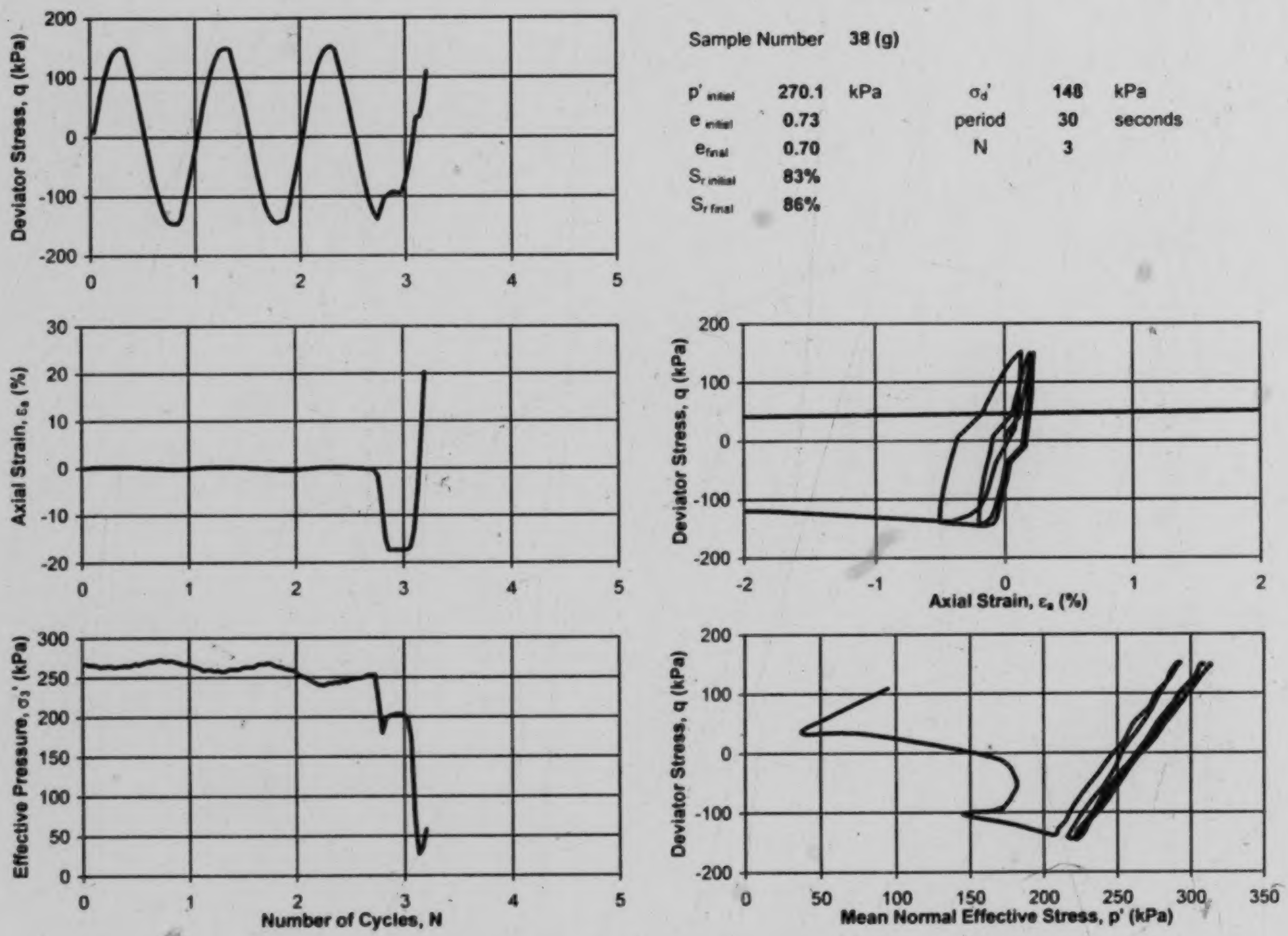

Sample Number 38 (g)

$p'_{initial}$	270.1	kPa	σ_d'	148	kPa
$e_{initial}$	0.73		period	30	seconds
e_{final}	0.70		N	3	
$S_{r\,initial}$	83%				
$S_{r\,final}$	86%				

Figure C.10 - Sample #38 (g), Gassy.

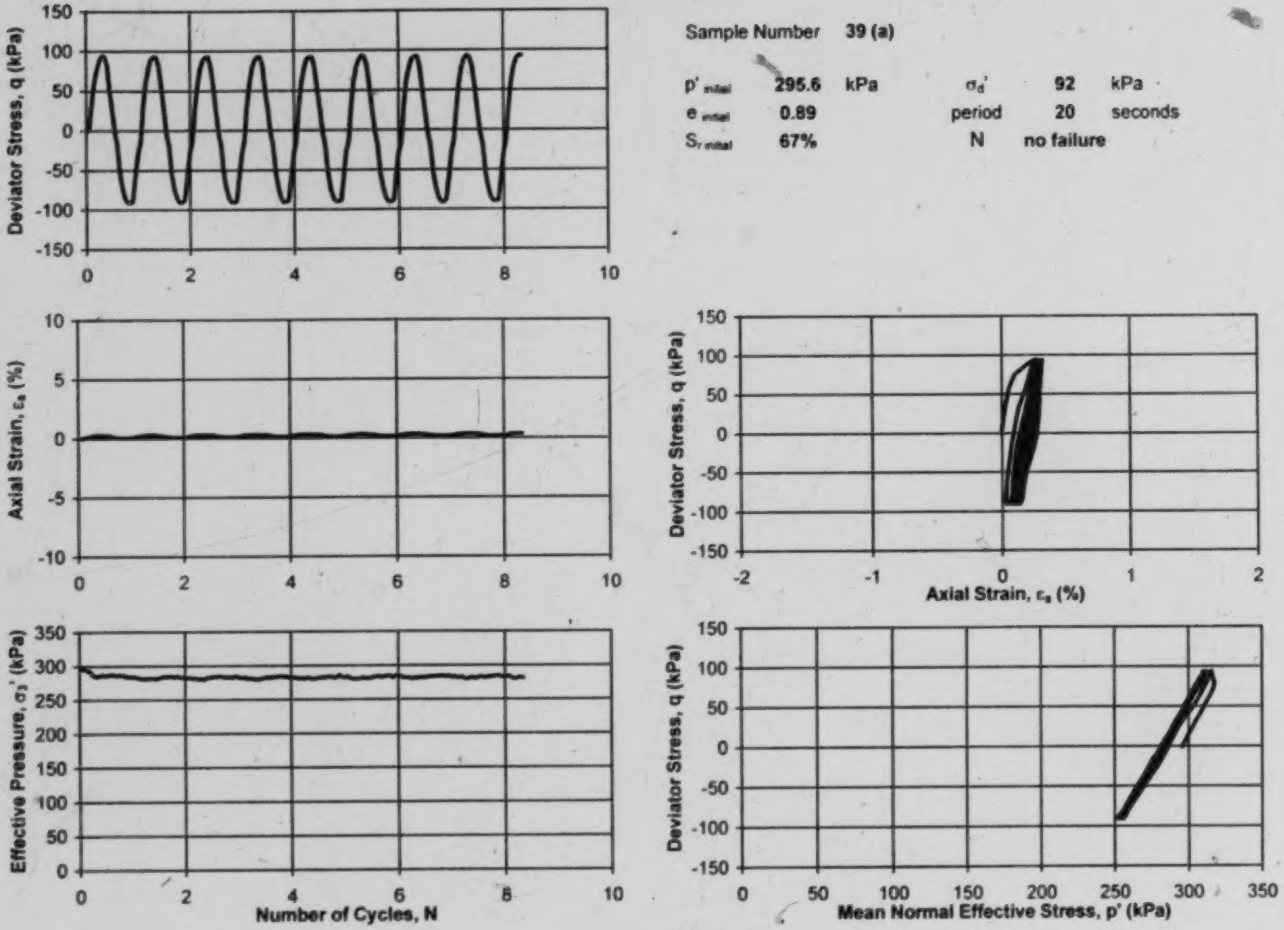

Sample Number 39 (a)

$p'_{initial}$	295.6	kPa	σ_d'	92	kPa
$e_{initial}$	0.89		period	20	seconds
$S_{r\,initial}$	67%		N	no failure	

Figure C.11 - Sample #39 (a), Gassy.

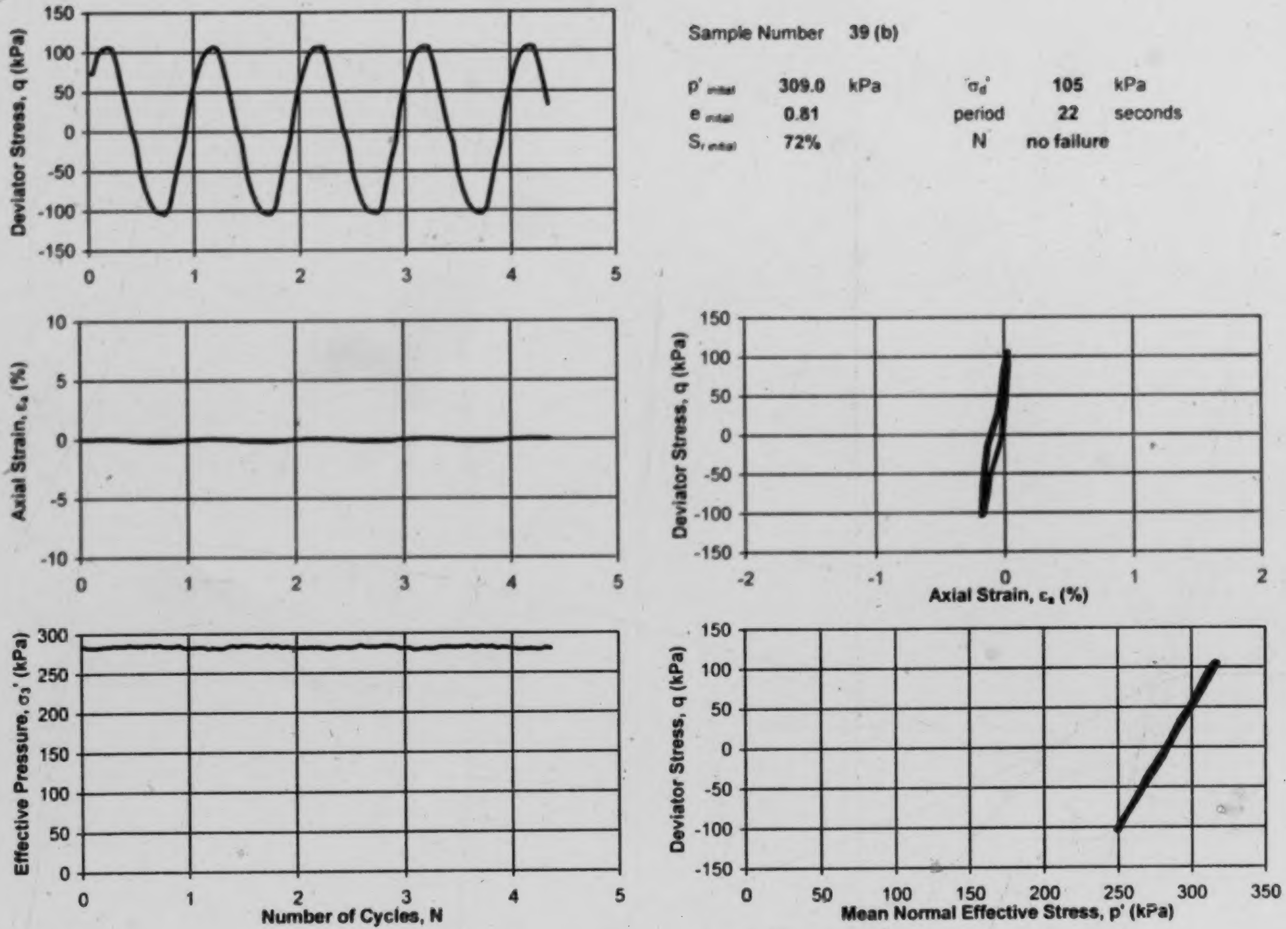

Sample Number	39 (b)				
$p'_{initial}$	309.0	kPa	σ_d'	105	kPa
$e_{initial}$	0.81		period	22	seconds
$S_{r\ initial}$	72%		N	no failure	

Figure C.12 - Sample #39 (b), Gassy.

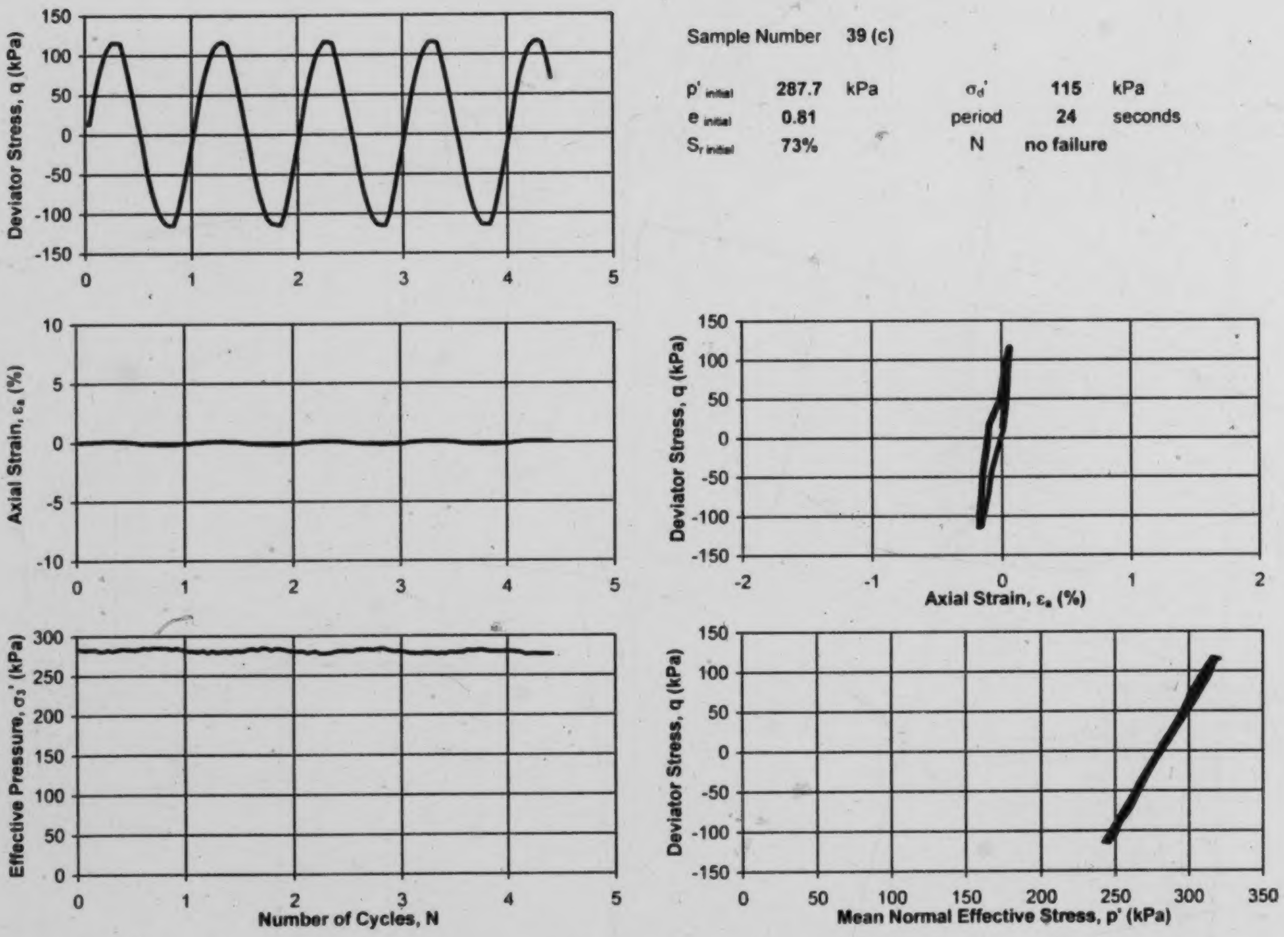

Sample Number 39 (c)

$p'_{initial}$	287.7	kPa	σ_d'	115	kPa
$e_{initial}$	0.81		period	24	seconds
$S_{r\,initial}$	73%		N	no failure	

Figure C.13 - Sample #39 (c), Gassy.

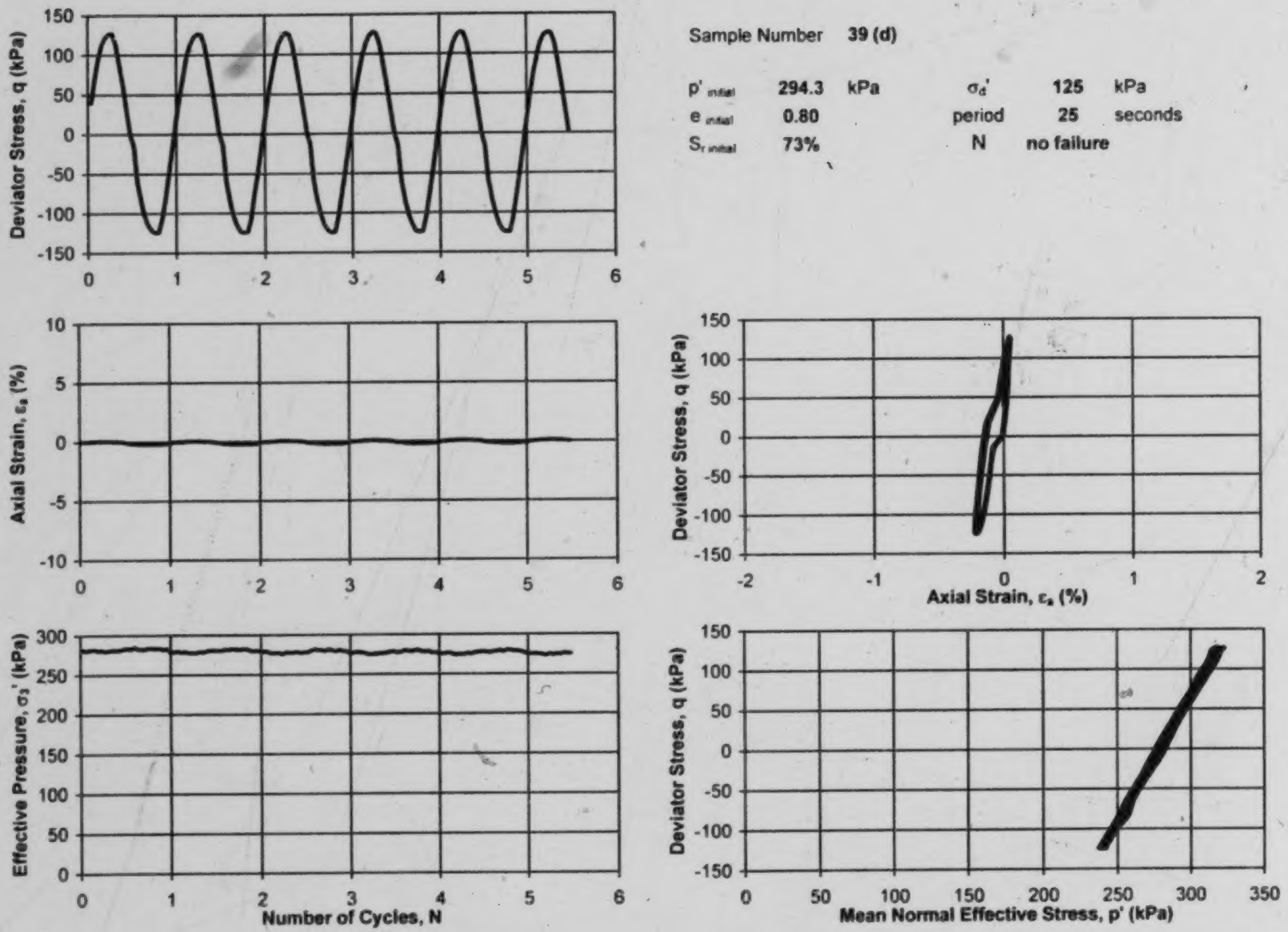

Sample Number 39 (d)

$p'_{initial}$	294.3	kPa	σ_d'	125	kPa
$e_{initial}$	0.80		period	25	seconds
$S_{r\ initial}$	73%		N	no failure	

Figure C.14 - Sample #39 (d), Gassy.

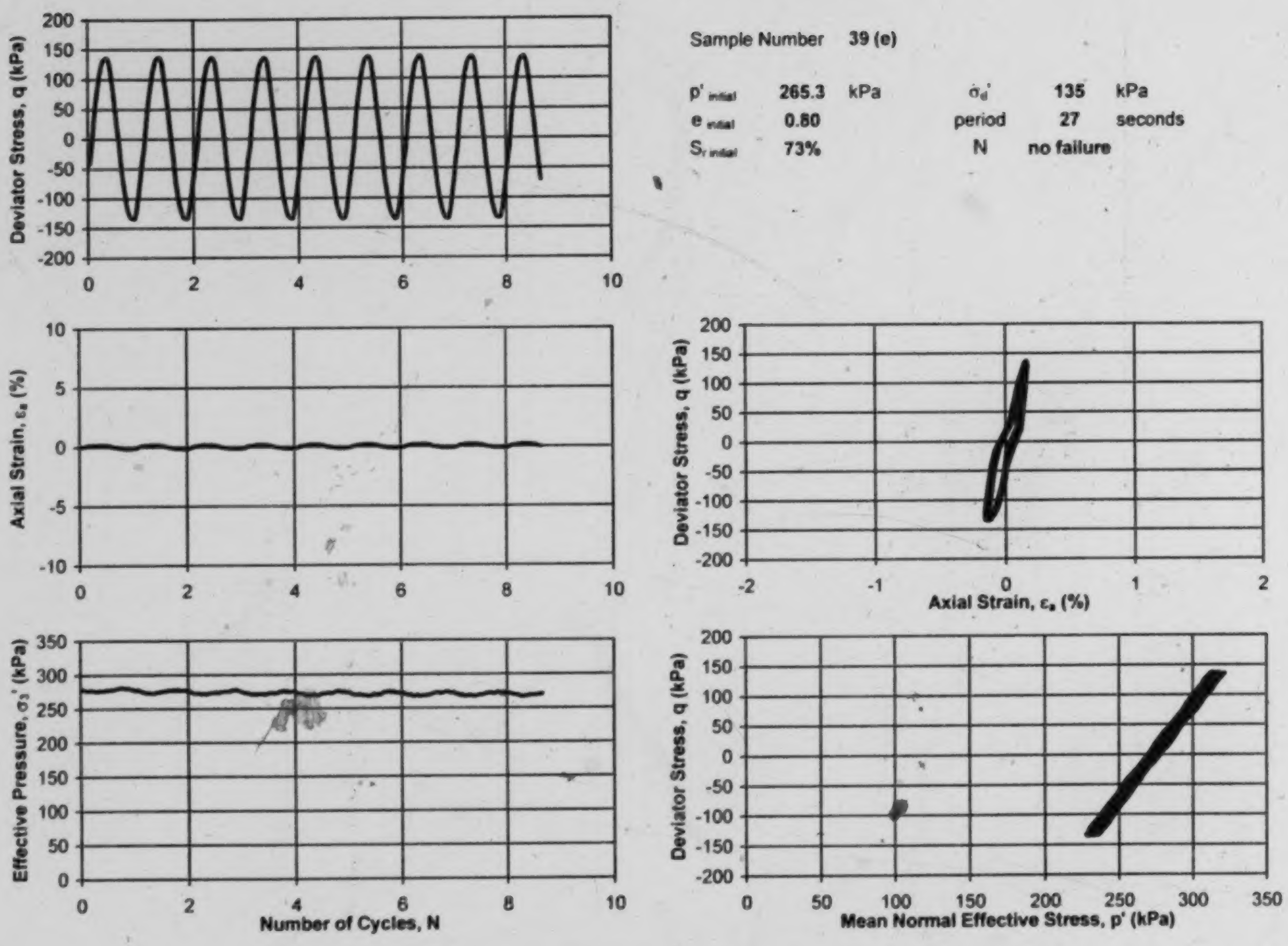

Sample Number 39 (e)

$p'_{initial}$	265.3	kPa	σ_d'	135	kPa
$e_{initial}$	0.80		period	27	seconds
$S_{r\,initial}$	73%		N	no failure	

Figure C.15 - Sample #39 (e), Gassy.

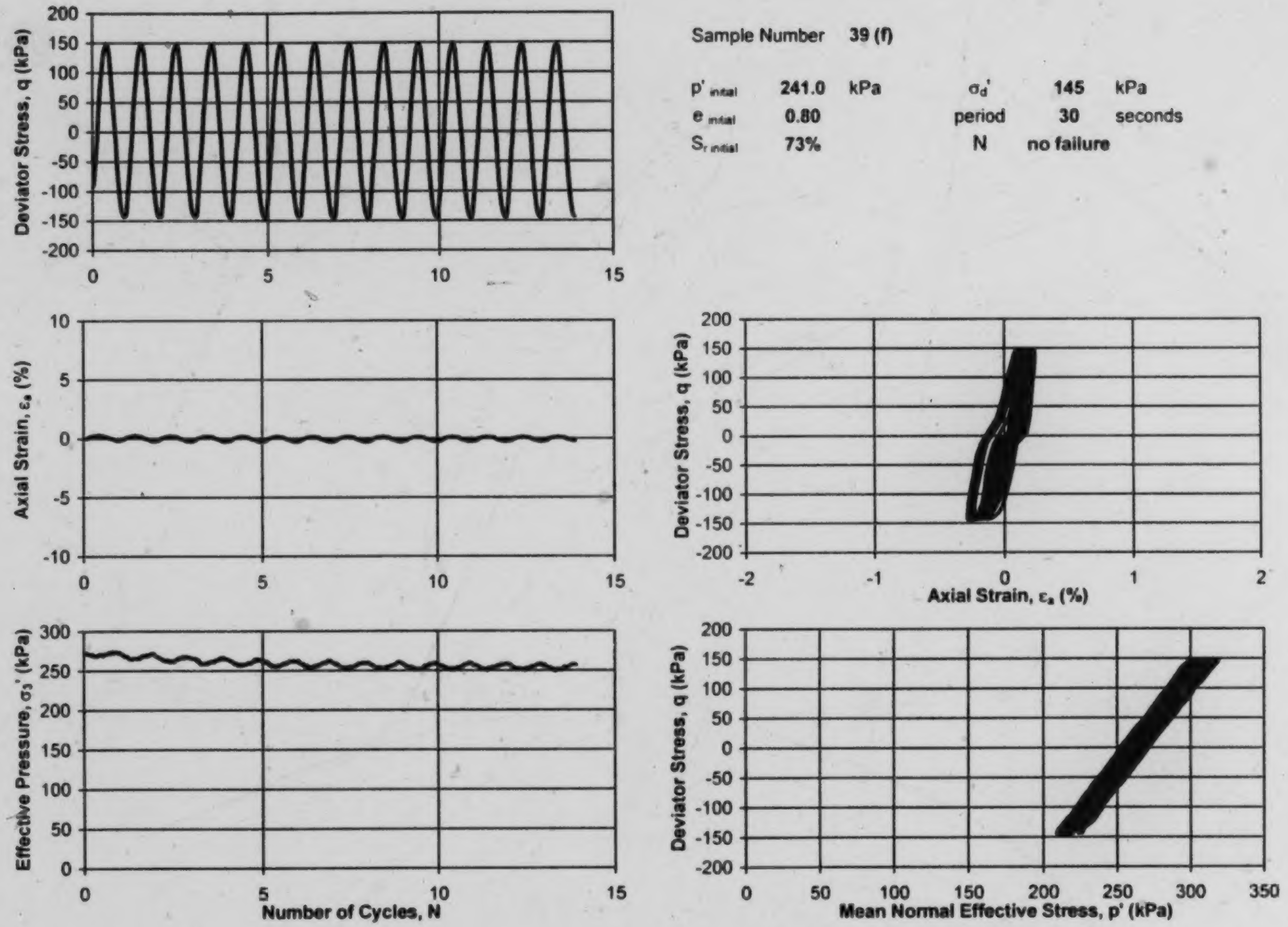

Sample Number 39 (f)

$p'_{initial}$	241.0	kPa	σ_d'	145	kPa
$e_{initial}$	0.80		period	30	seconds
$S_{r\,initial}$	73%		N	no failure	

Figure C.16 - Sample #39 (f), Gassy.

Sample Number 39 (g)

$p'_{initial}$	213.1	kPa	σ_d'	155	kPa
$e_{initial}$	0.79		period	31	seconds
e_{final}	0.69		N	2	
$S_{r\,initial}$	74%				
$S_{r\,final}$	83%				

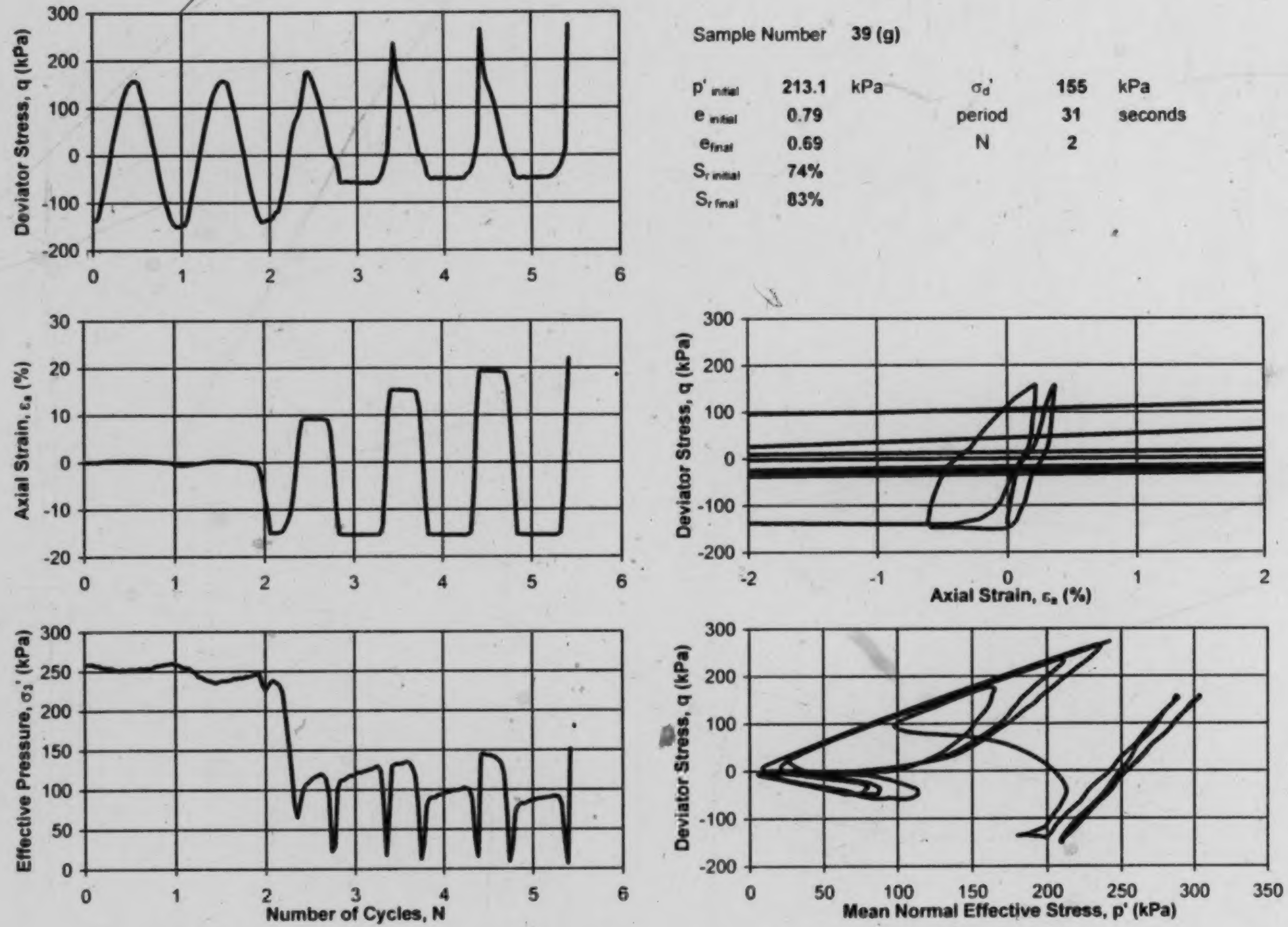

Figure [illegible]7 - Sample #39 (g), Gassy.

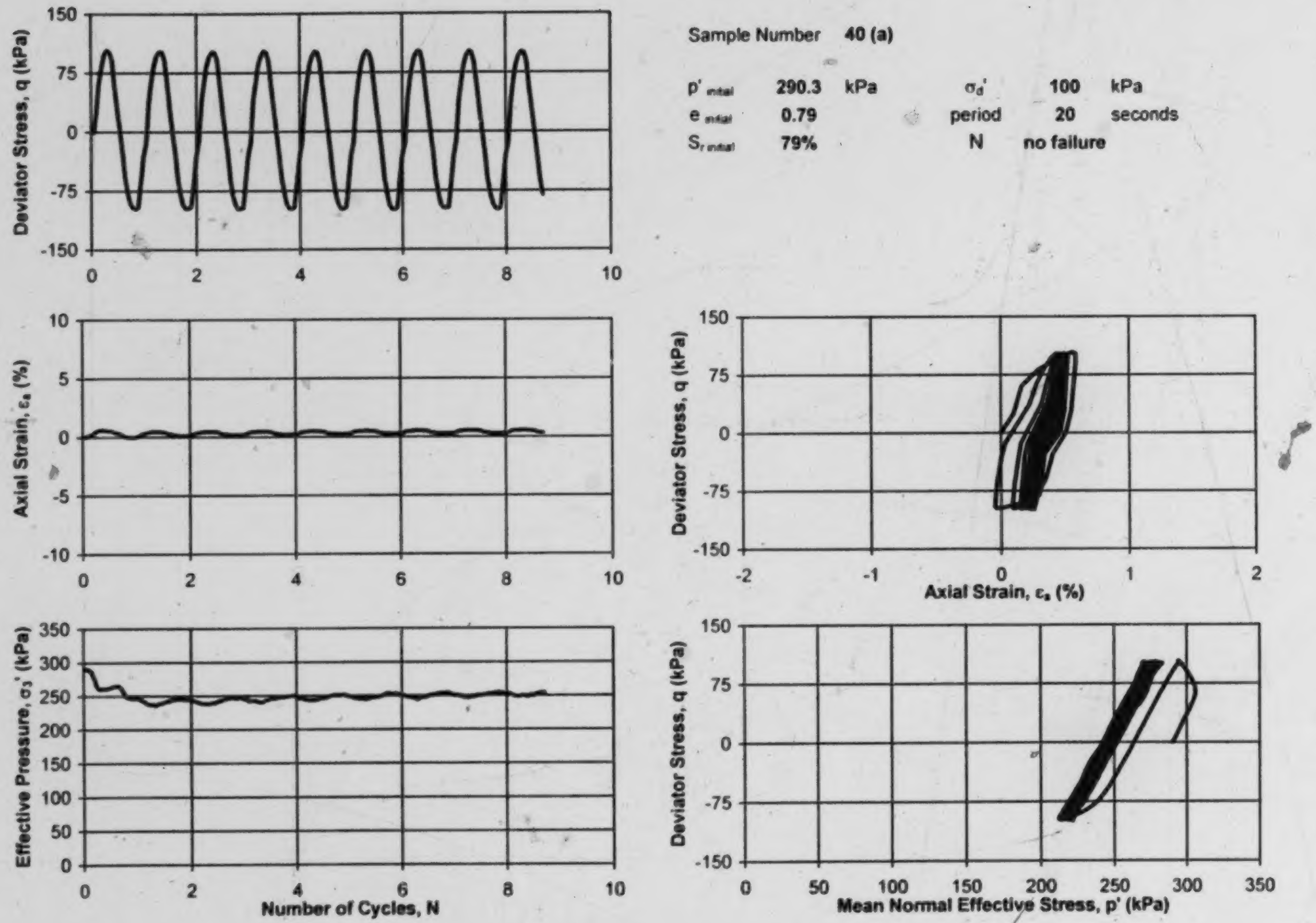

Sample Number 40 (a)

$p'_{initial}$	290.3	kPa	σ_d'	100	kPa
$e_{initial}$	0.79		period	20	seconds
$S_{r\,initial}$	79%		N	no failure	

Figure C.18 - Sample #40 (a), Gassy.

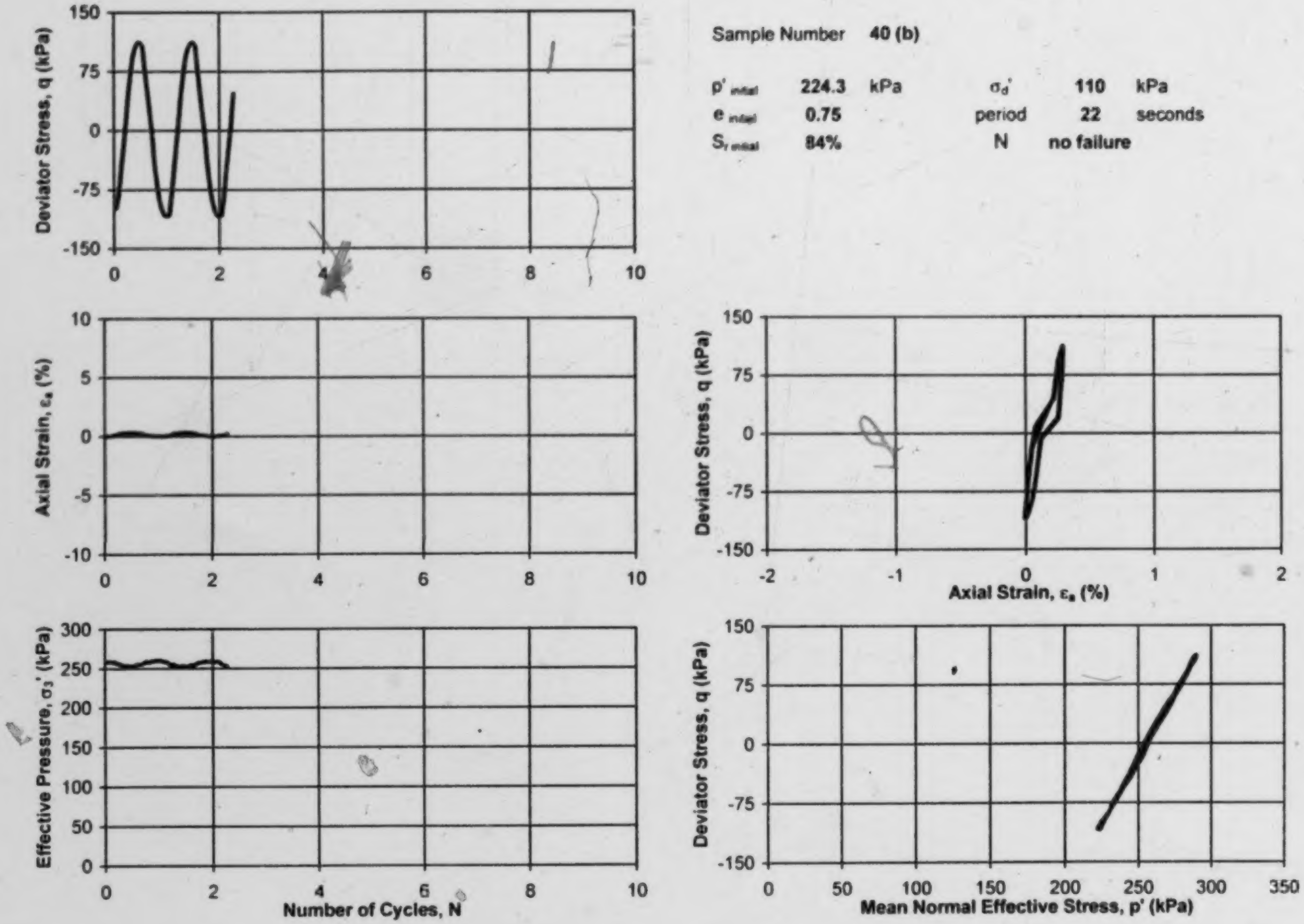

Figure C.19 - Sample #40 (b), Gassy.

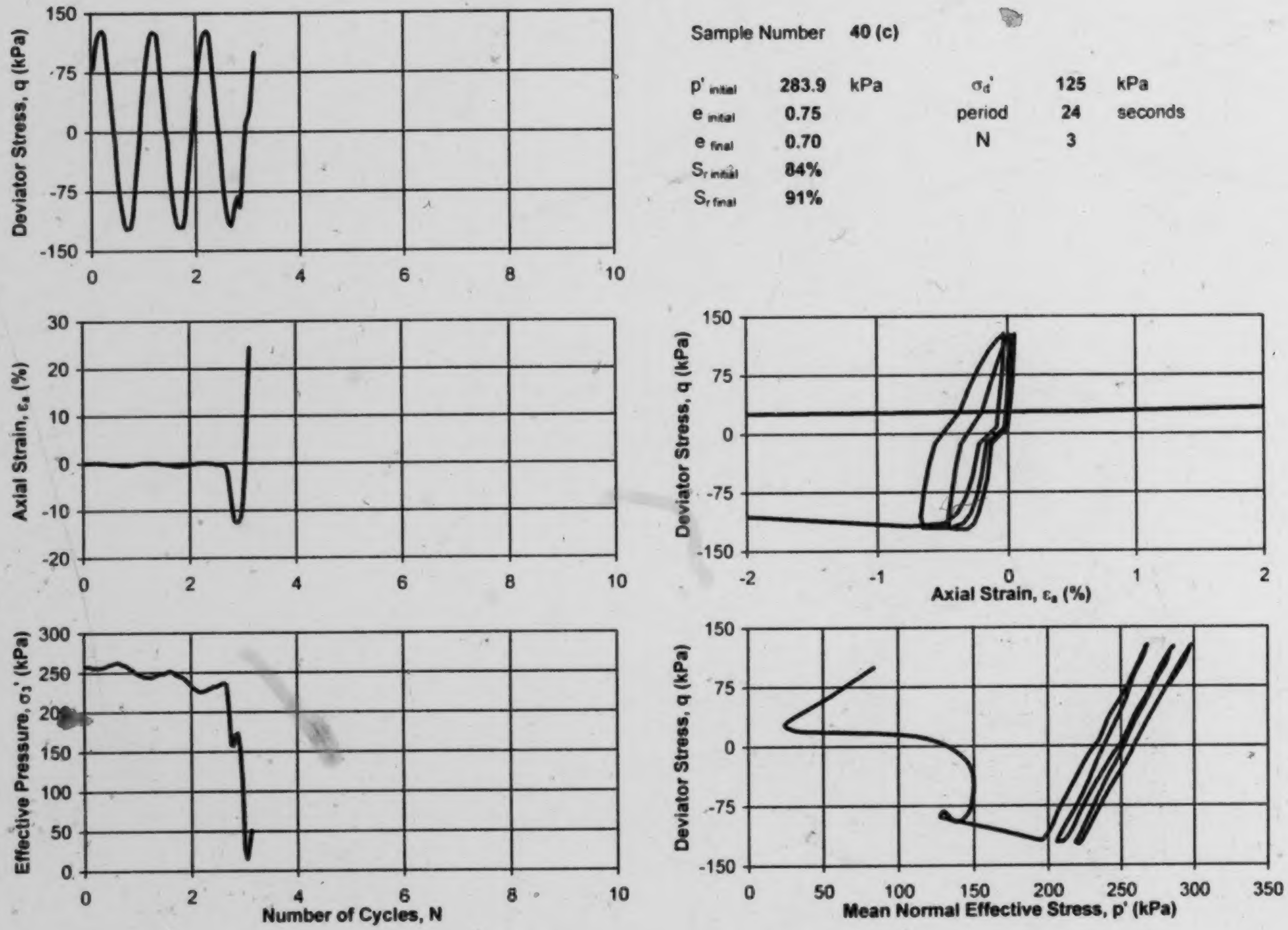

Sample Number	40 (c)				
$p'_{initial}$	283.9	kPa	σ_d'	125	kPa
$e_{initial}$	0.75		period	24	seconds
e_{final}	0.70		N	3	
$S_{r\,initial}$	84%				
$S_{r\,final}$	91%				

Figure C.20 - Sample #40 (c), Gassy.

Sample Number **41 (a)**

$p'_{initial}$	**295.2**	kPa	σ_d'	**125**	kPa
$e_{initial}$	**0.74**		period	**24**	seconds
$S_{r\,initial}$	**71%**		N	**no failure**	

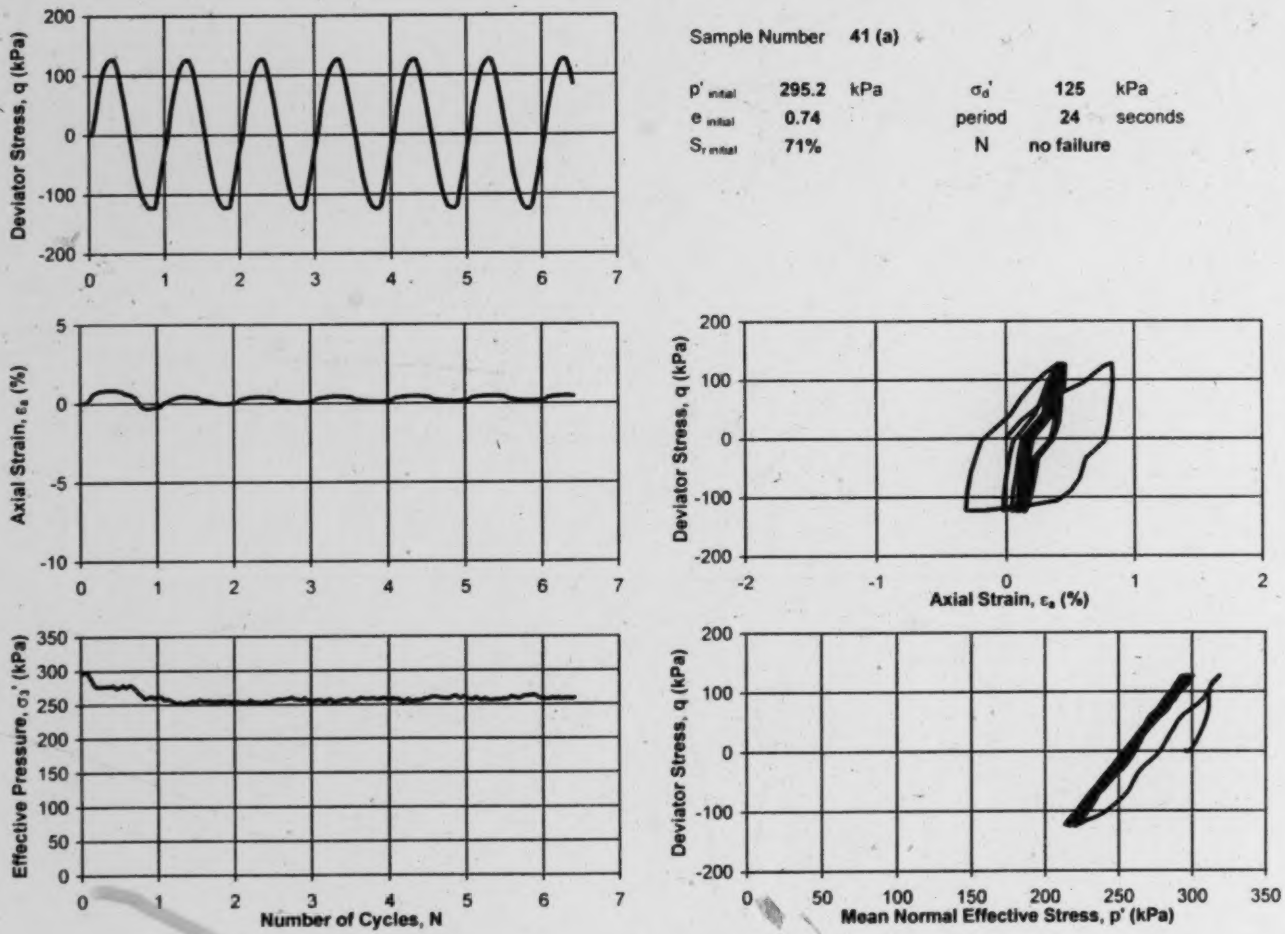

Figure C.21 - Sample #41 (a), Gassy.

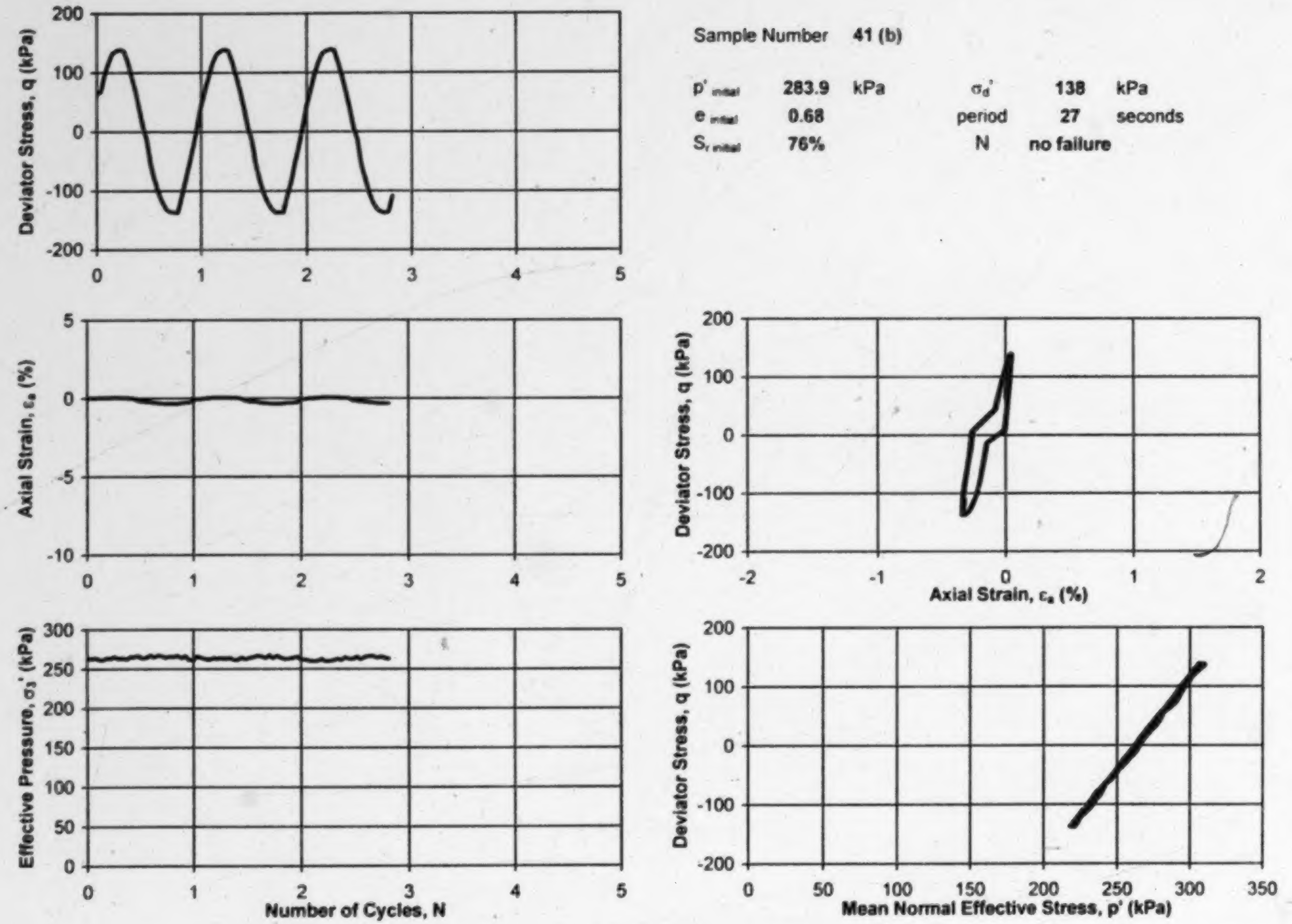

Figure C.22 - Sample #41 (b), Gassy.

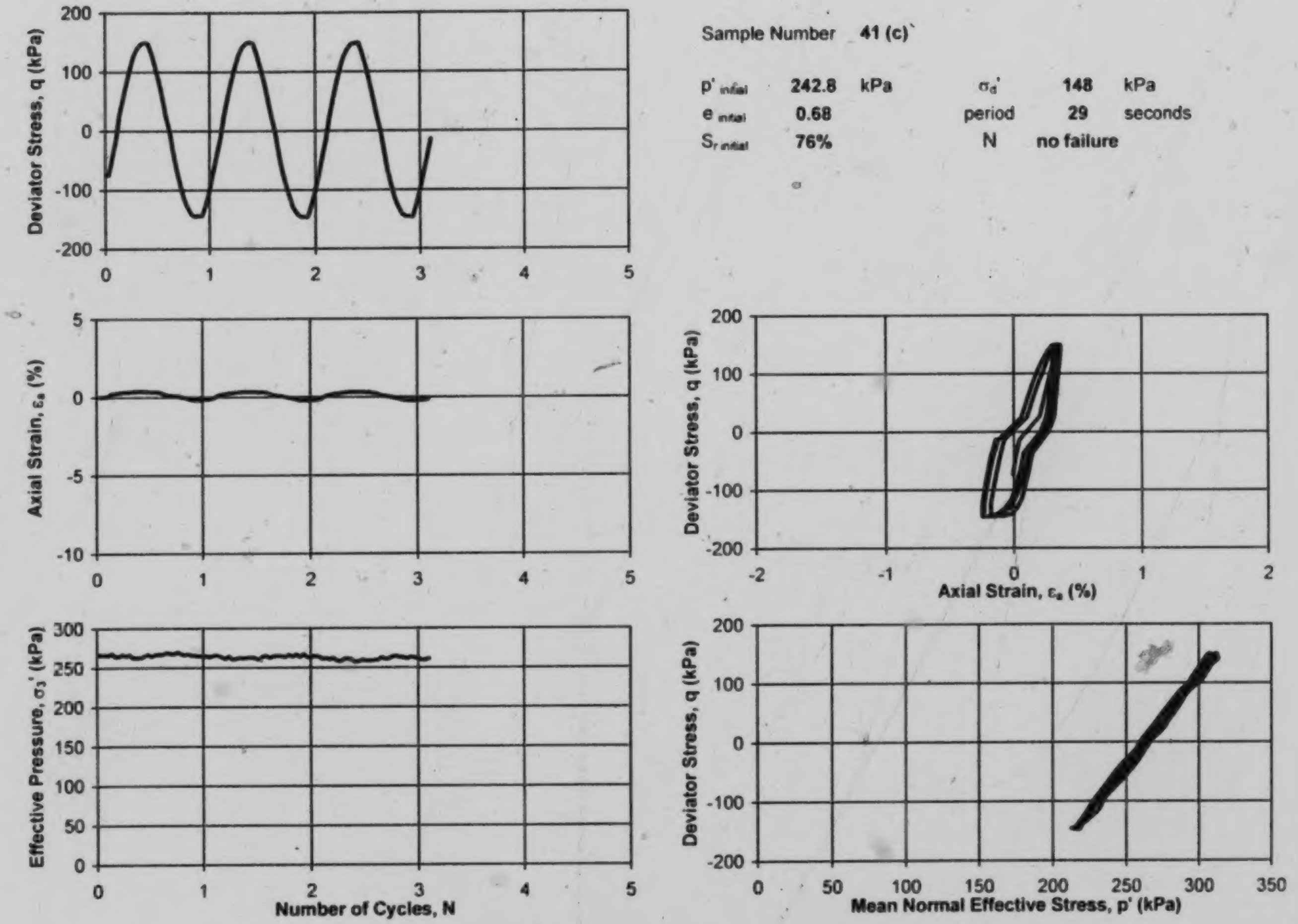

Sample Number 41 (c)`

p' initial	242.8	kPa	σd'	148	kPa
e initial	0.68		period	29	seconds
Sr initial	76%		N	no failure	

Figure C.23 - Sample #41 (c), Gassy.

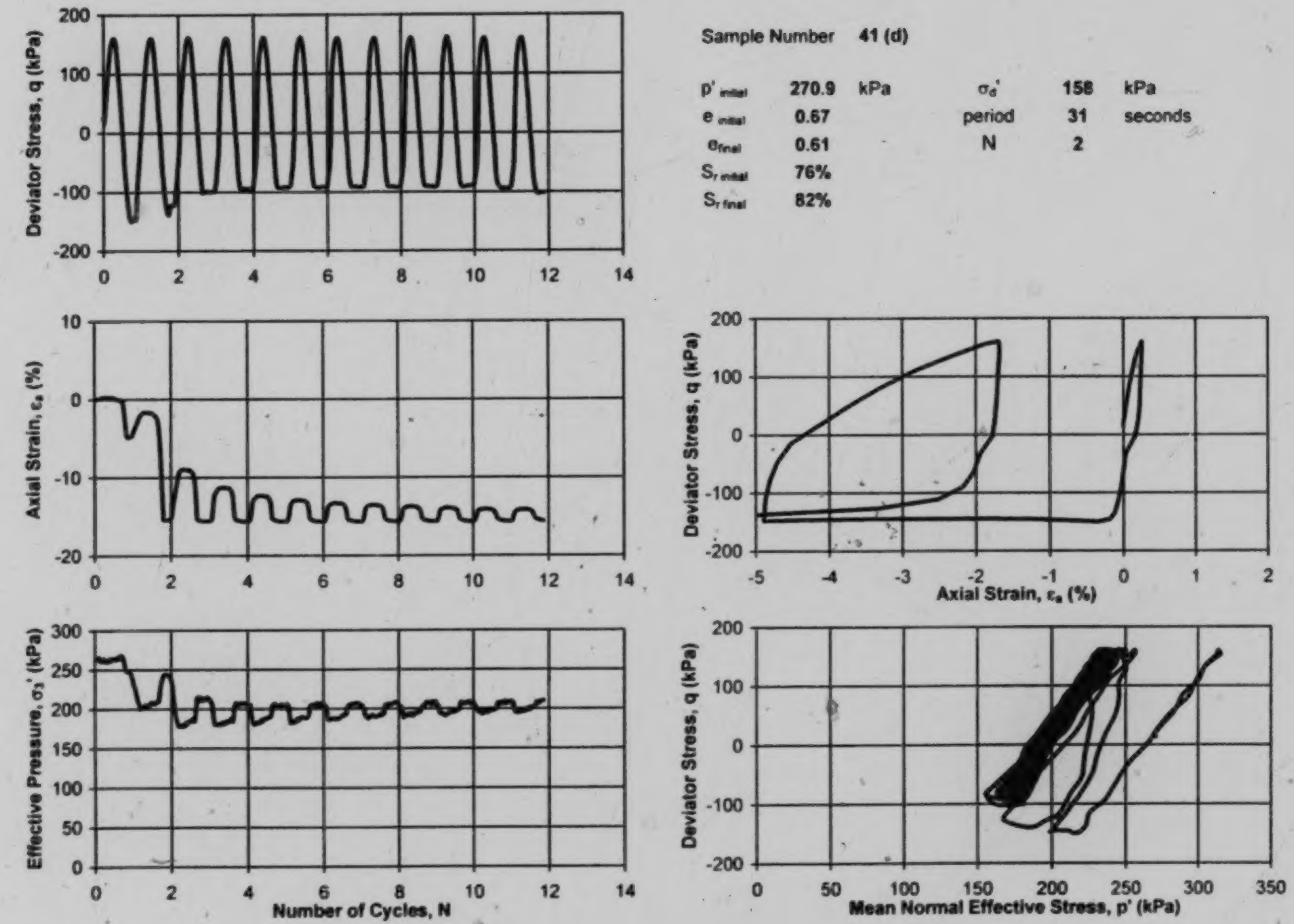

Sample Number 41 (d)

$p'_{initial}$	270.9	kPa	σ_d'	158	kPa
$e_{initial}$	0.67		period	31	seconds
e_{final}	0.61		N	2	
$S_{r\,initial}$	76%				
$S_{r\,final}$	82%				

Figure C.24 - Sample #41 (d), Gassy.

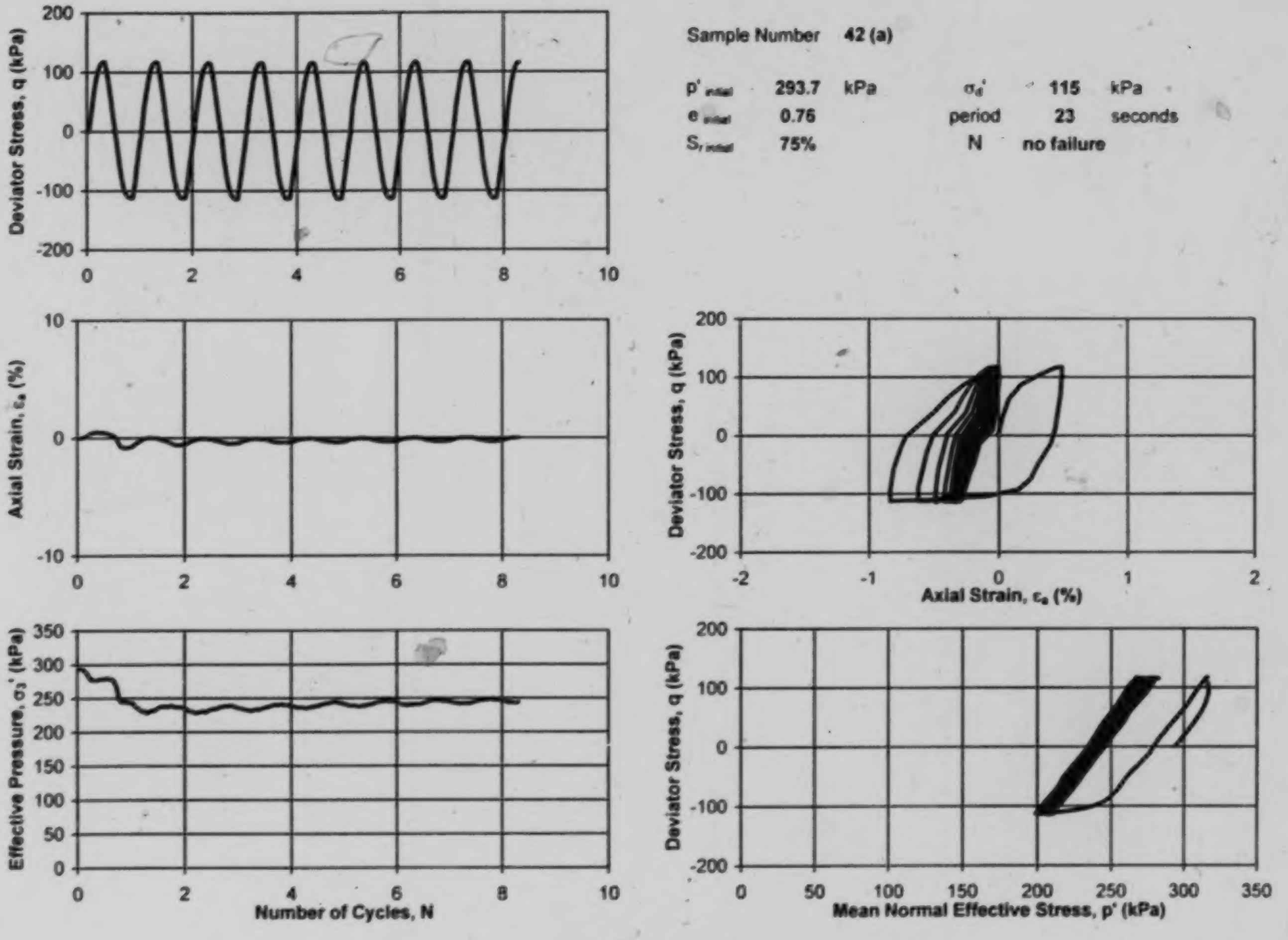

Sample Number 42 (a)

$p'_{initial}$	293.7	kPa	σ_d'	115	kPa
$e_{initial}$	0.76		period	23	seconds
$S_{r\,initial}$	75%		N	no failure	

Figure C.25 - Sample #42 (a), Gassy.

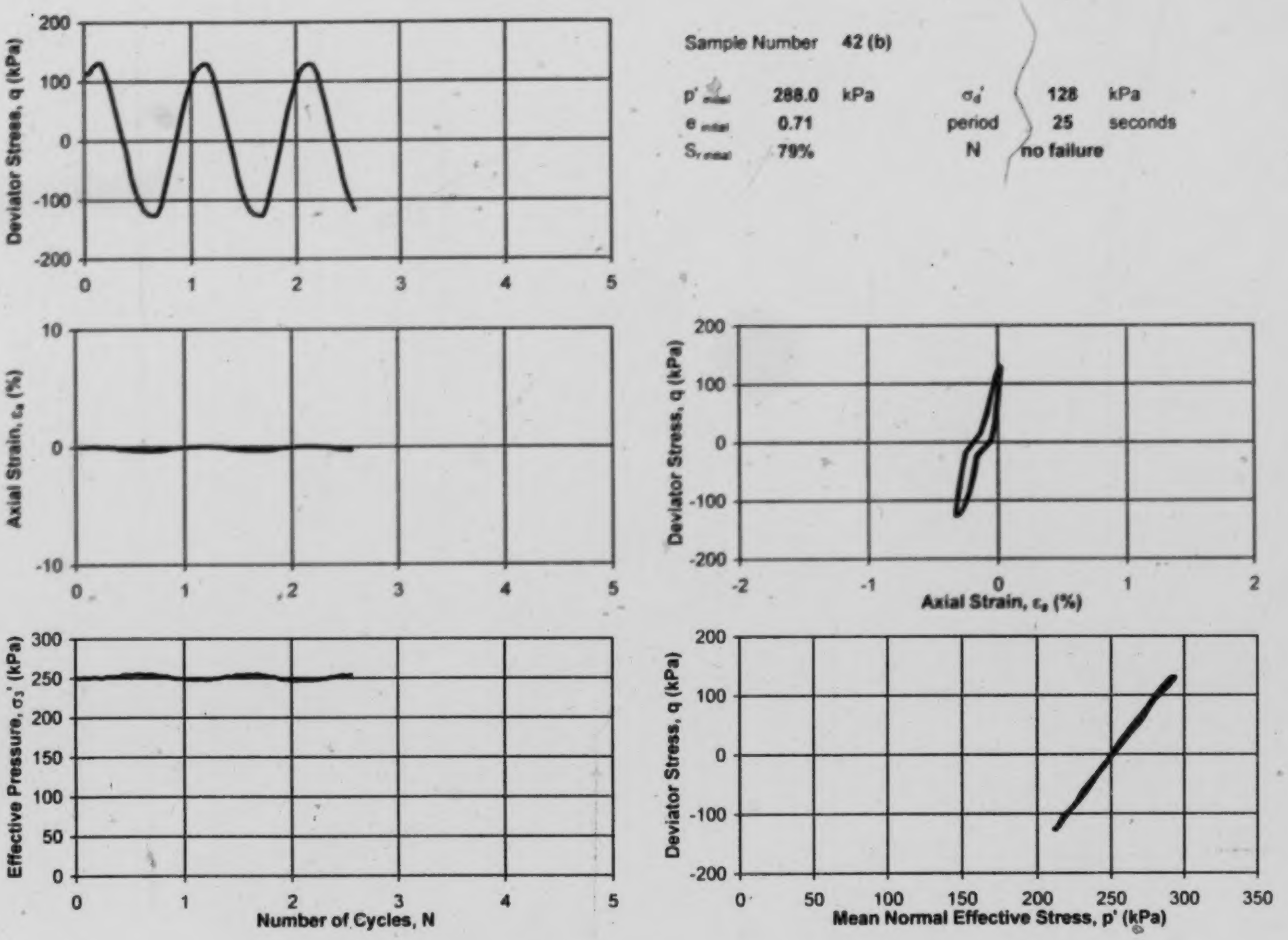

Figure C.26 - Sample #42 (b), Gassy.

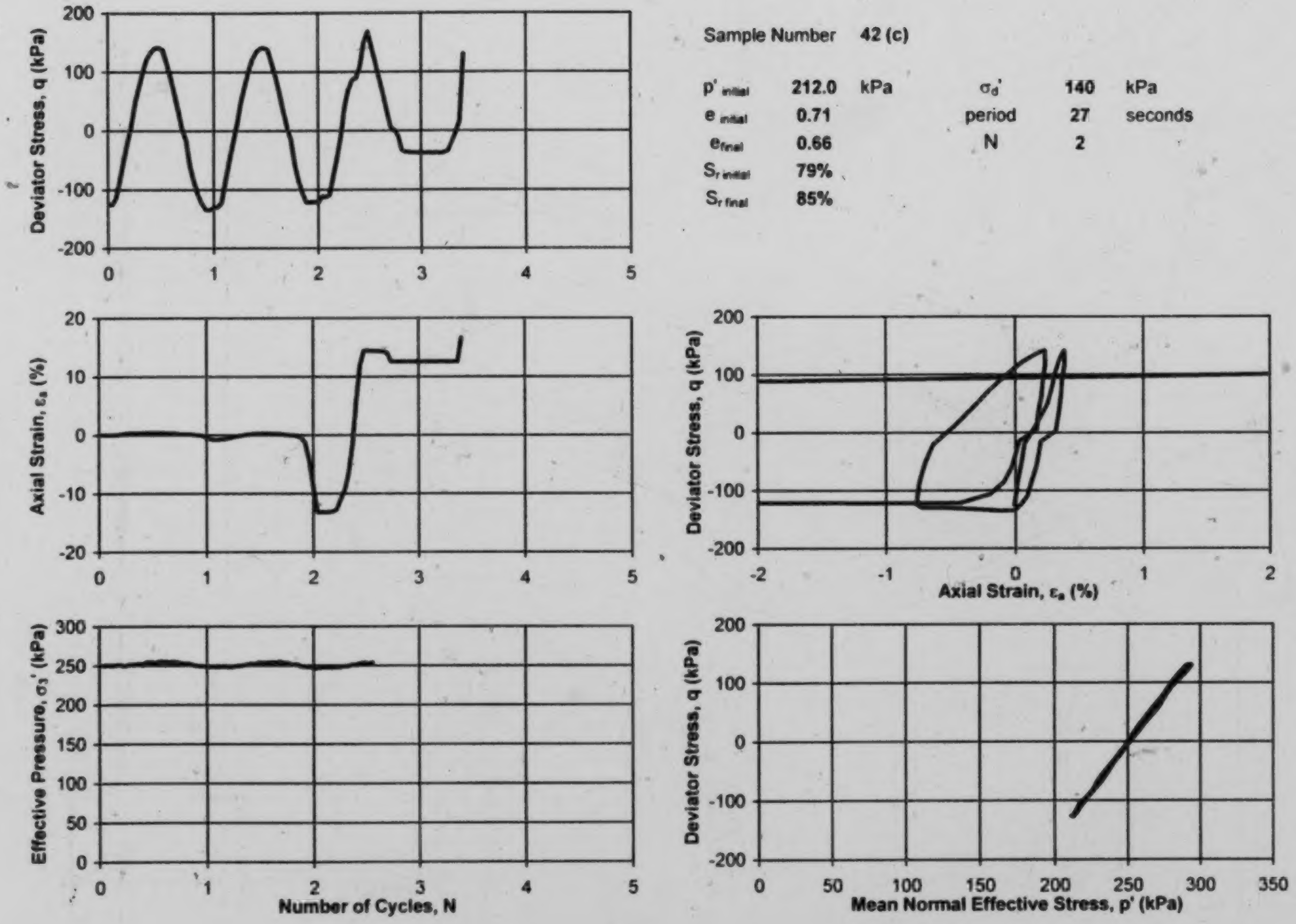

Sample Number 42 (c)

$p'_{initial}$	212.0	kPa	σ_d'	140	kPa
$e_{initial}$	0.71		period	27	seconds
e_{final}	0.66		N	2	
$S_{r\,initial}$	79%				
$S_{r\,final}$	85%				

Figure C.27 - Sample #42 (c), Gassy.